Design and Fabrication of One-dimensional and Two-dimensional Photonic Bandgap Devices

by

Kuo-Yi Lim

S.B., Electrical Science & Engineering, Massachusetts Institute of Technology (1994)
M.Eng., Electrical Engineering & Computer Science, Massachusetts Institute of Technology (1994)
Electrical Engineer, Massachusetts Institute of Technology (1996)

Submitted to the

Department of Electrical Engineering and Computer Science

in partial fulfillment of the requirements for the degree of

Doctor of Philosophy in Electrical Engineering

at the

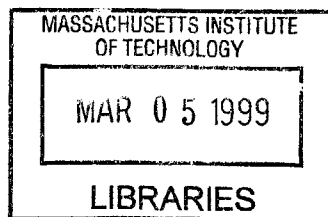## MASSACHUSETTS INSTITUTE OF TECHNOLOGY

February 1999

Author...
Department of Electrical Engineering and Computer Science
November 17, 1998

Certified by:..............................
Leslie A. Kolodziejski
Associate Professor of Electrical Engineering
Thesis Supervisor

Accepted by:..............................
Arthur C. Smith
Chairman, Department Committee on Graduate Students

Design and Fabrication of One-dimensional and Two-dimensional Photonic Bandgap Devices

by

Kuo-Yi Lim

Submitted to the Department of Electrical Engineering and Computer Science on November 17, 1998 in Partial Fulfillment of the Requirements for the Degree of Doctor of Philosophy in Electrical Engineering

Abstract

One-dimensional and two-dimensional photonic bandgap devices have been designed and fabricated using III-V compound semiconductors. The one-dimensional photonic bandgap devices consist of monorail and air-bridge waveguide microcavities, while the two-dimensional photonic bandgap devices consist of light-emitting devices with enhanced extraction efficiency. Fabrication techniques such as gas source molecular beam epitaxy, direct-write electron-beam lithography, reactive ion etching and thermal oxidation of $Al_xGa_{1-x}As$ have been employed. The III-V thermal oxide, in particular, is used as an index confinement material, as a sacrificial material for micromechanical fabrication of the air-bridge microcavity, and in the realization of a wide-bandwidth distributed Bragg reflector.

The one-dimensional photonic bandgap waveguide microcavities have been designed to operate in the wavelength regimes of $4.5\mu m$ and $1.55\mu m$. The devices designed to operate in the $1.55\mu m$ wavelength regime have been optically characterized. The transmission spectra exhibit resonances at around $1.55\mu m$ and cavity quality factors (Q's) ranging from 136 to 334. The resonant modal volume is calculated to be about $0.056\mu m^3$. Tunability in the resonance wavelengths has also been demonstrated by changing the size of the defect in the one-dimensional photonic crystal.

The two-dimensional photonic bandgap light-emitting device consists of a $In_{0.51}Ga_{0.49}P/In_{0.2}Ga_{0.8}As/In_{0.51}Ga_{0.49}P$ quantum well emitting at 980nm with a triangular photonic lattice of holes in the top cladding layer of the quantum well. The photonic crystal prohibits the propagation of guided modes in the semiconductor, thus enhancing the extraction of light vertical to the light-emitting device. A wide-bandwidth $GaAs/Al_xO_y$ distributed Bragg reflector mirror under the quantum well structure further enhances the extraction of light from the devices. The extraction efficiency of the two-dimensional photonic bandgap light-emitting device is expected to be at least 5 times that of a device without the two-dimensional photonic crystal. A photoluminescence measurement setup has been modified to optically characterize these devices.

Thesis Supervisor: Leslie A. Kolodziejski

Title: Associate Professor of Electrical Engineering

Acknowledgments

First and foremost, a large dose of gratitude is reserved for Professor Leslie Kolodziejski. She has been a friend, a mentor and a guidance counselor to me for the past six years. I consider it a great personal fortune to have signed on as an undergraduate research student with her. Her high standards of integrity, humaneness and professionalism remain yardsticks against which I measure myself and hope to match.

A big thank you to Dr. Gale Petrich, for without his assistance and friendship over the years, I wouldn't have gotten to this point. His MBE skills and machine-fixing prowess are well appreciated. He is certainly a great asset to the research group and a good friend to me personally.

I have also enjoyed working with Professors John Joannopoulos and Erich Ippen. Their mastery of the subject matter, their ability to convey that understanding and insight transparently, their enthusiasm and their awesome intellectual ability... what more do I need to say?

The experience of my collaboration with the other members of the crew, namely Daniel Ripin, Costas Tziligakis, Dr. Pierre Villeneuve and Dr. Shanhui Fan, have been uniquely enjoyable. These are the brightest and the nicest people, with the greatest amount of patience and humor, whom I have worked with. I truly appreciate their help in the completion of my thesis; guys, the success is as much yours as it is mine. Thanks for keeping faith.

To my officemate, Elisabeth Koontz, who have listened often to my diatribes against undesirable and subversive elements of this great Institution, your friendship is greatly, greatly appreciated.

To members of the Kolodziejski group, past (in particular, Drs Easen Ho and Jody House) and present (Steve Patterson, Alexei Erchak, Sajan Saini), thanks for simply being who you are.

To Cindy Ong, who has provided the support, companionship and care behind the scene, I hope you will share in my success as much as you have suffered with me in this degree-chasing joyride.

Finally, and most importantly, to my family. I can't say enough about how their patience, support and love from halfway around the world have kept me going. They have provided the constancy in this occasionally bumpy and unpredictable ride over the duration of my career at MIT. For this, I am blessed.

Table of contents

Chapter 1 Introduction

1.1 Motivation

The impact of the semiconductor integrated circuit on modern society is indisputably far-reaching and revolutionary. The "chip", as an IC is often referred to, has spawned multi-billion dollar industries and changed the way we live. Meanwhile, the increasing processing power of the IC and the drop in its cost are perpetuating the pervasiveness of the chip in every facet of our lives. The oft-cited Moore's Law has predicted a doubling in the number of transistors on an IC every 18 months. The Law has consistently foretold the trend in the semiconductor industry since its coinage by Gordon Moore in 1975.

Roadblocks, however, lie ahead in the path of this trend. As the density of transistors in an IC increases, interconnect latency presents the major bottleneck to increasing microprocessor performance. The limitation is especially dire in the distribution of clock signals and the transmission of data along common bus lines, where the transmission paths are the longest. The problem is largely a consequence of the use of the electron as the information carrier in the interconnects. Electrons are particles with both mass and charge. As a result, they interact with one another and with the metal atoms that form the interconnects. This limits the interconnect bandwidth and how closely the interconnects can be placed together. Problems such as electromigration and ohmic heating also arise. While innovations like copper interconnects have alleviated the problems, a new long-term strategy in interconnect technology is clearly necessary.

The photon is an attractive alternative to the electron as an information carrier. Photons are intrinsically faster than electrons in any medium and carries neither mass nor charge. The resultant bandwidth and transmission throughput of an optical interconnect is therefore considerably larger than in the case of the electron. Photons also propagate in free space, opening up other possibilities for transmitting signals. Recognizing that optical interconnects in tandem with electronic logic components may become the next paradigm of microprocessor design, investigation into the integration of optical and

electronic devices on the same chip is already under way [1]. Looking further ahead, the full fledge implementation of optical computing architecture is also being studied [2, 3].

From these efforts arises the need for nanoscale photonic devices that can be densely packed on a chip while consuming as little operating power as possible. Photonic circuit components like photoemitters and photodetectors will be necessary to allow the generation and reception of optical signals across the chip. Other components such as filters, resonators and switches will also be useful components of an optoelectronic circuit designer's toolkit. In short, the ability to manipulate light at the nanoscale while consuming minimal power will be critical to the implementation of a photonic integrated circuit and microprocessor.

Parallel to the development of the optoelectronic integration is the advancement in *microcavity* device research. It has been known for a while that the radiative dynamics of an atom can be affected by altering the environment in which the atom radiates [4, 5]. The density of optical modes for an atom radiating within a cavity with perfectly reflecting walls differs from an atom radiating in free space. When the cavity dimensions are reduced to those comparable to the transition wavelength, the density of modes becomes increasingly discrete. Depending on the overlap between the radiation and the cavity resonance wavelength the radiative transition may be enhanced or suppressed. When the transition wavelength overlaps only the resonant wavelength, radiation into the cavity resonant mode is enhanced. Conversely, the transition is inhibited when there is no overlap between the emission and any of the cavity modes. A cavity with dimensions comparable to the radiative wavelength of interest is called a microcavity.

The effect of a cavity on the radiative dynamics of atoms was initially demonstrated in the microwave regime, using Rydberg state atomic beams [6-8]. Subsequent experiments were conducted in the optical regimes with atomic beams [9-11] and organic dyes [12, 13]. Investigation with semiconductors at optical frequencies became possible with the advent of crystal growth techniques like molecular beam epitaxy (MBE) which allows the precise control of layer thickness. Nanofabrication techniques such as electron beam

8

lithography and reactive ion etching have further led to various novel microcavity structures like the air-post and the whispering gallery microcavities [14, 15].

A *raison d'être* of microcavity research is the ability to control spontaneous emission in semiconductor optical devices. Resonant cavity light emitting diodes (RCLED), for instance, have been developed where intensity enhancement and increased device efficiency is attained over conventional LED's. In the RCLED, spontaneous emission into the desired longitudinal mode is enhanced by a planar Fabry-Perot microcavity, while losses from emission into unwanted modes are reduced. The microcavity also changes the radiation pattern of the LED, leading to an increased directionality of emission along the axis of the LED [16]. The possibility of a thresholdless laser has also been predicted when spontaneous emission into the unwanted modes is eliminated[17]. The microcavity laser is expected to operate with a higher frequency response while being more efficient. Since microcavity devices are nanoscopic by design, they are ideal for optoelectronic circuit applications as compact devices with low power requirements.

In recent years, the concept of **photonic crystals** has given rise to exciting ways of manipulating light[1]. A photonic crystal is to a photon what a semiconductor crystal is to an electron. In a semiconductor crystal, the periodic arrangement of atoms leads to the presence of an electronic band structure and an electronic bandgap. The bandgap defines a range of energies within which electronic states cannot exist. The presence of an impurity in the crystal breaks the periodicity and introduces a defect state within the bandgap. In a photonic crystal, a photonic bandgap (PBG) is created by a periodic arrangement of dielectric material. An example of a photonic crystal is a diamond structure with dielectric spheres located at the lattice points and surrounded by air. The PBG defines a range of frequencies within which photons cannot propagate in all three directions. The introduction of a defect in the periodic arrangement of dielectrics leads to the presence of an allowed state within the PBG. Such a defect is created either by the removal or addition of dielectric material within the crystal. The optical mode associated with this defect is strongly bound around the defect region. A photonic crystal with a

---

[1] See Ref. 5 for an excellent textbook treatment of the field of photonic crystals. Other review articles [6-7] also provide summary views of this burgeoning field.

defect behaves essentially like a *microcavity* with a high quality factor, Q. Indeed, one of the attractive promises of photonic crystals is the realization of a nanoscale microcavity capable of trapping light along all three dimensions.

The notion that the photonic equivalent of a semiconductor crystal can lead to the control of spontaneous emission is first proposed by Yablonovitch in 1987 [21]. In Yablonovitch's words, "If a three-dimensionally periodic dielectric structure has an electromagnetic *band gap* which overlaps the electronic *band edge*, then spontaneous emission can be rigorously forbidden" (emphasis from original article). Yablonovitch [21] and John [22] also suggest that a defect introduced into the photonic crystal could create a localized electromagnetic mode. Appropriate design of a photonic crystal with a defect leads to the creation of a microcavity, where only one specific mode exists while other modes are suppressed. A thresholdless laser could, therefore, be realized with such a photonic crystal by inhibiting all but the lasing mode.

At the same time, the ability of photonic crystals to manipulate light presents potential applications in optical interconnect technology. A two-dimensional photonic crystal with a line defect, for instance, has been theoretically shown to guide light around a 90° bend with close to 100% transmission [23]. Such a two-dimensional photonic crystal may be formed by a square array of dielectric rods, with the line defect created by removing a row of rods. Apart from efficient guiding of light around tight corners, this would also effectively create a waveguide made of air, in contrast to conventional dielectric waveguides in optoelectronic devices.

Since its beginning in the late 1980's, the field of photonic crystal research has developed from the phase of understanding the photonic crystal in theory to one of engineering photonic crystal-based devices for practical applications. This thesis represents one such effort at demonstrating the use of photonic crystals in optical devices, with potential applications in optoelectronic circuits. Specifically, this thesis describes the design, fabrication and characterization of both one-dimensional and two-dimensional photonic bandgap (PBG) devices using III-V compound semiconductors. In the case of the 1-D PBG devices, waveguide-based photonic crystal microcavities are designed and

10

fabricated for operation at the wavelengths of 4.5μm and 1.55μm. The 1-D PBG microcavity, in particular, is manifested in two configurations, namely as a monorail and as an air-bridge. Both the monorail and air-bridge microcavities have been optically characterized and demonstrated to operate successfully at the optical communication wavelength of 1.55μm. The work presented in this thesis also represents the first successful operation of the air-bridge microcavities.

In addition to the 1-D PBG microcavities, this thesis also records the design, fabrication and characterization of a 2-D photonic crystal light-emitting device (LED) with enhanced extraction efficiency. In many LED applications, light emitted in the normal direction is of primary interest; light that propagates parallel to the plane of the LED junction through index guiding by the semiconductor material is often considered lost. The incorporation of a 2-D photonic crystal in the LED structure serves to inhibit guided modes in the device, hence precluding any loss due to lateral propagation of generated light. The 2-D photonic crystal consists of a triangular array of holes etched into the top cladding layer of a single quantum well structure. A distributed Bragg reflector mirror stack under the quantum well serves to further reflect light that would have escaped through the substrate, back toward the normal direction. This thesis will detail the design and fabrication processes of a 2-D photonic crystal LED, as well as present the preliminary characterization of the devices.

1.2   Thesis Accomplishments

The successful design of these devices represents the collective accomplishment of three groups of researchers at MIT. A group of physicists, led by Professor John Joannopoulos, has provided the theoretical expertise for the design of the PBG devices. A group led by Professor Leslie Kolodziejski (of which the author is a member) contributed to the material engineering and nanofabrication aspects, as well as the design of the waveguide components of the microcavity devices. Professor Erich Ippen's research group supplied the know-how of waveguide design and optical characterization.

The fabrication of the devices described in this thesis has entailed the use of cutting-edge technologies, such as electron beam lithography and the thermal oxidation of III-V

compound semiconductor material. The latter, in particular, has only recently been discovered and has since generated much excitement in the research community. An oxidation apparatus has been set up at MIT and thermal oxidation of $Al_xGa_{1-x}As$ has been demonstrated. In the 1-D PBG microcavities, the oxide material (Al_2O_3) serves three crucial purposes, by (a) forming a low refractive index confinement layer; (b) acting as the sacrificial material during the suspension of the air-bridge structure; and (c) stabilizing the device structure against ambient degradation of $Al_xGa_{1-x}As$. To the best of the author's knowledge, this is the first use of Al_2O_3 in a micromechanical system application. In the 2-D photonic crystal LED effort, the oxide material is instrumental in realizing a wide bandwidth DBR mirror made of GaAs-oxide multi-layers.

Overall, the thesis has demonstrated the ability to manipulate light in different ways with photonic crystals. The devices have been nanofabricated and are shown to operate at technologically important wavelength regimes. The successful device fabrication and subsequent optical measurements resulted in the verification of theoretical predictions. These devices may form important components in the future implementation of monolithic optoelectronic integration and full optical computing.

1.3   Thesis Outline

The rest of the thesis is organized as follows. Chapter 2 opens with a background in the field of photonic crystal research, followed by a theoretical treatment of the 1-D PBG microcavities. The structures of the one-dimensional photonic bandgap microcavities investigated at the wavelength regimes of λ=4.5μm and 1.55μm are next described. Simulated transmission characteristics for the microcavities operating at both λ=4.5μm and λ=1.55μm, as well as the relevant device dimensions, are given. The waveguides coupling light into and out of the microcavities are designed using the beam propagation method; results of the design process are described. A review of other 1-D microcavities closes the chapter.

Chapter 3 forms the heart of this thesis, and focuses on the development and results of the fabrication process for the 1-D PBG microcavities using III-V compound

12

semiconductors. The fabrication processes of the one-dimensional PBG microcavities at both λ=4.5μm and λ=1.55μm are first described. The characterization of various fabrication steps is next detailed. First, the electron-beam lithography process is outlined, together with a justification for the choice of lithographic techniques. Next, the issues involved in the fabrication of a micromechanical device like the air-bridge are delineated. A detailed description of the critical thermal oxidation process of $Al_xGa_{1-x}As$ follows, including a literature overview of the current understanding of the oxide and the oxidation process. The characterization of the oxidation process performed at MIT is recorded, with focus on the main features of the material salient to the devices at hand. Reactive ion etching (RIE), another important technique in the fabrication of the devices, will next be explained, together with the characterization of the various RIE processes in this work. Finally, the results of the fabrication process for the 1-D PBG microcavities will be presented.

Chapter 4 begins with a description of the optical setup used in the optical characterization of the 1-D PBG microcavities at λ=1.55μm. Results from the optical measurements are presented and compared to the simulated predictions.

Chapter 5 discusses the theory of the enhanced extraction efficiency of a light-emitting device with the use of a 2-D photonic crystal. The design of a device aimed at empirically verifying the theoretical predictions is then detailed. The process to fabricate the device in question is next described and the results of the process development are recorded. The results of the fabrication process are finally presented, together with preliminary findings from the optical characterization of the devices.

Finally, Chapter 6 summarizes the work that has been described at length in this thesis. Suggestions for extensions and future directions of the present work conclude the thesis.

Chapter 2 One-dimensional photonic bandgap microcavity: design

2.1 Photonic band structure and photonic band gap: Background

The allusion to a bandgap for a photon, in analogy to an electronic bandgap, was made as early as 1975 in a classic text on quantum electronics by Yariv [24]. It is, however, the seminal papers by Yablonovitch [21] and John [22] in 1987 that initiated the ensuing interests in photonic bandgap devices. Both Yablonovitch and John suggested that a structure with a periodicity of refractive index in all three dimensions, called a photonic crystal, could possess a photonic bandgap (PBG). An example of a photonic crystal is a diamond structure consisting of dielectric spheres at the lattice sites surrounded by air. The PBG would be much akin to the bandgap for an electron: photons within a certain range of frequencies will not be allowed to propagate within the crystal in all directions.

In a semiconductor crystal, the introduction of donor or acceptor impurities results in defect states in the electronic bandgap. Analogously, a defect in a photonic crystal would also lead to an allowed state in the PBG. The addition or removal of dielectric material at particular lattice sites in the photonic crystal would create such a defect. The electromagnetic mode associated with this defect is highly localized around the defect region. Figure 2-1, for example, shows the electric field distribution of a defect mode in a two-dimensional photonic crystal. In this example, a square lattice of dielectric rods in air defines the 2-D photonic crystal, while a point defect is created by making one of the rods smaller. The electric field for the TM mode is seen to be highly concentrated around the defect region. The notion of creating a microcavity that localizes light using photonic crystals then becomes immediately apparent. The potential of using a photonic crystal to control the spontaneous emission of atomic systems was emphasized by Yablonovitch, and remains a leading motivation for researchers in the field.
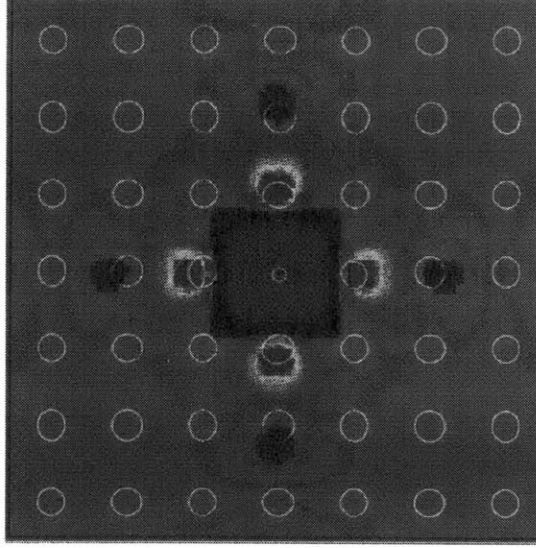
Figure 2-1: Electric field distribution of TM polarization in a 2-D photonic crystal with a point defect. The photonic crystal is defined by a square lattice of dielectric rods (white circles), with a defect creating by making a rod smaller in diameter. From Ref. [20].

To see the origin of the photonic band structure and the PBG, consider the following equation derived from Maxwell's equations:

$$\nabla \times \left(\frac{1}{\varepsilon(\mathbf{r})} \nabla \times \mathbf{H}(\mathbf{r}) \right) = \left(\frac{\omega}{c} \right)^2 \mathbf{H}(\mathbf{r})$$ Equation 2-1

In the equation, $\mathbf{H}(\mathbf{r})$ is the magnetic field, $\varepsilon(\mathbf{r})$ is the dielectric constant as a function of position, ω is the angular frequency and c is the speed of light. The equation has a form reminiscent of Schrödinger's equation. Since the electronic band structure stems essentially from Schrödinger's equation, a similar approach will lead to a photonic band structure from Equation 2-1. By introducing a periodic refractive index function, where $\varepsilon(\mathbf{r}) = \varepsilon(\mathbf{r} + \mathbf{R})$, the familiar Bloch theorem from solid state physics can be similarly applied. Furthermore, concepts like Brillouin zones, energy gaps and impurity states from electronic band theory also hold true for the photonic crystal. In fact, the presence of a bandgap in both the electronic and the photonic cases can be traced to the same physical basis. The electronic bandgap is attributed to the coherent interference of electron waves scattered from periodically positioned atoms in space. Conversely, the PBG is a result of

15

coherent interference of light scattered from periodically placed dielectric scattering centers.

An important property of a photonic crystal is the scalability in its physical dimensions relative to wavelength. In other words, the solution of a band structure at one frequency can be applied to other frequencies by proportionately scaling the feature sizes. Consequently, physical dimensions for a photonic crystal are often denoted as a function of wavelength. In addition, experimental results obtained for a photonic crystal structure at one wavelength can be extended to imply the validity of the structure at other wavelengths.

For a more complete and highly readable treatment of photonic crystals, the reader is referred to a text titled "Photonic Crystals" by Prof. John D. Joannopoulos [18].

2.2   Photonic crystals: Research Advancements

Initial research of photonic crystals focussed on the crystalline structure and the index contrast necessary to achieve a *complete* bandgap, i.e. one that would prohibit propagation of electromagnetic waves in all three directions. Physicists were also striving to achieve a maximum gap size with minimum index contrast. The first structure proposed was the face-centered cubic (fcc) structure [21], and the index contrast needed to open a gap was expected to be about 2:1 [22]. After several close attempts at achieving a true photonic crystal [25-27], the diamond structure eventually became the first crystal configuration that exhibits a complete PBG in theory [28]. In addition, an index-contrast ratio of greater than 2:1 was found to be necessary to open a gap. Subsequently, the simple cubic structure was also found to yield a complete PBG [29].

Early attempts at empirically verifying the existence of a PBG were carried out exclusively in the microwave regime. Consequently, fabrication of photonic crystals at the microwave regime involved, for instance, the drilling of holes using machine tools into a dielectric block. The process, though laborious, was achievable and provided a direct way to test the validity of theoretical predictions. Yablonovitch et. al. is credited with the first fabrication of a photonic crystal possessing a complete PBG on the

16

microwave length scale in 1991 [30]. The photonic crystal, called the Yablonovite, consisted of holes drilled into a dielectric block at different angles to the vertical axis (Figure 2-2). The evidence for the existence of a complete gap was compelling and generated immense interest in the scientific community as a whole. In addition, Yablonovitch et. al. [31] also verified the existence of "donor" and "acceptor" states within the PBG with the introduction of defects into the photonic crystal (Figure 2-3).

While the Yablonovite could potentially be fabricated in the optical wavelength regime using techniques like chemically assisted ion-beam etching (CAIBE), its actual realization is particularly difficult. The control of the etching angles and the depth to which the holes have to be etched both present great challenges to the fabrication engineer. Currently available semiconductor etching techniques, though allowing certain degree of latitude in etch directionality, are still essentially planar processes. Despite innovative efforts at fabricating the Yablonovite at optical lengthscales [33, 34], photonic
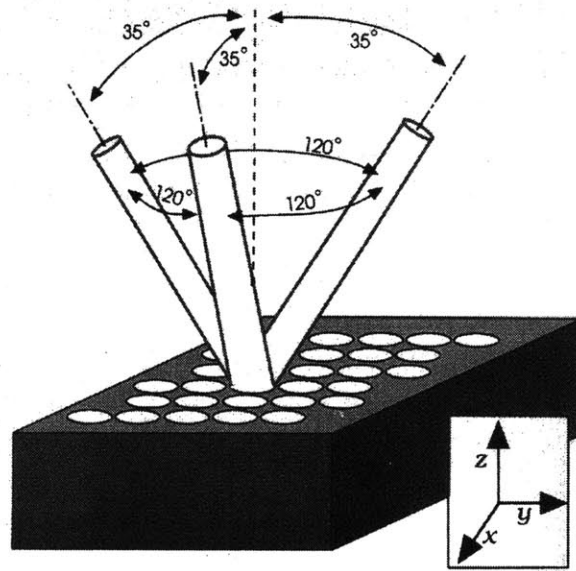
Figure 2-2:Schematic of the fabrication process for a Yablonovite structure. Air channels are drilled into a dielectric block from three different directions at each position. The three drilling directions are at an azimuthal angle of 120° to one another, while each drilling direction is at 35° to the vertical axis. [32]
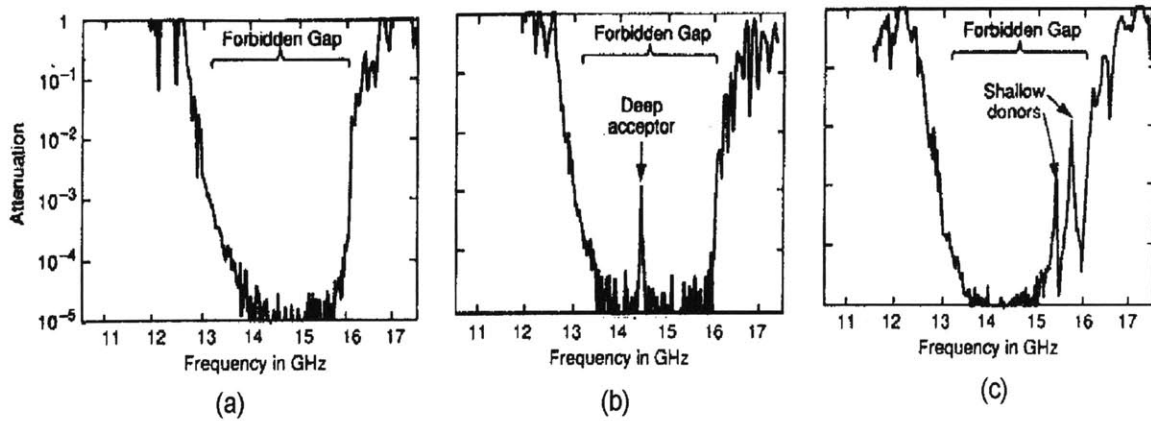
Figure 2-3: Empirical measurements of 3-D photonic crystals demonstrating the presence of "donor" and "acceptor" states in the photonic band gap. The measurements are performed in the microwave regime on photonic crystals made with polystyrene material and based on the Yablonovite structure. From Ref. [31]

crystals with good optical transmission characteristics are yet to be demonstrated using this scheme.

Subsequently, proposals for photonic crystals more amenable to conventional semiconductor fabrication techniques begin to appear. One of these is the "woodpile" [35] or "layer-by-layer" structure [36] (Figure 2-4(a)), where rows of dielectric rods are stacked upon one another. Attempts at fabricating this structure using silicon and III-V compound semiconductors with micron size features at far infrared wavelengths were made [36, 37]. Another approach to a fabrication-friendly photonic crystal requires the repeated etching of trenches and material overgrowth or deposition [38] [see Figure 2-4(b)]. To date, none of the above fabrication approaches has yielded a photonic crystal demonstrating a PBG at optical wavelengths.

Reducing the dimensionality of the PBG-based device relieves the demand on fabrication and leads to devices no less interesting than the three-dimensional counterparts. In fact, devices manifesting a PBG in one dimension, such as the distributed feedback Bragg (DFB) gratings and the distributed Bragg reflector (DBR), are already well studied and commercially exploited. Each of these devices exhibits a periodicity in refractive index along one dimension that creates a 1-D PBG. A phase shift in the DFB gratings, for instance, defines a defect region and gives rise to a resonant state within the PBG.

18

Two-dimensional PBG devices have also been explored, both theoretically [39, 40] and experimentally [41, 42]. In these devices, the 2-D photonic lattice is defined either by a periodic array of holes in a dielectric slab, or by an array of dielectric posts surrounded by air (Figure 2-5). The resultant 2-D PBG prohibits the propagation of optical modes in the planar direction. Interesting applications have been proposed using a 2-D photonic lattice, including (a) low loss waveguide bend [23]; (b) a high-Q microcavity [32]; and (c) enhanced extraction efficiency of a light-emitting diode structure [43]. Both the 1-D and 2-D PBG devices can be more readily fabricated using conventional fabrication techniques, due to the planar nature of the fabrication processes.

(a)   (b)
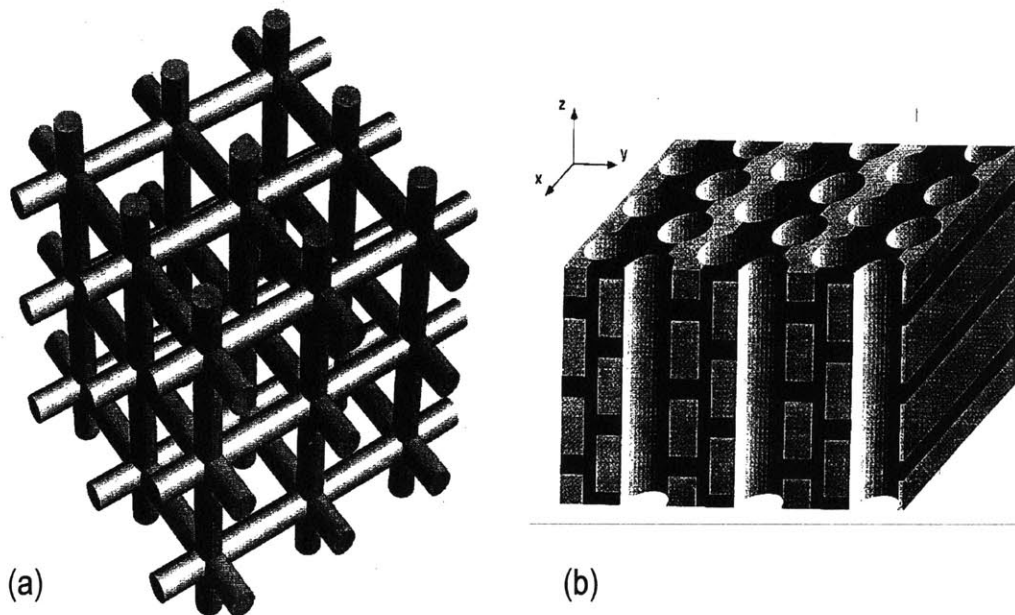
Figure 2-4: Schematic of photonic crystals exhibiting complete photonic bandgap and amenable to conventional fabrication techniques, namely the (a) "woodpile" or layer-by-layer structure and (b) structure proposed by Fan et. al. [38]

Figure 2-5: An example of a two-dimensional photonic lattice. The scanning electron micrograph shows the top view of a triangular lattice of air holes in a thin film of polymethylmethacrylate (PMMA). The holes are generated by electron beam lithography. (See Chapter 5)

2.3   One-dimensional photonic bandgap microcavities

2.3.A   General description

In this thesis, a novel microcavity based on a high index-contrast, one-dimensional photonic crystal is fabricated and demonstrated to ope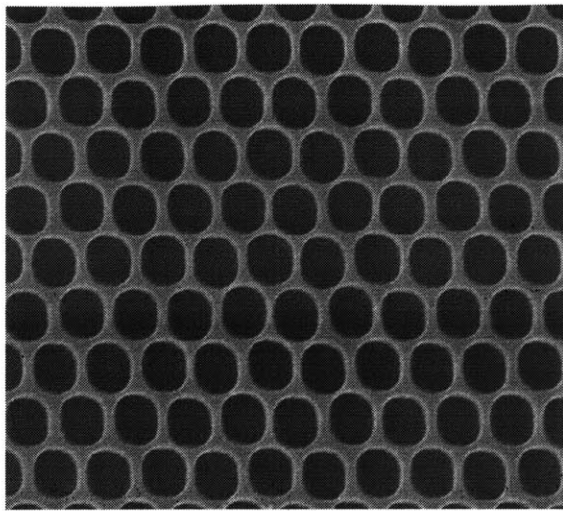rate at the optical wavelength regime. The microcavity consists of a one-dimensional photonic crystal integrated into a waveguide. The photonic crystal is defined by a periodic array of holes in the waveguide, with a cavity or defect region created by increasing the distance between two holes in the middle of the array. Light is strongly confined along the waveguide axis by the one-dimensional photonic crystal and in the other two directions by index guiding.

The devices are manifested in two configurations, namely the monorail and the air-bridge microcavities (Figure 2-6). The GaAs waveguide microcavity is either supported on a low refractive index Al_xO_y material (the monorail) or is suspended in air (the airbridge). Input and output waveguides (not shown) are included to allow testing of the microcavities. The air-bridge microcavity exhibits a higher cavity quality factor, Q, than the monorail microcavity, due to the larger index contrast between the waveguide microcavity and its surroundings. A direct bandgap III-V semiconductor material, GaAs, is chosen as the device material for this work both for its sufficiently high refractive index and the natural extension of these presently passive devices to active device applications.
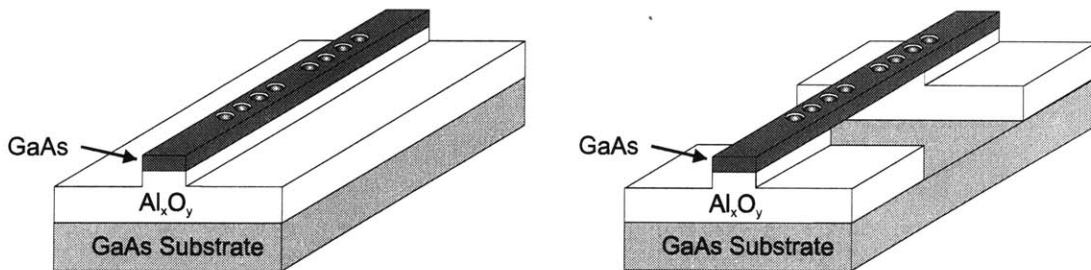

Figure 2-6: Schematic of one-dimensional photonic bandgap microcavities, consisting of the monorail (left) and airbridge (right) configurations.
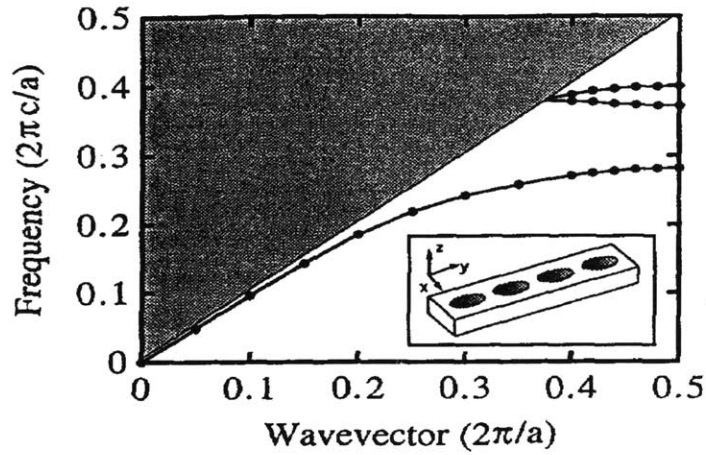
Figure 2-7: Dispersion relationship of a waveguide with a periodic array of holes (as shown in inset). The waveguide thickness and width, expressed in terms of the distance between holes (*a*), are 1.2*a* and 0.4*a* respectively. The hole diameter is 0.6*a* and the waveguide material is assumed to be GaAs [44].

The analysis of the one-dimensional PBG microcavity begins by considering the effect of introducing a periodic array of holes into a plain waveguide, as represented by the dispersion relationship for such a structure (Figure 2-7) [44]. The dispersion relationship is obtained by solving Maxwell's equation for the structure in the frequency domain, and then computing the lowest-frequency eigenstates for different values of wavevectors in the propagation direction. The bands in the dispersion relationship, plotted in the reduced-zone scheme, thus consist of collections of eigenstate solutions (denoted by solid circles). The computational method is detailed in Ref. [44].

In this example, the width and thickness of the waveguide are 1.2*a* and 0.4*a* respectively, where *a* is the distance between the centers of two neighboring holes and *c* is the speed of light in vacuum. The diameter of the holes is 0.6*a* and the waveguide material is assumed to be GaAs. This particular set of dimensions is chosen to achieve strong optical confinement in a microcavity based on this structure, as described below. The shaded area above the light line ($\omega = c/k$) in the plot represents a continuum of radiation modes into free space. The guided modes are denoted by the set of lines below the light line where only the TE polarization is shown. Multiple scattering of the guided modes from the array of holes and destructive interference result in the opening of a gap in the
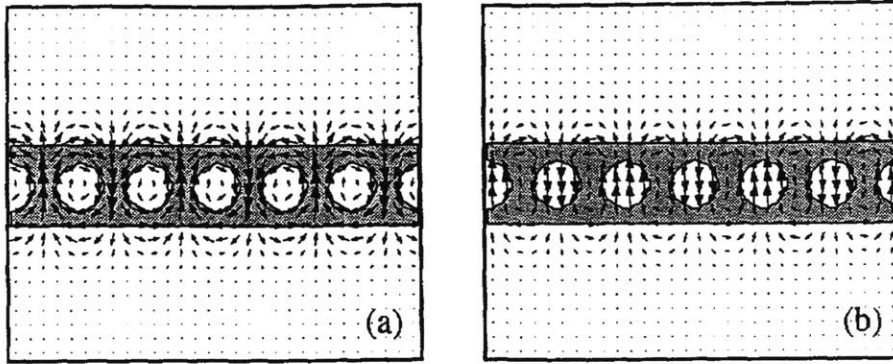
Figure 2-8: Vector plots of the electric field distribution for modes from (a) the first band; and (b) the second band at the Brillouin zone edge. The waveguide is denoted in gray. [44]

dispersion relationship, such as that between the first two bands at the Brillouin zone edge. The frequency range of the bandgap extends from $f=0.28c/a$ to $0.37c/a$, which translates to 27% of the mid-gap frequency (ie, $\Delta f_{gap}/f_{midgap} = 0.27$).

The nature of the photonic bandgap can be further understood by examining the electric field distributions associated with the guided modes in the first and second band at the Brillouin zone edge (Figure 2-8). The electric field for the first band resides mostly in the dielectric material, while that for the upper band is found mainly in the air-holes. At a particular wavelength, a mode has a lower frequency when it is in dielectric material than when it is in air. As the mode in the lower band experiences a higher effective refractive

Figure 2-9: Vector plot of electric field distribution around the defect region. [44]

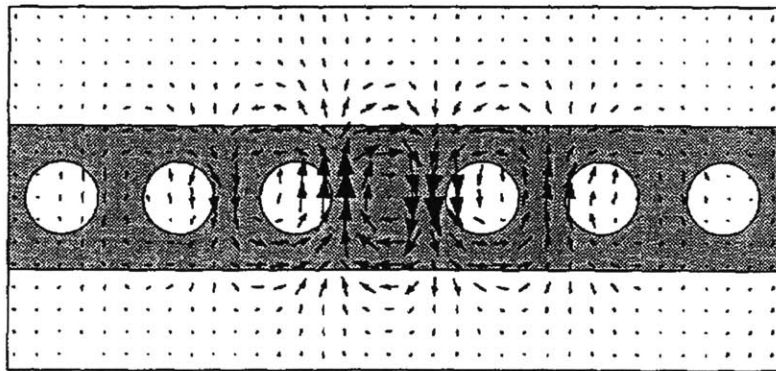index than the upper-band mode, a discrepancy in the respective mode frequencies is present. This difference in frequency accounts for the bandgap between the first two bands of guided modes at the Brillouin zone edge. The size of the bandgap is largely dependent on the size of the holes and the dielectric constant of the waveguide material.

When the periodicity in the 1-D photonic crystal is broken by increasing the distance between two neighboring holes, a defect state is created in the bandgap. The defect region in this example is defined by a distance of $1.5a$ between the two arrays of holes, where each array consists of three holes placed $1.2a$ apart. The defect results in a resonant state at $f=0.31c/a$. The resonant mode is strongly confined around the defect region (Figure 2-9), and couples evanescently through the holes to the guided modes in the waveguide. Using a finite-difference, time-domain (FD-TD) computational scheme, the simulated transmission spectrum for the microcavity is shown in Figure 2-10 (see Ref. [44] for more details on FD-TD). In this example, a pulse with a Gaussian frequency profile centered at $f=0.30c/a$ and having a width of $0.10c/a$ is propagated down the waveguide. Generally, as the distance between two holes is increased to form a defect region, the defect state in the gap first begins to appear closer to the upper band-edge; the resonant mode is said to be "pulled" down from the upper bands. Conversely, when a defect is formed by decreasing the distance between two holes, the defect state is pulled up from the lower band. Several parameters of the waveguide structure govern the number of
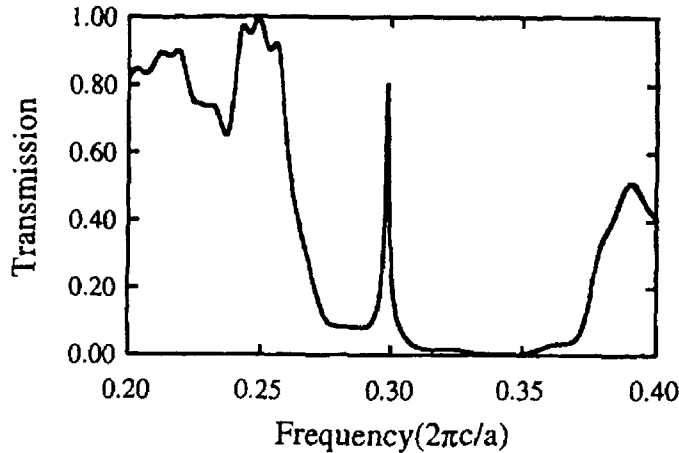
Figure 2-10: Theoretical transmission spectrum for the waveguide microcavity. [44]

24

resonant modes in the gap, the frequencies of these modes and the strength of the confinement in the microcavity. These parameters are namely the width and thickness of the waveguide, the radius of the hole, the number of holes and the defect width.

The quality factor, Q, of an optical cavity or resonator structure is defined as the number of optical oscillations before the electromagnetic energy of the resonant mode decays to $e^{-2\pi}$ of its initial value. Q is represented in mathematical terms as:

$$Q = \frac{\omega_o E}{P} = -\frac{\omega_o E}{dE/dt} \qquad \text{Equation 2-2}$$

In the equation, ω_o is the resonant frequency, E is the stored energy within the resonator/cavity, and P=(-dE/dt) is the dissipated power. In practice, Q can also be approximated by the ratio of the resonant frequency (ω_o) to the resonance linewidth ($\Delta\omega$), i.e.:

$$Q \approx \frac{\omega_o}{\Delta\omega} \qquad \text{Equation 2-3}$$

The Q of a cavity provides a measure of the loss of the microcavity. A cavity with a high Q implies a low loss system where the dissipation or loss of the resonant mode energy takes place over many optical cycles. The Q of the resonance in the present example (Figure 2-10) is calculated to be 271 while the coupling efficiency into the resonant mode exceeds 80%.

In the context of the discussion on optical microcavity, the resonant mode volume is also a relevant factor. The mode volume V is defined as

$$VP_{max} = \int P(r)d^3r \qquad \text{Equation 2-4}$$

where P(r) is the total electromagnetic energy density of the mode and P_{max} is the peak value of P(r). A mode with a low mode volume implies a mode profile with tight spatial extent as a result of strong optical confinement.

The importance of the Q and V associated with a microcavity can be seen by the equation governing the spontaneous emission enhancement factor (η) for a particular mode [17]:

$$\eta = \frac{Q}{4\pi V}\left(\frac{c}{n\nu}\right)^3 \qquad \text{Equation 2-5}$$

In the equation, Q is the quality factor of the cavity, ν is the transition frequency and V is the mode volume and n is the refractive index of the cavity material. The spontaneous emission enhancement factor is defined as the ratio of the spontaneous emission rate into a mode in a cavity to that in free space. A large η for a mode means that the spontaneous emission of a system into the particular mode is strongly enhanced, while emission into other modes is suppressed. From Equation 2-5, a large Q/V ratio is necessary for a high spontaneous emission enhancement factor.

To elucidate the determinants of Q for the one-dimensional photonic bandgap microcavity, the Q_{mode} of the resonant mode can be represented as:

$$\frac{1}{Q_{mode}} = \frac{1}{Q_{rad}} + \frac{1}{Q_{wg}} \qquad \text{Equation 2-6}$$

where $1/Q_{rad}$ measures the coupling of the resonant mode into radiation modes in free space, while $1/Q_{wg}$ measures the coupling into guided modes down the waveguide structure. This equation indicates that the rate at which the resonant mode loses its energy ($1/Q_{mode}$) depends on its coupling to the loss mechanisms ($1/Q_{rad}$ and $1/Q_{wg}$). The loss mechanisms in this instance are the coupling into the radiation and waveguide modes.

The array of holes in the photonic crystal on either side of the defect region is analogous to a highly reflective mirror. Increasing the number of holes in the array increases the reflectivity of the "mirror" and enhances the mode confinement within the defect region. The increased mode confinement reduces the loss through the waveguide modes and leads to a low $1/Q_{wg}$. As the number of holes increases, however, more of the light is scattered off the holes and loss through the radiation modes begins to dominate. In this one-dimensional photonic bandgap system, the radiation loss is finite and cannot be eliminated. Consequently, the Q for the resonant mode cannot be increased indefinitely
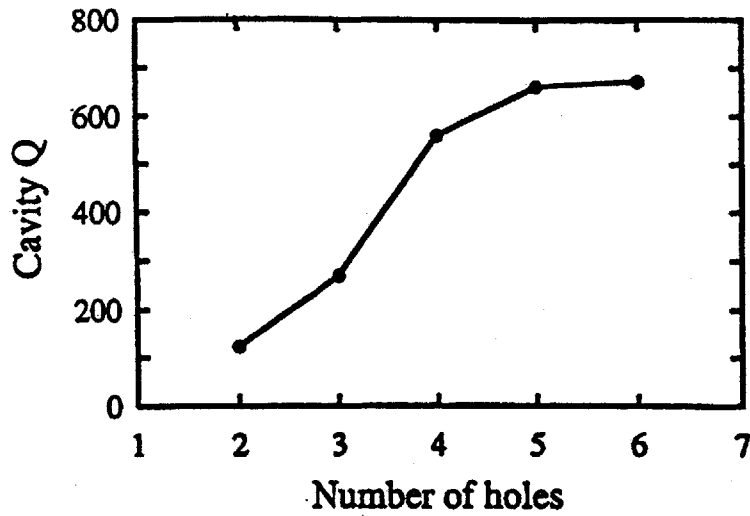
Figure 2-11: Plot of cavity quality factor, Q, versus number of holes on each side of the defect region in the one-dimensional photonic band gap microcavity [44].

by increasing the number of holes in the photonic crystal. Radiation loss therefore becomes the ultimate limiting factor in the design of the one-dimensional photonic bandgap device. To minimize the radiation loss for the 1-D system, the photonic crystal should be surrounded by material with the lowest refractive index possible. In the limit, this requires that the photonic crystal be suspended in air. The relationship between Q and the number of holes in the photonic crystal is shown in Figure 2-11.

2.3.B   Specific device description

The photonic bandgap microcavities have been investigated in two wavelength regimes, namely λ=4.5μm and λ=1.55μm. The attempt at the longer wavelength regime involves larger feature sizes for the devices, hence a less stringent demand on device fabrication. In particular, photolithography is used for the "4.5μm devices" while electron beam lithography is used for the "1.55μm devices". The 4.5μm device effort represents an initial attempt at providing proof of principle, particularly for the air-bridge configuration. The 1.55μm device is significant for its relevance to applications in optical communications.
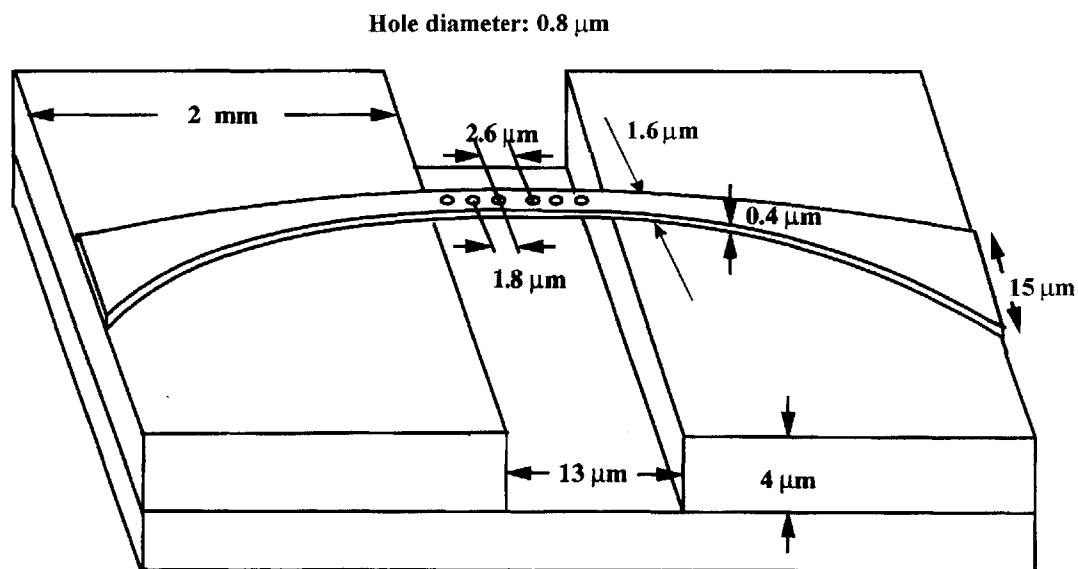
Hole diameter: 0.8 μm

Figure 2-12: Schematic of one-dimensional photonic bandgap air-bridge microcavity at the λ=4.5μm wavelength regime. The input and output coupling waveguides are also shown.

Only the air-bridge configuration has been attempted at the 4.5μm wavelength regime, primarily for its novelty and the fact that the monorail configuration is expected to have a low Q (due to the design compromises necessary, as described below). A schematic of the device structure is shown in Figure 2-12.

The effort at designing and fabricating the 4.5μm devices stems from the success in fabricating suspended air-bridge structures in June 1994 (see Chapter 3) [45, 46]. The air-bridge structures have been fabricated to demonstrate the feasibility of realizing a 1-D PBG structure proposed by Joannopoulos et al. [Figure 2-13(a)]. The suspended air-bridge structures have been fabricated with both silicon and III-V material systems using conventional optical lithography-based processes [see Figure 2-13(b) and (c)]. The success of the feasibility study provides further impetus for the experimental verification of the optical performance of a 1-D PBG microcavity, which would require the

(a)

(b)   (c)
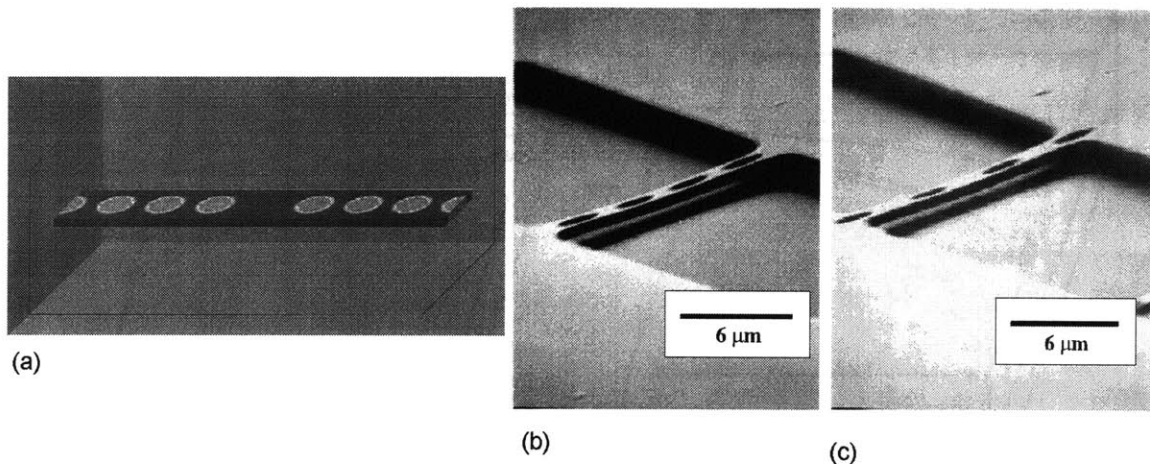
Figure 2-13: Motivation of designing and fabricating the 4.5μm air-bridge microcavity stemmed from the success of realizing initial idea of a PBG air-bridge microcavity. Schematic (a) shows an early rendering of a computation cell for the waveguide microcavity used in computer simulations. The computation cell shows the three-dimensional spatial distribution of dielectric material, and represents the theorist's vision of a waveguide microcavity structure. (Courtesy of Villeneuve et al, 1994). Scanning electron micrographs (b) and (c) show air-bridge structures successfully fabricated from Si (b) and GaAs (c) material systems. The Si air-bridge is 4μm wide, 10μm long, with hole diameters of 2μm placed 1μm apart. The GaAs air-bridges are all 20μm long with hole diameters of 2.5μm and widths ranging from 3.5μm to 5.5μm [45].

incorporation of coupling waveguides to allow the testing of microcavities.

Based on the experience gained from the work, an optical lithography-based process is chosen for the fabrication of the subsequent set of devices. The decision to use optical lithography in the device fabrication is a critical one. A fast time-to-completion for the fabrication is initially expected, since the optical lithographic equipment is readily available and the process is already well determined. The resolution limit of optical lithography, however, sets a lower limit on the attainable physical dimensions in the devices. This lower limit, in turn, defines the wavelength at which the devices will be designed. Finally, the ability to generate light at a particular range of wavelengths also determines the eventual operating wavelength.

The resolution limit on the optical lithographic equipment at MIT is determined to be $0.4\mu m$. The smallest feature present in the case of the photonic bandgap air-bridge structure is the distance between the edge of the hole and the edge of the bridge structure. After considerable discussion between the group of collaborating researchers, it is determined that $\lambda=4.5\mu m$ would be the operating wavelength. The resulting device dimensions are shown in Figure 2-12.

The device design incorporates several tradeoffs. Most significantly, the holes are placed further apart and the air-bridge structure made wider than the ideal design [46] to accommodate the fabrication limits. This effectively adds dielectric material in the plane of the device. As the photonic band properties depend on the dielectric-to-air ratio, the air-bridge structure is made thinner to adjust for the increase of material in the plane. The final theoretical transmission spectrum of the device at $\lambda=4.5\mu m$ is shown in Figure 2-14.
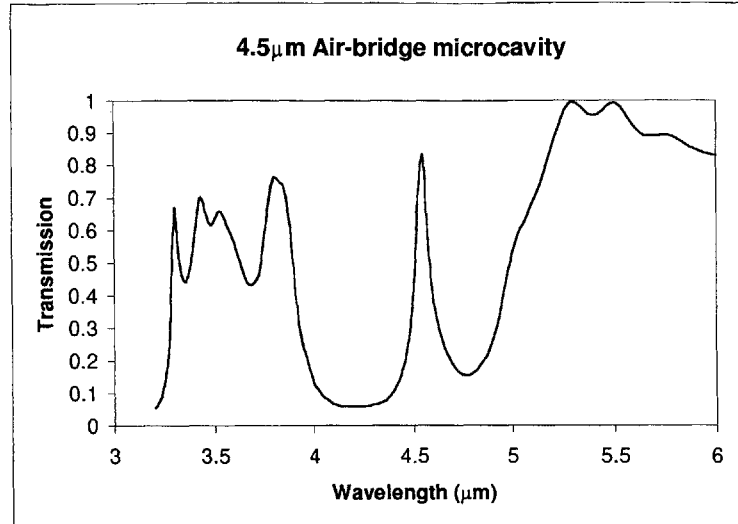
Figure 2-14: Simulated transmission spectrum of the air-bridge microcavity. (Courtesy of P.R. Villeneuve, S. Fan and J.D. Joannopoulos.)

The design of the device, however, leads to several difficulties in optical measurement. Generating the input beam to probe the devices, while achievable, requires considerable effort [47]. To complicate matters, the cavity Q is lowered by the design compromises. The cavity Q for the ideal design is on the order of 270; while the final device design is expected to have a Q of about 46. A lower Q translates to a broader resonant peak in practice, further imposing demand on the optical measurement setup to resolve the peak against a noise background. Finally, the thinner air-bridge structure leads to a lower optical power coupled into the waveguides from an external probe beam, thus reducing the signal/noise ratio of the optical measurement.

Given the difficulties presented to the measurement of these devices, several refinements are included in the coupling waveguides to ameliorate the situation. These design enhancements are as follows:

1. *Incorporation of over- and underlayers in the waveguide*: The cross-sectional view of the coupling waveguides is shown in Figure 2-15. As mentioned before, the amount of optical power coupled into the input waveguide is lowered because of the reduced thickness of the air-bridge section. The input beam is expected to have a Gaussian profile with a spot size of about 16μm, while the input facet is 15μm wide and 0.4μm

thick. Ideally, one would like to have a large cross-sectional area at the input facet to maximize the coupling of light into the input waveguide, while vertically tapering the waveguide thickness to that of the air-bridge over the length of the input waveguide. This is not easily achieved since the contiguous GaAs layer defining the waveguide and the air-bridge structure is grown by molecular beam epitaxy (MBE). The MBE growth process does not readily allow a deliberate variation in thickness across a sample.

To improve the coupling of light into the input waveguide, an overlayer of 0.2μm thick $Al_{0.3}Ga_{0.7}As$ and an underlayer of 0.2μm thick $Al_{0.7}Ga_{0.3}As$ are added to the 0.4μm thick GaAs waveguide/air-bridge layer. The bottom $Al_{0.9}Ga_{0.1}As$ layer would also be oxidized into Al_xO_y as part of the fabrication process. The addition of the overlayer has the effect of "pulling" up the optical mode away from the GaAs substrate, thus reducing the loss via leakage into the substrate modes. The underlayer serves to center the optical mode in the GaAs guiding layer. The low-index oxide layer isolates the guiding layer from the substrate, further reducing any leakage loss. The sum total of these modifications is a centering of the optical mode at the GaAs layer, both at the input facet and the air-bridge structure, as well as improved coupling into the waveguides with reduced loss into the substrate.
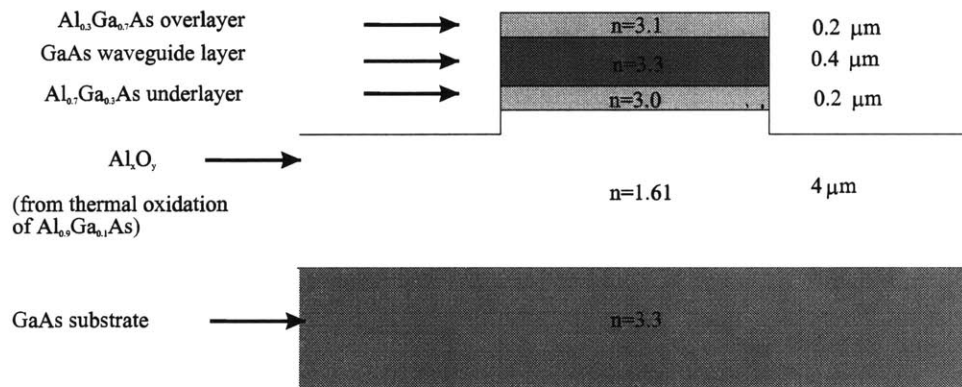

Figure 2-15: Cross-section of a coupling waveguide, showing the composition of various layers making up the waveguide structure. Also shown are the refractive indices and thicknesses of the respective layers.

2. *Horizontal tapering of input and output waveguides*: As shown in Figure 2-12, both the input and output waveguides are tapered from a width of 15μm at the facets to 1.6μm at the air-bridge structure over a length of 2mm. The widening of the waveguide at the input facet serves to increase the overlap between the waveguide and the input beam. The input beam is assumed to have a Gaussian intensity profile with a beam diameter of 16μm.

3. *Bends in the input and output waveguides*: One of the potential problems anticipated during the optical measurement is the difficulty in differentiating the light guided through the substrate from that guided through the waveguide. The problem is exacerbated by the inability to image the output facet onto a monitor at the operating wavelength of 4.5μm. Bends with a 6° vertical drop from the horizontal are thus included in both the input and output waveguides (see Figure 2-12). As seen in Figure 2-16, objective lenses are used to couple light into and out of the waveguides. The incorporation of the waveguide bends effectively results in the lenses being at an angle to one another. Consequently, the guided beam along the waveguide is routed away from the beam propagating straight through the substrate. The edge of the sample is also cut at a 6° angle to allow normal incident alignment of the input/output objective lenses with the respective facets.
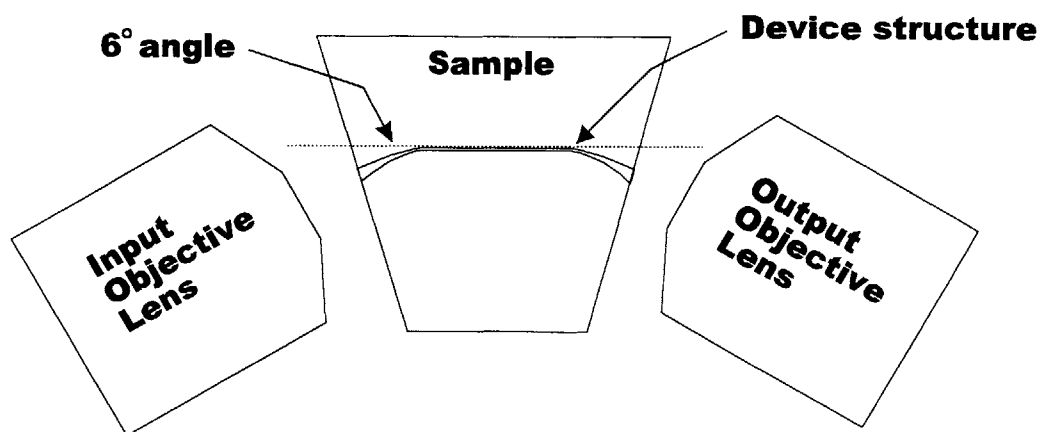

Figure 2-16: Relative position of input and output coupling objective lens to the device structure. Bends are included in the waveguides and the edges of the sample are cut at an angle to reduce noise arising from the substrate mode.

The feasibility of these design modifications is verified by Constantine Tziligakis (as part of his Master of Science thesis at MIT) [47] using the beam propagation method (BPM; see Ref. [48]). Figure 2-17(a)-(d) show the overlay of simulated electromagnetic mode profiles on cross-sections of the waveguide at different locations. The various lines within the cross-sectional plots further depict the refractive index distribution within the waveguide cross-sections. In Figure 2-17(a), for instance, the mode profile at the 15μm-wide input facet is shown. The top rectangle in the cross-sectional plot represents the overlayer, while the rectangle directly below represents the GaAs waveguide layer. Note that as the oxidation process is assumed to result in a 1μm-thick oxide, the $Al_{0.9}Ga_{0.1}As$ material at the input facet is only partially oxidized in the lateral direction. Similarly, the cross-sectional plot of the waveguide at 0.5mm before the air-bridge shows 2/3 of the 3μm-wide $Al_{0.9}Ga_{0.1}As$ region being oxidized [Figure 2-17(b)].

Overall, simulation results from the BPM mode solver indicate good confinement of the optical mode within the waveguide layer. Figure 2-17(a) shows the eigenmode solution at the 15μm-wide input facet, where the mode is roughly centered just below the GaAs waveguide layer. As the waveguide narrows to 3μm at a distance of 0.5mm from the air-bridge structure, the guided mode begins to be centered in the GaAs layer [Figure 2-17(b)]. At the waveguide/air-bridge interface, where the waveguide width is 1.6μm, the material underneath the waveguide consists entirely of the low-index oxide and the mode is well centered in the waveguide layer [Figure 2-17(c)]. The coupling efficiency between the waveguide eigenmode and the air-bridge eigenmode is calculated to be 98%. The mode remains centered in the GaAs layer structure as it propagates down the air-bridge structure [Figure 2-17(d)]. Taking into account the transmission through the air-bridge at resonance of 60%, and a 76% transmission at each facet due to reflection losses, the overall transmission through the structure is expected to be 34%.

In summary, the cross-section of the waveguide for the 4.5μm 1-D PBG air-bridge microcavity device consists of multiple epitaxial layers on a GaAs substrate (Figure 2-15), namely a 4μm-thick $Al_{0.9}Ga_{0.1}As$ sacrificial layer, a 0.2μm-thick $Al_{0.7}Ga_{0.3}As$ underlayer, a 0.4μm-thick GaAs waveguide layer and a 0.2μm-thick $Al_{0.9}Ga_{0.1}As$
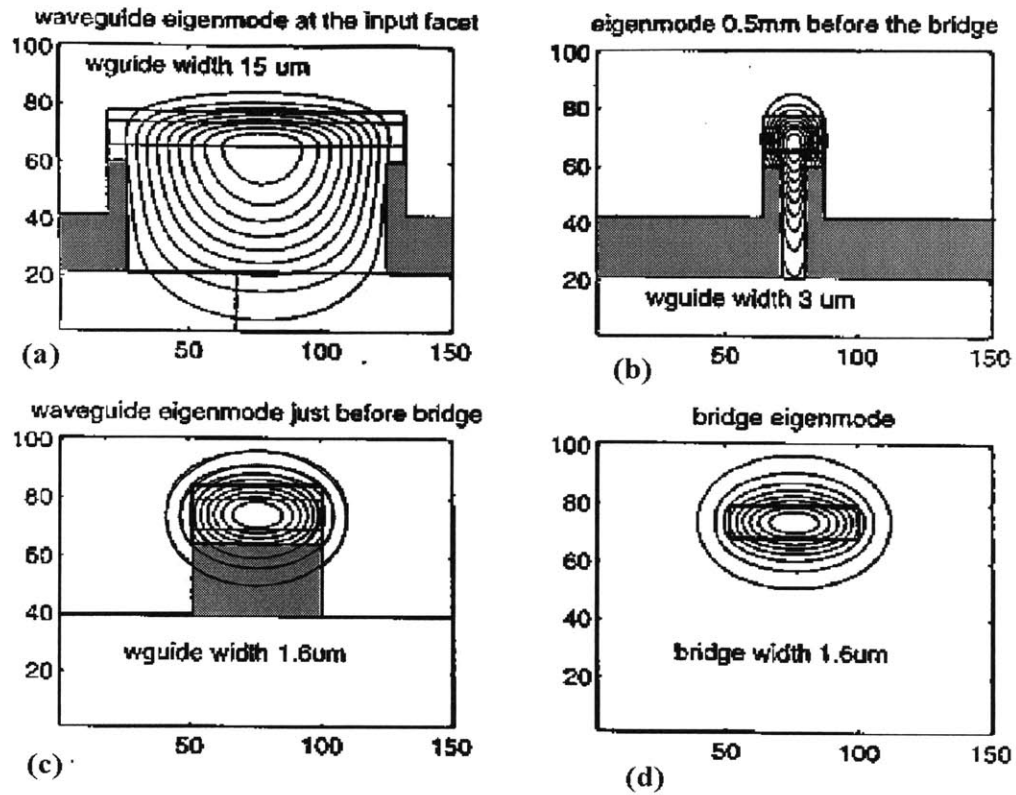
Figure 2-17: Simulated electromagnetic mode profiles overlaid on cross-sectional plots of refractive index distribution at various points along the 4.5μm air-bridge microcavity structure. The gray regions in each panel represent the oxidized portions of the sacrificial $Al_{0.9}Ga_{0.1}As$ layers. Plots of eigenmode solutions are shown at (a) 15μm wide input facet, with an oxide thickness of 1μm both vertically and laterally; (b) a distance 0.5mm before the air-bridge; (c) the waveguide/air-bridge interface; and (d) the air-bridge [47]. The scales in the vertical and horizontal axes denote distances in micrometers.

overlayer. The $Al_{0.9}Ga_{0.1}As$ layer becomes oxidized in the fabrication process, with the oxide extending 1μm from the surface. The input/output coupling waveguide flares from 15μm-wide at the input/output facet to 1.6μm-wide at the air-bridge structure, over a distance of 2mm (Figure 2-12). Theoretical simulation of the waveguide structure using BPM predicts the overall transmission through the entire microcavity device to be 3%.

The effort to investigate the one-dimensional photonic bandgap microcavity at the wavelength of 1.55μm arises from (a) the less-than-optimal design of the 4.5μm devices; (b) the difficulty of optically characterizing the 4.5μm devices; and (c) the importance of devices operating at 1.55μm for communications applications. Moving to the shorter wavelength, however, implies the need to employ more sophisticated lithography techniques like electron-beam or X-ray lithography. The relative ease of optical characterization at 1.55μm and the technological importance of the devices, nonetheless, justify the increase in fabrication complexity.

Both the monorail and air-bridge configurations are investigated at λ=1.55μm, using exclusively III-V compound semiconductors. The relevant physical dimensions for the optimal design are listed in Table 2-1. The smallest feature size is the distance between the hole and the edge of the waveguide structure, $(w-D)/2$, i.e. 180nm for the monorail and 162nm for the air-bridge configuration. Such feature sizes are routinely obtained with high-resolution lithography techniques.

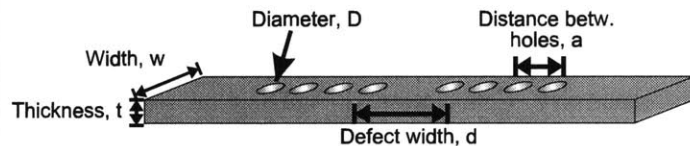| (All units in nm)	Monorail	Air-bridge
Thickness, t	185	192
Width, w	553	525
Hole diameter,D	194	201
Distance between holes, a	422	439
Defect width, d	561-708	585-738
Oxide thickness	2000	2000

Table 2-1: List of physical dimensions of both the monorail and air-bridge microcavities at λ=1.55μm.
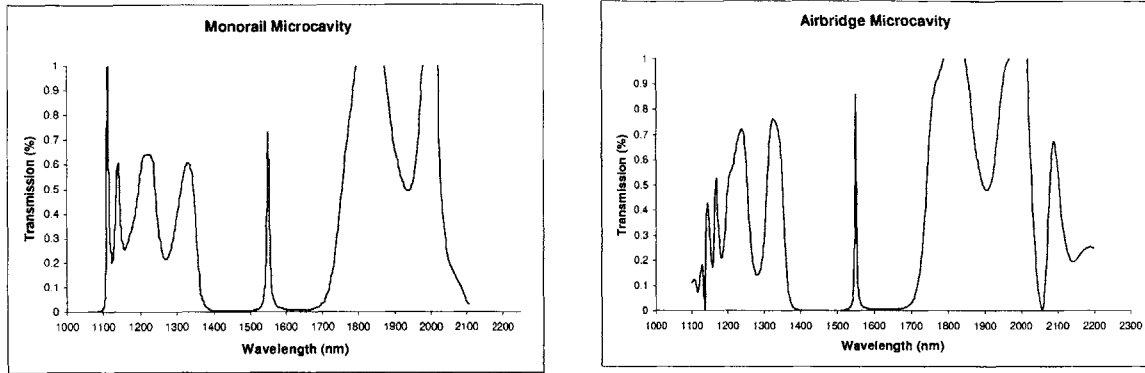
Figure 2-18: Simulated transmission spectra of the monorail (left) and the air-bridge (right) microcavities. The Q's for the microcavities are 270 for the monorail and 320 for the air-bridge respectively. Transmission at resonance is 72% for the monorail and 90% for the air-bridge.

The theoretical transmission spectra for both the monorail and air-bridge microcavities are shown in Figure 2-18. The cavity quality factors for the microcavities are predicted to be 270 and 320 for the monorail and the air-bridge respectively. The air-bridge microcavity is expected to have a higher Q due to the stronger optical confinement from the higher index contrast of the one-dimensional photonic crystal and its surroundings. Similarly, the transmission at the resonance wavelength is also higher in the air-bridge microcavity: 90% compared to 72% in the case of the monorail device.

In contrast to the 4.5μm devices, high-resolution lithographic techniques resulting in nanometer features sizes are employed in the fabrication of the 1.55μm devices. As such, restrictions encountered while designing the 4.5μm devices are obviated in the case of the 1.55μm devices. The geometry of the photonic crystal has thus been designed to maintain single mode operation of the waveguide structure and achieve optimal Q of the microcavity. Consequently, neither an over- nor under-layer is necessary in the device structure. The mode volume is also believed to be the smallest ever designed at 1.55μm [49], especially for the III-V compound semiconductor material system. As mentioned before, the use of the direct-bandgap material immediately suggests the integration of these photonic bandgap microcavities with other III-V based optoelectronic devices.

The single-mode nature of the waveguide-based microcavity structure effectively ensures the single-mode operation of the coupling waveguides with the same cross-sectional

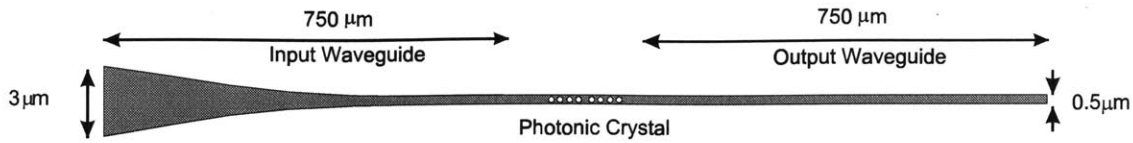Figure 2-19: Plan view schematic of 1.55μm PBG microcavity device detailing input and output waveguide design. The input waveguide flare extends over 100μm (not drawn to scale). The precise output waveguide width varies between that of the monorail and the air-bridge microcavities.

geometry and material system. A schematic of the overall device structure is shown in Figure 2-19, detailing the design of the waveguide. The input waveguide flares from 3μm wide at the input facet to the width of the photonic crystal over a length of 100μm. As in the 4.5μm devices, the wider input facet serves to increase the overlap between the input beam and the facet. The input waveguide is multi-mode at the flare section but becomes single-mode as it narrows to 0.5μm. The waveguide then maintains the width of about 0.5μm for another 650μm until the waveguide/photonic crystal interface. After the photonic crystal, the output coupling waveguide extends for another 750μm without any flaring in the structure. The overall length of the device is slightly in excess of 1.5mm.

The performance of the waveguide design is again verified using the beam propagation method (BPM). Figure 2-20 shows the eigenmode solutions for both the monorail and air-bridge structures, at the input facets and along the approximately 0.5μm-wide waveguide section. The eigenmodes are well guided within the core of the waveguide structure, with little spatial extension into the surrounding. Table 2-2 summarizes the results obtained from the BPM simulation for both microcavity configurations. Taking into consideration the transmission at resonance of 72% and 90% for the monorail and air-bridge microcavities respectively, the overall transmission through the respective device structure is 63% and 67%.

Transmission through:	Monorail microcavity	Air-bridge microcavity
Flare segment (input waveguide)	93.3%	89.9%
Straight segment (input waveguide)	97.1%	91.3%
Straight segment (output waveguide)	97.1%	91.3%

Table 2-2: Summary of BPM results for the 1.55μm microcavities

38
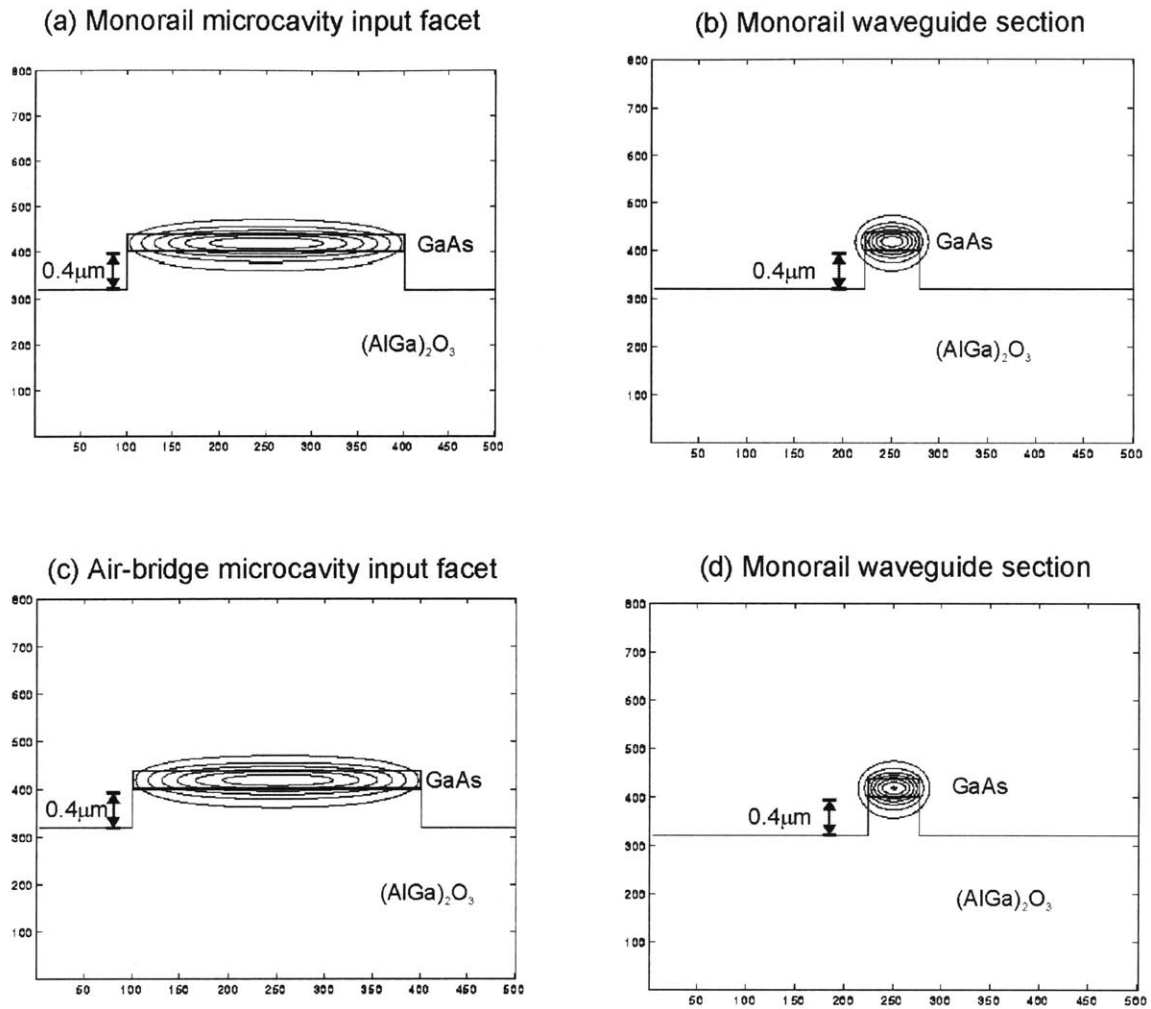
Figure 2-20: Beam propagation method simulation results for the 1.55μm coupling waveguide structures. In each panel, the mode profile is overlaid on the cross-sectional plot of the waveguide. Panel (a) shows the eigenmode profile at the input facet of the monorail microcavity coupling waveguide; panel (b) shows the eigenmode profile at the waveguide section before the monorail microcavity. Panels (c) and (d) shows the eigenmode profiles at the corresponding position along the coupling waveguides of the air-bridge microcavity.

2.4 Other one-dimensional microcavities

As mentioned previously, other microcavities exhibiting photonic bandgaps in one dimension have already been extensively studied. These devices include the distributed Bragg reflectors (DBR) and the distributed feedback Bragg (DFB) gratings which are characterized by weak index modulation [24]. In these devices, a larger number of periods in index variation are required to achieve good confinement of light within the defect region. Furthermore, the resonant mode has a large spatial extent, spreading well into the gratings or the DBR mirrors and leading to a large resonant mode volume.

Recently, there have been reports of one-dimensional photonic bandgap microcavities using high-index contrast systems. MacDougal et al, for instance, fabricated a DBR mirror stack using multiple GaAs (n=3.3) and Al_xO_y (n=1.61) layers [50]. Krauss et al. attempted a waveguide microcavity by using gratings with high aspect ratio etched deeply into semiconductor material [51]. Specifically, the gratings are etched into an $Al_{0.12}Ga_{0.88}As$ "core" layer on top of an $Al_{0.35}Ga_{0.65}As$ "cladding" layer. While optical confinement along the axis of the gratings is strong due to the high effective index contrast of the deep gratings, the low index contrast between the "core" and the "cladding" layers result in losses into the substrate. The deep grating approach is further analyzed by Villeneuve et al [52]. In both the high index-contrast DBR and deep gratings devices, the modal volume is large and results in a small Q/V ratio.

A particularly noteworthy demonstration of a one-dimensional photonic bandgap, waveguide microcavity is that of a monorail microcavity by Foresi et al. at MIT [49]. The study shows operation of a high index-contrast microcavity at 1.56μm wavelength using silicon-based material system. The Q for the microcavity is measured to be 265 and the mode volume is calculated to be $0.055μm^3$. This translates to a spontaneous emission enhancement factor of 35 and is believed to be the highest ever measured. The main drawback of this approach, however, is the use of the indirect bandgap silicon material system, where the ability to create light emitting devices lags that of direct bandgap semiconductors.

40

The air-bridge waveguide microcavity is first proposed by Villeneuve et al at MIT in 1995 [46]. The group of researchers, which includes this author, is also first to demonstrate the feasibility of fabricating these suspended structures using III-V semiconductor material. Subsequently, Zhang et al from Northwestern University report the fabrication of similar air-bridge structures, called "1-D photonic-bandgap structure along photonic wire" [53]. In that report, the air-bridge structure is made of an InGaAs-InGaAsP material system and is designed to operate at λ=1.55μm. The simulated performance of the structure using a 2-D finite-difference time-domain analysis shows a Q of 500. This result, however, is inherently flawed since it assumes a structure with an infinite extent in the vertical direction (i.e., that the waveguide is infinitely thick), which discounted a pathway of radiation loss. The Northwestern group did not include any optical measurement results in the publication and has not since reported any progress.

It is worthy to note that, apart from the potential of controlling spontaneous emission with the waveguide microcavities, other possible applications have also been forwarded. Chen et al., for instance, proposed the use of the air-bridge microcavity as an optical filter with sharp transmission resonance and wide stop bands [54]. Villeneuve et al, on the other hand, suggests the use of the single-mode waveguide microcavity for rapid optical switching through modulation of the resonant frequency [55]. The modulation of the resonant frequency can be achieved through the change in refractive index of the semiconductor arising from photoionization of deep donor levels.

2.5 Summary

In Chapter 2, the general properties of the one-dimensional photonic bandgap microcavity are described. The physics of the 1-D PBG microcavity is treated qualitatively, including its dispersion relationship and the nature of the PBG. The determinants for the Q of the microcavity are examined in detail, with attention to the loss mechanisms limiting the value of Q. The design of the 1-D PBG microcavities at the wavelength regimes of λ=4.5μm and 1.55μm, including that of the coupling waveguides used in the testing of these microcavities, is detailed. The beam propagation method

41

forms the basis for theoretically verifying the efficacy of the coupling waveguides. Other one-dimensional photonic bandgap devices have also been surveyed.

Chapter 3 **One-dimensional photonic bandgap microcavity: fabrication**

3.1 Fabrication of air-bridge structures: Feasibility study

When the one-dimensional photonic bandgap air-bridge microcavity was first proposed in 1994, a study was conducted to investigate the issues involved in the fabrication of suspended structures at micron length scale. The proposed air-bridge structure clearly required the technique of micromachining used in the fabrication of micromechanical systems (MEMS), a field that was attracting wide interest in the research community. In addition, the ability to fabricate these structures using both silicon and the direct bandgap III-V compound semiconductor was deemed highly desirable. An air-bridge microcavity device based on III-V material system was of particular interest for its potential integration with other optoelectronic elements.

At that time, most of the demonstrated MEMS devices were based predominately on silicon material system. This is due primarily to the maturity of silicon fabrication technology and the relatively lower cost of silicon processing (as compared to III-V compound semiconductors). In addition, silicon has a higher mechanical yield strength and lower thermal expansion mismatch with common dielectrics like silicon nitride and silicon dioxide than GaAs, a representative III-V material [56]. The latter is an important consideration because dielectrics are often used as electrical insulators and as protective materials of microstructures against certain chemical processing steps. A thermal mismatch would lead to residual stress in the thin films and the consequent failure of suspended thin film structures.

Several studies on III-V based MEMS devices had nonetheless been reported [56, 57]. These devices were designed to exploit properties unique to the III-V's, particularly the existence of the direct bandgap [58] and nonzero piezoelectric coefficients [59] in these materials. It was clear from the reports, however, that micromachining III-V materials

would be considerably more challenging than with silicon-based material. Surface micromachining, where the etching of sacrificial material is used to suspend thin film structures, was well developed in silicon due to the presence of a practically infinite etch selectivity between Si and SiO_2. In the Si/SiO_2 selective etch, a buffered hydrofluoric acid (HF) solution was typically used. The process had been used in the integrated circuit fabrication industry for a long time and was well understood. In contrast, $GaAs/Al_xGa_{1-x}As$ represented the primary III-V material system with a comparably high etch selectivity that was widely known. The selective etch available was either a solution of NH_4OH, H_2O_2 and HCl with a certain pH value, or HF (for Al concentration, x=0.8 or higher). The use of HF solution for the selective etch of high Al-percentage $Al_xGa_{1-x}As$ alloys, in particular, held great promise [60, 61].

The goal of the feasibility study was, therefore, to establish the processes for the fabrication of suspended structures using both Si and GaAs material systems with feature sizes at the micron length-scale. In the course of the work, it was also the intention to uncover details pertaining to the fabrication of MEMS devices (especially for the III-V's) not revealed in the literature. Figure 3-1 shows a schematic of the tri-layer structure used in the study. The top layer formed the suspended structure when the underlying sacrificial material was selectively etched. The various material systems studied were (top layer, sacrificial layer, substrate):

a) Polysilicon and low-temperature silicon dioxide (LTO), both deposited by low-pressure chemical vapor deposition (LPCVD) at 630°C and at 400°C respectively, on silicon substrate;

b) Amorphous silicon and LTO, deposited by LPCVD at 590°C and at 400°C respectively, on Si substrate;

c) GaAs/$Al_{0.3}Ga_{0.7}As$ heterostructure grown by gas source molecular beam epitaxy (GSMBE) on GaAs substrate;

d) GaAs/$In_{0.5}Ga_{0.5}P$ heterostructure grown by GSMBE on GaAs substrate; and

e) GaAs/AlAs heterostructure grown by MBE on GaAs substrate.

The structures investigated in this study for all material systems included both cantilevers and air-bridges. The cantilevers had physical dimensions ranging from 10 to 300μm in length and 2 to 10μm in width, while those for the air-bridges ranged from 10 to 100μm in length and 2 to 10μm in width. Holes were present in a subset of the air-bridge structures and their diameters range from 1 to 4μm. The fabrication processes employed in the study consisted of photolithography, reactive ion etching (RIE) and wet chemical etch (Figure 3-2). Different RIE gas chemistries and wet chemical etches were investigated for the various material systems.

Overall, suspended structures were successfully fabricated for material systems (b) amorphous silicon/LTO/Si and (e) GaAs/AlAs/GaAs. The polysilicon/LTO/Si material system did not yield any suspended structures due to the high compressive stress present in the polysilicon film. The thin-film MEMS structures buckled when they were suspended. Attempts using GaAs/$In_{0.49}Ga_{0.51}P$/GaAs were unsuccessful because of the poor etch selectivity between the GaAs and $In_{0.5}Ga_{0.5}P$. The GaAs/$Al_{0.3}Ga_{0.7}As$ material systems, on the other hand, suffered from a low etch rate and rough morphology of etched features. On top of the above problems, common to all material systems was also the phenomenon of stiction, where the structural film adhered permanently to the substrate surface during the drying process after the suspension etch (see Section 3.5.B).

For the amorphous Si/LTO/Si material system, a photolithography process was first used

Structural layer (500nm)
Sacrificial layer (1000nm)

Substrate
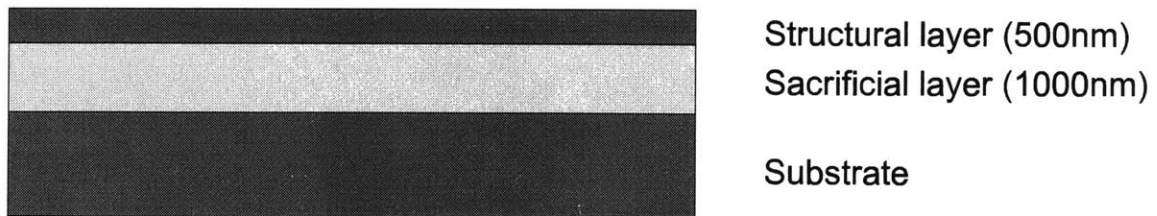
Figure 3-1: General material structure used in the feasibility study.

to define the patterns of the structures. The patterns were then transferred to the amorphous Si and LTO by RIE using CCl_4/O_2 and $CHF_3/CF_4/O_2$ gases respectively. A wet-etch using buffered HF solution removed the LTO and suspended the amorphous Si structures. For the GaAs/AlAs/GaAs material system, an identical photolithography step defined the patterns. An RIE step with $BCl_3/SiCl_4$ gases transferred the patterns to the GaAs/AlAs layers. Finally, the structures were released with a wet-etch using diluted HF solution [62]. The samples were rinsed in deionized (DI) water followed by methanol after the etch. Methanol is chosen as the final rinse liquid for its low surface tension with solid surfaces [62], thus avoiding any stiction problem.

Scanning electron micrographs of the suspended structures are shown in Figure 3-3. As seen in the micrographs, the structures did not exhibit any signs of buckling, implying the

Figure 3-2: Fabrication process sequence for the air-bridge structures employed in the feasibility study.

46

lack of excessive residual stress in the thin films at the end of the entire fabrication process. This is especially true for the cantilever structures, where any buckling in the structure would be more pronounced than in the air-bridge structur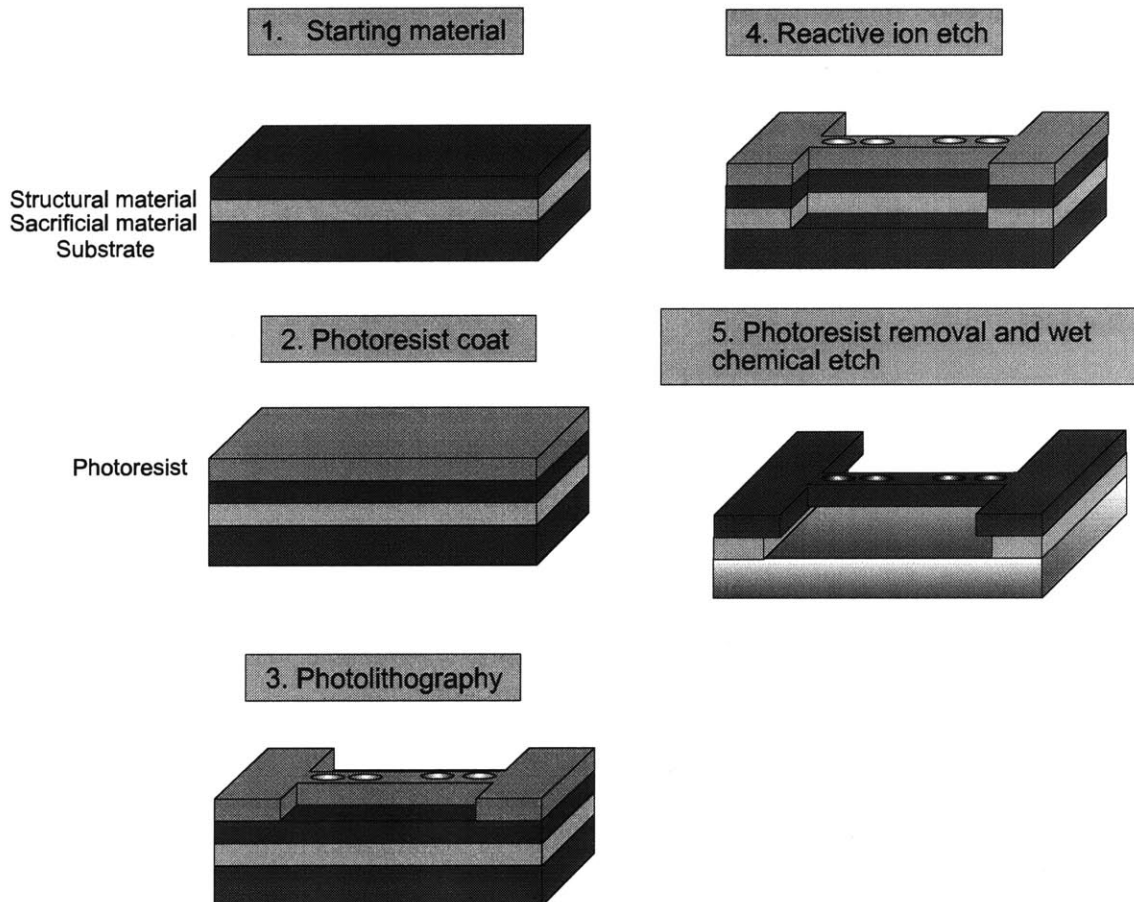es. The use of an amorphous silicon thin film, which had small tensile stress, prevented such problems in the case of the silicon-based structures. For the III-V's, the growth of the lattice-matched heterostructure by MBE implied the absence of stress in the thin films.

In addition, the sidewalls of the structures are also seen to be particularly straight and vertical, and were a testament to the excellent etch anisotropy of the RIE processes. There was also no visible deterioration of the structural material after the wet-etch release step. This implied a high etch selectivity between the structural and the sacrificial material. In other words, in the time needed to completely remove the sacrificial material from under the structural thin film, the acid etchant had barely (if any) effect on the structural material. The good etch selectivity was true for both the silicon-based and the III-V based devices. The smallest feature size realized was $1\,\mu m$, and was limited by the photolithography process as well as the quality of the mask used in the process.

The findings from this study would eventually form the basis of the fabrication process for the subsequent investigation of the 1-D PBG microcavities. The study is documented in Ref [45].
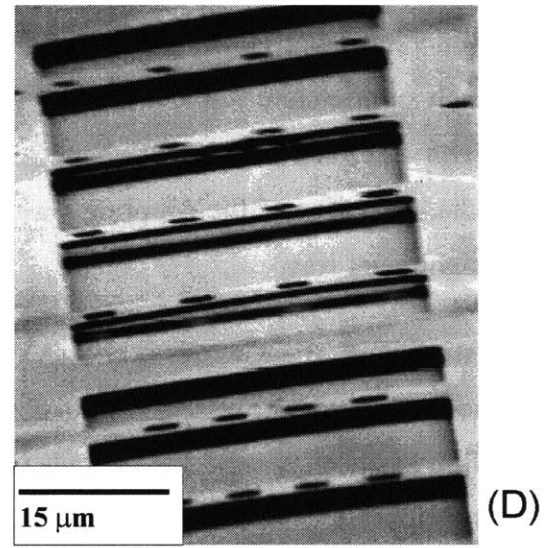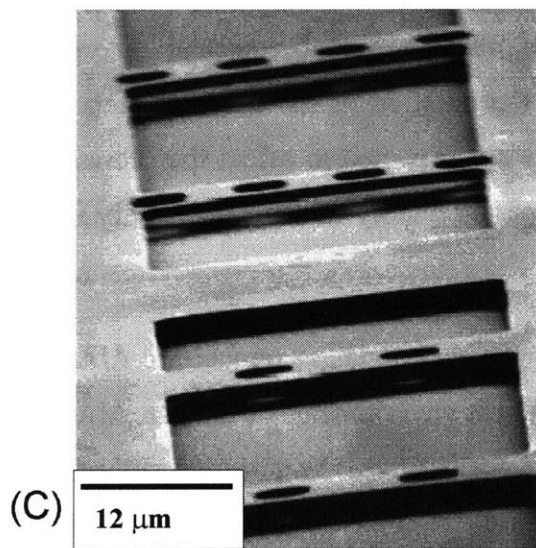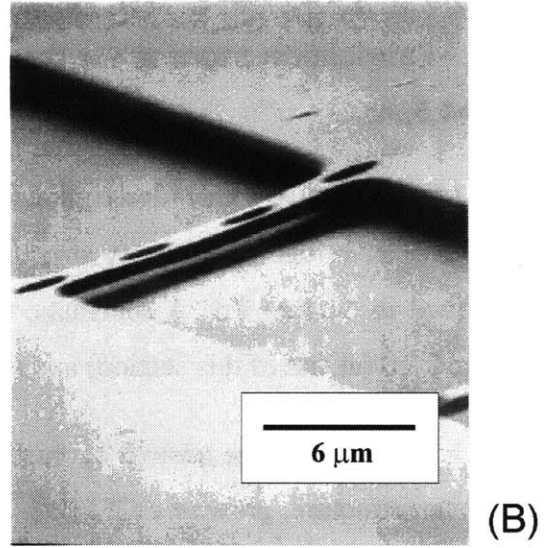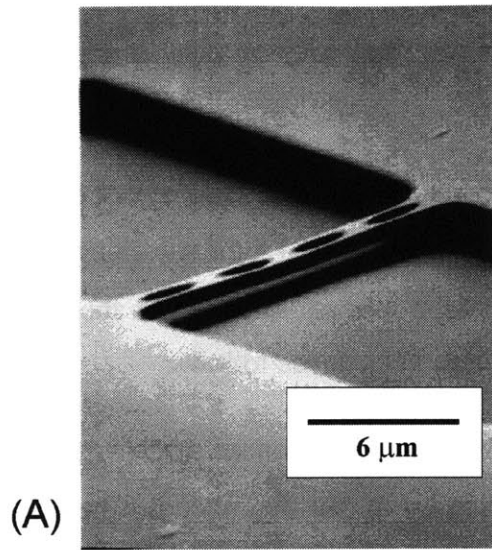
Figure 3-3: Scanning electron micrographs of suspended air-bridge structures in Si/SiO2 material system (A & B), and in GaAs/AlAs material system (C & D).

3.2   Fabrication process for the 1-D PBG air-bridge microcavity operating at λ=4.5μm

This section begins with a description of the process involved in the fabrication of the 1-D PBG air-bridge microcavity structure designed to operate at 4.5μm wavelength, as described in Section 2.3. A schematic of the fabrication process sequence is shown in Figure 3-10 (at end of this section) and is described in more detail as follows:

Step 1. *Heterostructure growth by gas source molecular beam epitaxy (GSMBE)*. The heterostructure, grown by GSMBE, is almost identical to that described in Chapter 2 in the design of coupling waveguides (Figure 2-15), except for the addition of a 50nm-thick $In_{0.49}Ga_{0.51}P$ etch stop layer between the overlayer ($Al_{0.3}Ga_{0.7}As$) and the structural layer (GaAs). The etch-stop layer prevents the subsequent overlayer wet etch from etching the GaAs layer as well. The addition of the thin etch stop layer, with a refractive index of about 3.3 [63], is not expected to affect the propagation characteristics of the coupling waveguides or the quality of the microcavity in any significant way.

In addition, $Al_{0.9}Ga_{0.1}As$ is chosen as the sacrificial material, as opposed to AlAs, due to the rapid hydrolyzation of AlAs in an ambient environment. In fact, an AlAs thin film has been observed to degrade into flakes peeling from the substrate within hours of exposure to the room, especially under humid conditions. The thermal oxidation of $Al_xGa_{1-x}As$, where $x \neq 1.0$, also yields a more stable oxide than if x=1.0 (see Section 3.6 below). $Al_{0.9}Ga_{0.1}As$, with a high Al composition, is expected to exhibit an equally high etch selectivity against GaAs as AlAs.

The GSMBE is performed with a Riber Instruments S.A. 32P reactor, which forms a part of the chemical beam epitaxy (CBE) system at MIT (as shown in Figure 3-4). The group III elements for the crystal growth are provided by the thermal sublimation of solid sources, including Ga, Al and In. The group V elements, As and P, are obtained from the thermal cracking of gaseous arsine and phosphine. The entire CBE system is constantly maintained under ultrahigh vacuum conditions ($<1 \times 10^{-10}$ torr),

49

and the substrate on which the heterostructure is grown can be transferred between the various chambers of the system in vacuum by a robotic arm. During the crystal growth, a Reflection High-Energy Electron Diffraction (RHEED) system provides in-situ, real-time monitoring of the growth rates. Details on the CBE system and the technique of MBE, RHEED and the various compound semiconductors that have been grown in the system can be found in Refs. [64-66].

The heterostructure is grown on a full 2-inch diameter GaAs substrate. The epi-ready substrate is first loaded into an introduction chamber on the CBE. The substrate is then baked at 210°C to remove any moisture on the substrate surface. After the bake, the substrate is transferred to the III-V reactor where it is heated up to the growth temperature. In the process, the native oxide on the substrate surface is desorbed at 580°C (as measured by a pyrometer). During the entire growth process, the substrate is continually rotated to ensure uniform growth of material on the entire wafer. The growth rates for the various layers are monitored during the growth using RHEED oscillations.

The use of MBE to grow the heterostructure has several advantages. First, the layers are lattice-matched and are hence inherently stress-free. Second, MBE allows compositional control to 3% accuracy and monolayer thickness control. Third, MBE-growth results in a crystal of high quality with low defect density across the wafer, thus providing a large sample area for device fabrication.
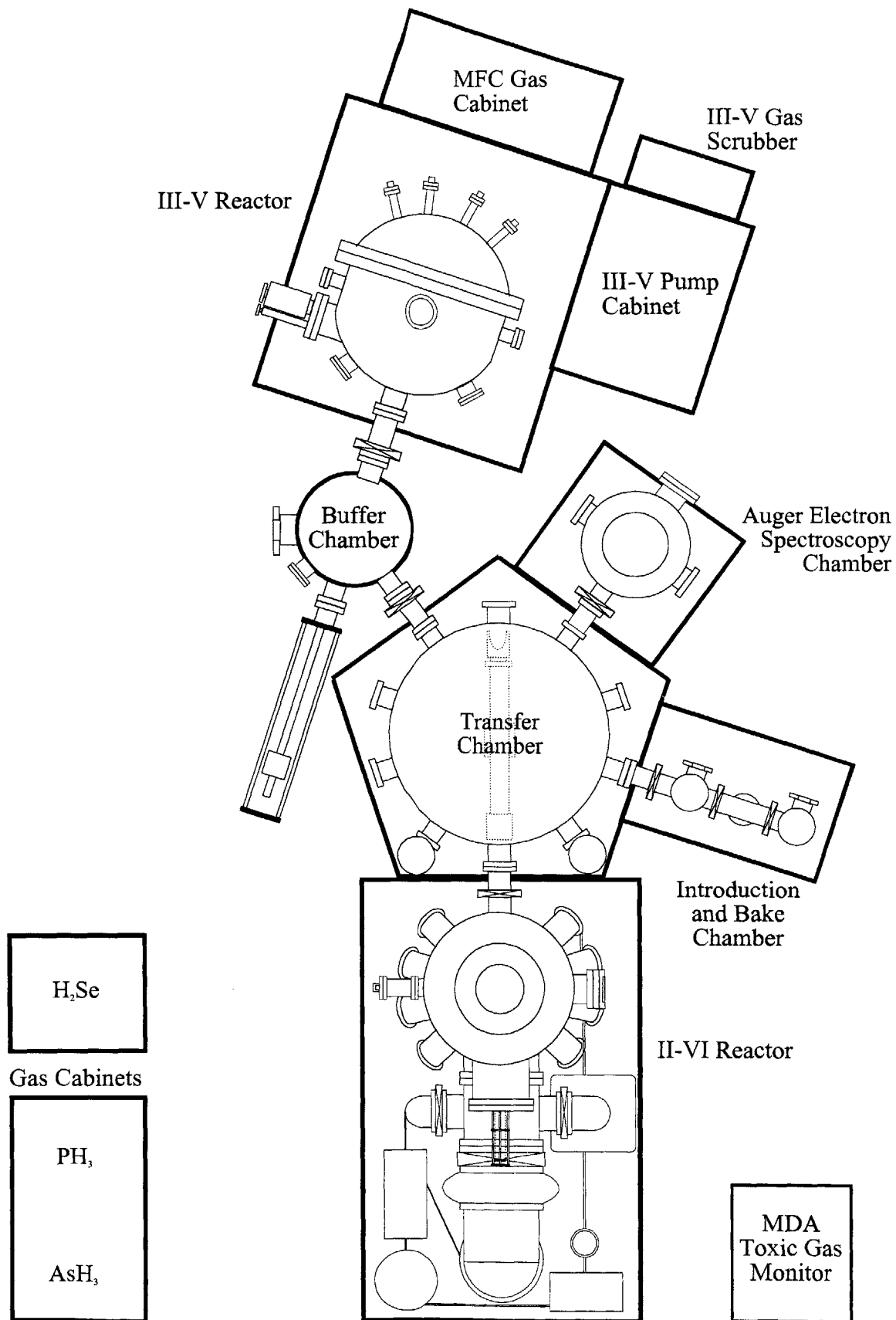
Figure 3-4: Schematic of the layout of the Chemical Beam Epitaxy laboratory.

Step 2. *Photolithography to define mask of overlayer.* The purpose of this process step is to create a photoresist mask for the etching of the overlayer. At the end of this step, the surface outside the air-bridge regions will be covered by photoresist and protected from the subsequent wet etch to remove the overlayer from the air-bridges (Figure 3-5). Prior to the start of the photolithography step proper, the 2-inch diameter wafer is first cleaved into four quarters. Each quarter ("process sample") is then processed individually, typically accompanied by three other quarters of 2-inch plain GaAs wafers as control samples (also called "dummy samples"). The process and dummy samples are then subjected to a solvent clean to prepare the surface for subsequent processing in a Class 10 cleanroom[2]. The solvent clean consists of two cycles of 2min-long rinse in 75°C trichloroethylene (TCE), followed by 2 cycles of 2min-long rinse in acetone in an ultrasonic bath, and 2 cycles of 2min-long rinse in methanol in an ultrasonic bath.

Thereafter, the samples are vapor-coated with hexamethyldisilazane (HMDS) in an oven maintained at a temperature of 150°C and under a vacuum of about 1mTorr. The high temperature in the oven drives off any moisture on the surface of the
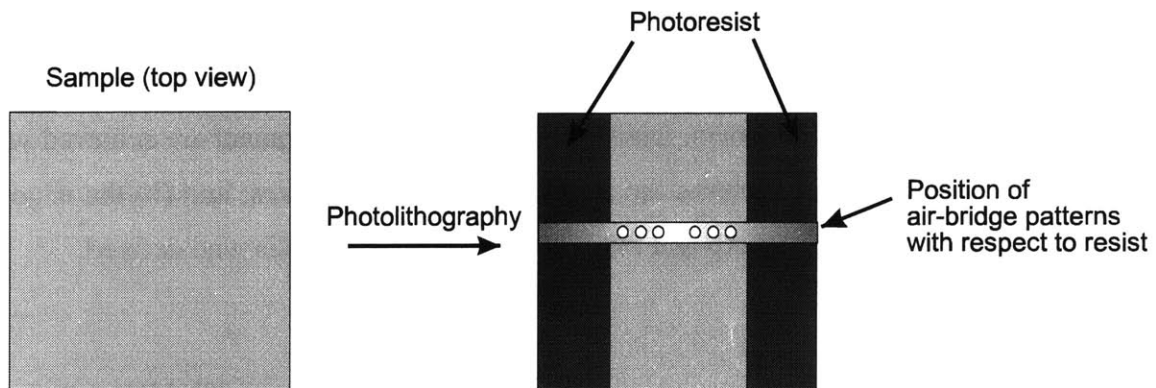
Figure 3-5: Photolithography process to define overlayer region. At the end of the process, photoresist film covers and protect area on sample from overlayer wet etch. The overlay of the air-bridge pattern shows relative position of the air-bridge and waveguide regions with respect to the current lithography step.

---

[2] A Class 10 cleanroom is one where the air in the room is controlled to contain less than 10 particles of 0.5μm size per cubic feet.

samples, while the HMDS coating promotes the adhesion of photoresist. A commercially available positive photoresist[3], Shipley Microposit 1808, is then spin-coated onto the samples. The photoresist is statically dispensed by a glass dropper and the samples go through two spin cycles: a "spread" cycle of 6s at 750rpm, followed by a "spin" cycle of 60s at 4000rpm. The expected photoresist thickness is 750nm±10nm. The samples are next baked at 90°C for 30min (also called the "soft bake") to remove the solvents in the photoresist, to further improve resist adhesion and to reduce any shear stress in the resist film from the spin-coating.

After the soft bake, the samples are loaded onto a Karl-Suss MA4 optical aligner and brought into close contact with an optical mask. The optical mask is a quartz plate printed with the desired patterns in chrome. For the photolithography of the overlayer, the patterns consist of a series of clear rectangles, 10μm wide and about 100μm long, surrounded by chrome (see Figure 3-6). During the exposure step, ultra-violet light penetrates the quartz plate at the clear regions but is absorbed by chrome at other parts of the plate. When the sample is subsequently dipped into a chemical developer, the photoresist that has been exposed to the UV light is removed. The end result is a transfer of the quartz plate patterns into the photoresist film. A set of alignment marks, made up of a cross in a box, is also included to allow subsequent alignment of the air-bridge patterns with respect to the overlayer patterns. Finally, special markers as shown in Figure 3-6 are added to the mask for purposes of determining the quality of exposure and development. Optimal exposure and development are achieved when (a) the dark and open patterns are deemed to be of equal sizes; and (b) the edges of the square patterns are sharp and the gap between the squares is well defined.

---

[3] A positive photoresist is a resin-based material that, after exposure to ultra-violet (UV) light, is removed when subjected to a photoresist developer. Conversely, a negative photoresist will remain impervious to the developer after UV light exposure.
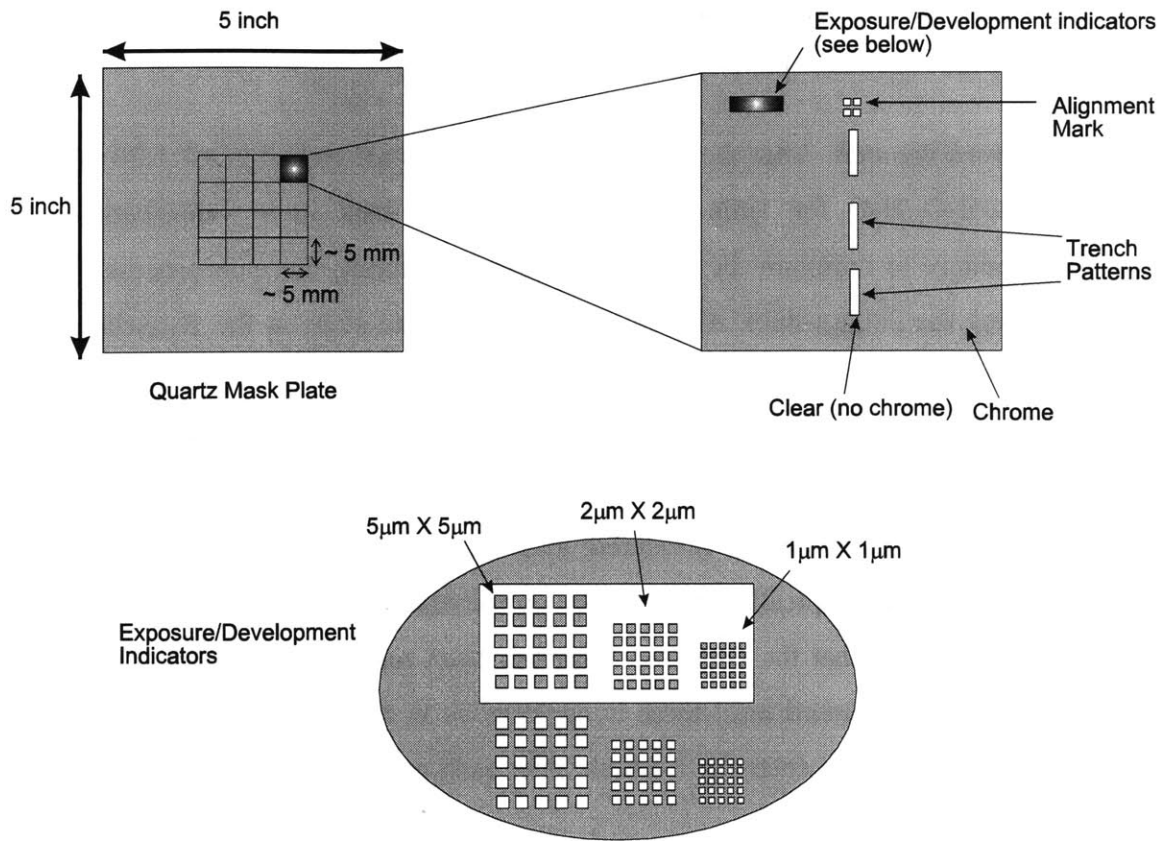
Figure 3-6: Illustration of mask with trench patterns used in photolithography steps for the 4.5μm air-bridge microcavity process.

The sample is exposed on the aligner in 7 cycles of 2s exposure, with 4s separation between each cycle. The "wait" time between exposures allow any gaseous byproducts from the exposed photoresist to diffuse away from the exposed area. A mercury lamp generates the UV-light with a peak wavelength at 320nm and intensity calibrated at $6.0mW/cm^2$. After the exposure, the sample is typically developed in Shipley MF319 Positive Resist Developer for 60s. The exposed patterns are then examined under the microscope to determine if additional exposure or development time is necessary. The dummy samples are usually exposed prior to the process sample, thus allowing final adjustments in any slight process variation that may be present from run to run. The post-development microscope examination is of particular importance since an unsatisfactory resist pattern can be easily removed and reworked, before proceeding to further, irreversible processing steps like wet etching.

The samples are then baked at 120°C for 30 min (also called the "hard bake") to harden the final resist patterns for further processing.

Step 3. ***Overlayer etch***. After the hard bake, the samples are etched in a 1:1:20 mixture of $H_2SO_4/H_2O_2/H_2O$ for 1min 10s. The mixture is kept in a water bath at room temperature to maintain the mixture temperature during the etch process. The etch removes the 200nm-thick $Al_{0.3}Ga_{0.7}As$ overlayer and stops at the $In_{0.49}Ga_{0.51}P$ etch-stop layer, hence removing the overlayer material from the air-bridge regions as defined by the photoresist. The etch rate in this process is more than 3nm/s and the etch depth is monitored with a profilometer. After the sample has been etched for 1 minute, the etch depth is measured; after an additional 10s etch, the etch depth is measured again. Typically, there will be no increase in the etch depth after the second etch, indicating that the etch-stop layer has been reached. Otherwise, an additional 10s etch is performed until there is no increase in the etch depth. The samples are rinsed in deionized water for 1 minute after each etch and blown dry with a nitrogen air gun.

After the overlayer etch has been completed, the photoresist is removed by rinsing the sample in acetone followed by methanol. An oxygen plasma etch is then performed to remove any residual photoresist on the sample surface.

Step 4. ***Plasma-enhanced chemical vapor deposition of SiO$_2$***. In this step, a layer of approximately 100nm-thick SiO_2 is deposited on the sample by plasma-enhanced chemical vapor deposition (PECVD). The dielectric layer would act subsequently as the mask material for the reactive ion etch of the III-V compound semiconductor material underneath (see Step 7). This process is performed in the deposition chamber of a dual chamber Plasmatherm Inc. Series 700 Wafer'Batch RIE/PECVD system. The sample is maintained at a temperature of 250° C and the flow rates for the reactant gases are 900sccm for nitrous oxide (NO) and 400sccm for 2% silane (2% SiH_4 in N_2). The plasma is driven at a radio frequency of 13.56MHz and power of 20W. A mechanical pump regulates the process pressure at 900mTorr, while a base pressure of 5×10^{-5} Torr in the chamber is achieved with a turbomolecular pump. At

the deposition rate of about 40-50nm/min, a total process time of 2min is employed to attain 100nm of SiO_2. The SiO_2-covered sample takes on a turquoise-blue coloration characteristic of the particular oxide thickness. The oxide thickness is further confirmed by measuring the oxide thickness, using variable angle scanning ellipsometry (VASE), on a Si wafer that has been included in the deposition process.

Step 5. *Photolithography of air-bridge and waveguide patterns.* In this photolithography step, the 1-D photonic crystal and the waveguide patterns are simultaneously defined. As in step 2, the samples are first primed with HMDS vapor in a dedicated oven, spin-coated with Shipley 1808 positive photoresist and soft-baked, prior to the exposure process. The mask used in this step consists of a series of waveguides integrated with the photonic crystal as designed in Chapter 2. The physical dimensions of the photonic crystals are varied to allow for process variation; the pattern dimensions incorporated in the mask are listed in Table 3-1. Alignment marks, in correspondence to those in the mask used in Step 2, are added to facilitate alignment of the patterns in the two lithography steps. The patterns on this particular optical mask, due to the small feature sizes involved, are created by a commercial vendor using electron-beam lithography.

The 1808 photoresist is part of a family of positive photoresist called the 1800-series

Type	C1	C2	C3
Number of holes	3	3	3
Air-bridge width (μm)	1.6	1.8	2.0
Diameter (μm)	0.8	1.0	1.2
Lattice spacing (μm)	1.6	1.8	2.0
Defect width (μm)	2.3	2.5	2.7
Air-bridge length (μm)	12.5	13.5	14.9

Table 3-1 : Dimensions of photonic crystals included in the mask design.

offered by Shipley Corporation (Marlboro, MA) and is chosen for its consistently thin resist film after spin-coating. The thinness of the resist film is of particular importance in the ability to achieve the required linewidth for the patterns using an optical lithography system. The minimum linewidth in the air-bridge pattern is the separation between the hole and the edge of the air-bridge, i.e. 400nm. Such a narrow linewidth is considered to be close to the limit of the capability of a conventional optical lithography system like the Karl-Suss MA4. As the side profile of a resist film is typically sloped, thicker resist film will result in wider deviation from the ideal linewidth. The thickness of the 1808 resist film spin-coated at 4000rpm for 30s is about 780nm, and the typical slope of the film is about 5%. This translates to a deviation of about 40nm in the linewidth, or about 10% of the minimum linewidth, deemed acceptable for the performance of the devices.

In addition to the choice of a thin photoresist for the process, the use of the "Hard Vacuum Contact" mode on the Karl-Suss MA4 Aligner is also necessary to attain the minimum linewidth. In this contact scheme, a circular chuck with a rubber O-ring on the circumference and the sample in the center is raised into close contact with the quartz mask plate with a mechanical lever. Vacuum is then established in the space between the chuck and the mask plate by evacuating the space through holes present on the surface of the chuck. A vacuum seal is formed between the O-ring and the mask, and the sample is sucked further onto the plate. This is the closest possible contact using the aligner. The exposure time on the Karl-Suss MA4 with a peak exposure wavelength of 320nm is similar to that in Step 2, i.e. 7 cycles of 2s exposure with 4s wait time between exposures. The development time in the Shipley MF319 developer is 60s, followed by a 60s rinse in DI water. The linewidth of the resist pattern is verified using the scanning electron microscope (Figure 3-7). The linewidth of 400nm represents the narrowest linewidth ever achieved with the Karl-Suss MA4 Optical Aligner at MIT.

During the exposure step on the process samples, the air-bridge patterns have to reside within the rectangular patterns that resulted from the overlayer etch. The air-bridge patterns are aligned with respect to those from the first photolithography

step by using the alignment marks as mentioned in Step 2. In particular, the alignment marks from Step 2 consists of a cross within a square. The corresponding mark in the present mask is a smaller cross that is designed to fit within the larger cross from the first mask (Figure 3-8). The Karl-Suss aligner is equipped with a microscope with a 25X objective lens (100X total magnification, including the 4X eyepiece) to aid in alignment.

Following the exposure, the sample is again developed in Shipley MF319 developer for 60s, rinsed in DI water for 60s and examined under a high-power microscope. Thereafter, the sample is post-baked in a convection oven at 120°C for 30min.

Step 6. ***Wet-etch of SiO₂ with BOE to transfer bridge patterns.*** The device patterns from the previous photolithography step are transferred into the SiO_2 film using buffered oxide etch (BOE). BOE is essentially HF acid with aluminum fluoride added to maintain the pH of the mixture. The semiconductor material under the oxide film, namely GaAs (in the air-bridge region) and $Al_{0.3}Ga_{0.7}As$ (in the waveguide region), are not etched by BOE. The etch rate on the PECVD oxide film from Step 4 is calibrated to be 400nm/min. The total etch time on the sample thus translates to 15s, followed by a rinse in DI water for 60s. The bulk of the photoresist film is subsequently removed with acetone and methanol, and the sample is inspected under
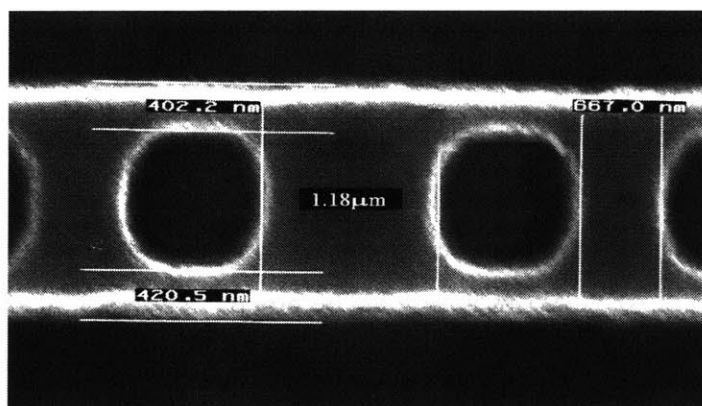
Figure 3-7: Scanning electron micrograph showing plan view of Shipley 1808 resist exposed with the air-bridge patterns on the Karl-Suss MA4 optical aligner. The dimensions for the various critical features as shown on the micrograph are ~400nm for distance between the holes and the edge of the waveguide, 1.18µm for the defect size, and 667nm for the distance between the edges of the two holes. The indistinct appearance of the waveguide edges is due to the slope in the resist layer.
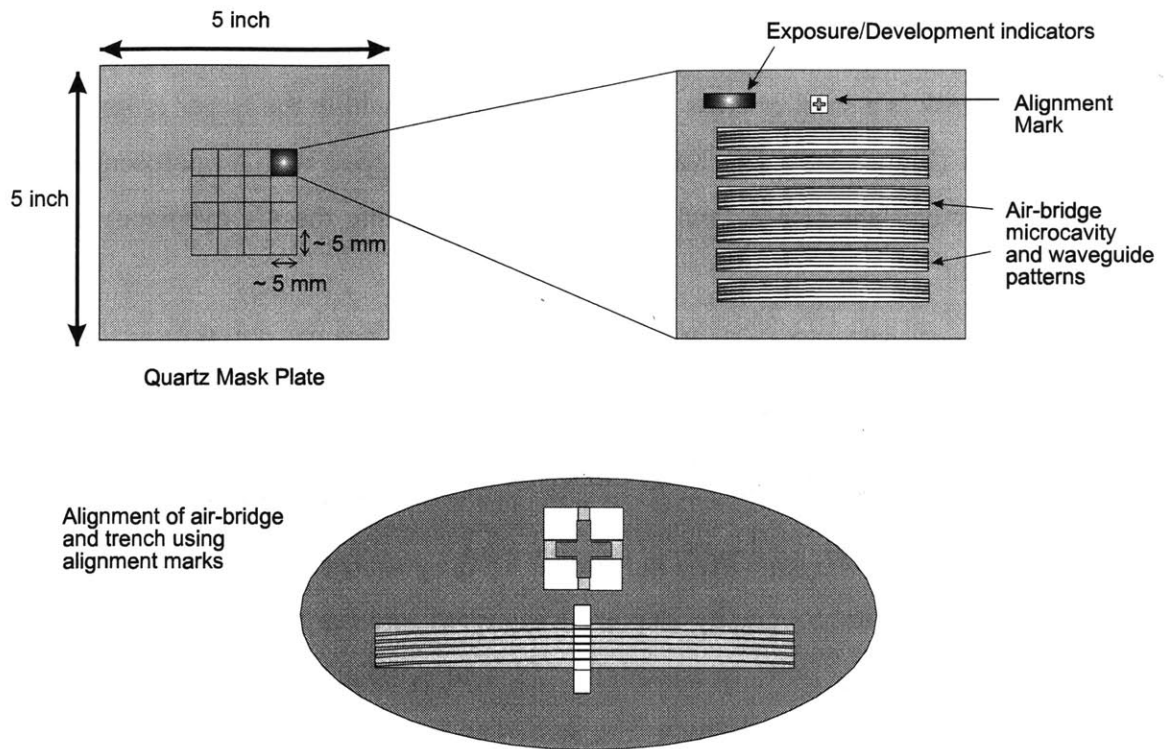
Figure 3-8: Illustration of alignment scheme with crosses as alignment marks to position air-bridge patterns within the trench patterns.

an optical microscope. An oxygen plasma etch is performed to remove any residual resist film.

Step 7. **_Reactive ion etch of $Al_{0.3}Ga_{0.7}As/In_{0.49}Ga_{0.51}P/GaAs/Al_{0.7}Ga_{0.3}As/Al_{0.9}Ga_{0.1}As$ layers._** In this process step, the device patterns defined in the SiO_2 layer in the previous step is further transferred anisotropically to the heterostructure using reactive ion etching (RIE). The process entails the use of a chlorine-based chemistry to etch through the entire heterostructure, i.e. $Al_{0.3}Ga_{0.7}As$, $In_{0.49}Ga_{0.51}P$, GaAs, $Al_{0.7}Ga_{0.3}As$ and $Al_{0.9}Ga_{0.1}As$ in order. The process parameters are: 30sccm flow rate of boron trichloride (BCl_3), 20sccm flow rate of silicon tetrachloride ($SiCl_4$), process pressure of 30mTorr and incident RF power of 250W. The etch rate at these process parameters is approximately 180-220nm/min, and is lower for an $Al_xGa_{1-x}As$ layer with higher Al composition. The total etch time is 8min, with the intention of etching into the $Al_{0.9}Ga_{0.1}As$ sacrificial layer by about 200nm. Note that a thicker $In_{0.49}Ga_{0.51}P$

59

layer than the one present in this heterostructure would have required a different RIE gas chemistry; for instance, a methane/hydrogen-based process. As the etch-stop layer is thin (nominally 50nm), however, the $BCl_3/SiCl_4$ RIE sputters through the thin $In_{0.49}Ga_{0.51}P$ layer with ease.

The selectivity between the mask material and the semiconductor material to be etched is a major consideration when developing an RIE process. In this instance, SiO_2 is chosen as the mask material, instead of photoresist, because of its higher etch resistance to the $BCl_3/SiCl_4$ etch chemistry. The etch rate of the Shipley resist is approximately equal to that of GaAs. As the photoresist film has to be thin to achieve good photolithographic pattern transfer in Step 5, it will not be sufficiently thick to withstand the duration of the RIE process. As such, the SiO_2 layer is necessary as a "hard" mask for pattern transfer into the heterostructure with the RIE process. It should be noted, however, that SiO_2 does not have infinite etch resistance against the $BCl_3/SiCl_4$ RIE process. An oxide mask layer that is less than 80nm in thickness has been observed to degrade after the RIE step. The etch rate for SiO_2 under these etch conditions is slightly over 10nm/min, implying an approximately 20:1 etch selectivity versus GaAs.

The RIE process is a particularly important technology in the fabrication of the microcavities, and will be dwelled upon in greater detail later (Section 3.6).

Step 8. *Photolithography to define trench patterns.* The previous RIE step results in the definition of the entire air-bridge microcavity device, including the coupling waveguides, into the heterostructure. A photolithography step is next performed to demarcate the region on the device that would form the suspended air-bridge section. Similar to Step 2, where the overlayer photoresist pattern was defined, this process step results in the coverage of areas on the sides of the air-bridge structure, as shown in Figure 3-6. In essence, a "trench" is being defined under the air-bridges. The photoresist patterns protects the area outside of the air-bridge patterns from the subsequent wet etch to suspend the air-bridges.

As before, the sample is first primed with HMDS, spin-coated with Shipley 1813 positive photoresist and soft baked for 30min at 90°C. The Shiply 1813, a variant of the Shipley 1808 used in the other photolithography steps in this process, yields a resist layer that is about 1.3μm thick when spin-coated at 4000rpm for 30s. The thicker resist is required for the subsequent RIE step. While the resolution of the Shipley 1813 lags that of the Shipley 1808, the resolution required for this photolithography step is on the order of 5μm and can be adequately achieved with the Shipley 1813. Exposure is again made on the Karl-Suss MA4, using the same quartz mask as that used in Step 2, with an exposure of 13 cycles of 2s with 4s wait between cycles. The alignment marks are instrumental in positioning the air-bridge structure within the trenches. After exposure, the sample is developed in Shipley MF319 developer. The hard bake process is omitted in this particular case because of the stress that the baking process induces in the photoresist film. The presence of such stress would present problems during the suspension wet-etch of the air-bridge structures.

Step 9. *RIE to remove trench material.* After the trench has been defined, an RIE of 3-min duration using the $BCl_3/SiCl_4$ gas chemistry and the same parameters as in Step 7 is performed. The purpose of this step is to remove most of the semiconductor material in the trench, hence reducing the amount of material that has to be removed by the suspension wet-etch. By reducing the amount of time required to suspend the air-bridge structure, the amount of lateral undercut into the sides of the trenches is also reduced. In this RIE step, the air-bridge section is still covered with SiO_2 and is hence immune to the etching action. The photoresist film on the side of the trench is also sufficiently thick that the relatively short RIE step would not deplete the photoresist layer completely.
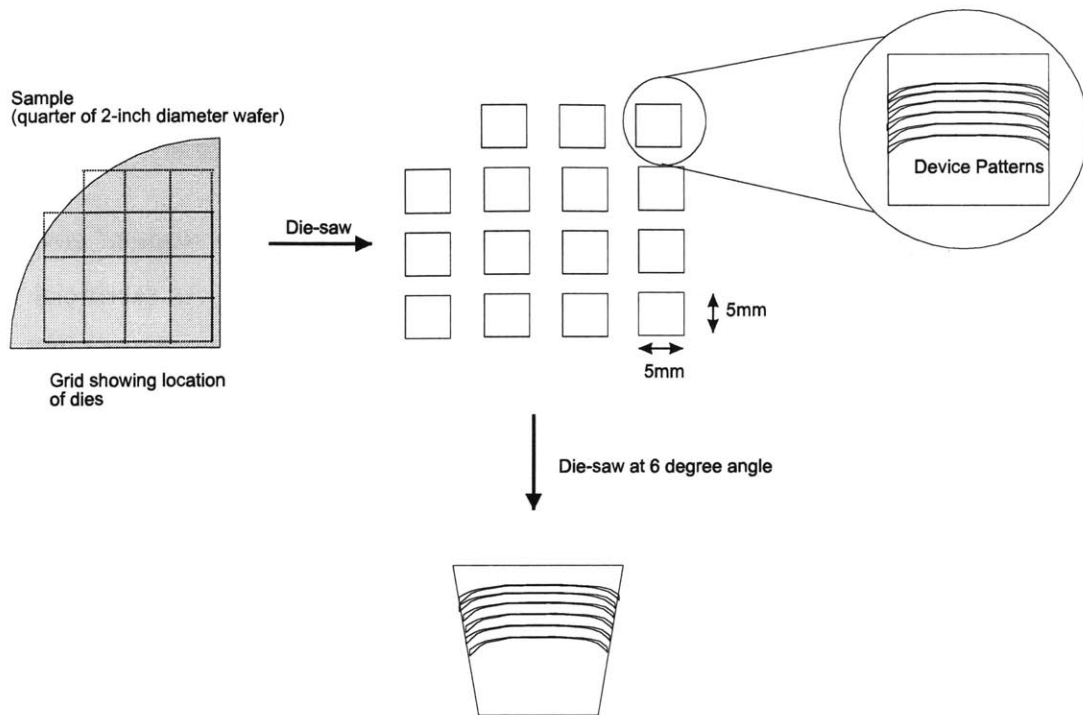
Figure 3-9: Diagram depicting the process of separating the dies on a single quarter of a 2-inch wafer, followed by the sawing of the edges of each die at a 6° angle to the vertical.

Step 10.   ***Die-sawing of facets.*** The size of the sample at this juncture is a quarter of a 2-inch diameter circular wafer (Figure 3-9). Each sample consists of ten to twelve usable dies, where the same set of device patterns is repeated in each die. The dies are separated using a die-saw, and the dimension of each die is about 5mm by 5mm on the side. After the dies on the quarter wafer have been separated, each die is further sawed at a 6° angle to the waveguide facets. The direction and position of the saw with respect to the sample can be controlled by the precise stage control of the die-saw machine. During the entire die-sawing process, the samples are mounted with wax on a larger silicon wafer for ease of handling.

Step 11.   ***Facet polish.*** The die-sawing process results in extremely rough waveguide facets. Excessive roughness on the waveguide facets causes scattering at both the input and output facets. As such, the waveguide facets are polished to a mirror-finish so that light can be coupled into and out of the waveguides efficiently. In this step, a die is mounted on a tripod using wax and the facets gradually polished

with a rotating polishing wheel. Polishing pads of 1.0μm and 0.3μm grit size, in that order, are used on the polishing wheel to gradually smoothen the facets.

Step 12.   ***Selective wet etch of $Al_{0.7}Ga_{0.3}As$ and $Al_{0.9}Ga_{0.1}As$ to suspend air-bridge structure.*** In this step, the $Al_{0.7}Ga_{0.3}As$ underlayer and $Al_{0.9}Ga_{0.1}As$ sacrificial layer under the 1-D photonic crystal is preferentially etched using a diluted HF acid solution. The other layers in the heterostructure, namely GaAs and the thin $In_{0.5}Ga_{0.5}P$ etch-stop, are left unaffected. The undercutting of the GaAs air-bridge occurs only within the trench region as defined by the previous photolithographic step; the heterostructure under the photoresist film is protected from the acid solution. The die is first dipped into a Teflon dish containing a mixture of 10ml HF: 750ml DI water for 2min. A rinse in DI water for 1min and in methanol for 1min follows. Finally, the photoresist is removed by dipping the die in acetone followed by methanol. The die is then removed from the solvent and left to dry in the exhaust hood.

Step 13.   ***Thermal oxidation of $Al_{0.9}Ga_{0.1}As$.*** Prior to the thermal oxidation step to preferentially oxidize $Al_{0.9}Ga_{0.1}As$, the die is first subjected to a solvent clean to remove the wax on the back of the die. The solvent clean consists of a 1-min dip in warm trichloroethylene, followed by a 1-min dip in acetone and 1-min dip in methanol. At the end of the solvent clean, the sample is again left to dry in the exhaust hood.

The die is next introduced to a furnace maintained at a temperature of 435°C with dry nitrogen flowing through the furnace. The die is left in the furnace for 15min to allow the temperature to stabilize at the initial level of 435°C, after an initial drop in temperature when the die is first introduced. Thereafter, steam from a water-bubbler maintained at 95°C is flown into the furnace tube with nitrogen as the carrier gas. After 1 hour, the steam flow is stopped, dry nitrogen flow through the furnace resumes and the furnace temperature is reduced to 200°C. The die is finally removed after the furnace has cooled down to 200°C.

The thermal oxidation rate for $Al_xGa_{1-x}As$ is a strong function of the percentage composition of Al in the alloy, i.e. the value of x. The parameters used in this process step result in the complete oxidation of $Al_{0.9}Ga_{0.1}As$ and negligible oxidation of $Al_{0.7}Ga_{0.3}As$. The GaAs, $Al_{0.3}Ga_{0.7}As$ and $In_{0.5}Ga_{0.5}P$ layers are unaffected by the oxidation process. The oxidation of $Al_xGa_{1-x}As$ using steam is a relatively new technology to the research community, and forms a key technology in the fabrication of the III-V based PBG devices. Details on the current understanding of the oxidation process, the characterization of the oxidation apparatus and process at MIT, as well as properties of the oxide as observed by the author will be discussed in a later section (Section 3.7).

| 1 | Heterostructure grown by GSMBE |

200nm
200nm
200nm
4μm
400μm

$Al_{0.3}Ga_{0.7}As$
GaAs
$Al_{0.7}Ga_{0.3}As$
$Al_{0.9}Ga_{0.1}As$
GaAs
Substrate

| 4 | Plasma-enhanced chemical vapor deposition (PECVD) of SiO_2 |

| 2 | Photolithography to define mask for overlayer etch |

| 5 | Photolithography to define waveguide and air-bridge patterns |

| 3 | Wet etch of $Al_{0.3}Ga_{0.7}As$ overlayer and photoresist removal |

| 6 | Wet etch of SiO_2 to transfer patterns from step 5 and photoresist removal |

Figure 3-10: Fabrication process sequence for the 1-D PBG air-bridge microcavity operating at 4.5μm wavelength.

65

7 Reactive ion etch through
Al$_{0.3}$Ga$_{0.7}$As/GaAs/Al$_{0.7}$Ga$_{0.3}$As/Al$_{0.9}$Ga$_{0.1}$As
heterostructure and oxide removal
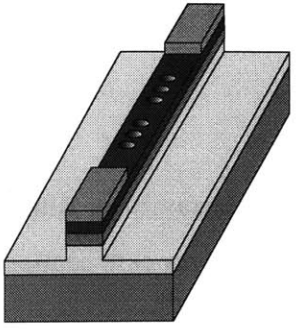
10 Diesaw of facets at 6 degree angle to
vertical,followed by polish to
mirror-finish

6° angle → | Sample | Device structure
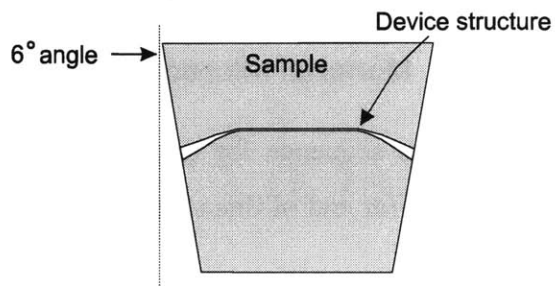
8 Photolithography to define trench
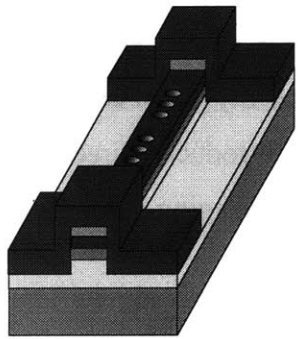
11 Wet etch removal of sacrificial material
to suspend air-bridge structure; followed
by removal of photoresist
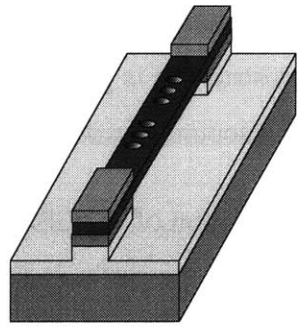
9 RIE to carve out trench
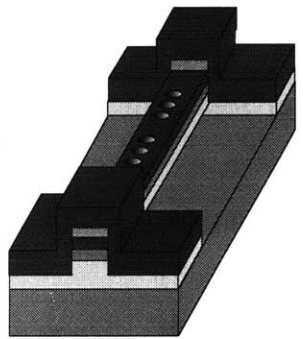
12 Thermal oxidation of Al$_{0.9}$Ga$_{0.1}$As
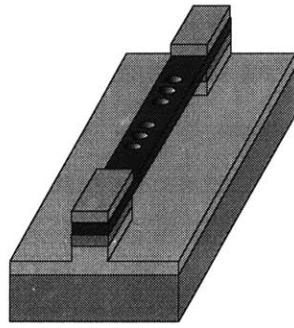
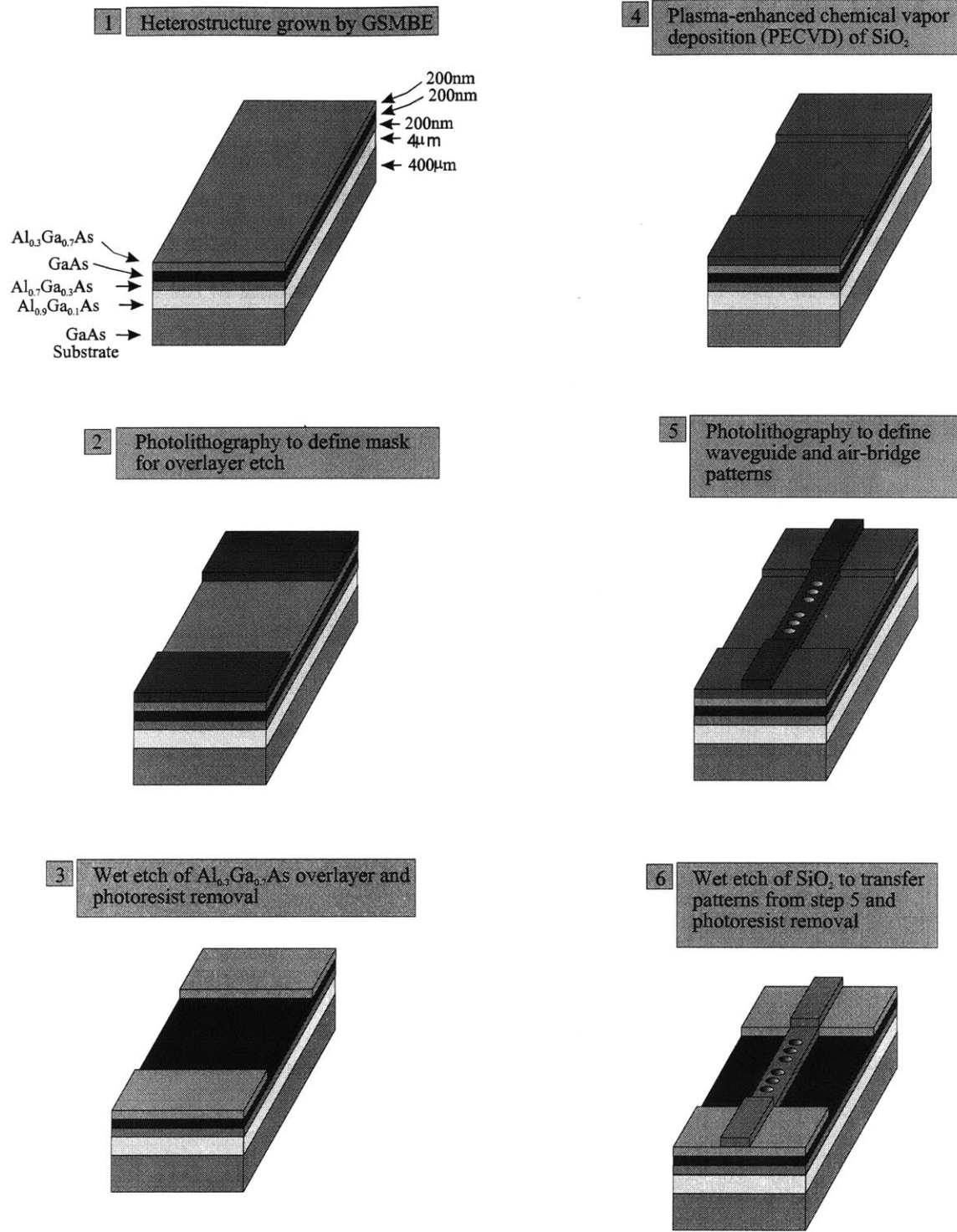Figure 3-10 (continued): Fabrication process sequence for the 1-D PBG air-bridge microcavity operating at 4.5µm wavelength.

3.3   Fabrication process for the 1-D PBG microcavities operating at λ=1.55μm

3.3.A   Monorail microcavity

The process sequence for the fabrication of the monorail microcavity is illustrated in Figure 3-15 (at end of this section). The details for the fabrication process sequence is as follows:

Step 1. ***Growth of heterostructure with GSMBE.*** The heterostructure required for the fabrication of the 1-D PBG monorail structure is grown by GSMBE; the trilayer structure is shown in Figure 3-11. As before, $Al_{0.9}Ga_{0.1}As$ is chosen as the sacrificial material, in preference to AlAs, because of its relative stability when exposed to air. The heterostructure is grown on a full 2-inch GaAs wafer, introduced directly into the ultra-high vacuum crystal growth system from its original packaging.

At the completion of the GSMBE process, the 2-inch wafer is cleaved into 4 quarters. One quarter of the wafer is typically used for a complete fabrication sequence, thus preserving sufficient unprocessed material for process iterations and material analysis.

Step 2. ***PECVD of SiO₂.*** A layer of 100nm-thick SiO_2 is next deposited on the wafer quarter by PECVD and serves as the hard mask material for an RIE later in the process. The deposition parameters are identical to those in Step 4 of the 4.5μm device process, with a total deposition time of 7min. As before, the surface of the sample takes on a turquoise-blue hue at the end of the deposition process. The wafer

GaAs (192nm)
$Al_{0.9}Ga_{0.1}As$ (2000nm)

GaAs substrate

Figure 3-11: Heterostructure grown by GSMBE for the fabrication of the air-bridge microcavity operating at 1.55μm wavelength.

quarter is then cleaved into dies of approximately 5mm by 5mm, and each die is processed individually from this point onward.

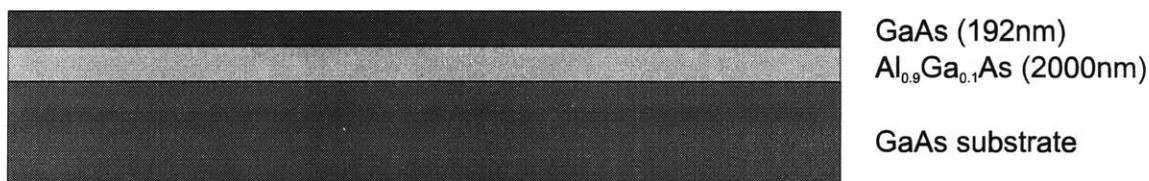Step 3. *Spin-coating of polymethylmethacrylate (PMMA).* In this process step, a die is coated with a layer of electron-beam resist, polymethylmethacrylate (PMMA). PMMA is a positive e-beam resist that becomes amenable to removal by a chemical developer when exposed to an electron-beam of appropriate dose. The PMMA used in this process step is a mixture of 3% 750K PMMA in chlorobenzene. A drop of the PMMA mixture is statically dispensed onto the die with a clean glass dropper, and the die is spun at 3600rpm for 60s, resulting in a 200nm-thick PMMA. The die is then baked in a convection oven at 180°C for 60min to remove the remaining solvent in the PMMA film and to smoothen the film surface.

Step 4. *Direct-write electron beam lithography (EBL).* The die is next loaded into an electron-beam lithography system where the device patterns are written with an e-beam directly on the PMMA film. The range of patterns written on the sample is listed in Table 3-2. The e-beam current is set at 50pA, while the beam scan speed is typically set at around 0.300MHz during the EBL process. An additional set of patterns, called the wedge patterns, is also included for purposes of determining if the sample is adequately developed. The wedge patterns consist of three rows of 5 rectangles, each 10µm-by-30µm in dimensions. The e-beam dose for the wedge pattern increases exponentially from one corner of the array to the opposite array,

Type	Description
MRWG	Plain waveguides without photonic crystals, including 3 straight waveguides of 2µm, 1µm and 0.553µm width, and 2 waveguides with flares from 3µm to 0.553µm.
MRDIA	Change in hole diameter, keeping all other physical parameters constant. Hole diameters (in nm; ideal dimension in boldface): 183, **195**, 207, 220, 232, 244.
MRHOLE	Change in number of holes, keeping all other physical parameters constant. Total number of holes in each PBG structure: 4, 6, 8, 10, 12, 14.
MRAD	Change in defect width, keeping all other physical parameters constant. Defect width (in nm; ideal dimension in boldface): 476, 500, 531, 561, **592**, 622, 653, 683, 708, 738, 769

Table 3-2: Description of monorail microcavity patterns generated in the EBL process.

with the rectangle in the middle of the array exposed with the target dose.

Further details of the EBL process, including system description, data representation and dose calibration, will be described in Section 3.4.

Step 5. *PMMA development.* After the device patterns have been written on the die, the PMMA film is developed in a mixture of 100ml methyl iso-butyl ketone (MIBK): 200ml iso-propanol (IPA) at $20.0°C^4$ for 90s. Thereafter, the sample is rinsed in IPA and blown dry with a nitrogen air gun. The device patterns are then inspected under a Nomarski microscope to determine if a longer development time is required to resolve the patterns. The wedge patterns provide the primary indication of proper exposure and development: the rectangle in the middle of the array should exhibit the sharpest edges. A secondary indication is a subjective judgment on the resolution of the critical dimension, i.e. the distance between the hole and the edge of the waveguide in the photonic crystal. This is particularly difficult given that resolving such a small critical dimension (~0.1μm) under the optical microscope is difficult. It should be noted that the use of a scanning electron microscope (SEM) to inspect the development results is avoided since the e-beam from the SEM will effectively expose the PMMA film and distort the existing patterns.

Step 6. *Electron-beam evaporation of nickel.* After the device patterns on the PMMA film have been satisfactorily developed, 30nm of nickel is then deposited on the die by electron-beam evaporation. The directional deposition of nickel by e-beam evaporation, together with the slight undercut characteristic of an e-beam exposed PMMA film (due to back-scattering of electrons at the sample surface), eases the lifting-off of the nickel film in the next step (Figure 3-12). Nickel is chosen in this process because (a) it can be lifted off easily; (b) it acts as a good mask for the subsequent etch of SiO_2 in Step 8; and (c) the etchant to remove it in Step 8 does not attack GaAs.

---

[4] The mixing of MIBK and IPA results in a moderately endothermic reaction. The temperature of the solution, when first mixed, is about 17°C. The mixture is then hand-warmed to 20°C by simply wrapping one's hands around the beaker containing the mixture. The mixture temperature hovers between 20 and 21°C in the cleanroom for more than 15min thereafter.
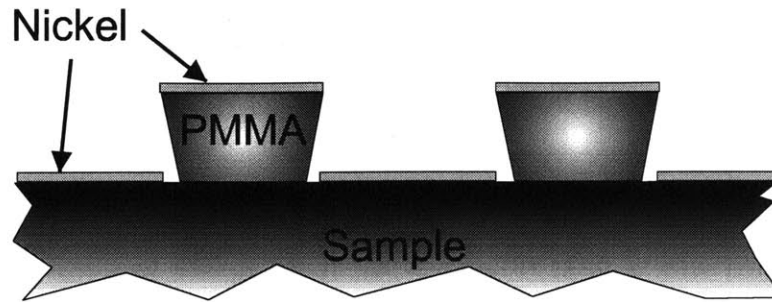
Figure 3-12: Schematic showing sample after e-beam evaporation of nickel. The undercut profile of the PMMA is a result of the electron backscattering off the sample surface during the e-beam lithography. The directionality of the e-beam evaporation, in tandem with the undercut PMMA profile, yields a discontinuous nickel film and is ideal for the liftoff process.

Step 7. ***Nickel lift-off.*** This step involves the removal of the PMMA film using warm 1,1-methyl pyrrollidinone (NMP), which in turn removes the nickel on top of the PMMA. The end result of this process step is the definition of the device patterns in the nickel film. The entire sequence of e-beam exposure, PMMA development, nickel deposition and lift-off is commonly known as an image reversal process. The reasoning behind the use of the image reversal process is as follows: PMMA is a positive e-beam resist, implying that the area on the PMMA film exposed to the e-beam will be cleared after development. If PMMA were to be used as a mask for the subsequent RIE of GaAs, the area outside the waveguides and within the holes would have to be exposed by the e-beam. Such a large area would require a prohibitively long exposure. The use of a negative resist would shorten the exposure time, since only the area within the waveguide and around the hole in the photonic crystal will be written. Negative resists, however, have lower resolution than PMMA and require a more stringent process control for good results. (See Section 3.4 for a report on the experience with SAL601, a negative e-beam resist). The image reversal process allows one to generate the required patterns with short write-time.

During the nickel lift-off process, the die is introduced into a beaker of NMP that has been warmed on a hotplate set at 100°C. The nickel film on the PMMA film can be observed to peel off the surface of the sample, leaving behind the nickel device patterns. After most of the nickel film has lifted off, the die (in the warm NMP) is

placed in an ultrasonic bath for 1min. The ultrasonic agitation ensures that any residual PMMA is removed from the surface, particularly in the area that would form the holes in the photonic crystal (Figure 3-13). The die is then rinsed in acetone and iso-propanol, and blown dry with a nitrogen air gun. The nickel device patterns are finally inspected with a SEM (Figure 3-14). If the device patterns are found to be unsatisfactory, the nickel patterns can be stripped off with nickel etchant and the entire image-reversal process repeated.

Step 8. **_RIE of SiO₂ and wet-etch removal of nickel mask._** Once the nickel device patterns are deemed acceptable, the patterns are anisotropically transferred to the SiO_2 layer using an RIE with the following parameters: trifluoromethane (CHF_3) gas flow of 50sccm, oxygen gas flow of 5sccm, process pressure of 30mTorr, incident RF power of 250W. The RIE process is performed with the die on either a graphite or a polymer plate. The total etch time is 7min with an etch rate of about 15nm/min. The resulting SiO_2 patterns act as the hard mask for the subsequent RIE of GaAs and

(A)

(B)

(C)

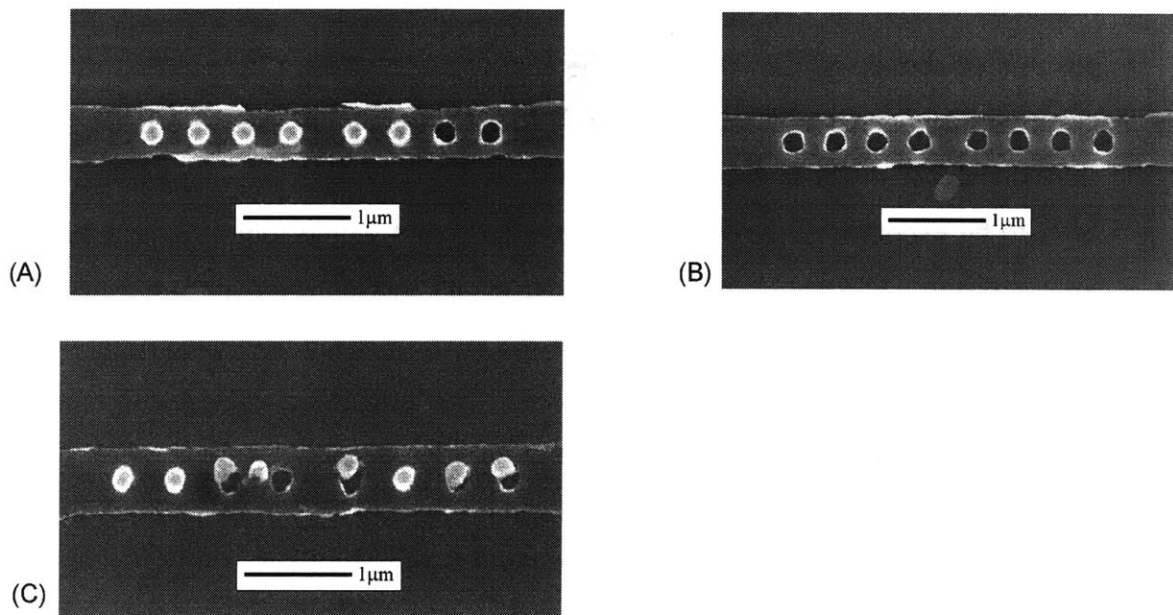Figure 3-13: Scanning electron micrographs illustrating effect of ultrasonic agitation on nickel liftoff. Note the presence of PMMA covered with nickel in the holes of the photonic crystal before ultrasonic agitation (A). The PMMA is removed after the sample has been subjected to 1min of ultrasonic agitation (B). In (C), the PMMA is only partially removed on another sample not subjected to the ultrasonic treatment.
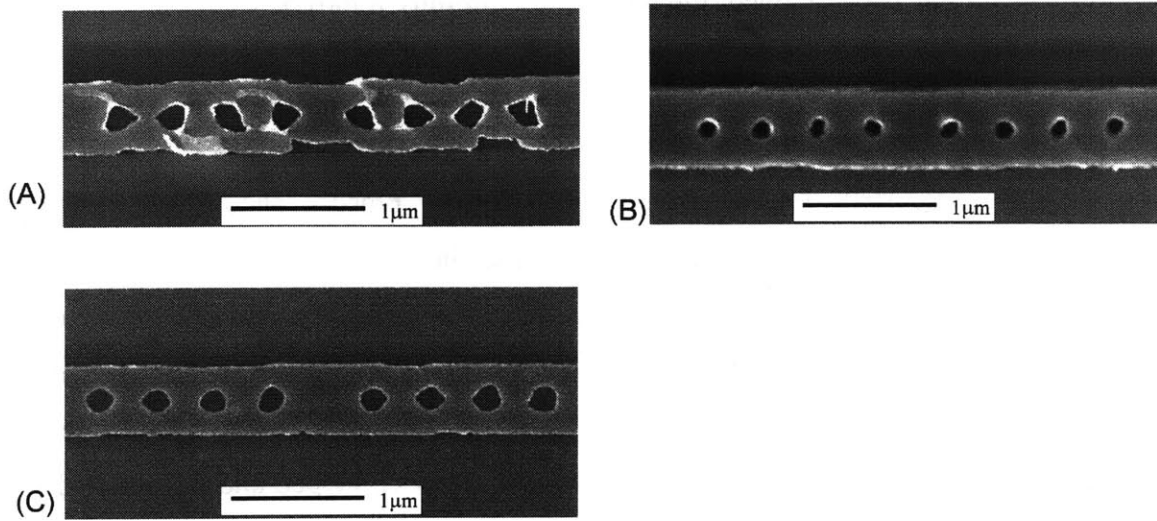
Figure 3-14: Scanning electron micrographs illustrating results of nickel liftoff for a sample that is (A) underexposed or underdeveloped; (B) overexposed or overdeveloped; and (C) correctly exposed and developed.

$Al_{0.9}Ga_{0.1}As$. It should be noted that the nickel patterns cannot be used as the hard mask for the $GaAs/Al_{0.9}Ga_{0.1}As$ RIE process. This is due to the fact that the etchant used to remove the nickel patterns would etch the $Al_{0.9}Ga_{0.1}As$ material exposed by the RIE process.

After the RIE pattern transfer into the SiO_2 layer, the nickel patterns are removed with Transene Corp. type TFB nickel etchant (primarily nitric acid). The SiO_2 patterns are then inspected with the SEM to ensure good pattern transfer.

Step 9. *Substrate thinned by lapping.* The next step in the process involves the thinning of the sample from about 475µm to 175µm by lapping away the backside of the substrate. Thinning of the sample greatly facilitates the cleaving of the waveguide facets later in the process. If the sample were too thick, the cleave may not be successful or the cleaved facets may not be smooth. In the lapping process, the die is first mounted with wax, face down, onto a flat glass block. The backside of the die is then lapped away by gently pushing the glass block back and forth against a polishing paste smeared over another larger glass block. The polishing paste is made from a mixture of 5µm-size polishing grit, household detergent and water. The thickness of the die is monitored intermittently throughout the lapping process. Once the thickness

of 175μm has been attained, the die is then carefully removed from the glass block with warm TCE, and rinsed in acetone and methanol.

While thinning the die eases the cleaving of the sample facets, it also renders the sample particularly fragile. Ideally, the lapping process should be performed immediately before the cleaving process, i.e. the present lapping step should be inserted between Step 12 and 13 below. This approach is eschewed in favor of the current process because it would involve mounting the sample with Al_xO_y on its surface on the glass block. An attempt at this approach has resulted in the oxide layer peeling off the GaAs surface after the sample has been lapped and dismounted with warm TCE, acetone and methanol. It is speculated that the bond between the oxide and the GaAs substrate is weak, and the entire sequence of mounting, lapping and dismounting the sample causes the oxide layer to dissociate from the GaAs substrate.

Step 10. **RIE of GaAs/$Al_{0.9}Ga_{0.1}As$.** An RIE process is next performed on the thinned sample to etch into the GaAs/$Al_{0.9}Ga_{0.1}As$ heterostructure with the SiO_2 device patterns as the mask. The process parameters are BCl_3 flow rate of 30sccm, $SiCl_4$ flow rate of 20sccm, process pressure of 30mTorr and incident RF power of 250W. The total etch time is 3min, with an average etch rate of about 200nm/min. The sample is placed on an alumina plate during the process to protect the bottom aluminum electrode in the RIE system from the etch. The RIE process penetrates about 400nm into the $Al_{0.9}Ga_{0.1}As$ layer.

Step 11. **RIE of SiO_2 mask.** Another RIE step is next performed to remove the SiO_2 mask on the surface of the monorail. The process parameters are CF_4 flow rate of 50sccm, O_2 flow rate of 5sccm, process pressure of 45mTorr and incident power of 225W. The sample is placed on a graphite plate during the process. After the RIE step, the blue coloration attributed to the SiO_2 layer can be clearly observed to have disappeared under the optical microscope.

Step 12. **Thermal oxidation of $Al_{0.9}Ga_{0.1}As$.** After the previous RIE step, the sample is introduced immediately into the oxidation furnace to prevent any extensive ambient hydrolyzation of the exposed $Al_{0.9}Ga_{0.1}As$ material. The sample is then oxidized at

435°C for 30min, with steam in nitrogen carrier gas flowing through the furnace tube. Thereafter, the sample is allowed to cool down to 200°C before its removal from the furnace.

Step 13.   *Cleavage of waveguide facets.* The final step in the process involves the cleaving of the waveguide facets. Narrow nicks are first made on the edge of the sample with a diamond-tipped scribe on a scriber. The nicks are aligned with the ends of the waveguides and would later act as the initiation points for the cleaves down the sample. After the nicks have been made, a thin rod is rolled over the back of the sample to propagate the cleaves from the nicks. The scriber has a precision stage control to allow the accurate position of the nicks such that the cleave would run over the ends of the waveguides, resulting in clean, mirror-like facets. After the waveguide facets have been cleaved, the sample is mounted on a stub and is henceforth ready for optical measurement.

1 Heterostructure grown by MBE

185nm
2000nm
4.75×10^{5} nm
$(475 \ \mu m)$

GaAs →
$Al_{0.9}Ga_{0.1}As$ →
GaAs →
Substrate

4 Direct-write electron beam lithography

PMMA →

2 Plasma-enhanced chemical vapor deposition (PECVD) of SiO_2

SiO_2
(150nm)

5 E-beam evaporation of nickel

Ni
(30nm)

3 Spin-coating of PMMA (E-beam litho. resist)

PMMA
(200nm)

6 Nickel lift-off

Ni

SiO_2
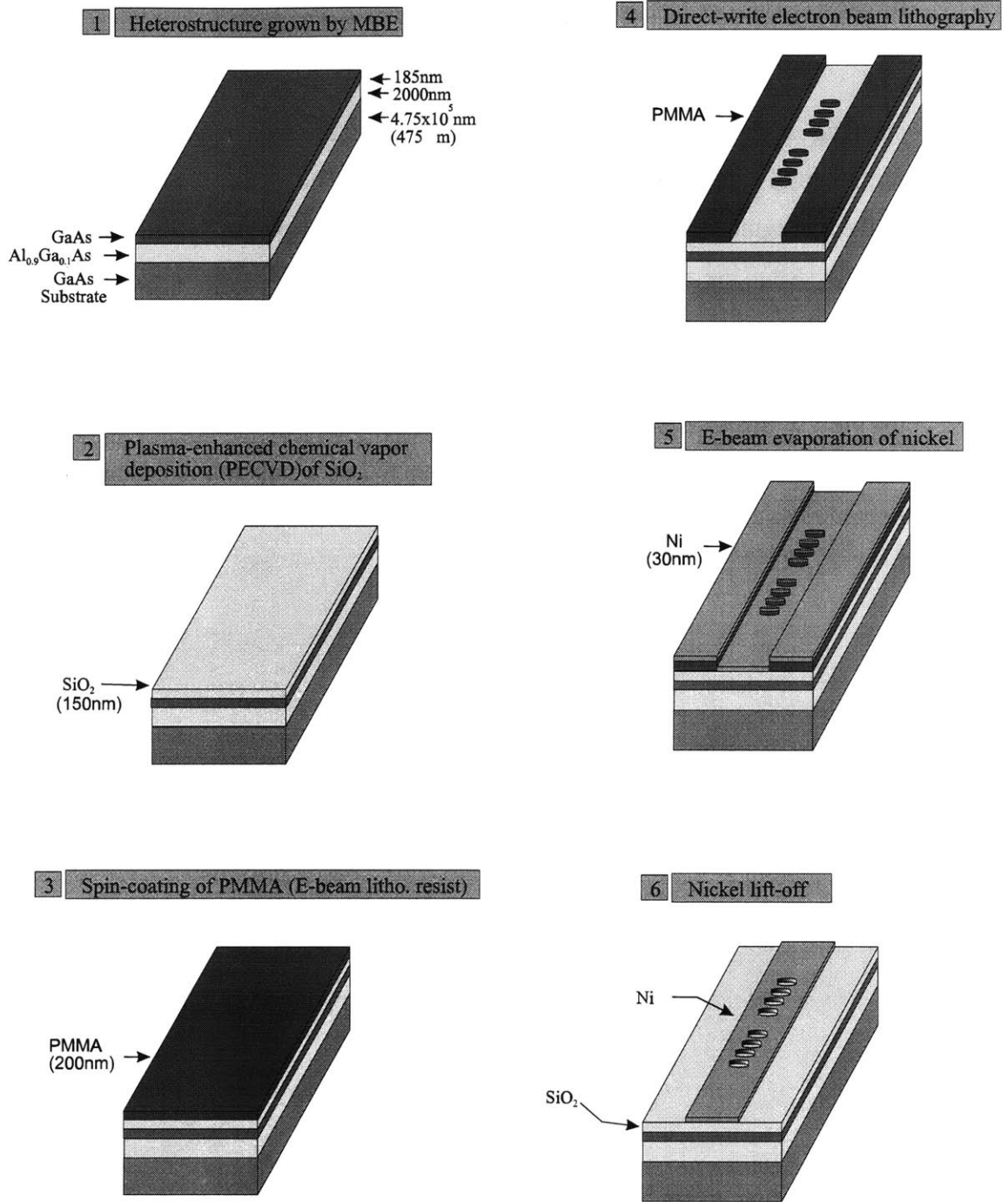
Figure 3-15: Fabrication process sequence for the 1-D PBG monorail microcavity operating at 1.55μm wavelength.

7 RIE of SiO$_2$, followed by wet-etch removal of nickel

9 RIE of GaAs/Al$_{0.9}$Ga$_{0.1}$As

8 Substrate thinned by lapping.

← 2x10^5 nm (200 μm)

GaAs Substrate →

10 RIE of SiO$_2$ and thermal oxidation of Al$_{0.9}$Ga$_{0.1}$As

11 Cleavage of waveguide facets

750 μm

750 μm

3000nm

Input Waveguide

Output Waveguide

525nm

(TOP VIEW)

Photonic Crystal Monorail
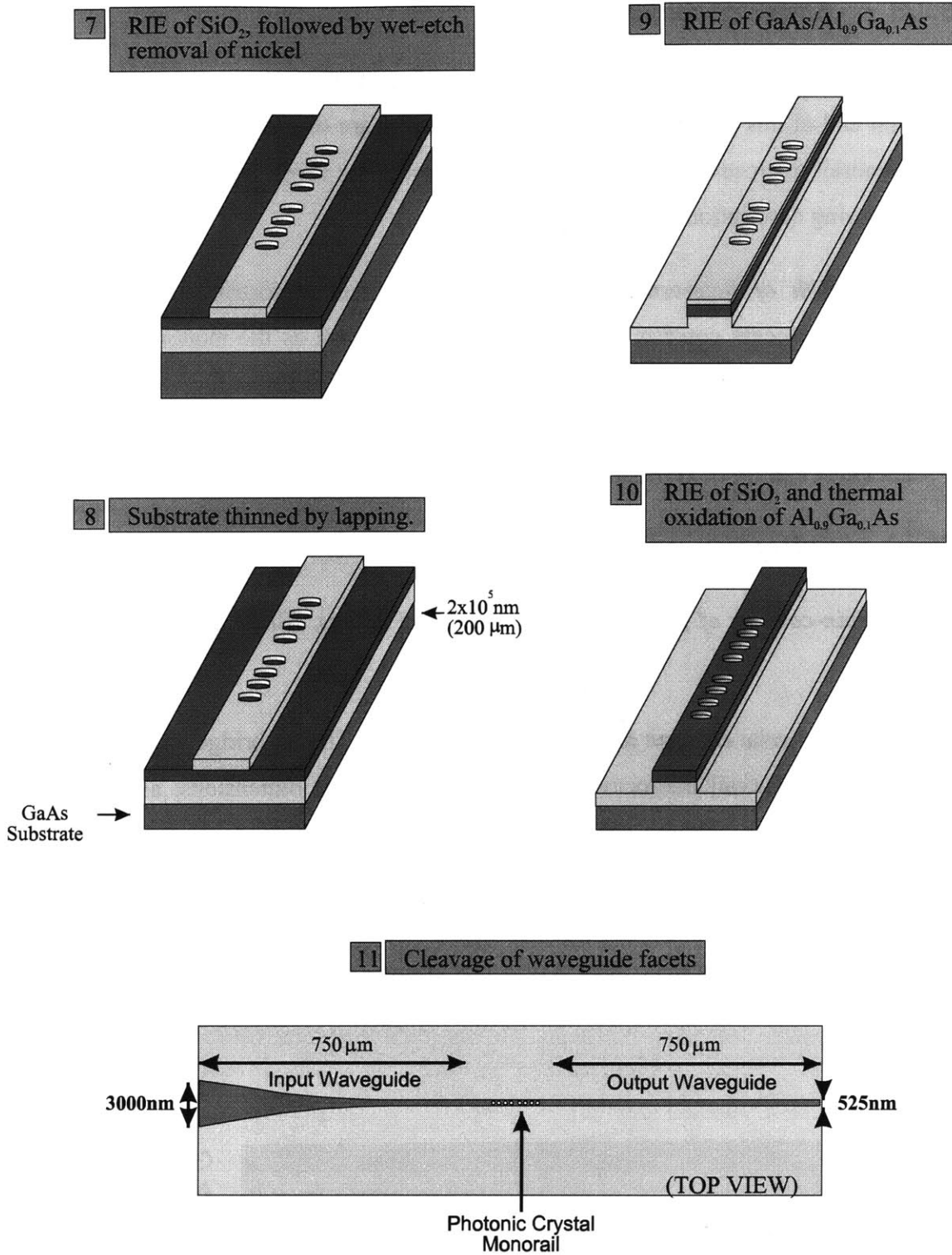
Figure 3-15:(continued): Fabrication process sequence of the 1-D PBG monorail microcavity.

3.3.B   Air-bridge microcavity

The fabrication process sequence for the air-bridge microcavity is illustrated in Figure 3-18 (at end of this section). Steps 1-9 of the process are essentially identical to those in the monorail microcavity fabrication process, except for several differences as noted in the following description:

Step 1. ***Growth of heterostructure with GSMBE.*** The heterostructure grown by the GSMBE process consists of the same material system as the monorail microcavity structure except for a difference in the thickness of the GaAs layer of 7nm (Figure 3-16). This thickness difference, while small, can be resolved with the precise thickness control of GSMBE.

Step 2. ***PECVD of SiO$_2$.*** (Same as Step 2 in Section 3.3.A)

Step 3. ***Spin-coating of polymethylmethacrylate (PMMA).*** (Same as Step 3 in Section 3.3.A)

Step 4. ***Direct-write electron beam lithography (EBL).*** The air-bridge microcavity differ from the monorail microcavity in its various physical dimensions, as described in Chapter 2. The patterns generated in this step is listed in Table 3-3. In addition, alignment marks are added to facilitate the positioning of the patterns in subsequent lithography steps. Note that the alignment marks are not necessary in the monorail microcavity process since there is only one lithography step involved.
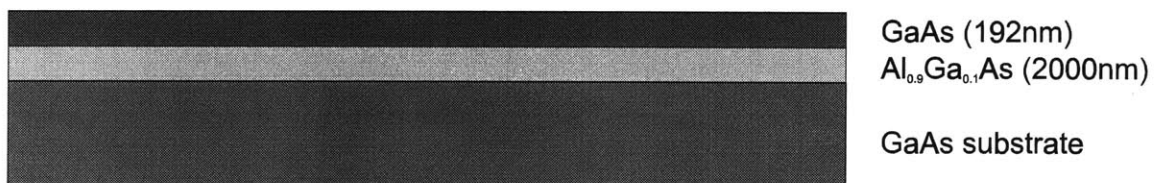
GaAs (192nm)
Al$_{0.9}$Ga$_{0.1}$As (2000nm)

GaAs substrate

Figure 3-16: Heterostructure grown by GSMBE for the fabrication of the air-bridge microcavity operating at 1.55μm wavelength.

Type	Description
BRWG	Plain waveguides without photonic crystals, including 3 straight waveguides of $2\mu m$, $1\mu m$ and $0.525\mu m$ width, and 2 waveguides with flares from $3\mu m$ to $0.525\mu m$.
BRDIA	Change in hole diameter, keeping all other physical parameters constant. Hole diameters (in nm; ideal dimension in boldface): 191, **201**, 211, 221, 231, 241.
BRHOLE	Change in number of holes, keeping all other physical parameters constant. Total number of holes in each PBG structure: 4, 6, 8, 10, 12, 14.
BRAD	Change in defect width, keeping all other physical parameters constant. Defect width (in nm; ideal dimension in boldface): 488, 519, 549, 580, **610**, 641, 671, 702, 732, 763, 793

Table 3-3: Description of air-bridge microcavity patterns generated in the EBL process step.

Step 5. *PMMA development.* (Same as Step 5 in Section 3.3.A)

Step 6. *Electron beam evaporation of nickel.* (Same as Step 6 in Section 3.3.A)

Step 7. *Lift-off of nickel.* (Same as Step 7 in Section 3.3.A)

Step 8. *RIE of SiO$_2$ and wet-etch removal of nickel mask.* (Same as Step 8 in Section 3.3.A)

Step 9. *Substrate thinned by lapping.* (Same as Step 9 in Section 3.3.A)

Step 10. *RIE of GaAs/Al$_{0.9}$Ga$_{0.1}$As.* (Same as Step 10 in Section 3.3.A)

Step 11.   *Photolithography to define trench.* After the previous RIE step, the sample is immediately coated with a positive photoresist (Shipley Corp. Microposit 1813) to prevent excessive ambient hydrolyzation of the exposed Al$_{0.9}$Ga$_{0.1}$As material. The photoresist is statically dispensed onto the sample with a clean glass dropper and spin-coated at 4000rpm for 30s. The resultant resist layer thickness is about $1.3\mu m$. The sample is next soft-baked at 90°C for 30min. An exposure is then performed on the sample using a Karl-Suss MJB-3 optical aligner to create a $10\mu m$-wide trench pattern in the photoresist layer. The trench pattern is positioned such that the center of the photonic crystal lies approximately in the middle of the trench (Figure 3-17). As the photonic crystal itself can barely be discerned under the
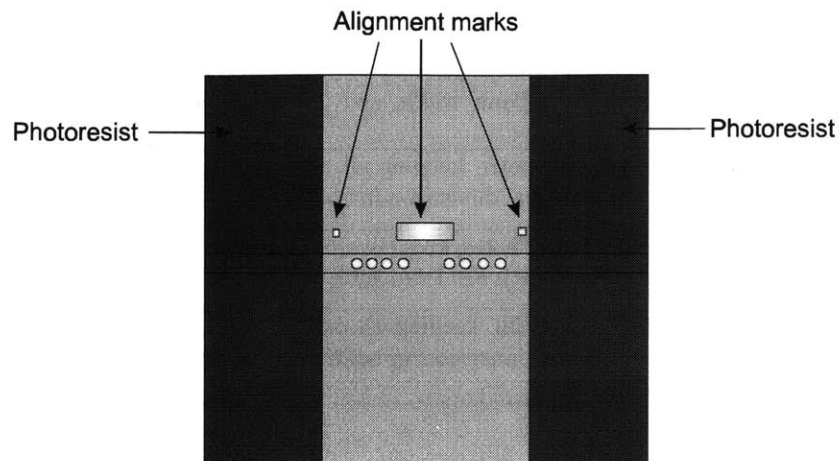
78

Figure 3-17: Schematic showing the alignment of the trench pattern with respect to the photonic crystal, as described in Step 10 of the air-bridge microcavity process.

microscope on the aligner, the larger center rectangle in the set of alignment marks serve as the proxy for the location of the center of the PBG structure. The exposure time on the aligner is typically 8s, with the aligner calibrated to emit 360nm wavelength UV-light at $6.5mW/cm^2$. The sample is then developed with Shipley Corp. MF319 developer and inspected under the optical microscope. Thereafter, the sample is hard-baked for 30min at 120°C.

Step 12.　　**RIE of $Al_{0.9}Ga_{0.1}As$ followed by photoresist removal.** After the sample has been removed from the hard-bake, it is subjected to 3min of $BCl_3/SiCl_4$ RIE using the same process parameters as in Step 9. The purpose of this RIE step is to remove the bulk of the sacrificial material that would otherwise have to be removed by the wet-etch later in the process. This ensures sufficient clearance between the bridge and the substrate to prevent the problem of stiction (see Section 3.5.B below). The photonic crystal between the photoresist trench pattern is unaffected by the RIE since the SiO_2 mask is still present on the surface of the photonic crystal. The SiO_2 layer is also sufficiently thick to withstand a total of 6min of $BCl_3/SiCl_4$ RIE (including Step 9). The photoresist is then removed by rinsing the sample in acetone followed by iso-propanol.

Step 13.　　**RIE of SiO_2 mask.** The SiO_2 mask is next removed with a CF_4/O_2 RIE using the same process as in Step 11 of the monorail microcavity process.

79

Step 14.   *Thermal oxidation of $Al_{0.9}Ga_{0.1}As$.* As in Step 12 of the monorail microcavity process, the sample is oxidized at 435°C with steam in N_2 carrier gas for 45min. Again, the sample is allowed to cool down to 200°C before being removed from the furnace.

Step 15.   *Photolithography to define trench.* The photolithography process in Step 10 is repeated to define the trench pattern again. The purpose of the trench pattern in this step is to define the air-bridge region, in anticipation of the wet-etch removal of the sacrificial material.

Step 16.   *Wet-etch of sacrificial material to suspend air-bridges.* A solution of 10ml HF:250ml DI water is first prepared at room temperature. The sample is then dipped into the diluted HF acid solution for 10 seconds. Thereafter, the sample is rinsed in DI water followed by methanol. The photoresist is then immediately removed with a dip in acetone and methanol.

Step 17.   *Cleavage of waveguide facets.* Finally, the waveguide facets are cleaved using the same method as for the monorail microcavity. Care is taken to avoid rolling the rod over the air-bridge region when propagating the cleaves down the waveguide facets. Thereafter, the sample is mounted on a stub and introduced to a measurement setup, marking the conclusion of the fabrication process for the air-bridge microcavity.

1 Heterostructure grown by MBE

185nm
2000nm
4.75×10^5 nm
(475μm)

GaAs
$Al_{0.9}Ga_{0.1}As$
GaAs
Substrate

4 Direct-write electron beam lithography

PMMA

2 Plasma-enhanced chemical vapor deposition (PECVD) of SiO$_2$

SiO$_2$
(150nm)

5 E-beam evaporation of nickel

Ni
(30nm)

3 Spin-coating of PMMA (E-beam litho. resist)

PMMA
(200nm)

6 Nickel lift-off

Ni

SiO$_2$

Figure 3-18: Fabrication process sequence for the 1-D PBG air-bridge microcavity operating at 1.55μm wavelength. (To be continued on next page)

7 RIE of SiO$_2$, followed by wet-etch removal of nickel

8 Substrate thinned by lapping.

2×10^5 nm (200 μm)

GaAs Substrate

9 RIE of GaAs/Al$_{0.9}$Ga$_{0.1}$As

10 Photolithograpy to define trench pattern

Photoresist

Photoresist

11 RIE of Al$_{0.9}$Ga$_{0.1}$As to create trench, followed by resist removal and RIE of SiO$_2$

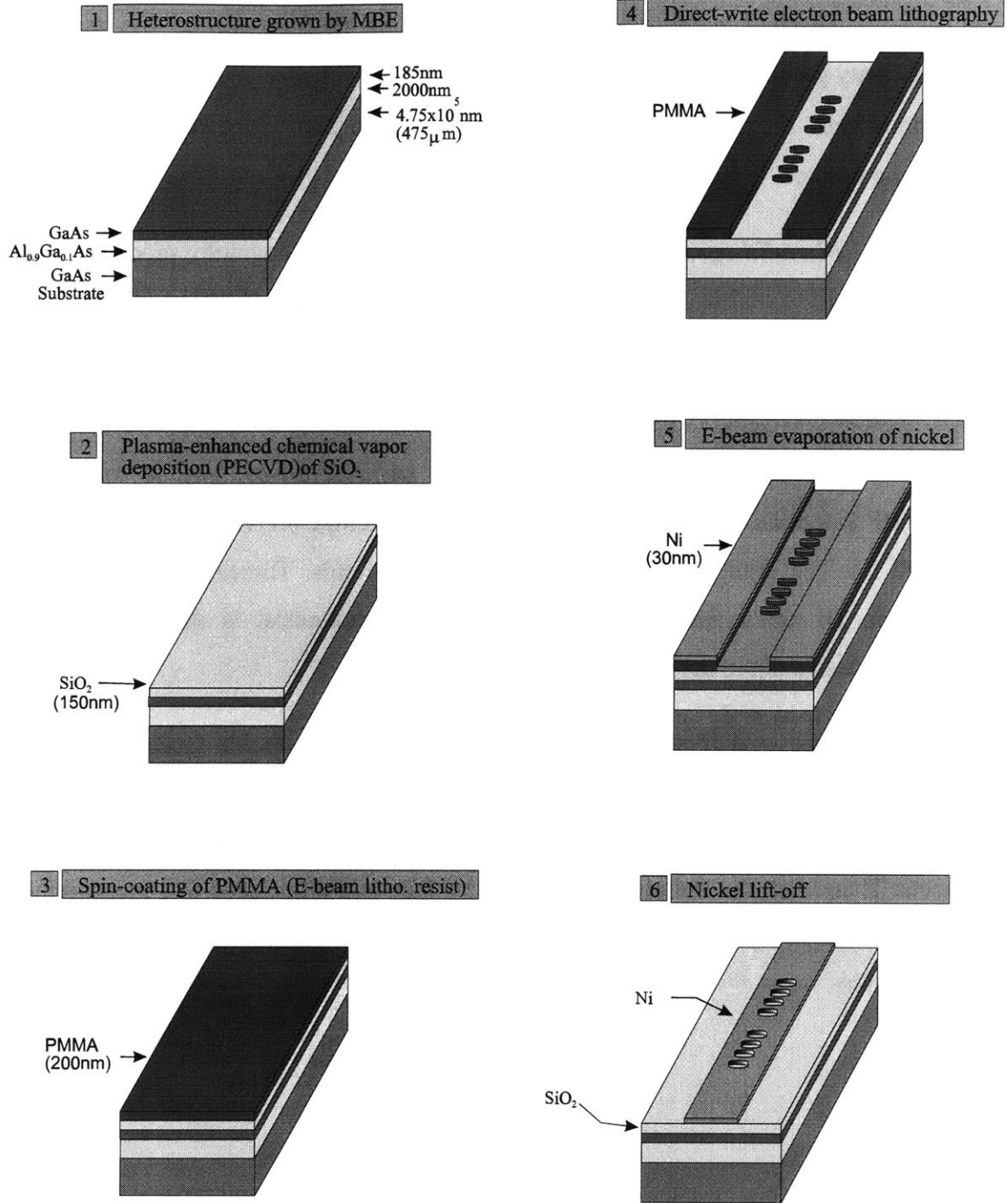**12** Thermal oxidation of Al$_{0.9}$Ga$_{0.1}$As

Figure 3-18: Fabrication process sequence for the 1-D PBG air-bridge microcavity operating at 1.55μm wavelength. (To be continued on next page)
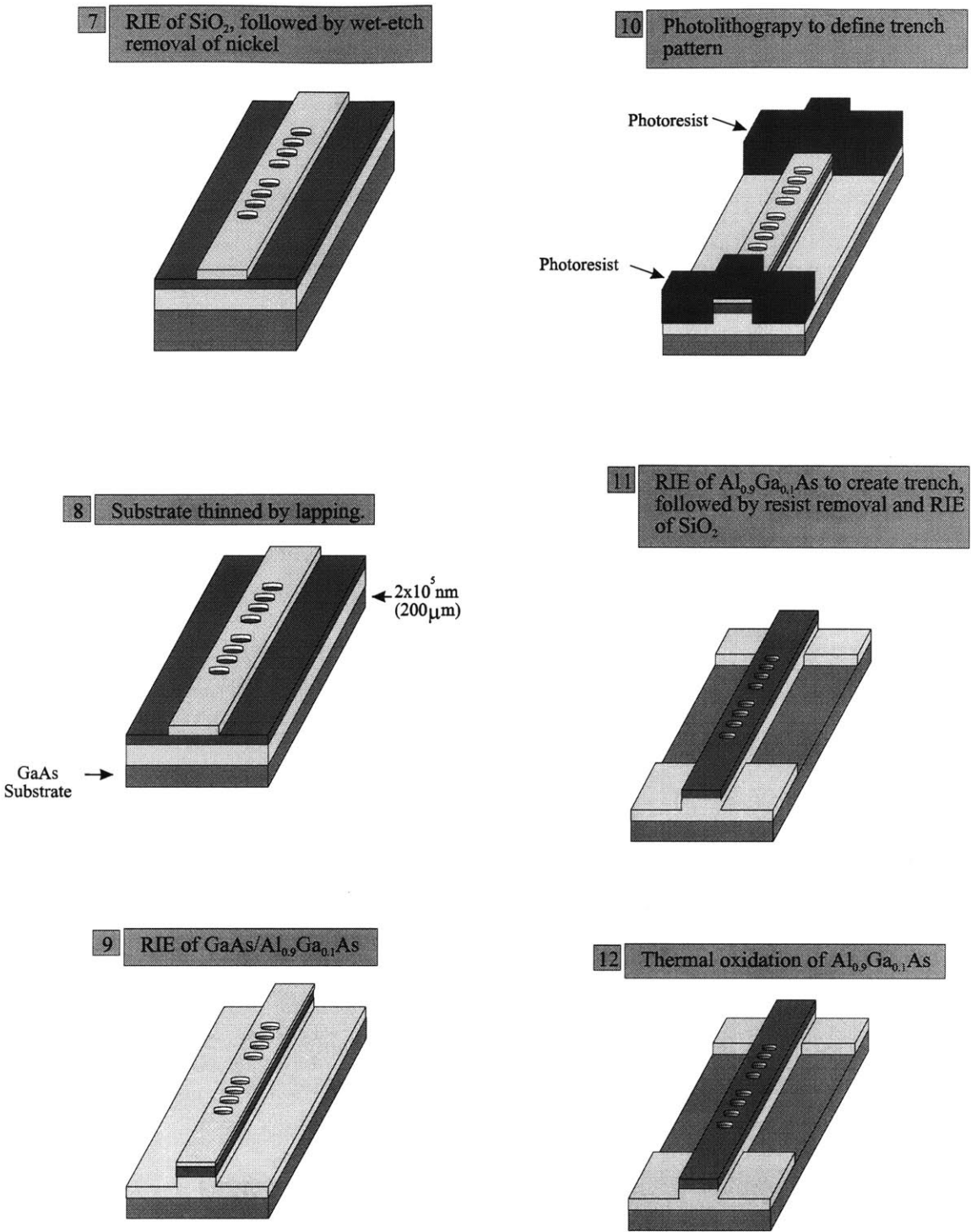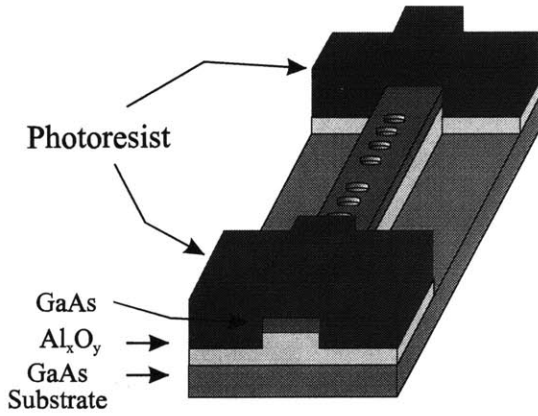
82

| 13 | Photolithography to define trench |

Photoresist

GaAs
Al_xO_y
GaAs
Substrate

| 14 | Sacrificial etch of Al_xO_y with HF solution to suspend air-bridge |

GaAs
Al_xO_y
GaAs
Substrate

| 15 | Cleavage of waveguide facets |

750 µm
Input Waveguide

750 µm
Output Waveguide

3000nm

525nm

Photonic Crystal
Air-bridge

(TOP VIEW)
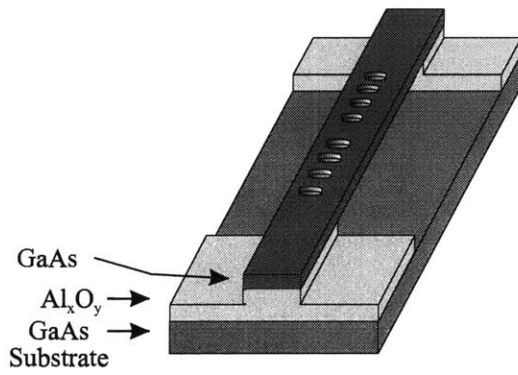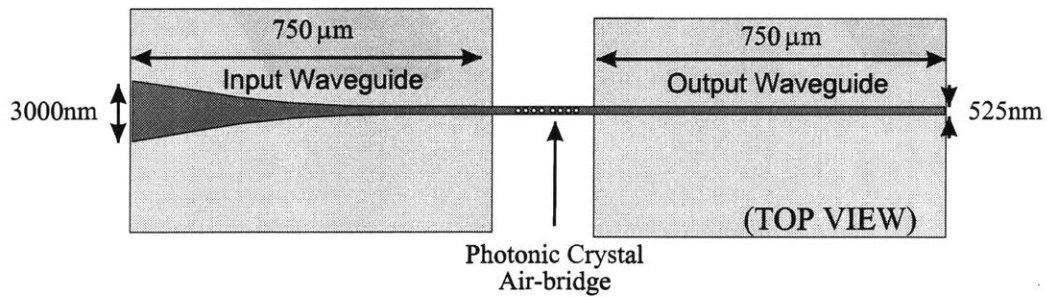
Figure 3-18 (continued): Fabrication process sequence for the 1-D PBG air-bridge microcavity operating at 1.55µm wavelength.

3.4 Direct-Write Electron Beam Lithography

3.4.A Why Direct-Write EBL?

The minimum feature size in the 1-D PBG microcavities operating at $1.55\mu m$ wavelength is approximately $0.1\mu m$. Such small feature size cannot be easily achieved with conventional optical lithography techniques. More sophisticated nanoscale lithography techniques like electron-beam lithography, deep-UV lithography and X-ray lithography hence become necessary for the consistent and reproducible generation of these fine features. In general, these high-resolution lithography techniques can be categorized as either a (a) contact/proximity lithography or (b) direct-write lithography (Figure 3-19). The former approach first involves the generation of the desired patterns on a mask using typically an electron beam. The patterns are then reproduced on a substrate by coating the sample with a resist film, and then irradiating the resist through the mask with short wavelength light (e.g. deep-UV or X-ray). The mask can either be in close *contact* with or at close *proximity* to the sample. In comparison, the direct-write approach obviates the use of a mask by directly printing the patterns onto a resist-coated sample with, for instance, an electron or ion beam.

To decide which approach to use in a fabrication process requires an understanding of the tradeoffs inherent in each technique. The main advantage of the contact/proximity lithography is its high throughput. First, a set of device patterns is repeated in an array on the mask. For instance, one can incorporate, within an area on the mask equivalent to a quarter of a 2-inch diameter wafer, an array of 16 dies of 2mm by 1mm dimension. Each die would contain 40 devices, translating to a total of 640 devices generated during each exposure with the mask. Second, once a mask has been created[5], the mask patterns can be reproduced almost *ad infinitum* onto one sample after another.

---

[5] Generating a mask at such a fine length-scale for contact/proximity lithography (for instance, X-ray lithography) is by no means a straightforward and trivial endeavor. The mask quality and ease of mask manufacturing remain points of contention between proponents of the different contact/proximity techniques.
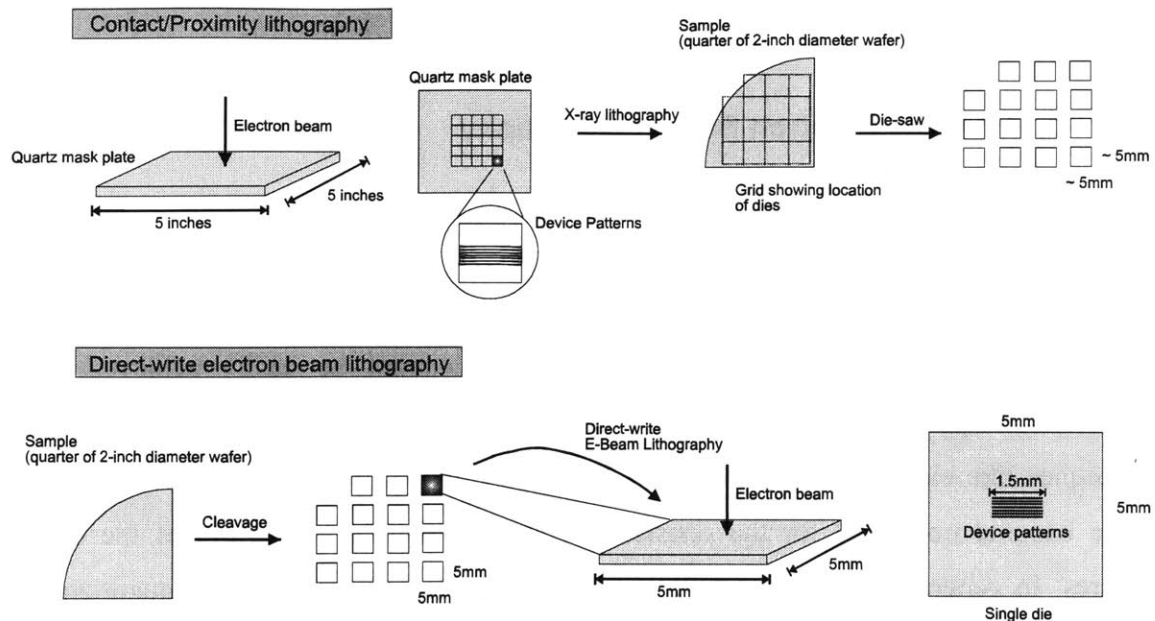
Figure 3-19: Difference between contact/proximity lithography (e.g. X-ray lithography) and direct-write lithography (e.g. direct-write EBL). The top row depicts the contact/proximity process involving an e-beam generated X-ray mask. The bottom row shows the parallel sequence involving direct-write EBL. In the top process, the mask generation incurs a one-time cost in time and material. Once generated, the mask can be used repeatedly to create a large number of dies. In the bottom process, the device patterns are written on each individual die. The direct-write EBL process has a much lower throughput but offers greater flexibility in design changes between process iterations.

A downside to the contact/proximity approach is the inflexibility in mask design. For a small-volume, research-oriented project, knowledge accrued from prior fabrication runs and optical measurements often necessitate design changes. In a process using an exposure mask, implementing the design changes would entail the time-consuming and costly fabrication of a new mask. One could conceivably include a wider array of design variation on a larger mask, in the hope of covering as much of the "design space" as possible. But this would reduce the number of useful devices per lithography step, since a certain proportion of the devices will always be outside the design specification. In addition, a larger mask consumes more precious real estate on a sample, and a GSMBE-grown sample can cost an estimated $5,000 per 2-inch diameter wafer. Finally, there is often a slew of parameters that can be varied in any design. Without the guidance of data from previous iterations, to design a wide range of patterns on a single mask can be both impractical and daunting.

In contrast, the direct-write approach offers design flexibility but a much lower throughput than contact/proximity lithography. As will be described in greater detail below, direct-write EBL involves the deflection of an electron beam to expose specific areas on a sample. A computer data file, translated from a CAD-generated mask layout, controls the electron beam deflection. As such, the patterns can be varied between iterations by simply changing the CAD data file. The throughput of the direct-write EBL, however, is considerably lower since exposing a large area on the sample would consume a long write time. A direct-write EBL of a single set of 40 microcavity devices within a total area of 1.5mm by 0.5mm, for instance, lasts approximately 1 hour.

In the fabrication process for both the monorail and air-bridge microcavity, direct-write EBL is the lithography method of choice primarily because of the short turnaround time between design iterations. Volume production is not a goal in a research effort such as the one described in this thesis. As such, flexibility in mask design between iterations is considered more critical than the number of devices generated per fabrication run. The fact that two different sets of mask design are required for the two different types of microcavity further boosts the argument for using a direct-write lithography.

3.4.B   Scanning electron beam lithography (SEBL) system

The electron-beam lithography system used in the fabrication process is an IBM VS2A Scanning Electron Beam Lithography (SEBL) system and is essentially a modified scanning electron microscope (Figure 3-20) [67]. The VS2A is a vector scan system, where the electron beam is directed to locations on the sample requiring exposure[6]. The electron beam is accelerated from the source with an applied potential of 50kV and is focussed onto the substrate plane by a lens through the use of electric or magnetic fields. The system is capable of focusing the beam to a spot size of 8nm. The electron beam can be deflected within a certain area (called the "field") by applying electric or magnetic fields perpendicular to the trajectory of the beam. The amount of beam deflection within the field is controlled by signals from a computer system. In addition, a pair of

---

[6] A raster scan system, in contrast to the vector scan system, scans through every pixel in a field. A blanker turns the electron-beam on or off such that only specific pixels are exposed.

electrostatic plates is used to turn off, or "blank" off, the electron beam by deflecting it into the rim of an aperture plate.

The focus and uniformity of an electron beam degrades when the beam is deflected beyond a certain extent. Consequently, a large pattern is typically fractured into different fields. After a field has been written, the stage shifts the sample such that the neighboring field can be exposed. The series of fields making up the desired patterns is then stitched together to form an integral image. The stage movement can be accurately monitored using a laser interferometer, with state-of-the-art transducers yielding a placement resolution of 5Å.

In the EBL of the monorail and air-bridge microcavity patterns, for instance, a set of devices 1.5mm long and less than 100μm wide is fractured into 16 fields, each 100μm by 100μm in dimensions. The 16 fields are stitched end-to-end into a complete integrated-waveguide microcavity structure. Each field is addressed by a 14-bit digital signal, effectively dividing the field into 2^{14}=16384 pixels by 16384 pixels. This further translates to a pixel size of (100μm/16384)=6.1035nm. But because the numerical accuracy of the e-beam deflection system can only be specified to 6.1nm, the resultant
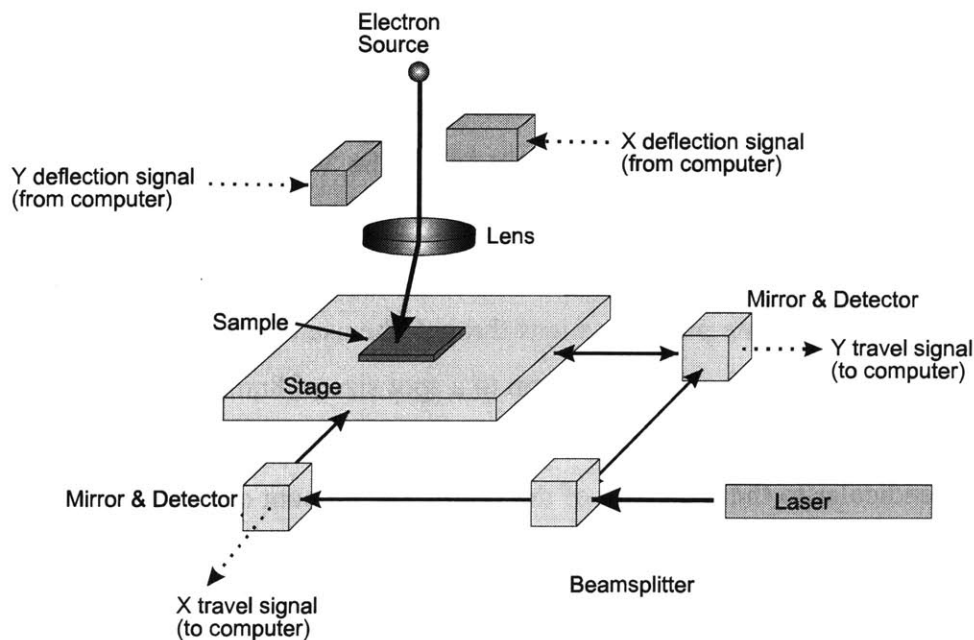

Figure 3-20: Schematic of a typical electron beam lithography system.

field size is actually (6.1nm x 16384 pixels) = 99.9424µm by 99.9424µm.

3.4.C   Pattern generation errors in EBL

The errors incurred during the EBL process can be classified as either an interfield or intrafield error. Interfield error occurs when one field is placed incorrectly with respect to other fields. One form of interfield distortion, called a stitching error, is manifested in the misalignment between adjacent fields (Figure 3-21) where the fields are either overlapping or separated by a gap. The stitching errors could be a result of a miscalibration between the field size definition on the EBL system and the actual field size measured by the laser interferometer. The presence of pitch or yaw in the sample stage, errors in stage position detection, thermal expansion of system parts and drifts in the electrical sources can also contribute to interfield errors. Intrafield errors, on the other hand, result in distortion of patterns within a single field. These errors are often traced to aberrations in the lens and deflection fields, miscalibration of digital-to-analog converters (DAC), electrostatic charging of sample and the e-beam column, and thermal expansion of system parts. Both types of errors are detailed in Ref. [67].

Improved design of the EBL system electronics have led to the overall reduction of the
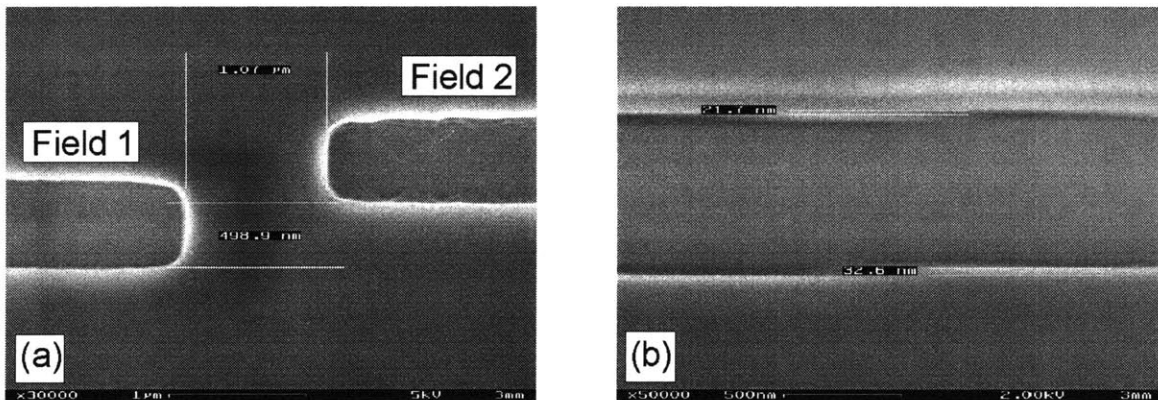

Figure 3-21: Scanning electron micrographs illustrating stitching errors from an EBL exposure using the "shift and drop" alignment scheme (see text). Micrograph (a) shows the offset at the boundary between adjacent fields (Fields 1 and 2). The features in Field 1 and Field 2, when stitched together, form a 500nm-wide waveguide segment. The vertical and horizontal offsets are 1.07µm and 499nm respectively, and represent clearly an unacceptable alignment. Micrograph (b) shows a typical offset when the "shift and drop" scheme is properly executed. The errors are in the order of 20-30nm (less than 10% of the waveguide width) and are deemed tolerable.

88

intrafield distortions. The eradication of interfield errors, however, remains an active area of research. Interfield distortions have arguably a greater impact on the viability of EBL as a manufacturing tool since the errors affect not only the integrity of a structure spanning several fields, but also the placement accuracy of one feature (in one field) to another feature (in another field).

In the EBL of the 1.5mm-long integrated-waveguide 1-D PBG microcavities, a field alignment scheme is used where the mismatch between the laser interferometer-mediated stage movement and the e-beam deflection is minimized. First, a gold particle that has been previously placed at a corner of the sample is imaged onto a frame-grabber via a back-scattered electron detector. The stage is then shifted by, for instance, 40μm in the horizontal and 40μm in the vertical directions, as determined by the laser interferometer. At the same time, the e-beam is deflected also by the same amount. If the beam deflection and the stage movement were calibrated perfectly, the gold speck should reside in the same location within the image frame before and after the shift. However, the presence of signal conversion errors in the DAC (amongst other factors), often results in a mismatch between the two movements. An autocorrelation program using the back-scattered electron images calculates the error correction signal that is necessary to rectify this mismatch. The entire alignment process is iterated to gradually minimize the errors.

The eventual stitching error resulting from such an alignment scheme is typically on the order of 20-30nm, i.e. less than 10% of the overall waveguide width (Figure 3-21). The effect of the error on the optical transmission of the waveguide is deemed tolerable. Indeed, as subsequent optical measurement will show, a relatively strong optical signal is shown to be detectable at the output of the device. Nonetheless, the presence of such errors at the boundaries of each 100μm-size e-beam field essentially creates sets of gratings along the sidewalls of the 1.5mm-long devices. Further, the strongly confined optical mode in the high index-contrast waveguide structure is also more sensitive to waveguide imperfections, and may experience higher scattering loss from these stitching errors. There is clearly a strong incentive to reduce the stitching errors as much as possible.

The aforementioned alignment scheme is based on the premise that the laser interferometer controlled stage movement is highly precise and well calibrated. The scheme is open-looped in that the stage movement and the beam deflection are monitored separately. Approaches to a close-loop process have led to more sophisticated exposure schemes like spatial-phase-locked EBL (SPEBL) [67, 68]. The employment of such a scheme will certainly lead to reduced interfield distortions, at a cost of increased process complexity.

3.4.D   Choice of electron-beam resist & Dose Calibration

The choice of an e-beam resist for a particular process depends on several resist properties, including sensitivity, contrast, attainable resolution, process complexity, and etch resistivity (if the resist is to be used as an etch mask). The resist clearly has to be sufficiently sensitive to the electrons generated in the EBL system such that a reasonable amount of electrons (or dose) is required to attain complete resist development. A relatively less sensitive resist will require a higher dwell-time per pixel for a given beam current to achieve complete development, and the overall write-time will thus be higher. The contrast of e-beam resist is a consequence of the resist's nonlinear response to irradiation. A perfect contrast is achieved when the exposed resist area becomes absolutely developed while the unexposed area is completely unaffected. The resolution of an e-beam resist is limited by the swelling of the resist film during development and the extraneous exposure due to electron scattering. Finally, the resist has to withstand the etch process if it is to act as a mask. The etch resistivity of the resist depends on the specific etch process involved.

E-beam resists are generally categorized as either a positive or a negative resist (Figure 3-22). A positive resist is typically made of a high molecular weight polymer chain that undergoes scission when irradiated. The lower molecular weight polymer chains become soluble in a chemical developer while the unexposed resist remains insoluble. A negative resist, on the other hand, usually consists of polymer chains that crosslink when irradiated. The heavier, crosslinked polymer chains become insoluble in the developer, while the unexposed area will be clear of resist after development.
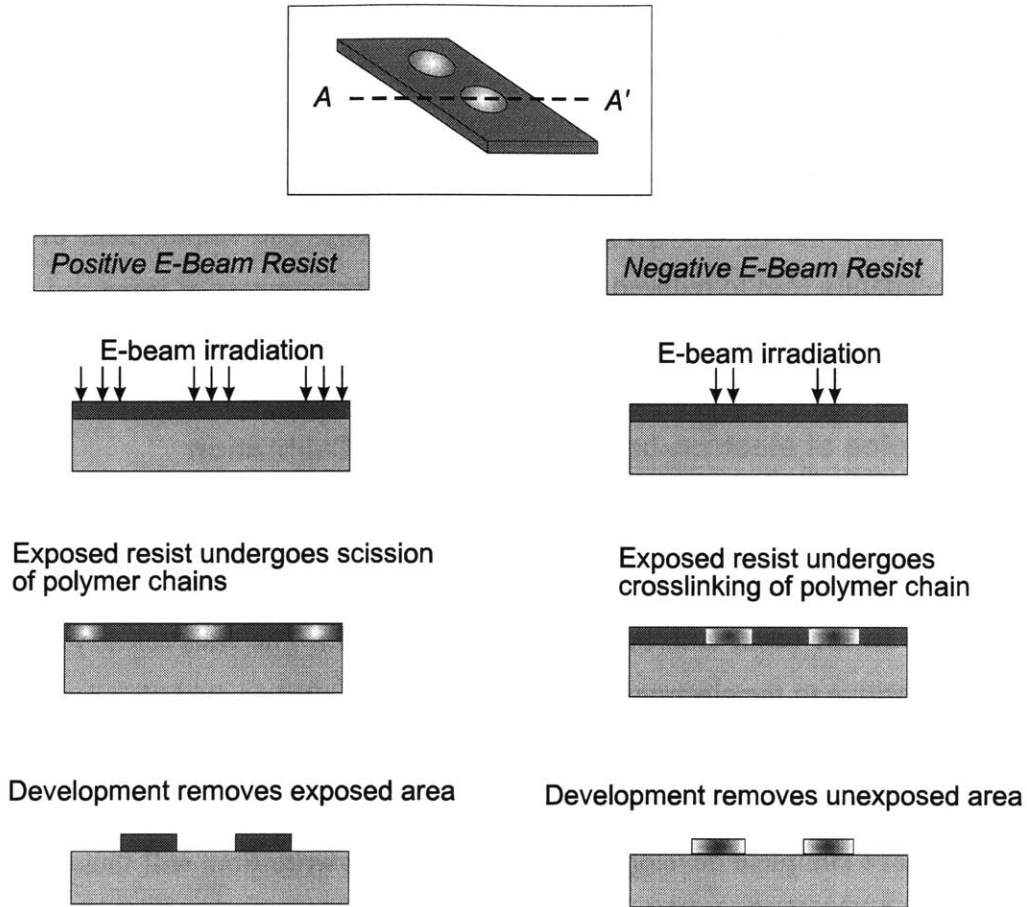
90

Figure 3-22: Illustration of the difference between a positive and a negative e-beam resist. The desired profile, as depicted, is the cross-section (*A-A'* in top inset) of a-hole in the 1-D photonic crystal.

In the 1-D PBG microcavity fabrication process, both a negative (SAL601) and a positive (PMMA) e-beam resist have been investigated. The negative resist is attractive for this particular process, as the exposure area necessary to generate the PBG pattern is smaller than if a positive resist had been used. This would translate to a shorter write-time on the EBL machine. The SAL601 is a chemically amplified resist consisting of an alkaline soluble base polymer (novolac), a crosslinking agent and a photoacid generator (PAG). Acid is generated from the PAG when exposed to an electron-beam and diffuses into the surrounding area. The extent of diffusion is determined by a carefully controlled post-exposure bake (PEB). The acid catalyzes a thermally-activated reaction between the crosslinking agent and the base polymer that results in the crosslinking of the base polymer. Subsequent development in an alkaline developer removes the area of the resist

91

that has not been crosslinked. SAL601 has been demonstrated to exhibit high sensitivity, high resolution (due to the absence of development-induced swelling) and good etch resistivity against typical dielectric etches (Table 3-4)[69].

The main disadvantage of SAL601 is the requirement for tight control of the PEB process. The PEB recommended by the resist manufacturer entails a 1min bake on a vacuum hotplate at 115 ± 1°C. The process variation is reported to be a change in the exposure width of 0.02μm/°C for a temperature range of 110°C and 125°C, and 0.003μm/s for bake time ranging between 54 and 63 seconds. In addition, coated SAL601 film is also known to have a short stability and exhibits degradation within 2 weeks of coating when stored at ambient temperature [70]. The shelf life is extended to 6 weeks when the coated wafers are refrigerated.

During the investigation of SAL601 for the 1-D PBG fabrication process, the resist's high sensitivity turns out to pose a problem to the EBL system. The high sensitivity of the resist implies that fewer electrons are required, per unit exposure area, to achieve complete resist development. To attain a lower e-beam dose on the EBL machine, the beam current will either have to be reduced or the scan rate of the e-beam has to be increased. SAL601 has a sensitivity of about $7\mu C/cm^2$ at a beam voltage of 20keV (Table 3-4). The beam current required of the VS2A EBL system is on the order of 1.5pA and the scan rate is about 0.8MHz for a field size of 100μm by 100μm. These parameters are close to the limits of the EBL system, and their reproducibility is questionable. A

	SAL601	PMMA
Sensitivity ($\mu C/cm^2$) at 20keV	5	100
Contrast	5	2
Resolution (nm)	200	<100

Table 3-4: Comparison of SAL601 and PMMA as an electron-beam resist. (Source: [71])

92

preliminary test exposure is, nonetheless, performed on a GaAs sample coated with SAL601 and exposed with a 50keV e-beam of at least $27\mu C/cm^2$. The PEB is performed at 103.4°C for 1min. Results from the study are less than satisfactory (Figure 3-23) and the decision to pursue the use of a different resist is made.

In contrast to SAL601, PMMA has been in use for a considerably longer period and its process characteristics are well determined on the EBL system at MIT. PMMA is a positive e-beam resist and is known by its various other trade names like Plexiglas and Lucite. If PMMA were to be used as an etch mask in the 1-D PBG microcavity fabrication process, however, the area between adjacent waveguide structures will have to be exposed. This translates to an inordinately large area and long write-time. Consequently, the technique of image reversal is employed which entails the lift-off of a thin nickel film (as described in Section 3.3), since image reversal with a positive e-beam resist involves the same exposure area as a process using a negative e-beam resist.

To determine the e-beam dose that would yield the correct critical dimensions in the 1-D PBG microcavity structures, a matrix of exposure with varying doses is performed. A total of 16 photonic crystal patterns within a 100µm by 100µm field are generated using a base dose of $270\mu C/cm^2$ (beam current of 50pA and a scan rate of 0.500MHz). The dose is increased by varying the scan rate linearly through the 16 patterns. After the exposure
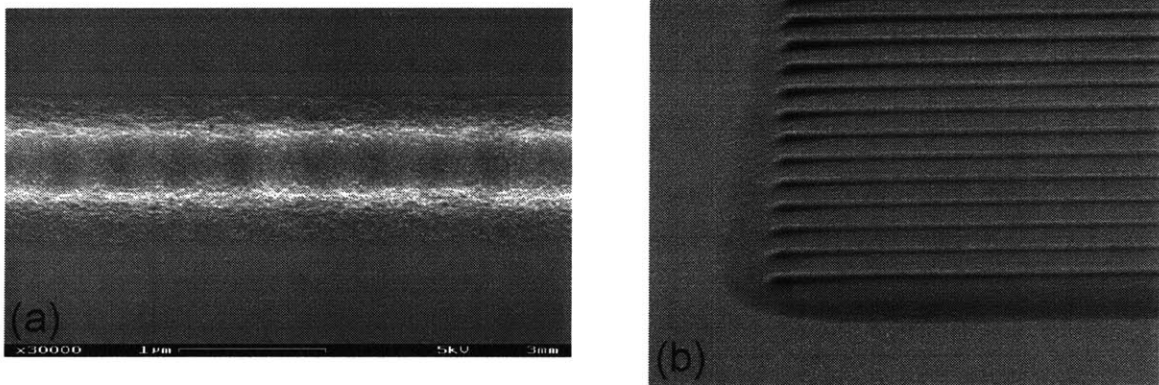

Figure 3-23: Scanning electron micrographs showing results from a test exposure of 1-D PBG microcavity patterns using SAL601, a negative e-beam resist. The beam dose used in the exposure is $27\mu C/cm^2$ at 50keV. Micrography (a) shows the top view of a 1-D photonic crystal that is 550nm wide with 8 holes. The location of the holes can be barely made out, and the contrast of the resist pattern is clearly too low (due to the over-exposure). Micrography (b) shows a side view of a series of waveguide ends, demonstrating the lack of contrast between adjacent features.

has been performed, the sample is developed and coated with 30nm of nickel. The nickel film is next lifted off by soaking the sample in warm NMP (see Section 3.3). The final patterns in the nickel film are then observed under the SEM. The dose corresponding to the structure that has the correct dimensions is used for the EBL of the actual devices. Figure 3-24 shows the nickel patterns as observed under the SEM. The patterns that have been underexposed lead to a tattered nickel film after the lift-off process (for instance, those in micrographs (a) and (b) of Figure 3-24), while overexposure yields structures with undersized holes (e.g., micrographs (g) and (h)).

It is important to note that the ideal dose may drift over time, particularly after the EBL machine has undergone any repairs that involve the realignment of the e-beam column. In the 1-D PBG microcavity fabrication process, the critical dimensions are especially sensitive to a dose drift, as witnessed by the variation in feature sizes realized in Figure 3-24 with a change in dose of merely 1/16 times the base dose. Consequently, the dose calibration exercise has to be conducted periodically and after a major repair to the e-beam column, to ensure that the correct feature sizes are achieved during an EBL.
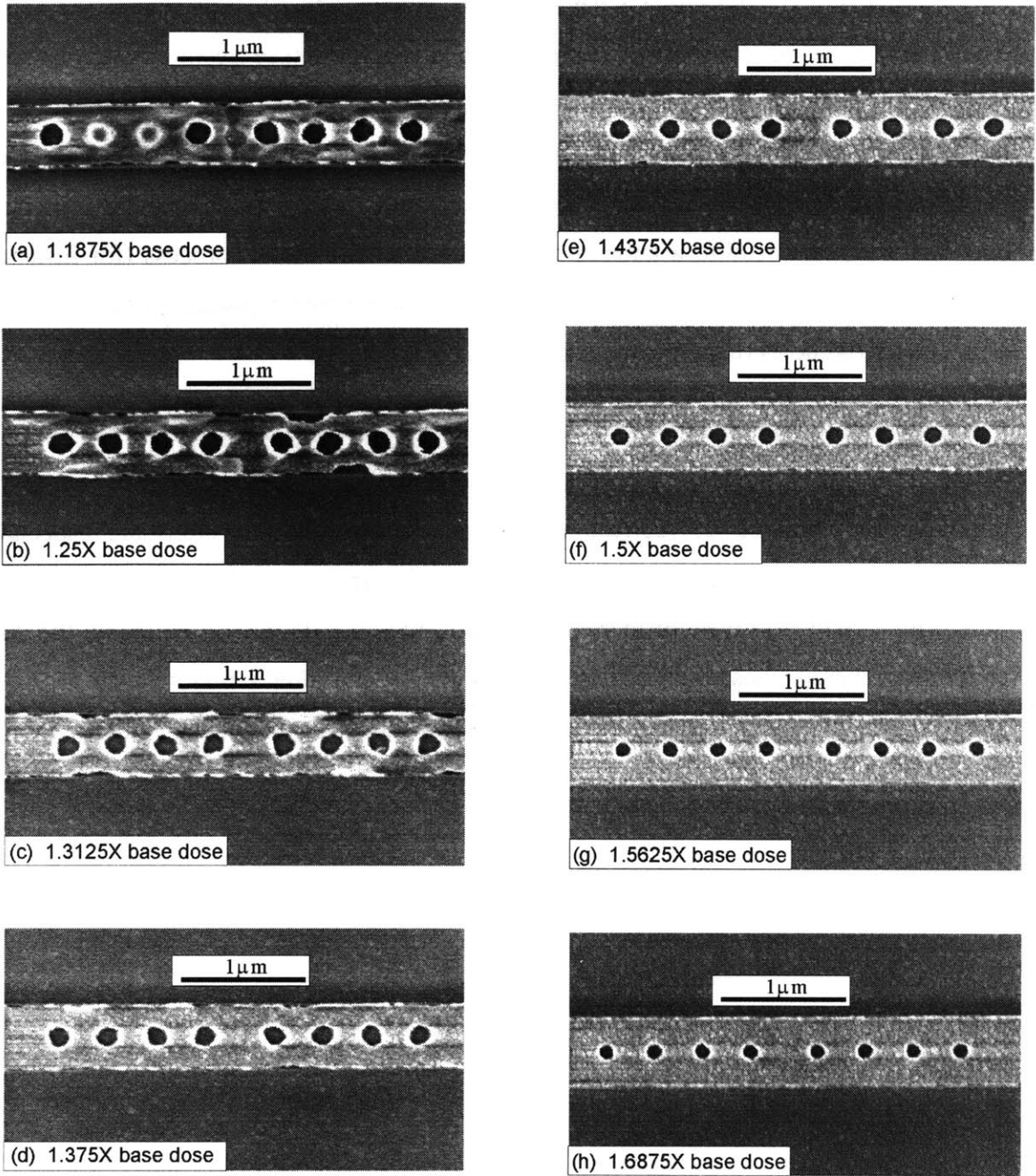
Figure 3-24: Scanning electron micrographs of 1-D photonic crystal patterns in nickel film after lift off, as part of a dose calibration matrix (base dose: $270\mu C/cm^2$). By measuring the dimensions of the holes and the width of the waveguides (measurements not shown) with the SEM, the dose to be used for the actual devices is determined. In this instance, a dose between 1.375X [micrograph (d)] and 1.4375X [micrograph (e)] the base dose is deemed to be ideal.

3.5 Micromechanical fabrication issues

The fabrication of the air-bridge microcavity involves certain issues unique to micromechanical structures. These issues are examined in further detail in this section.

3.5.A Sacrificial etch

An effective sacrificial etch is the key process in the surface micromachining of semiconductor material. Ideally, the sacrificial etch has to exhibit infinite etch selectivity of the sacrificial material versus the structural material. In other words, the structural material should be unscathed during the sacrificial etch process, while the sacrificial material should be removed quickly with as little debris remaining as possible. As previously mentioned, the success of silicon-based surface micromachining is largely due to the existence of an effectively infinite etch selectivity between silicon and SiO_2. Surface micromachining with III-V compound semiconductors has begun to attract considerable attention over the last few years as a library of highly selective etch recipes between pairs of compound semiconductors has recently been documented [72]. Research in the field of III-V surface micromachining continues to uncover interesting new etch chemistries [73].

In the fabrication of the air-bridge microcavity, the sacrificial etch of $Al_xGa_{1-x}As$ and Al_xO_y using diluted HF solution is employed to suspend the GaAs air-bridge structures. To determine the process parameters for this critical sacrificial etch, a series of etch experiments is performed. First, three samples are grown by GSMBE with each consisting of a $1\mu m$-thick $Al_xGa_{1-x}As$ layer on a GaAs substrate. A 500nm-thick GaAs cap layer is grown on top of the $Al_xGa_{1-x}As$ layers to prevent ambient hydrolyzation. The Al compositions in the respective $Al_xGa_{1-x}As$ layers of the three samples are 70%, 80% and 90%. Rows of $25\mu m$-wide stripes separated by $5\mu m$ gaps are next created on the samples via photolithography. The patterns are then transferred into the GaAs/$Al_xGa_{1-x}As$/GaAs heterostructure using reactive ion etching with $BCl_3/SiCl_4$ gases, as described in Sections 3.2 and 3.3. A section of the etched GaAs/$Al_{0.9}Ga_{0.1}As$/GaAs sample is also oxidized for 1 hour at 435°C and is used for the investigation of the oxide sacrificial etch.

The samples are then etched in a diluted HF solution of 10ml HF (49% concentration) and 250ml DI water at room temperature. The GaAs/Al$_x$Ga$_{1-x}$As/GaAs samples are etched in the solution for 30s, while the GaAs/Al$_x$O$_y$/GaAs sample is etched for 15s. The samples are finally cleaved and the etch profiles observed at the cleave facets using a scanning electron microscope (Figure 3-25). As shown in the micrographs, the sacrificial etch removes both the Al$_x$Ga$_{1-x}$As and the oxide material without visibly affecting the surrounding GaAs material. The etch rates for the various materials are approximately (a) 1.2μm/min for x=0.7; (b) 2.3μm/min for x=0.8; (c) 11μm/min for x=0.9; and (d) 14μm/min for the oxide. Clearly, a higher percentage of Al composition in the alloy renders the material more amenable to the sacrificial etch. A large increase in etch rate is, in fact, observed when the Al-composition increases from 80% to 90%. Such a drastic
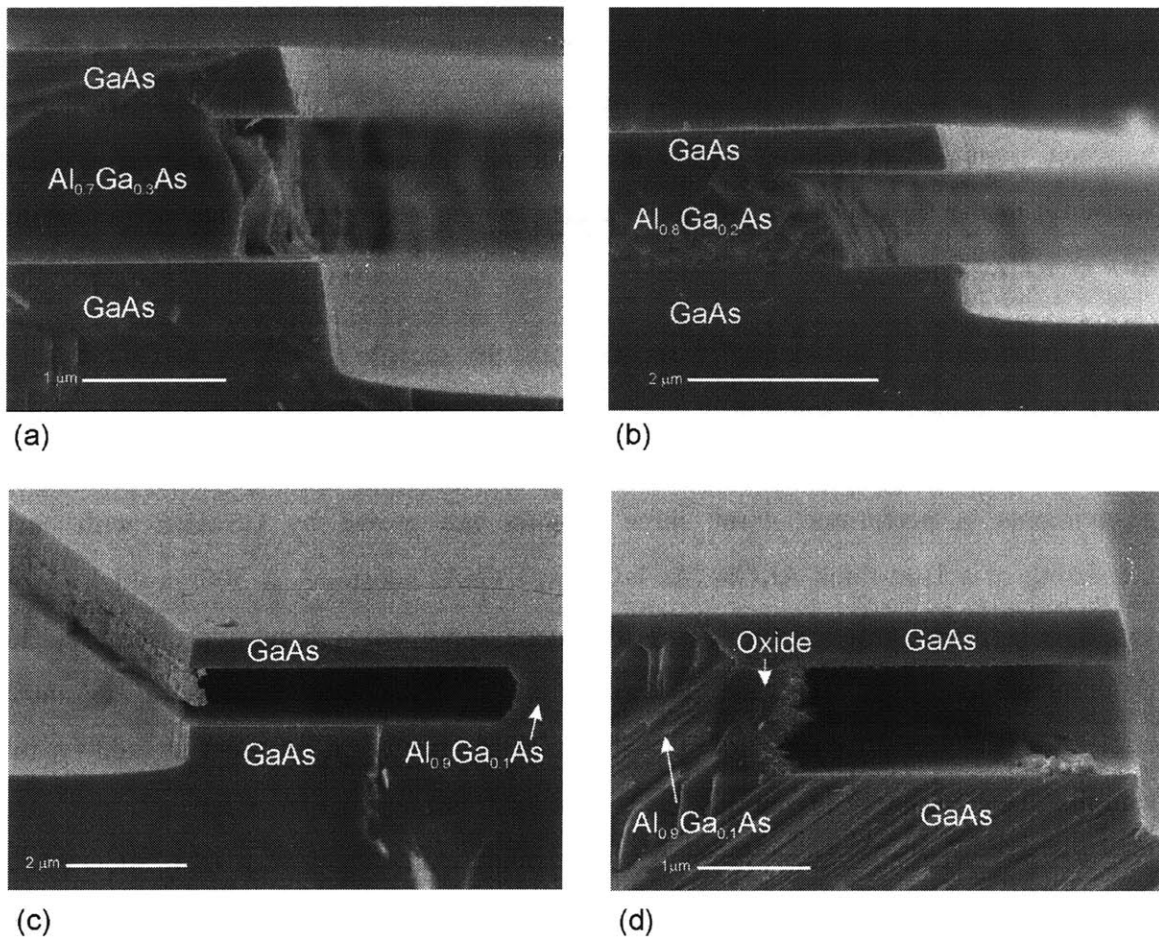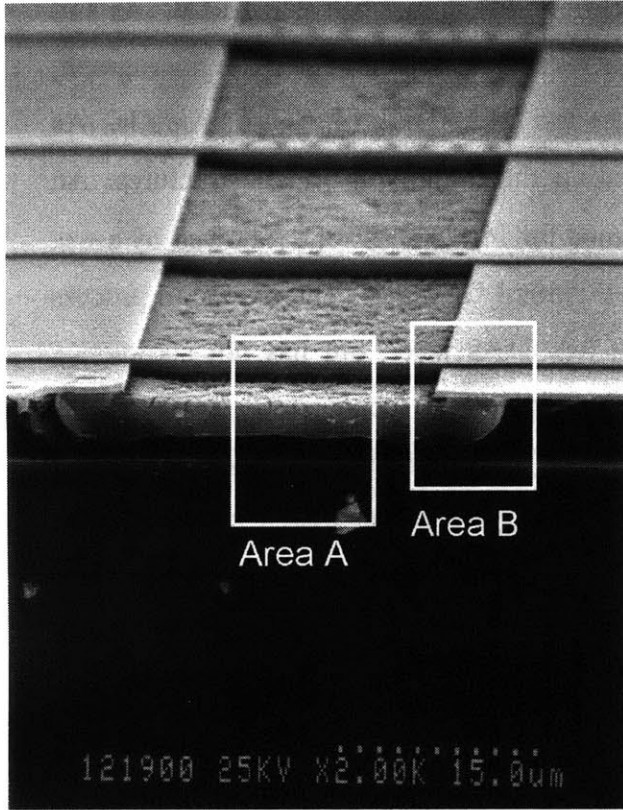

Figure 3-25: Cross-sectional scanning electron micrographs showing etch profiles in the sacrificial etch of Al$_x$Ga$_{1-x}$As or Al$_x$O$_y$ using a diluted HF solution. The sacrificial materials depicted in the micrographs are (a) Al$_{0.7}$Ga$_{0.3}$As; (b) Al$_{0.8}$Ga$_{0.2}$As; (c) Al$_{0.9}$Ga$_{0.1}$As; and (d) Al$_x$O$_y$.

97

change in etch rate indicates that the $Al_xGa_{1-x}As$ etch rate may be particularly sensitive to Al-composition when $x>0.8$.

Another interesting result arising from the etch-rate differential between $Al_xGa_{1-x}As$ and its thermal oxide is depicted in Figure 3-26. As seen in the scanning electron micrograph, a RIE process has etched partially through the top GaAs layer of a $GaAs/Al_{0.9}Ga_{0.1}As$ heterostructure, during an attempt at fabricating the 4.5μm air-bridge structures. An oxidation process is then subsequently performed for 15min at 425°C, followed by a wet etch for 60s in a diluted HF solution (10ml HF:750ml DI water). The oxidation process has proceeded laterally under the remaining top GaAs layer, but has not completely oxidized all the $Al_{0.9}Ga_{0.1}As$ material. From the micrograph, the $Al_{0.9}Ga_{0.1}As$ material is clearly etched at a higher rate than the oxide material, resulting in an oxide "ledge" forming over the receded $Al_{0.9}Ga_{0.1}As$ layer. This suggests an apparently lower etch rate for the oxide with respect to $Al_{0.9}Ga_{0.1}As$, in contradiction to the result reported in the previous paragraph. It is speculated that the $Al_xGa_{1-x}As$ material in this instance may actually contain a slightly higher Al-composition than the intended 90% Al-composition. This suggests that there may exists a certain Al-composition, m, such that the etch rate of $Al_xGa_{1-x}As$ is greater than its thermal oxide if $x>m$, and less than its thermal oxide otherwise.

It is also worthy to note that in further preliminary experiments, the oxide material derived from the thermal oxidation of $Al_xGa_{1-x}As$ with higher Al-composition is observed to be etched at a higher rate in the same diluted HF solution at room temperature.
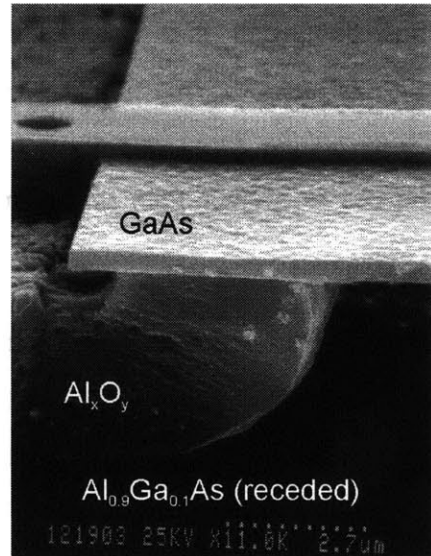
Area A
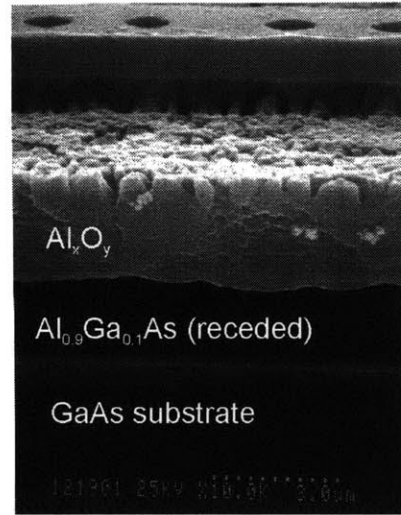
Area B

Figure 3-26: Cross-sectional scanning electron micrographs depicting effects of etch-rate differential between $Al_{0.9}Ga_{0.1}As$ and its thermal oxide.

3.5.B Problem of stiction

The phenomenon of stiction, where a free-standing micromechanical structure is permanently adhered to another surface, is a notorious problem in the field of microelectromechanical systems (MEMS) research. When two surfaces come into contact, the adhesion force may exceed the restoring elastic forces and result in the irreversible adhesion of the surfaces. The smoothness of the surfaces, typical in micromachined semiconductor structures, worsens the problem further. The occurrence of stiction can be traced to several physical origins, namely (a) capillary forces; (b) hydrogen bridging; (c) electrostatic forces between mobile charges; and (d) Van der Waals forces [74].

Capillary forces arise primarily during the drying process after a structure has been suspended. As the rinsing liquid gradually evaporates, it forms a bridge that draws the suspended structure towards the substrate (Figure 3-27). The free-standing structure may come into contact with the substrate as the liquid finally evaporates, and become permanently adhered [75]. Hydrogen bridging occurs when two hydrophilic surfaces become hydrated and come into contact. Hydrogen bonds may form between the hydrogen and the oxygen atoms of the adsorbed water molecules and lead to permanent adhesion of the surfaces. Certain wafer-bonding techniques rely on the adhesive strength of the hydrogen bridging effect [76, 77]. Electrostatic forces between mobile charges may occur during the operation of MEMS system, especially due to charging of rubbing surfaces or charge accumulation in dielectric insulators [77]. Finally, van der Waals forces between surfaces arise because of the mutual electric interaction of induced dipoles in two separate structures [77].
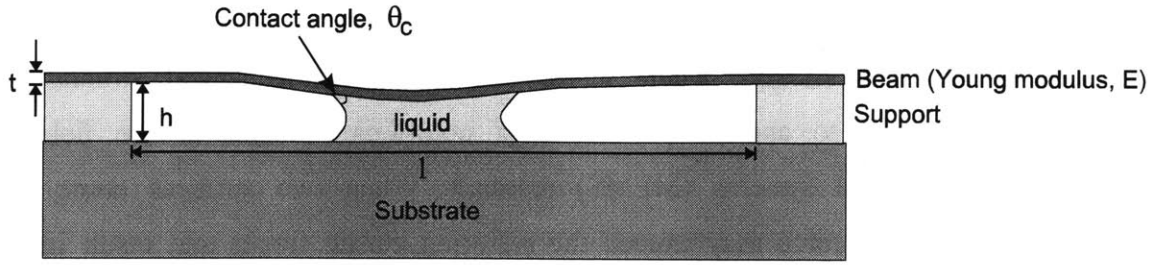
Figure 3-27: Schematic of a free-standing beam deflected by a drying liquid, after a wet-etch to suspend the structure.

In the fabrication of the 1-D PBG air-bridge microcavity, stiction due to capillary forces during the drying process poses the biggest threat to the integrity of the suspended structure. The maximum or critical length, l_{crit}, of a suspended beam that remains free from stiction after a liquid-drying process is given by [78]:

$$l_{crit} = \sqrt[4]{\left(\frac{128Eh^2t^3}{15\gamma_l \cos\theta_c}\right)\left(1 + \frac{2\sigma_R l_{crit}^2}{7Et^2}\right)}$$

Equation 3-1

In Equation 3-1 and as depicted in Figure 3-27, h and t are the dimensions of the suspended beam, E is the Young's modulus of the structural material, γ_l is the adhesion energy of the liquid-solid system, θ_c is the contact angle of the liquid with respect to the solid and air, and σ_R is the lateral residual stress in the beam. From the equation, γ_l clearly has to be as low as possible to maximize the critical length of a structure of specific h and t, and made of a particular material with a given E. In addition, one should strive to achieve a structure where $\sigma_R \geq 0$; in other words, the lateral residual stress in the structural material should be either neutral ($\sigma_R = 0$) or tensile ($\sigma_R > 0$). In GSMBE-grown material, σ_R is effectively neutral, thus reducing Equation 3-1 to:

$$l_{crit} = \left(\frac{128Eh^2t^3}{15\gamma_l \cos\theta_c}\right)^{\frac{1}{4}}$$

Equation 3-2

The adhesion energy, γ_L, of a liquid-solid system depends strongly on the smoothness of the solid surface, as well as the surface tension of the drying liquid. This has led to various schemes devised by the MEMS research community to reduce the occurrence of stiction. For example, bumps are often added to the tips of cantilever structure to reduce the contact area available for adhesion [79]. Deliberate roughening of the surfaces, with a fluorocarbon coating or with a focussed ion-beam for instance, is another tactic used to eradicate stiction [79-81].

Various approaches to the drying process present another front to solving the stiction problem encountered during fabrication. Figure 3-28 illustrates the phase transitions involved in these drying techniques [82]. In the simple approach of the evaporation of the drying liquid, one seeks the use of a liquid with the lowest surface tension. This reduces the capillary effect during the liquid to vapor transition. For example, methanol (surface tension[7] = 22.50mN/m [62]) is preferred to water (surface tension = 72.94mN/m) as the
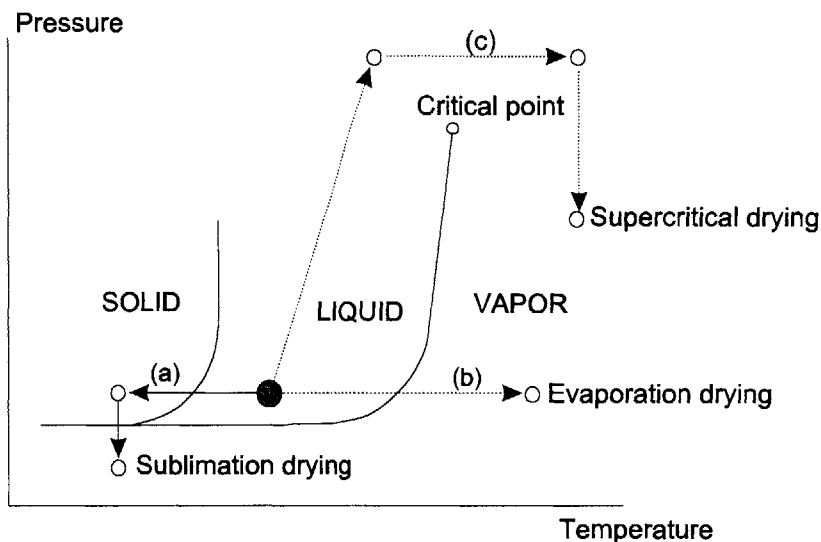
Figure 3-28: Phase diagram illustrating the phase transition pathways for the different drying process: (a) sublimation drying; (b) evaporation drying; and (c) supercritical drying. [82]

---

[7] The surface tension values of the liquids quoted here is more accurately that of a liquid-vapor system at 20°C, as the notion of surface tension only makes sense when considering two different phases of a compound, or between two different surfaces. Since only a relative comparison is intended, the quoted values seek to provide a sense of the surface tension present when methanol or water is used in the post-suspension drying of a microstructure like the air-bridge microcavity.

final drying liquid after a suspension wet-etch.

Other approaches attempt to further reduce the capillary effect by avoiding the liquid-vapor transition altogether. Sublimation drying with t-butyl alcohol, for example, involves the rinse and subsequent refrigeration of a sample immersed in the alcohol [83]. As t-butyl alcohol has a low melting point of 26°C, the liquid freezes readily. The sample in the frozen alcohol is then placed in a vacuum system, where the reduced pressure induces the sublimation of the alcohol. In the technique employing the supercritical drying with carbon dioxide (CO_2), on the other hand, a chamber containing the sample immersed in methanol is first filled and flushed with CO_2. As the pressure in the chamber is increased (typically from 800psi to 1350psi), the temperature is brought above the supercritical temperature ($\approx 40°C$). As CO_2 is then gradually vented out of the chamber, the pressure is lowered to atmospheric pressure while maintaining the temperature without the CO_2 condensing [82].

For the air-bridge microcavity structure, h is approximately 2000nm and t is nominally 192nm. For simplicity, θ_c is considered to be 0°, though a larger contact angle would be favorable for a higher l_{crit}. The Young's modulus of single-crystal GaAs is 75GPa [84], while γ_l with water as the drying liquid is about 270 mJ/m^2 [78]. The resultant critical length of the beam is only 2860nm. The use of methanol as the drying liquid, with about one-third the surface tension of water, is certainly expected to increase the critical length. In addition, the presence of the holes in the middle of the air-bridge structure also serves to increase the effective roughness of the surface and further increase l_{crit}.

In addition, the RIE process in Step 11 of the 1-D PBG air-bridge microcavity fabrication process is also critical in preventing the occurrence of stiction. To recapitulate, this RIE step removes the bulk of the material in the trench, hence reducing the amount of material that needs to be etched by the subsequent suspension wet-etch. Consequently, the suspension wet-etch time is shortened, thus reducing the undercut into the sides of the trenches while optimizing the clearance between the air-bridge and the substrate surface. The scanning electron micrograph in Figure 3-29 illustrates the necessity of this particular RIE step. The RIE step is bypassed during the fabrication of the structures

shown in the micrograph. The wet-etch time is then extended from 15s to 30s in an attempt to increase the clearance between the air-bridge and the substrate. The longer etch time induces a wider undercut, thus resulting in an air-bridge that is significantly longer than the intended 10μm length (see Figure 3-29). Further, the absence of the trench appears to retard the vertical etch rate, resulting in a clearance of only about 0.8μm. The combination of the extended bridge length and reduced clearance height results in the structures sticking to the substrate surface, as shown in Figure 3-29.

Overall, the incorporation of the RIE step to define the trenches, together with the use of methanol during the post-suspension etch drying process, appears to be adequate in fabricating 10μm long air-bridge structures. Indeed, empirical observation during the fabrication process indicates that 10μm-long structures have close to 100% success rate, while about 90% of 15μm-long structures remain suspended after post-etch drying.

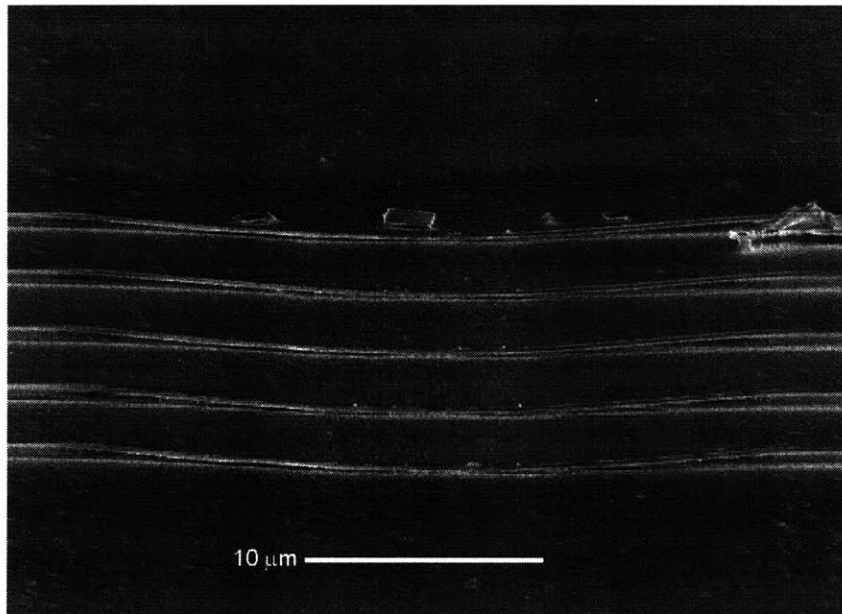Figure 3-29: Scanning electron micrograph demonstrating the phenomenon of stiction in the fabrication of the 1.55μm 1-D PBG air-bridge microcavity structures.

3.6   Reactive ion etching

The technique of reactive ion etching (RIE) represents a critical step in the fabrication of the photonic bandgap devices in this thesis. A key advantage of RIE over wet chemical etching is the highly anisotropic etch profile that can be attained, independent of the crystallographic orientation. The etch anisotropy allows the faithful transfer of mask patterns into the etched materials with minimal deviation from the desired feature sizes. The ability to etch vertically into a semiconductor thin-film becomes particularly salient in device and circuit fabrication, as feature sizes of devices shrink and features become more densely packed. The advent of RIE and other plasma-etch processes forms a cornerstone of the rapid miniaturization in the semiconductor industry today.

A schematic representation of a typical RIE system, such as the PlasmaTherm Inc. Series 700 RIE/PECVD system used in this thesis, is shown in Figure 3-30. The system consists primarily of a vacuum chamber, a gas-flow control system and a radio-frequency power supply. A stainless steel vacuum chamber is connected to a high vacuum pumping system capable of maintaining a chamber pressure on the order of less than 1×10^{-6} Torr. A throttle valve between the pumps and the chamber regulates the chamber pressure during
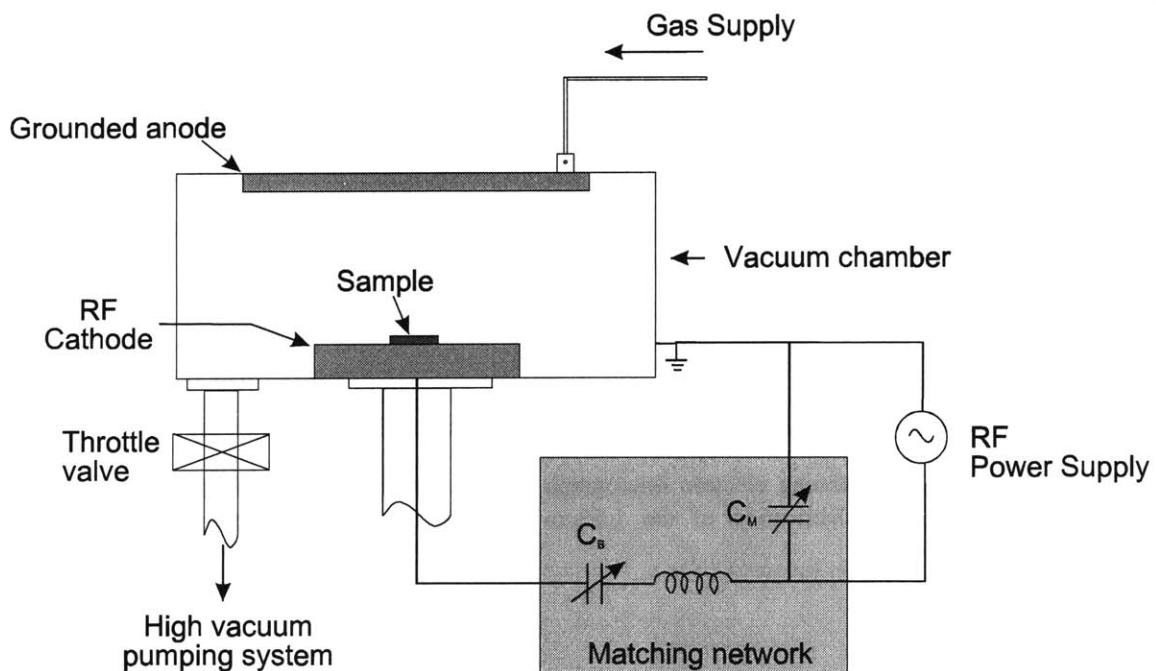
Figure 3-30: Schematic representation of a typical RIE system.

the RIE process. The gas-flow control system controls the flow of process gases through calibrated mass flow controllers. The RF power supply typically operates at a frequency of 13.56 MHz in the United States and provides power to a cathode through an impedance matching network. In Figure 3-30, the matching network consists of a pair of variable capacitors and an inductor. The blocking capacitor, C_B, serves to prevent the electrode from discharging through the power supply. In the case of the PlasmaTherm Inc. system, the sample is placed on the cathode during the RIE process. The anode usually consists of the rest of the chamber and is electrically grounded. In most modern RIE systems, all the sub-systems are controlled by a computer, which also allows the operator to program a sequence of process steps to be executed during an etch.

During an RIE process in the fabrication of the PBG devices, the vacuum chamber is first evacuated to a base pressure on the order of 5×10^{-5} Torr. The process gases are then introduced into the chamber with the chamber pressure regulated by the throttle valve. RF power is then supplied to the electrodes through the impedance matching network. High local electric field in the chamber induces ionization of a neutral gas molecule, accelerating the free electron toward the anode. Inelastic collisions occurring between the free electron and other gas molecules result in further ionization of these molecules. Repeated collisions bring about the formation of more charged particles, raising the density of the plasma that has thus been formed. Relaxation of neutral atoms/molecules and ions from their excited electron states may occur through photoemission and accounts for the glow discharge typical of plasma-etch processes. In the process, some of the charged particles become neutralized through collision with the chamber walls or, more rarely, with other ions. A dynamic equilibrium is reached when the average number of charged particles becomes constant; the plasma is then self-sustaining.

The etching action of a reactive plasma on a sample surface is often cited as consisting of a physical and a chemical component. The physical component is attributed to the sputtering of surface material via ion bombardment, when the radicals in the plasma are accelerated towards the electrodes. The chemical component involves the chemical reaction between the chemically active neutral and ionic species in the reactive plasma with the surface material. In the chemical process, the reactive particles are first adsorbed

on the sample surface. Chemical reaction between the reactive species and the surface material then forms volatile byproducts, which desorb from the sample surface. Note, however, that in certain etch processes, the etch rate cannot be accounted for simply by the addition of a sputtering rate to a chemical reaction rate. In these instances, the ion bombardment is believed to either enhance the desorption of the volatile byproducts or induce surface damage and render the material amenable to chemical reaction.

When incorporating an RIE step into a fabrication process sequence, several factors need to be taken into consideration. These factors include the anisotropy of etch profile, etch rate, mask resistance, post-etch mask removal and selectivity against other material. For the etch of large-area samples, uniformity will also be a relevant issue. In the fabrication of the 1-D PBG microcavities at $\lambda=1.55\mu m$, RIE is performed to transfer the photonic crystal patterns on a nickel mask into 100nm-thick SiO_2. The patterned SiO_2 layer acts subsequently as a mask for the RIE of the $GaAs/Al_{0.9}Ga_{0.1}As$ heterostructure. In this instance, the SiO_2 etch should transfer the nickel mask patterns into the SiO_2 layer without affecting both the mask and the GaAs layer directly underneath the oxide film. Thereafter, the removal of the nickel mask should have no effect on either the exposed GaAs or SiO_2 material. The SiO_2 mask also has to be sufficiently selective against GaAs during the RIE of the III-V heterostructure, so that the mask pattern can be transferred faithfully into the $GaAs/Al_{0.9}Ga_{0.1}As$ layers. Required of both the SiO_2 and the GaAs RIE processes are also good etch rates and (ideally) perfectly vertical etch profiles.

The anisotropy property of the RIE is particularly critical, as the high index-contrast of the PBG structures are relatively sensitive to deviation in feature sizes. A 5% increase in the size of the defect region in the 1.55μm microcavity structure, for example, would result in a 2% increase in the resonant wavelength (i.e. 30nm). Since an RIE-induced deviation in feature sizes affects all the relevant features (i.e., hole diameters, waveguide width etc), the lack of etch anisotropy could have a devastating effect on the transmission characteristics of the microcavity. The importance of the etch anisotropy is illustrated in the following experiment with the SiO_2 RIE process using a 30nm-thick e-beam evaporated nickel mask. The process gases used are CHF_3 and O_2, with a process pressure of 30mTorr, incident RF power of 250W. The gas flow rates are 50sccm and

5sccm for CHF_3 and O_2 respectively. In this RIE process, CF_3 radicals in the plasma react with SiO_2 to form the volatile SiF_4, CO and CO_2 as byproducts. The addition of O_2 in the process gas mixture serves to enhance the formation of CF_3 radicals from CHF_3, hence increasing the etch rate [85]. The presence of O_2 also reduces excessive formation of polymer from unsaturated CF_2 [86].

Figure 3-31 shows scanning electron micrographs of the etch profiles from two samples that have been etched for 10min using the above mentioned parameters. In micrograph (a), the sample has been placed directly on the stainless steel cathode during the etch process. Micrograph (b), on the other hand, shows a sample that has been placed on a polymer (known commercially as Ardel) platen covering the cathode during the etch. The difference between the etch profiles of the two samples is profound; micrograph (a) shows a profile with approximately 70° slope while the profile in micrograph (b) is effectively vertical (90°). For an oxide thickness of 100nm used in the 1-D PBG microcavities operating at 1.55µm, this translates to a lateral deviation in feature size of 36nm. For the air-bridge microcavity, such a deviation implies an effective waveguide width of 624nm (versus the intended 552nm), and an effective hole diameter of 129nm (versus 201nm). The effective increase in semiconductor material of the photonic crystal will not only shift the transmission spectrum towards the longer wavelength regime, but the decreased hole sizes will also mean a drop in cavity quality, Q.
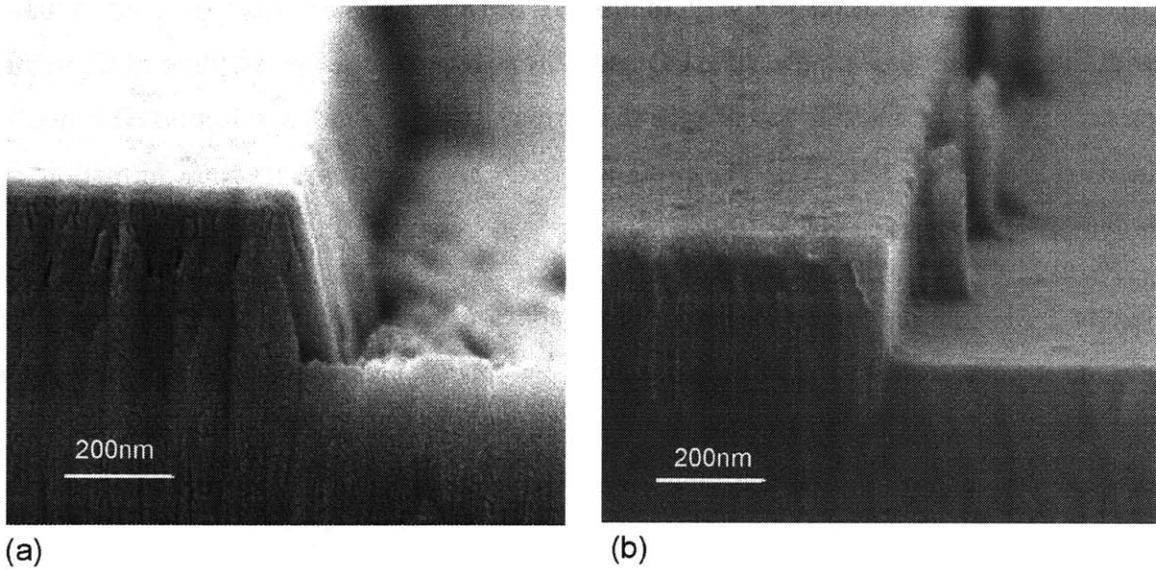
(a)

(b)

Figure 3-31: Scanning electron micrographs showing etch profiles of SiO$_2$ layers using CHF$_3$/O$_2$ RIE. In micrograph (a), the sample is place directly on the stainless steel electrode, while in micrograph (b), the sample is placed on a polymer ("Ardel") platen covering the electrode.

The sloped profile shown in Figure 3-31(a) may be traced to two possible sources. First, the sputtering action from ion bombardment on the cathode may result in deposition of material on the sidewalls of the etch feature. The material deposited serves as mask material and effectively widen the original mask feature. The sloped feature develops from the widened mask as the etch process proceeds further into the SiO$_2$ layer. Second, the high negative bias voltage of the sample in the RIE process may result in strong sputtering action at the surface of the etched material. As sputtering rates for ions impinging at an angle to normal incidence is typically higher than that at normal incidence [85], the sloped profile develops. The addition of the polymer platen may serve to reduce deposition of material on the feature sidewalls by covering the electrode. The polymer platen also lowers the absolute bias voltage of the sample by separating the sample from the cathode and raising the sample to a higher (more positive) voltage plane. In other words, the polymer platen acts effectively as the dielectric material of a capacitor between the parallel plates formed by the cathode and the sample.

The RIE of the GaAs/$Al_{0.9}Ga_{0.1}$As heterostructure represents the other critical etch process in the fabrication of the 1-D PBG microcavities. A gas mixture of BCl_3 and $SiCl_4$, with gas flow rates of 30sccm and 20sccm respectively, is used in this process. The process pressure is 30mTorr and incident RF power applied is 250W. As the process also etches aluminum, the sample is placed on an alumina plate that protects the stainless steel cathode. During the etch, volatile $GaCl_3$ and $AsCl_3$ are formed which desorb from the surface of the sample at room temperature in the vacuum chamber. Both BCl_3 and $SiCl_4$ provide the reactive chlorine species, though the latter alone has been shown to etch Al_xGa_{1-x}As [87]. BCl_3 is also believed to enhance the etch rate through its highly reducing nature by scavenging any residual water and oxygen in the chamber, and by removing the native oxide on the Al_xGa_{1-x}As material at the start of the etch. This particular etch process results in highly anisotropic profiles, as seen in Figure 3-32. The smoothness on the sidewalls of the etched features is ultimately limited by the edge roughness of the mask material.
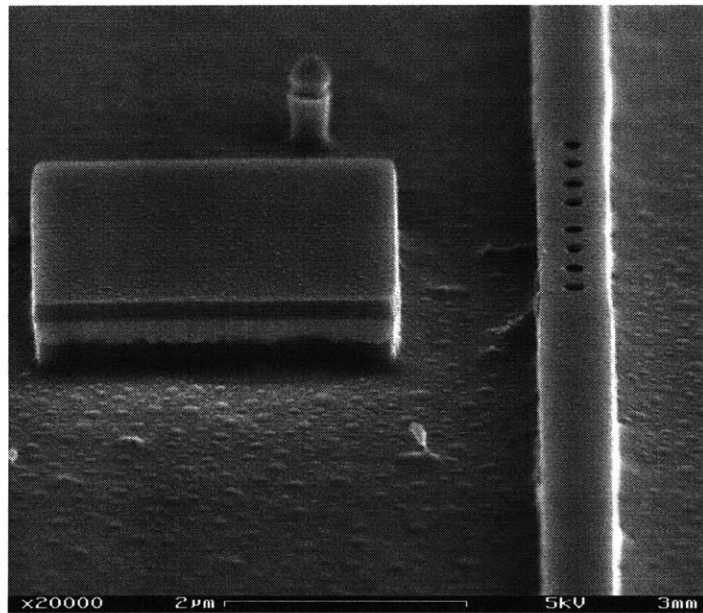

Figure 3-32: Scanning electron micrograph showing the RIE etch profile of a GaAs/$Al_{0.9}Ga_{0.1}$As heterostructure with SiO_2 as mask material, with the $Al_{0.9}Ga_{0.1}$As material having been oxidized. The mask and the heterostructure layers are visible in the mesa on the left. Note the anisotropic etch profile of the mesa feature. The structure on the right is a 1-D photonic crystal, as part of a monorail microcavity structure operating at 1.55μm.

110

3.7 Thermal oxidation of $Al_xGa_{1-x}As$

The thermal oxidation of $Al_xGa_{1-x}As$ represents a key enabling technology in the successful design and operation of the 1-D PBG microcavities. The product of the oxidation process, Al_xO_y, with a low refractive index of 1.6 makes possible the high index-contrast necessary for good optical mode confinement in the device. This section will provide a summary of the current understanding of the thermal oxidation process in the literature, as well as a description of the work that has been performed in developing this critical process at MIT.

3.7.A Literature Review

The existence of a dense and robust native oxide on silicon forms arguably the key to the multibillion-dollar semiconductor industry today. For decades, an oxide of comparable quality and based on the III-V compound semiconductor material system has eluded researchers. For instance, an early study of a native oxide on a III-V compound semiconductor had led to the first report of the thermal oxidation of AlAs at an elevated temperature in 1978 [88]. The oxide was formed by passing steam in nitrogen carrier gas over an MBE-grown AlAs sample at 100°C. The goal of the work was to develop an oxide of comparable quality to SiO_2, specifically for metal-insulator-semiconductor (MIS) applications. The thermal oxide, however, did not display comparable quality (in terms of breakdown voltage and interface trap density) achieved in the silicon metal-oxide-semiconductor devices. Apart from a subsequent report of the use of the thermal oxide in a MIS device by Tsang et al [89], the process drew little interest from the research community.
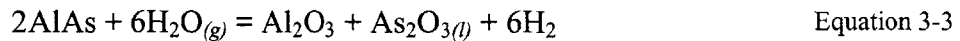
Slightly more than a decade later, a study of the environmental degradation of $Al_xGa_{1-x}As$ led to the discovery of a mechanically robust, low refractive-index Al_2O_3 formed by steam oxidation of $Al_xGa_{1-x}As$ at elevated temperature (>300°C) [90, 91]. Since then, the oxide has been utilized in various optoelectronic device applications, including in edge emitting laser structures as an index-guiding layer and as a buried dielectric current aperture [92-94]. More dramatically, the native oxide has been instrumental in the realization of vertical cavity surface emitting lasers (VCSEL's) with the lowest ever

threshold current [95] and voltage [96], as well as record high power conversion efficiency [97]. The low refractive index of the oxide has also led to the fabrication of high index-contrast distributed Bragg reflector (DBR) mirrors consisting of GaAs-Al$_2$O$_3$ layers [98]. Other applications of the oxidation process include birefringent optical waveguides [99], low-loss waveguide bends [100], microlenses [101], a host for rare-earth dopants [102], and MIS transistors [103, 104]. The success of the thermal oxidation process for Al$_x$Ga$_{1-x}$As has further led to efforts at oxidizing other Al-containing III-V compound semiconductors such as AlAsSb [105] and InAlAs [106].

The following sub-sections attempt to summarize the current understanding of the oxidation process, as well as the nature of the thermal oxide. The reader should note that the oxidation process remains an area of very active research, with results being published at a rapid pace.

3.7.A.i   Chemistry

The Al$_x$Ga$_{1-x}$As thermal oxidation process typically entails passing steam in N$_2$ carrier gas over a sample heated to 300-500°C. The primary reactants are Al$_x$Ga$_{1-x}$As and H$_2$O, with Al$_2$O$_3$ as the final product. Clearly, arsenic (As) in the starting Al$_x$Ga$_{1-x}$As material is removed as a by-product, but the form and the chemical pathway in which it is removed remains a topic of investigation. Ashby et al suggest that the hydrogen atom in H$_2$O plays a pivotal role [107]. To oxidize Al in Al$_x$Ga$_{1-x}$As from Al$^{\delta+}$ to the Al^{3+} valence state, another participant in the chemical reaction has to be similarly reduced. As the oxygen atom in H$_2$O already has a valence of –2, the H+ atom presents the remaining possible reducing agent. The chemical reactions leading to the formation of Al$_2$O$_3$ are proposed to be[8]
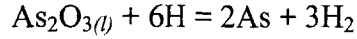
$$2AlAs + 6H_2O_{(g)} = Al_2O_3 + As_2O_{3(l)} + 6H_2 \qquad \text{Equation 3-3}$$

$$\Delta G^{698} = -473 \text{ kJ/mol}$$

$$As_2O_{3(l)} + 3H_2 = 2As + 3H_2O_{(g)} \qquad \text{Equation 3-4}$$

$$\Delta G^{698} = -131 \text{ kJ/mol}$$

---

[8] ΔG^{698} denotes the excess free energy at 698K (425°C).

$$As_2O_{3(l)} + 6H = 2As + 3H_2$$

$$\Delta G^{698} = -1226 \text{ kJ/mol}$$

Both As_2O_3 and As act as intermediate products in the process, with As_2O_3 eventually becoming reduced to As through the energetically favorable pathways (Equation 3-3 and Equation 3-4). The formation of AsH_3 through the reaction of As and atomic H is also energetically favored (ΔG^{698}= -471kJ/mol), though the reaction of As and H_2 (ΔG^{698}= +77kJ/mol) is unfavorable. Results from the Raman spectroscopy of samples at the beginning and the end of thermal oxidation seem to substantiate this postulation (Figure 3-33). The features associated with $Al_xGa_{1-x}As$ (~400cm^{-1}) diminish as the material is converted to Al_2O_3. At the same time, the relatively constant As_2O_3 (~475cm^{-1}) and As (200-300cm^{-1}) features indicate a steady state condition between the formation of the former as an intermediate product and the latter as a final by-product.

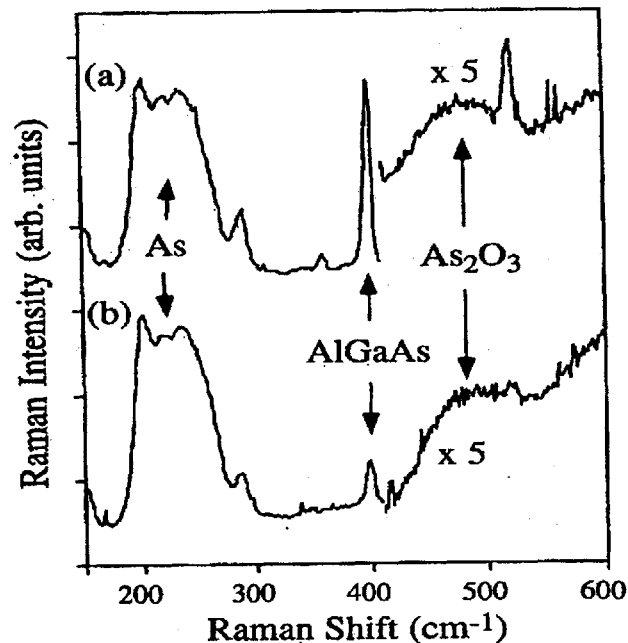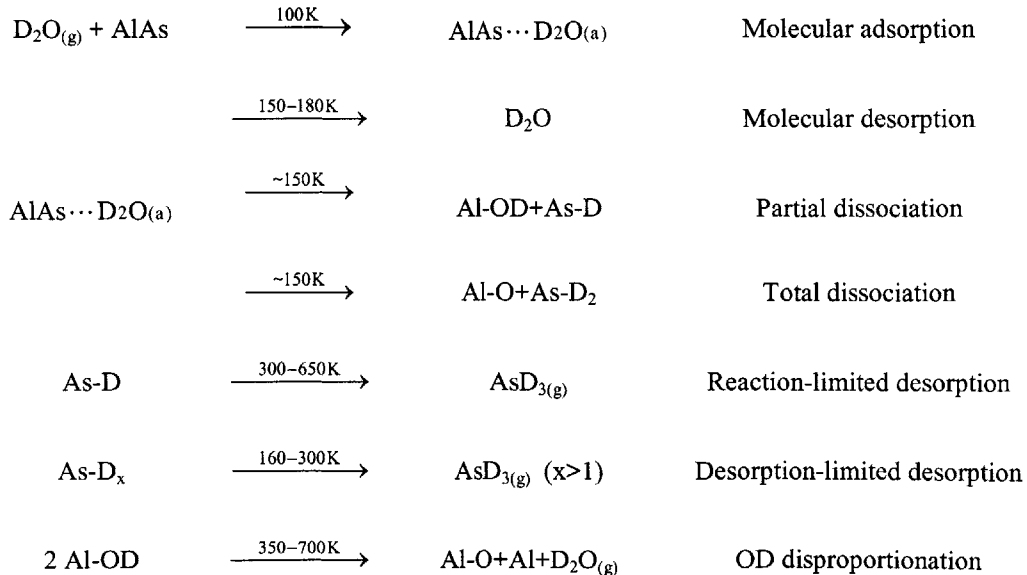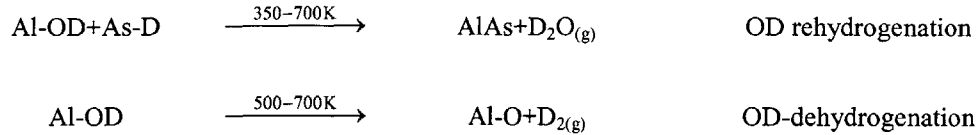The importance of atomic H is further demonstrated by two observations. First, when

Figure 3-33: Raman spectra of partially oxidized $Al_{0.98}Ga_{0.02}As$ layer at (a) the beginning and (b) the end of the oxidation process. From Ref. [108]

113

partially oxidized samples are annealed in forming gas (H_2-Ar), the Raman spectra show no change. When the samples are annealed in atomic H, however, the As_2O_3 signal in the spectra shows a 10% decrease in intensity, accompanied by a 10% increase in the As signal. Second, oxidation is observed to be completely suppressed when oxygen is used as the carrier gas, due to the competitive depletion of atomic H by O_2 to form H_2O (ΔG^{698}= -1148kJ/mol).

In another report, the initial stages of the oxidation process are investigated with Auger electron spectroscopy (AES) and temperature-programmed desorption (TPD) under ultra-high vacuum conditions [109]. To reduce the distortions due to any background water contamination, D_2O is used in lieu of H_2O in the experiments. In the AES analysis, the signal associated with O increases as the sample is repeatedly exposed to D_2O time at 300K. As D_2O desorbs at about 150K, the O signal is attributed not to the presence of adsorbed D_2O, but to adsorbed Al-OD or O adatoms. Corresponding increase in the Al-O signal and decrease in the Al-As signal are also observed, leading to the suggestion that a near-surface Al-O or Al-OH phase is being formed in the process. In the TPD analysis, the molecular species that are desorbed from the sample surface are monitored as the process temperature is gradually increased. The thermal oxidation sequence deduced from the TPD results are:

$D_2O_{(g)}$ + AlAs	$\xrightarrow{100K}$	AlAs$\cdots D_2O_{(a)}$	Molecular adsorption
	$\xrightarrow{150-180K}$	D_2O	Molecular desorption
AlAs$\cdots D_2O_{(a)}$	$\xrightarrow{\sim150K}$	Al-OD+As-D	Partial dissociation
	$\xrightarrow{\sim150K}$	Al-O+As-D_2	Total dissociation
As-D	$\xrightarrow{300-650K}$	$AsD_{3(g)}$	Reaction-limited desorption
As-D_x	$\xrightarrow{160-300K}$	$AsD_{3(g)}$ (x>1)	Desorption-limited desorption
2 Al-OD	$\xrightarrow{350-700K}$	Al-O+Al+$D_2O_{(g)}$	OD disproportionation

114

$$\text{Al-OD+As-D} \xrightarrow{\text{350–700K}} \text{AlAs+D}_2\text{O}_{(g)} \qquad \text{OD rehydrogenation}$$

$$\text{Al-OD} \xrightarrow{\text{500–700K}} \text{Al-O+D}_{2(g)} \qquad \text{OD-dehydrogenation}$$

In essence, water adsorbs on the sample at 100K, with a large fraction dissociating and reacting at higher temperatures with AlAs to produce aluminum oxide and hydroxide, as well as arsenic hydride. The remainder of the undissociated water molecules desorbs at 150-180K. Arsenic hydride species associate to form arsine, which also desorbs and depletes the surface of As. The resultant Al dangling bonds are hence open to further oxidation.

In summary, Mitchell et al [109] provide a picture of the initial stages in the thermal oxidation process, beginning with the adsorption of water, and up until the formation of arsine as a by-product. On the other hand, Ashby et al [110] suggest a chemistry that is essentially similar, except for the presence of As, in addition to arsine, as a by-product of the oxidation process. The existence of elemental As is particularly salient as As accumulation at interfaces or interstitial sites may affect the electrical and chemical properties of the material surrounding the Al_2O_3 layer, as well as the quality of any MIS device based on the $GaAs$-Al_2O_3 system [111].

3.7.A.ii   Microstructure

A detailed study of the microstructure of the oxide has been performed by Twesten et al using transmission electron microscopy (TEM), electron diffraction pattern (EDP), energy-dispersive X-ray spectra (EDXS) and elastic recoil detection (ERD) of oxidized $Al_xGa_{1-x}As$ samples [112]. The EDP results of oxidized AlAs samples reveal broad rings in the patterns indicative of amorphous-phase oxide. Cross-sectional, bright field TEM images of the samples also exhibit granular, amorphous contrast in the oxide layer (Figure 3-34). Prolonged exposure to the imaging electron beam, however, is seen to crystallize the amorphous oxide into polycrystalline γ-Al_2O_3 (as deduced from the EDP images). In fact, extended observation under the TEM results in the formation of voids at the $GaAs/Al_2O_3$ interface attributed to the local contraction of the oxide upon crystallization (see also Section 3.7.F).

The EDXS analysis of an oxidized $Al_{0.92}Ga_{0.08}As$ sample indicates that the oxide is composed of the solid solution $(Al_xGa_{1-x})_2O_3$. The signal attributed to As is also surprisingly low, in view of the reports suggesting the presence of As precipitates or As_2O_3 as by-products of the oxidation process (see Section .3.7.A.i above.) Using ERD of atoms scattered from the oxide film using Si^{3+} ions, the hydrogen content in the oxide is deduced to be on the order of $1x10^{21}$ cm^{-3}, or an Al-to-H ratio of 20:1. This implies that the oxide film consists of predominately Al_2O_3 as opposed to various forms of aluminum hydroxides, such as $Al(OH)_3$ or $AlOOH$.

High resolution TEM observation of the $GaAs/(Al_xGa_{1-x})_2O_3$ interface shows a sharp transition, with no indication of the presence of As precipitates. Extended oxidation time appears to oxidize GaAs at the interface, leading to the formation of cubic Ga_2O_3 (Figure 3-35). The Ga_2O_3 thickness depends on the Al composition of the neighboring $Al_xGa_{1-x}As$ layer, with a higher Al-% layer apparently mediating the oxidation process better than a lower Al-% layer. Further, an interface zone of approximately 20nm is also seen in all samples and consists of a form of oxide that remains amorphous despite prolonged electron-beam irradiation. The composition of the oxide in this zone remains unknown.
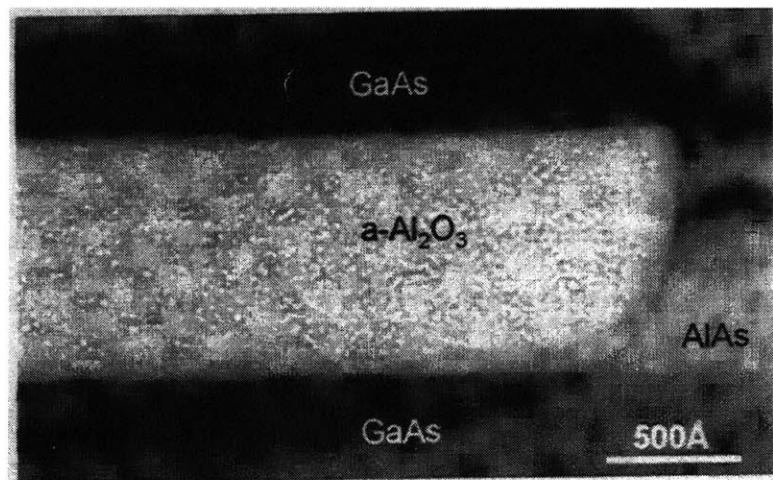

Figure 3-34: Bright field, cross-sectional transmission electron micrograph of an oxide terminus from the thermal oxidation of AlAs between two GaAs layers. Note the granular quality of the oxide, as well as the curved front of the terminus. From Ref. [112].
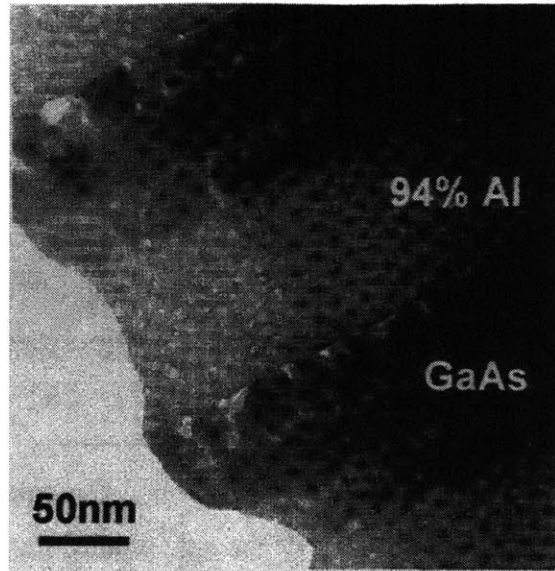
116

Figure 3-35: Transmission electron micrograph of the edge of a mesa consisting of alternating GaAs and $Al_xGa_{1-x}As$ layers, the latter of which have been oxidized. Cubic Ga_2O_3 grains are visible at the GaAs/$Al_xGa_{1-x}As$ interface. The grains are seen only near the edge of the mesa, and grow in thickness with increased Al-% of surrounding $Al_xGa_{1-x}As$ layers. From Ref. [112].

3.7.A.iii   Kinetics

The dependence of the $Al_xGa_{1-x}As$ oxidation rate on various process parameters has been reported in several early studies (for instance, Refs. [96], [113] and [114]). These parameters include temperature, Al composition, $Al_xGa_{1-x}As$ layer thickness and composition of neighboring layers. Agreement about specific nature of these parameter dependencies, however, has generally been lacking in the reports. These discrepancies are attributed to the subtle differences in which the oxidation process has been performed, including the exact configuration of the oxidation furnace [115]. For instance, Geib et al show that the lateral oxidation rate of AlAs in a 4-inch diameter furnace tube at 440°C follows a linear relationship versus gas flow when the N_2 carrier gas flow is below ~2.5 l/min; the oxidation rate remains constant above this flow rate. The authors also demonstrate that the oxidation rate depends on the water temperature in the N_2 bubbler supplying the steam for the process. For example, a 60°C bubbler results in approximately 75% of the oxidation rate attained with a 90°C bubbler. In addition, the surface temperature of the boat containing the sample depends both on the boat's position and the moisture content in the furnace. Overall, Geib et al has emphasized the need to

control both temperature and gas flow in the oxidation process, in order to achieve reproducible and tractable oxidation rates.

Empirically, the lateral oxidation extent of $Al_xGa_{1-x}As$, d_{ox}, is found to fit the Deal and Grove model [116] (which is also used in silicon oxidation):

$$d_{ox}^2 + Ad_{ox} = Bt \qquad \text{Equation 3-6}$$

where B is the parabolic rate constant, and B/A is the linear rate constant. For short oxidation time or small oxide extent, d_{ox} is derived from Equation 3-6 as

$$d_{ox} = \frac{Bt}{A} \qquad \text{Equation 3-7}$$

Such a linear relationship is observed for oxidation at different temperatures (Figure 3-36), as reported in Ref. [108]. Within this linear regime, the oxidation is reaction rate limited, as opposed to the limit imposed by the diffusion of oxidants to the oxide/$Al_xGa_{1-x}As$ interface. At longer oxidation time and/or larger oxidation extent, the diffusion-limited regime, as described by Equation 3-6, becomes relevant. The parabolic relationship in oxidation rate has been reported by several researchers for processes with longer oxidation times or at higher temperatures [117, 118].

The dependence of the oxidation rate on temperature exhibits an Arrhenius relationship, as illustrated in Figure 3-36 [108]. From the plot, the activation energy for the oxidation of an $Al_xGa_{1-x}As$ layer of a particular thickness is abstracted. Figure 3-36 also shows the strong rate dependence on the Al composition in the $Al_xGa_{1-x}As$ layer. The rate sensitivity to Al-% allows the highly selective oxidation of $Al_xGa_{1-x}As$ layers with different Al-% to different extent. On the other hand, such sensitivity also implies the necessity for tight compositional control during crystal growth.

In addition to the above parameters, the oxidation rate is also dependent on the $Al_xGa_{1-x}As$ layer thickness. For instance, the oxidation rate of AlAs sandwiched between two GaAs layers is found to decrease dramatically for AlAs thickness of less than 60nm [108]. Yoshikawa et al also reports the effective cessation of oxidation for low AlAs

118

thickness of 15nm or less [119]. Yoshikawa et al also demonstrates the selective oxidation across a sample by selectively regrowing AlAs over a patterned GaAs(80nm)/AlAs(15nm)/GaAs sample, such that oxidation occurs only where the total AlAs thickness is greater than 15nm.

The rate dependence on $Al_xGa_{1-x}As$ layer thickness is postulated to be due to the surface tension effects present at the oxide/$Al_xGa_{1-x}As$/GaAs intersection (assuming a GaAs/$Al_xGa_{1-x}As$/GaAs structure) [120]. In this surface energy model, the activation energy for the reaction rate constants A and B (Equation 3-6) at the oxidation front is shown to be inversely proportional to the layer thickness. Consequently, thinner $Al_xGa_{1-x}As$ layer will present higher activation energy, and hence exhibit lower oxidation rate. Below a certain critical thickness, the surface tension present is sufficiently high that oxidation is effectively inhibited. This model also predicts the existence of a curved oxide terminus (as seen in Figure 3-34).

Finally, the oxidation rate of an $Al_xGa_{1-x}As$ layer is also found to depend on the composition of the neighboring layers [121]. For example, a thinner GaAs barrier between an $Al_{0.98}Ga_{0.02}As$ and an $Al_{0.94}Ga_{0.06}As$ layer is found to increase the oxidation rate of the $Al_{0.94}Ga_{0.06}As$ layer. The barrier layer is believed to influence the oxidation rates of the neighboring layers by mediating the diffusion of oxidant from one oxidizing layer to the other. In addition, an $Al_xGa_{1-x}As$ layer with higher Al-% is seen to enhance the oxidation rate of an adjacent $Al_xGa_{1-x}As$ layer with lower Al-%, by virtue of the supply of reactants vertically through the layers [122].
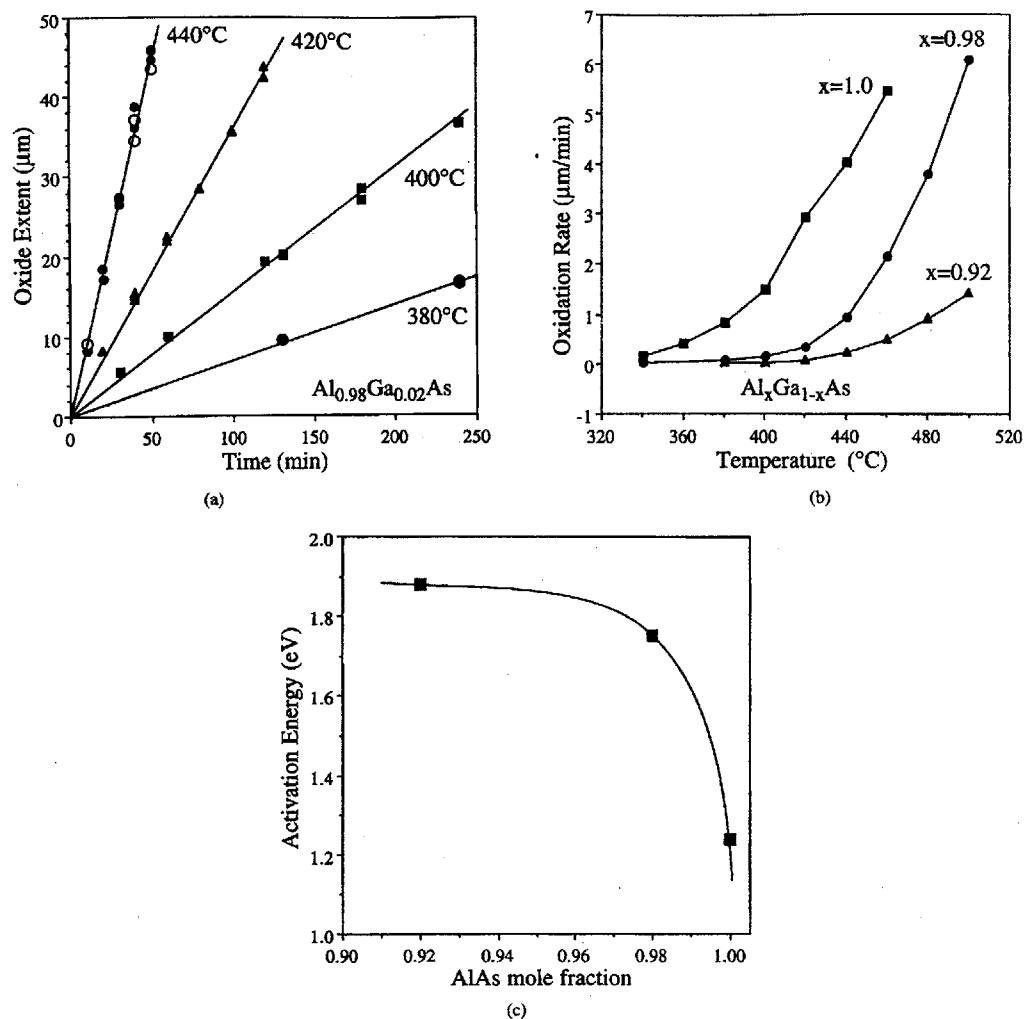
Figure 3-36: (a) Lateral oxidation rate of 84-nm thick $Al_{0.98}Ga_{0.02}As$ layer at different temperatures. The open circles in the plot for 440°C represents data obtained from samples that have been exposed to the atmosphere for 70days prior to oxidation. (b) Lateral oxidation rate versus oxidation temperature for different Al-composition in 84nm-thick $Al_xGa_{1-x}As$ layers, for x=0.92, 0.98 and 1.0. (c) Arrhenius activation energy for the oxidation of $Al_xGa_{1-x}As$ as a function of Al-composition. From Ref. [108].

3.7.A.iv   Other observations of the oxide and semiconductor/oxide interface quality.

A key concern in the inclusion of the thermal oxide in a device is the mechanical stability of the oxide layer. It has been reported that a sample containing an oxidized AlAs layer delaminates along the oxide layer when the sample is subjected to further thermal

120

processes [123, 124]. In contrast, samples containing oxidized $Al_{0.98}Ga_{0.02}As$ layers are unaffected by the additional anneal steps [123]. Grading the GaAs/AlAs interface with $Al_xGa_{1-x}As$ also enhances the mechanical stability of the AlAs-derived oxide in a distributed Bragg reflector [124]. The mechanical instability of the AlAs-derived oxide layer is attributed to the stress caused by the shrinkage of the AlAs layer during the oxidation process [125]. The shrinkage of oxidized AlAs layer has been reported to be as large as 20%, while $Al_{0.98}Ga_{0.02}As$ is measured to contract by 6.7% when oxidized. It is worthy to note, however, that another study has found no difference in the induced stress within a GaAs layer adjacent to either an oxidized $Al_{0.98}Ga_{0.02}As$ or AlAs layer [126]. The lateral induced deformation in the GaAs lattice is measured by Raman spectroscopy to be only slightly tensile ($8\pm1\times10^{-4}$) in both GaAs/oxidized-AlAs and GaAs/oxidized-$Al_{0.98}Ga_{0.02}As$ structures. This result is contrary to the suggestion by the delamination phenomenon that high stress is present in the GaAs/oxidized-AlAs structure.

Of particular importance to device designers is also the carrier recombination at the semiconductor/oxide interface. Through time-resolved photoluminescence (PL) of the GaAs emission at the band-edge in unoxidized and oxidized GaAs/AlAs structures, Kash et al show that recombination at the GaAs-AlAs interface is greatly increased in the oxidized structure [127]. The recombination at the GaAs/oxide interface is comparable to a free GaAs surface in air. Similarly, the PL of quantum-well (QW) structures placed in the vicinity of an oxide layer is also found to diminish, compared to the initial unoxidized structure [128, 129]. In another study using light beam induced current technique, the recombination velocity of minority carriers at the oxide/semiconductor interface is found to be 3.13×10^5 cm/s for oxidized AlAs and 1.90×10^4 cm/s for oxidized $Al_{0.98}Ga_{0.02}As$ [130]. The reduced recombination in the latter further emphasizes the benefit of adding Ga in the AlAs alloy in the oxidation process.

Several approaches have been demonstrated to mitigate the oxide-induced non-radiative recombination. The introduction of an $Al_xGa_{1-x}As$ barrier layer between the active region and the oxide layer, for instance, is shown to improve the PL intensity considerably [127-129]. Further, hydrogen ion treatment of a sample with a QW separated from an oxide layer by a $Al_xGa_{1-x}As$ barrier is found to partially restore the PL intensity, and is

presumably due to the reduction of excess arsenic into arsine at the oxide interface [128]. Post-oxidation hydrogenation is, however, not a panacea since the PL improvement is only seen if the $Al_xGa_{1-x}As$ barrier is sufficiently thick. This observation is attributed to the traps formed by the oxide-induced disordering in the barrier layer. A QW separated by a thinner barrier layer is thus speculated to be more severely affected by the disordering [128].

Another concern of the optoelectronic device designer is the thermal conductivity of the oxide layers, especially in the case of a VCSEL employing GaAs-oxide DBR mirrors. Thermal energy generated during operation of the VCSEL has to dissipate through the DBR mirror to reach a heat sink. MacDougal et al [131] has investigated the thermal impedance of an oxide-GaAs mirror in a VCSEL by first measuring the wavelength change in the output spectrum of a VCSEL as the temperature changes $(\Delta\lambda/\Delta T)$. The change in the wavelength spectrum due to change in dissipated energy of the VCSEL is next measured $(\Delta\lambda/\Delta P)$. The temperature change is thus correlated to the energy dissipated $(\Delta T/\Delta P)$ by dividing one quantity over the other. Through the study, the authors found the thermal impedance of an oxide-GaAs DBR mirror in a VCSEL to be comparable to that of a VCSEL with a conventional GaAs-AlAs DBR. As such, the oxide layer is deemed to pose no significant barrier to heat transport from a VCSEL's active region.

Finally, the refractive index of the oxide has been reported to be on the order of $n_{ox}=1.5$ to 1.6. Sugg et al, for instance, measured the refractive index of oxidized $Al_{0.8}Ga_{0.2}As$ to be 1.63 [132]. MacDougal et al measured the refractive index of oxidized AlAs as between 1.5 and 1.55 by using ellipsometry [50]. MacDougal et al also extracted the refractive index of the AlAs-derived oxide to be 1.55 by fitting the experimental spectrum of a GaAs-oxide DBR mirror and assuming a 87.9% contraction of the AlAs layers after oxidation. In general, the large index contrast between GaAs and oxidized $Al_xGa_{1-x}As$ gives rise to DBR mirrors with particularly wide stop-bands [50, 133].

3.7.B Experimental setup at MIT; Qualification of Oxidation Process

This section describes the system that has been set up at MIT to perform wet thermal oxidation of $Al_xGa_{1-x}As$, as well as the experimental procedure entailed in an oxidation process. The qualification of the oxidation process has focussed primarily on $Al_{0.9}Ga_{0.1}As$, since the design and fabrication of the 1-D PBG devices is based on this particular material. Experiments have been carried out to confirm the presence of a low-index oxide and are described below. Further, both the lateral and vertical oxidation rates for $Al_{0.9}Ga_{0.1}As$ have been determined. The chemical etch properties of the oxide, salient to the sacrificial wet etch in the suspension of the air-bridge structure, have also been investigated. Finally, other empirical observations on the nature of the oxide during the fabrication process are described.

A schematic of the experimental setup is shown in Figure 3-37. The sample is placed in the center of a quartz boat that is 4 inches long and 0.5 inch deep. The boat is positioned in the middle of a quartz tube, which is in turn placed in a single-zone furnace. A digital temperature controller regulates the temperature of the furnace. Two thermocouples are installed such that both the tips of both thermocouples are placed in the middle of the furnace. One of the thermocouples is connected to the temperature controller, while the other supplies an independent temperature reading of the furnace. The quartz tube is 36.5 inches long with an inner diameter of 46mm and outer diameter of 50mm. Steam is generated in a flask containing DI water that is, in turn, heated in a hot water bath. A thermometer in the flask indicates the temperature of the water in the flask. Dry nitrogen is flown into the flask through a flowmeter, bubbles into the DI water and carries the steam into the quartz tube. The quartz section between the outlet of the flask and the inlet of the quartz tube is heated with a heating-tape to prevent steam condensation. Excess steam and any gaseous by-products of the oxidation process are vented into an exhaust at the outlet of the quartz tube. Care is taken to promptly control the following parameters during an oxidation process: (a) N_2 flow rate; (b) water temperature; (c) temperature of center of furnace; (d) position of the quartz tube with respect to the furnace; (e) position of the sample boat with respect to the quartz tube; and (f) position of the sample on the sample boat.
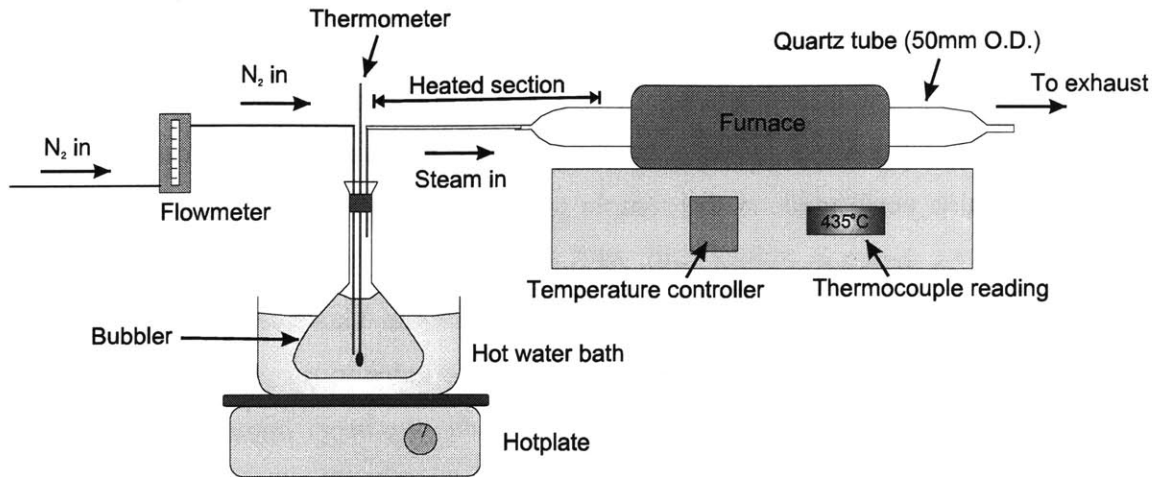
Figure 3-37: Experimental setup for the thermal oxidation of $Al_xGa_{1-x}As$.

During the oxidation process, the furnace temperature is first ramped up to the oxidation temperature, with the sample boat in the quartz tube so that it is also heated to the process temperature. When a sample is ready to be oxidized, the boat is pulled from the furnace and the sample placed on the boat. The boat is then reintroduced into the furnace. The temperature in the furnace drops as the boat first returns to its position, and is allowed to stabilize at the process set point for about 15min. During this waiting period, the quartz tube is kept dry by flowing N_2 through it. Thereafter, steam is introduced into the quartz tube by bubbling nitrogen through the flask. At the end of the oxidation process, the steam flow is cut off and dry N_2 flow through the tube is resumed. The furnace is allowed to cool down to 200°C before the sample boat is pulled from the furnace and the sample removed.

To qualify the oxidation setup, a preliminary experiment is performed using a sample with the heterostructure shown in Figure 3-38. Circular mesas of 500μm diameter are first defined using photolithography followed by a wet etch with 1:8:80 mixture of $H_2SO_4{:}H_2O_2{:}H_2O$. The sample is then oxidized in the furnace at 500°C for 2 hours. The temperature of the water in the bubbler decreases from an initial 95°C to a steady 85°C as 2 liter/min of N_2 is flown through the bubbler. After the oxidation process, the mesa

features are observed under the optical microscope and show a circular ring within the mesa that is suggestive of the extent of oxidation (Figure 3-39).

Depth profiling using Auger electron spectroscopy (AES) coupled with argon ion-beam sputtering is also performed on the sample to probe the elemental composition of the circular rings. As shown in Figure 3-40, AES shows a high Al and O intensity in tandem with a low As intensity immediately after the top 150nm GaAs layer. The Ga signal cannot be sufficiently resolved against the background noise to provide any information about its presence in the oxide layer. *The strong reduction in As intensity together with the presence of the high O intensity suggests the oxidation of AlAs into some form of* Al_xO_y. The oxidation rate for AlAs in this particular instance is estimated from the optical microscope images to be 50μm/hr.

In Figure 3-40, the O signal appears to correspond only to the AlAs layer only and may suggest the lack of oxidation in the other $Al_xGa_{1-x}As$ layers. This is probably not the case as the AES analysis is performed at one particular spot within the circular ring on the mesa structure. The vertical projection of this spot through the mesa has apparently intersected only the oxidized AlAs, and not the oxidized $Al_{0.9}Ga_{0.1}As$ or $Al_{0.8}Ga_{0.2}As$ sections of the mesa. Furthermore, the ion-sputtering rate in this particular measurement seems to have decreased significantly after the first 20min of sputter time. As such, it is not clear if the ternary alloy layers have been reached.
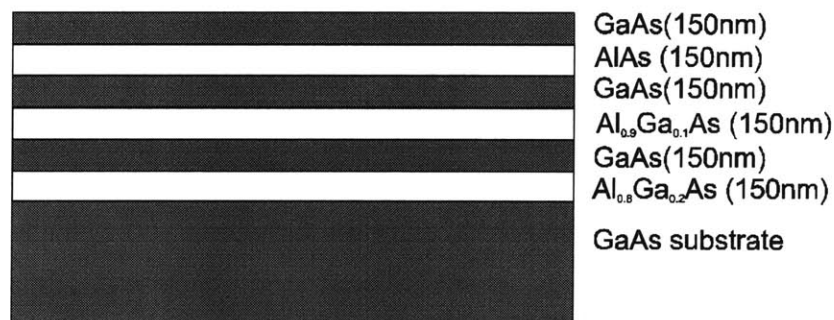

GaAs(150nm)
AlAs (150nm)
GaAs(150nm)
$Al_{0.9}Ga_{0.1}As$ (150nm)
GaAs(150nm)
$Al_{0.8}Ga_{0.2}As$ (150nm)

GaAs substrate

Figure 3-38: Heterostructure of sample used in the confirmation of the oxidation
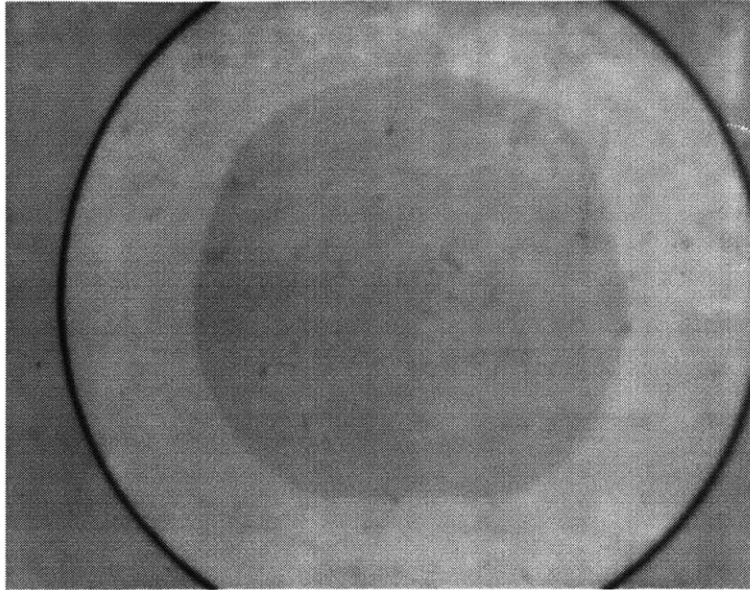
Figure 3-39: Top view optical micrograph of a mesa structure, 500-μm in diameter and made up of multiple GaAs-Al$_x$Ga$_{1-x}$As layers, with x=1.0, 0.9 and 0.8. The lighter donut-shape region defines the extent of lateral oxidation in the AlAs layer, which is closer to the surface than the ternary Al$_x$Ga$_{1-x}$As alloy layers.
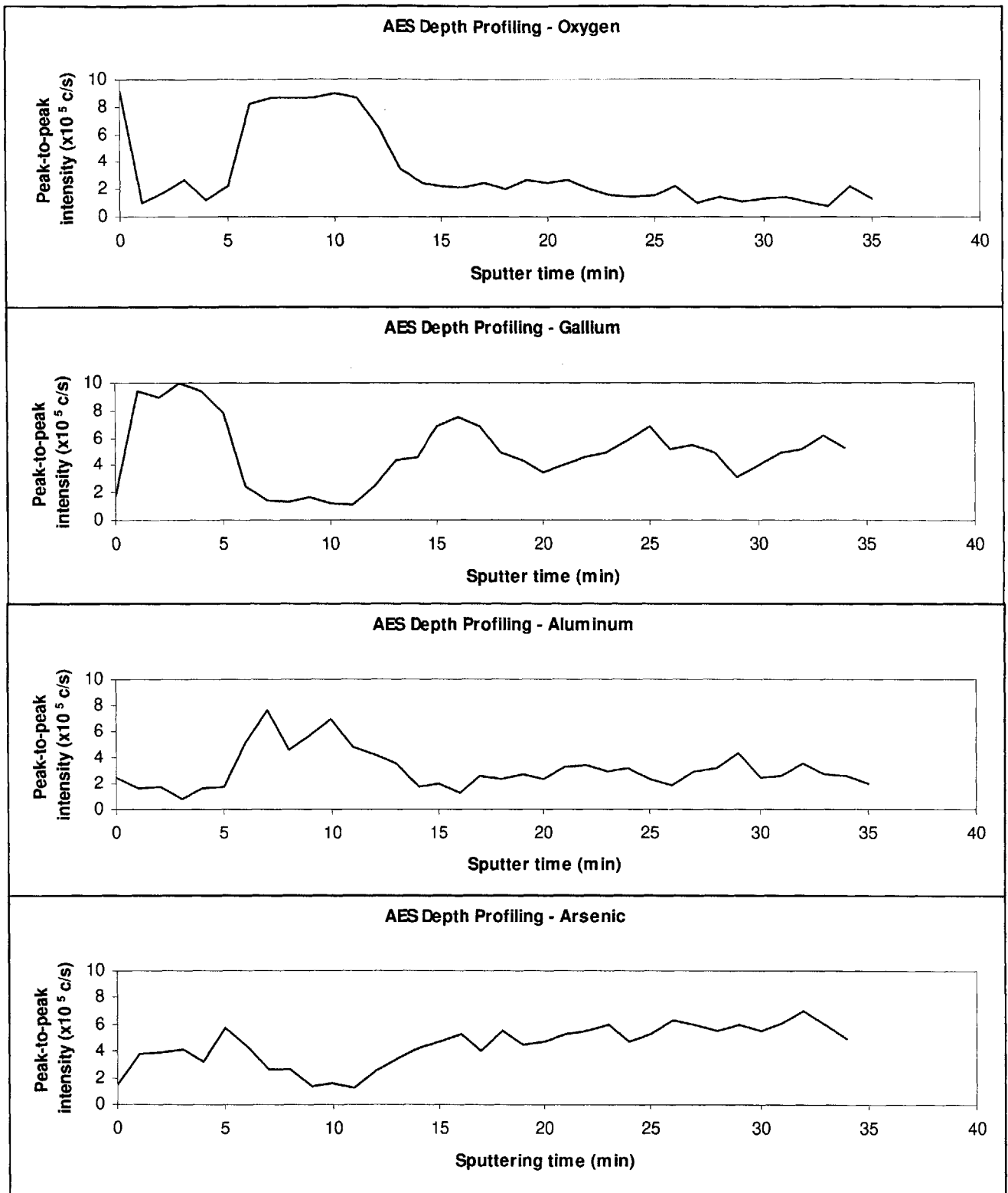
Figure 3-40: Depth profiling of oxidized mesa structure using AES in conjunction with argon ion-beam sputtering. The layer sputtered away within the first 5min corresponds to the top GaAs layer in the structure, while that within the next 10min corresponds to the oxidized AlAs layer. The sputtering rate appears to decrease after the 20th minute, as the layered features become unclear. The apparent drop in sputtering rate may be because the point on the sample being analyzed lies not in the center but on the slope of the sputtering-induced crater.

3.7.C   Importance of oxide thickness and refractive index

In the 1-D PBG microcavity devices, the III-V oxide forms an integral part of the waveguide sections and the monorail microcavity. The oxide provides the index contrast to GaAs necessary for the mode confinement along the GaAs waveguides. The monorail microcavity also relies on the high index-contrast between the 1-D photonic crystal and the underlying oxide for high Q and low modal volume of the cavity mode. To design such integrated-waveguide 1-D PBG microcavity structures, one needs to have confidence in attaining the low refractive index and prescribed thickness of the oxide layer.

To demonstrate the importance of oxide thickness control and knowledge of the oxide refractive index, transmission through a 400μm straight waveguide section of the 1.55μm wavelength 1-D PBG air-bridge microcavity is simulated for different oxide thickness
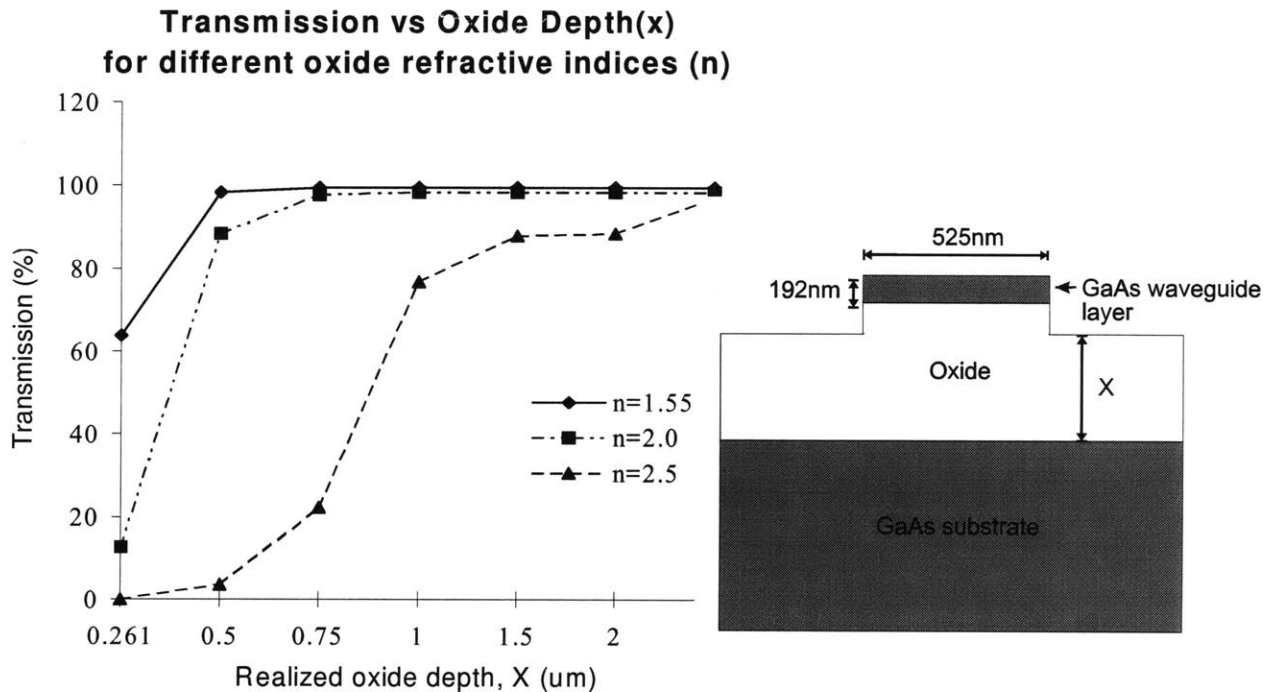

Figure 3-41: BPM simulation results for a 400μm straight waveguide section of the 1.55μm 1-D PBG air-bridge microcavity device, using different assumptions of realized vertical oxide thickness (x) and oxide refractive indices (n). The inset shows a schematic of the simulated structure. The horizontal axis for x starts at 0.261μm as the lateral oxidation of the material directly under the waveguide layer is assumed to be complete. Consequently, the minimum vertical oxide thickness will be 0.261μm (assuming vertical and lateral oxidation rates are equal, as verified in latter part of section).

128

and indices using BPM (Figure 3-41). With less than 0.5μm of realized oxide thickness, the transmission efficiency of the 400μm long waveguide section falls below 100% even if n=1.55, and reaches less than 10% if n=2.5. The dramatic drop in transmission is due to the leakage of the waveguide mode into the high-index material below the thin oxide layer. As such, the oxide layer, if insufficiently thick, will fail as an index-confinement layer. Note that for n=2.5, the transmission approaches close to 100% only if the oxide thickness is greater than 2μm. A thicker $Al_xGa_{1-x}As$ layer, together with a longer oxidation time, would thus be necessary in this instance.

3.7.D   Oxidation rate characterization

The vertical oxidation rate of $Al_{0.9}Ga_{0.1}As$ is investigated using the heterostructure that has been grown for the fabrication of the 1.55μm 1-D PBG air-bridge microcavity structures. The top 192nm thick GaAs layer and about 400nm of $Al_{0.9}Ga_{0.1}As$ are first etched away with RIE using the same amount of etch time as in the actual fabrication process, (see Section 3.3). The exposed $Al_{0.9}Ga_{0.1}As$ layer is oxidized at 435°C for duration of 10min, 20min and 30min on three different samples. The samples are then cleaved and the facets examined under the SEM (Figure 3-42). In micrograph (a), where the sample has been oxidized for 10min, the oxide layer with a characteristic granular structure is about 600nm thick and makes up about 1/3 of the initial $Al_{0.9}Ga_{0.1}As$ thickness. The unoxidized $Al_{0.9}Ga_{0.1}As$ material presents a relatively smoother cleaved

(a)   (b)   (c)
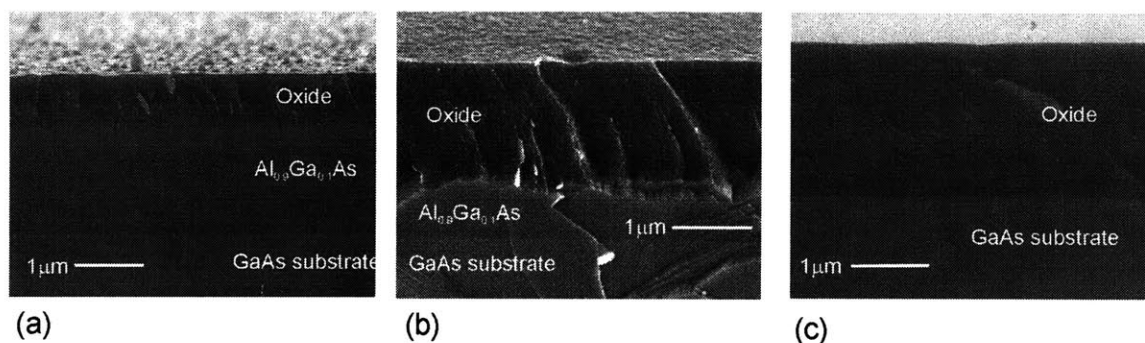
Figure 3-42: Cross-sectional scanning electron micrographs of three different samples, each with ~2.5μm thick $Al_{0.9}Ga_{0.1}As$ top layer, that have been oxidized at 435°C for (a) 10min, (b) 20min and (c) 30min. The oxide layer manifests a characteristic granular texture, while the unoxidized $Al_{0.9}Ga_{0.1}As$ and the GaAs substrate remain smooth. The oxide thicknesses are approximately 600nm, 1.37μm and 1.8μm in micrographs (a), (b) and (c) respectively.

facet, in contrast to the oxide layer. Micrograph (b) shows the result of a sample that has been oxidized for 20min with about 2/3 of the $Al_{0.9}Ga_{0.1}As$ layer ($\sim$1.37μm) oxidized. Finally, the 30min-long oxidation is seen to result in an oxide layer that extends to the GaAs substrate [micrograph (c)]. It is thus concluded that oxidation at 435°C for 30min or longer should suffice in attaining an oxide that is 1.8μm thick, for a nominal oxidation rate of 60nm/min.

To determine the lateral oxidation rates of $Al_{0.9}Ga_{0.1}As$, samples as described in Section 3.5.A are used. To recapitulate, heterostructures consisting of 500nm-thick GaAs/1000nm-thick $Al_xGa_{1-x}As$/GaAs substrate are patterned and etched into 25μm wide stripes separated by 5μm-wide trenches. The Al-compositions present in the heterostructures are x=0.7, 0.8 and 0.9. The samples are then oxidized at 435°C for 30min, where the oxidation of the $Al_xGa_{1-x}As$ layer proceeds laterally. Subsequently, the sample is cleaved and the facets examined under the SEM (Figure 3-43). As seen in the micrographs, the lateral oxide extent depends strongly on the Al-composition in the $Al_xGa_{1-x}As$ layer. For x=0.7, the oxide thickness is about 95nm, implying a lateral oxidation rate of about 3nm/min. For x=0.8, the oxide thickness is about 155nm, translating to a lateral oxidation rate of about 5nm/min. For x=0.9, the lateral oxide extent is measured to be 1.8μm and the lateral oxidation rate increases dramatically to 60nm/min, equaling the vertical oxidation rate.

The sum total of the results in this section implies that a 30min oxidation at 435°C of $Al_{0.9}Ga_{0.1}As$ will provide the oxide thickness necessary for the structures described in Chapter 2. Further, the high oxidation rate differential between $Al_xGa_{1-x}As$ material with x=0.7 and x=0.9 also confirms that the $Al_{0.7}Ga_{0.3}As$ underlayer in the 4.5μm 1-D PBG microcavity structure will be effectively unaffected by the oxidation process as intended (see Chapter 2).
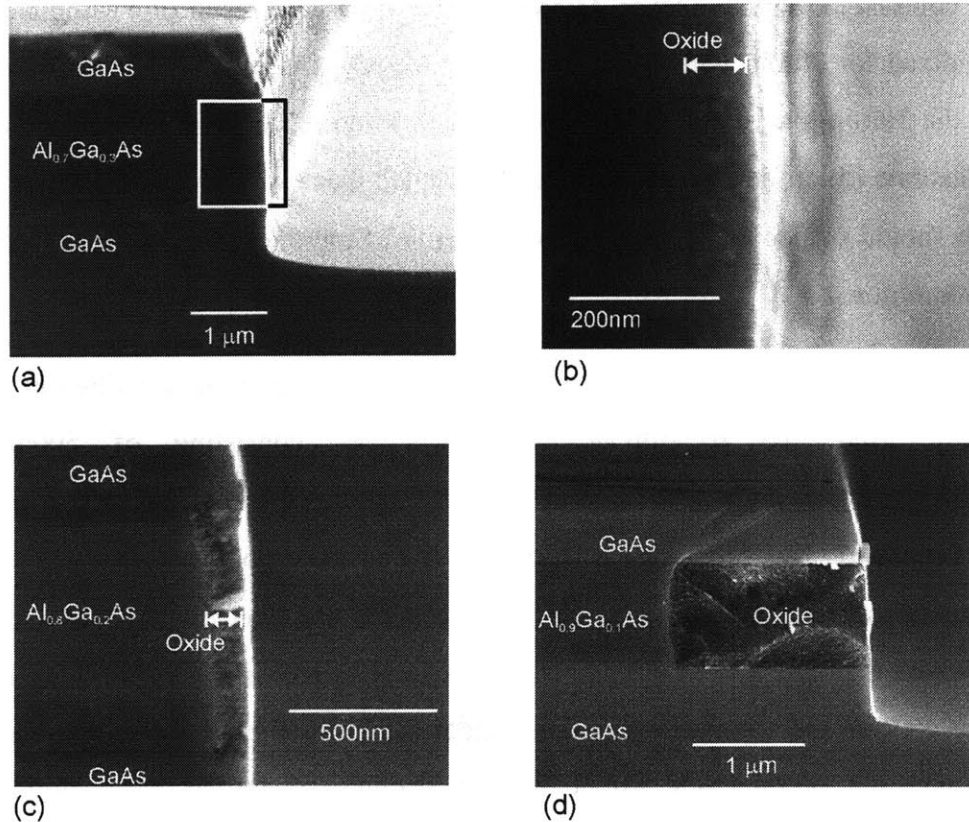
Figure 3-43: Cross-sectional scanning electron micrograph demonstrating lateral oxidation of $Al_xGa_{1-x}As$ at 435°C for 30min. Micrograph (a) shows the lateral oxide extent for x=0.7, where a higher magnification image of the oxide material is shown in micrograph (b). Micrographs (c) and (d) show the lateral oxide extent for x=0.8 and 0.9 respectively.

3.7.E   Refractive index characterization

To characterize the refractive index of the thermal oxide, the transmission spectrum of an oxidized $GaAs-Al_{0.92}Ga_{0.08}As$ multi-layer DBR structure is measured using Fourier-transform infrared (FTIR) spectroscopy. The measured transmission is then fitted against a theoretically derived spectrum using transfer matrix formulation.

The heterostructure consisting of 4 pairs of $GaAs-Al_{0.92}Ga_{0.08}As$ layers is first grown by GSMBE, with the target thicknesses of the GaAs and $Al_{0.92}Ga_{0.08}As$ layers as 115nm and 387.5nm respectively. The heterostructure is designed initially for a GaAs-air DBR operating at 1550nm where the $Al_{0.92}Ga_{0.08}As$ layers are to be selectively etched away, creating a high index-contrast DBR mirror with freestanding GaAs layers. As such, the

thickness of the $Al_{0.92}Ga_{0.08}As$ layer follows from the intended "air-layer" thickness of $\lambda/4n_{air}$, where $\lambda=1550nm$ and $n_{air}=1.0$. Similarly, the thickness of the GaAs layer is also $\lambda/4n_{GaAs}$, where $\lambda=1550nm$ and $n_{GaAs}=3.3737$. During the GSMBE growth process, the layer thicknesses are monitored in-situ with an experimental variable-angle spectroscopic ellipsometry (VASE) setup, in addition to the monitoring of the growth rates of the various layers with reflection high-energy electron diffraction (RHEED).

Stripe patterns with widths ranging from 5μm to 100μm are next defined in the heterostructure using photolithography and RIE. The RIE etch penetrates sufficiently deep such that the $Al_{0.92}Ga_{0.08}As$ layers are exposed. Thereafter, the sample is oxidized at 425°C for varying amounts of time. Depending on the oxidation time, the $Al_{0.92}Ga_{0.08}As$ layers under the stripe patterns are laterally oxidized to different extents, as observed under the optical microscope (see Figure 3-44). The widest stripe that has been completely oxidized is 20μm wide with a total oxidation time of 2 hours.

(a)   (b)
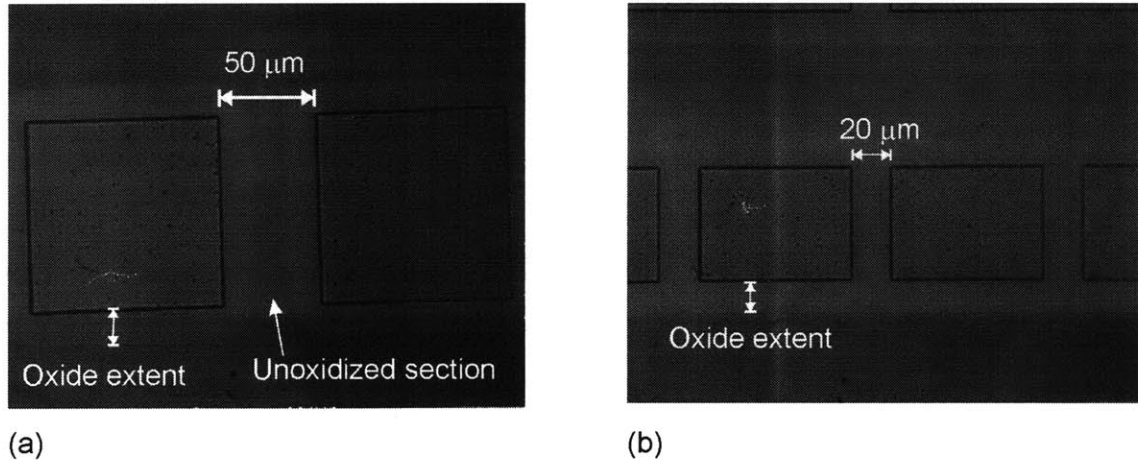
Figure 3-44: Top-view optical micrographs of oxidized DBR stripes. The rectangular patterns in the micrographs represent regions where the GaAs-$Al_{0.92}Ga_{0.08}As$ layers have been removed by RIE. The lateral oxide extent is manifested as a lighter region, extending from the side-walls of the remaining GaAs-$Al_{0.92}Ga_{0.08}As$ layers. A 50μm-wide stripe (micrograph (a)) is partially oxidized while a 20μm-wide stripe is completely oxidized (micrograph (b)).

Reflectance characteristics of the GaAs-oxide DBR structures are measured with FTIR spectroscopy[9]. A tungsten-halogen source is used, together with a silicon-on-CaF_2 beamsplitter and a HgCdTe detector. The wavelength range for the operation of the various components as specified by the manufacturers are: $0.63\mu m$ to $3.57\mu m$ for the source, $0.74\mu m$ to $8.33\mu m$ for the beamsplitter, and $0.86\mu m$ to $16.67\mu m$ for the detector. The detector is housed in a specially designed microscope that allows both the viewing of a sample (VIEW mode) and the collection of the signal through an objective from the sample (INFRARED mode). The area of interest on the sample is first located using the VIEW mode. A variable aperture serves to restrict the signal source to the area of interest (i.e. the DBR stripe patterns) and its size is set by adjusting the positions of four knife-edges. During the signal collection, the microscope is set in the INFRARED mode and the light source is routed from an external optical bench setup. The detected signal is then processed on a computer, yielding the reflectance spectrum of the DBR structures. A gold mirror serves as the 100% reflectance reference.

Figure 3-45 shows the measured reflectance spectrum of an unoxidized, unprocessed sample. The noise manifested in the shorter wavelength range is a result of the drop in the detector's sensitivity. The measured spectrum is fitted with theoretical curves using a transfer-matrix formulation. One of the two theoretical fits is based on the target thicknesses of the various layers in the DBR structure. The other theoretical fit uses the thicknesses of the GaAs and $Al_{0.92}Ga_{0.08}As$ layers as determined by the in-situ VASE thickness measurement during MBE growth. The parameters employed result in a relatively close fit between the experimental spectrum and both theoretical fits.

---

[9] Extensive treatment of the FTIR technique can be found in several texts, for instance, "Introductory Fourier Transform Spectroscopy" by Robert J. Bell, Academic Press (1972), or "Fourier Transform Infrared Spectroscopy" Vols. I and II by J.R. Ferraro and L.J. Basile editors, Academic Press (1978,1979).
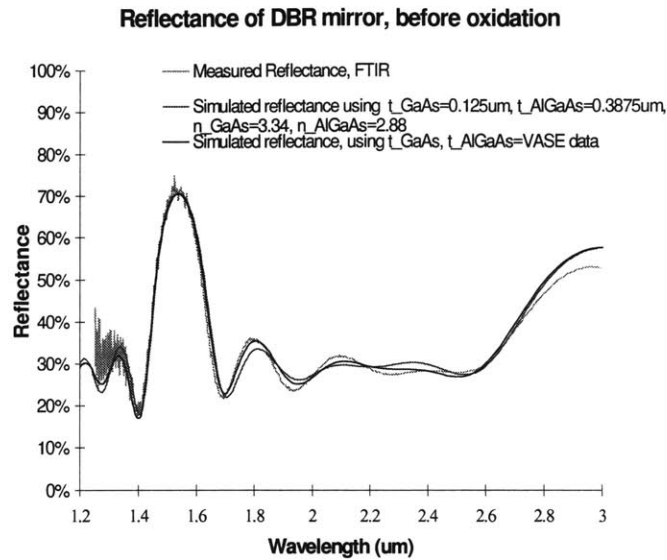
Reflectance of DBR mirror, before oxidation

Figure 3-45: Reflectance spectrum of an unoxidized GaAs-Al$_{0.92}$Ga$_{0.08}$As DBR-mirror sample as measured with Fourier-transform infrared (FTIR) spectroscopy. Theoretical fits to the measured spectrum are obtained using a transfer-matrix formulation based on either the target thicknesses of the various layers, or the layer thicknesses as determined by the in-situ variable-angle spectroscopic ellipsometry (VASE) measurement during MBE growth.

The reflectance spectrum of an oxidized DBR structure is shown in Figure 3-46. The FTIR measurement is obtained from a 20μm by 40μm DBR mirror, with the area of measurement defined with the variable size. A theoretical fit to the measured spectrum is also shown in Figure 3-46. The simulated spectrum is again obtained with a transfer-matrix formulation. Note that the wide stop band in the reflectance spectrum (~1.3μm to 2.3μm) depends strongly on the large index-contrast between the high-index GaAs and low-index oxide layers, given that the thickness and refractive index of the GaAs layers are unaffected by the thermal oxidation process. The oxide refractive index required to fit the width of the stop band is 1.61, which is comparable to the indices reported in the literature.

On the other hand, the positions of the primary stop band (λ=1.3μm to 2.3μm) and the secondary peaks in the reflectance spectrum (λ=2.3μm to 3μm) depends on both the layers' thicknesses and refractive indices. Using the oxide index of 1.61, the oxide

thickness in the theoretical fit is about 300nm, implying shrinkage in the initial $Al_{0.92}Ga_{0.08}As$ layer of about 22.5%. Such shrinkage, however, is much larger than reported in the literature. A possible source of error may be the fact that the measurement area defined by the variable aperture has included regions outside the DBR structure. Also, the sample may not be perfectly orthogonal to the source light beam when placed on the microscope. The main parameter extracted from the experiment, however, is the refractive index of the oxide; the low oxide index of n=1.61 is well substantiated by the wide stop band in the reflectance measurement.
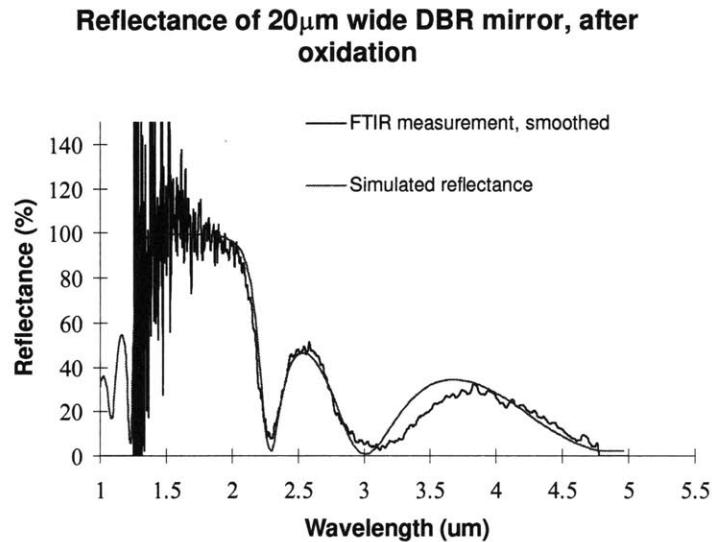
Reflectance of 20μm wide DBR mirror, after oxidation

Figure 3-46: Reflectance spectrum of a 20μm by 40μm DBR mirror measured with FTIR, after the $Al_{0.92}Ga_{0.08}As$ layer has been fully oxidized laterally. The theoretically-fitted curve is obtained with transfer-matrix formulation, assuming an oxide refractive index, n=1.61, and final oxide thickness of 300nm.

3.7.F   Other observations

This section summarizes several observations made during the fabrication process in regard to the oxide material. First, observation of the GaAs-oxide interface under the scanning electron microscope is seen to affect the interface itself, as reported in the literature [112]. Figure 3-47 shows the formation of voids at the GaAs/unoxidized $Al_{0.9}Ga_{0.1}As$/oxide intersection after observing the area with a 5keV scanning electron beam for approximately 3min. Figure 3-47(a) shows the area in question before the viewing window is zoomed in to that shown Figure 3-47(c). As the electron beam scans the reduced viewing window, the void is observed to form spontaneously. After the viewing window has been zoomed out to that shown in Figure 3-47(b), an extensive void
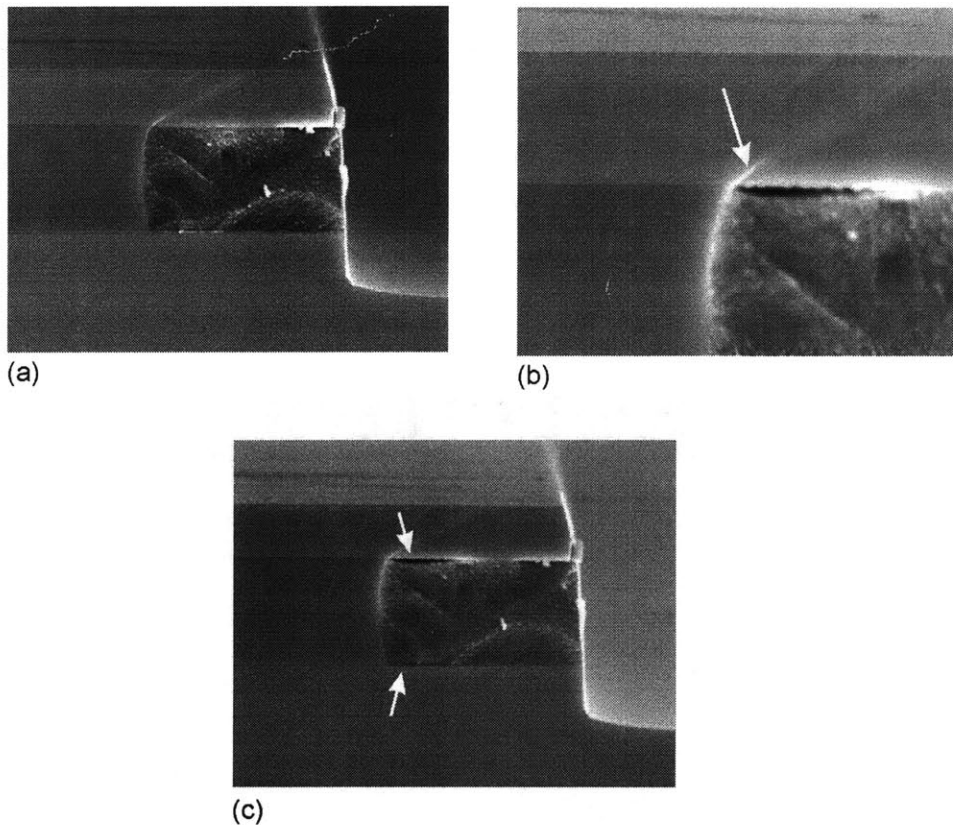

(a)

(b)

(c)

Figure 3-47: Scanning electron micrographs illustrating void formation at the GaAs-$Al_{0.9}Ga_{0.1}As$-oxide interface during extended exposure to an electron beam. Micrograph (a) shows a cross-sectional view of a tri-layer structure, identical to that shown in Figure 3-43. After micrograph (a) has been imaged, micrograph (b) is obtained under higher magnification and centered at the intersection. A void is observed to form spontaneously at the intersection. Micrograph (c) shows the sample a few minutes later, at a lower magnification. The void indicated by the bottom arrow in micrograph (c) is due to a high-magnification scan at the lower intersection after micrograph (b) has been imaged.

136

has been formed at the area of interest. As reported by Twesten et al. [112], the oxide recrystallizes from the initial amorphous to a polycrystalline phase when irradiated by the electron beam. As seen in Figure 3-47, the initiation of the void at the intersection of the three materials and its propagation along the GaAs/oxide interface may indicate that (a) the tri-material intersection presents a high-stress region amenable to initiation of void formation; and (b) the oxide is weakly bonded to GaAs, presenting a favorable path for void propagation.

Another observation is the deleterious effects of thermal recycling on an existing oxide layer. In particular, an oxide layer has first been formed by the thermal oxidation of $Al_{0.9}Ga_{0.1}As$ at 435°C for 30min, as part of the 1.55µm monorail cavity fabrication process. After the sample has cooled and is reintroduced (> 24 hours later) into a dehydration oven set at 200°C for 30min as part of a photolithography process, thin flakes are seen peeling off the surface of the sample. Under the optical microscope, the shiny surface characteristic of the GaAs substrate is observed, devoid of any patterns that have been previously etched in the GaAs-$Al_{0.9}Ga_{0.1}As$ epitaxial layers. Figure 3-48 shows a scanning electron micrograph depicting the delamination phenomenon on another sample, where the delaminated film is barely adhering to the substrate. The
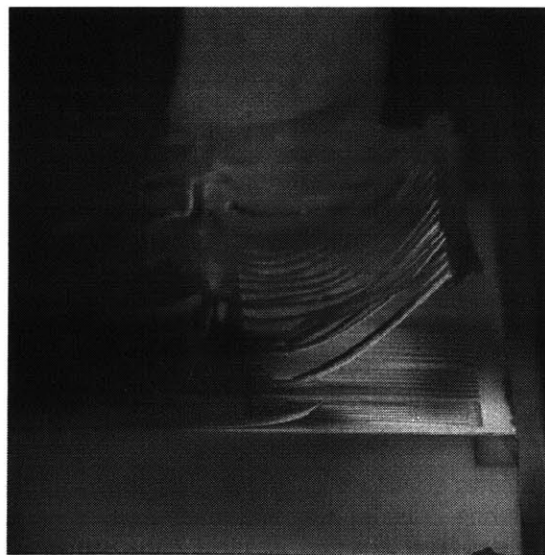

Figure 3-48: Scanning electron micrograph showing delamination of an oxide film along the oxide-GaAs substrate interface of a GaAs/oxide/GaAs substrate heterostructure. The oxidized sample has been reintroduced into an oven set at 200°C.

137

delamination phenomenon is speculated to be a result of the thermal expansion mismatch between the different materials in the system. The same delamination problem of the oxide film, from thermal cycling or otherwise, has also been reported elsewhere [108, 124].

3.8   Fabrication Results

The results of the fabrication process are primarily assessed using a Zeiss DSM scanning electron microscope via a back-scattered electron detector. The images provide visual confirmation of the quality of the devices, including the structural integrity, waveguide smoothness and realized feature sizes.

3.8.A   1-D photonic bandgap air-bridge microcavity operating at $\lambda=4.5\mu m$

Scanning electron micrographs of the 1-D PBG air-bridge microcavity structures designed to operate at the 4.5μm wavelength regime are shown in Figure 3-49 and Figure 3-50. Figure 3-49 shows air-bridge microcavity structures that have been fabricated without the over- and under-layers that are present in the device described in Chapter 2. The under- and over-layers have been deliberately omitted to reduce process complexity in this exploratory fabrication process.

As seen from the micrographs, the air-bridge structures are generally straight without any signs of mechanical distortion. The steep sidewalls in the trenches underneath the air-bridges are attributed to the anisotropy of the RIE process. As previously mentioned (see Section 3.5.B), this specific RIE step is crucial in removing the bulk of the trench material before the suspension wet-etch process. Interestingly, the air-bridge structures can be observed to cast shadows at the bottom of the trenches.

Figure 3-50 shows a scanning electron micrograph of an air-bridge structure where both under- and over-layer have been included in the device. The overlayer can be clearly seen to exist on both ends of the suspended photonic crystal. The smoothness of the top surface of the photonic crystal is a testament to the efficacy of the $In_{0.49}Ga_{0.51}P$ etch-stop

layer in the selective etch of the over-layer (step 3 in Section 3.2). Again, the structure exhibits no sign of mechanical distortion.

(a)

(b)

(c)

(d)
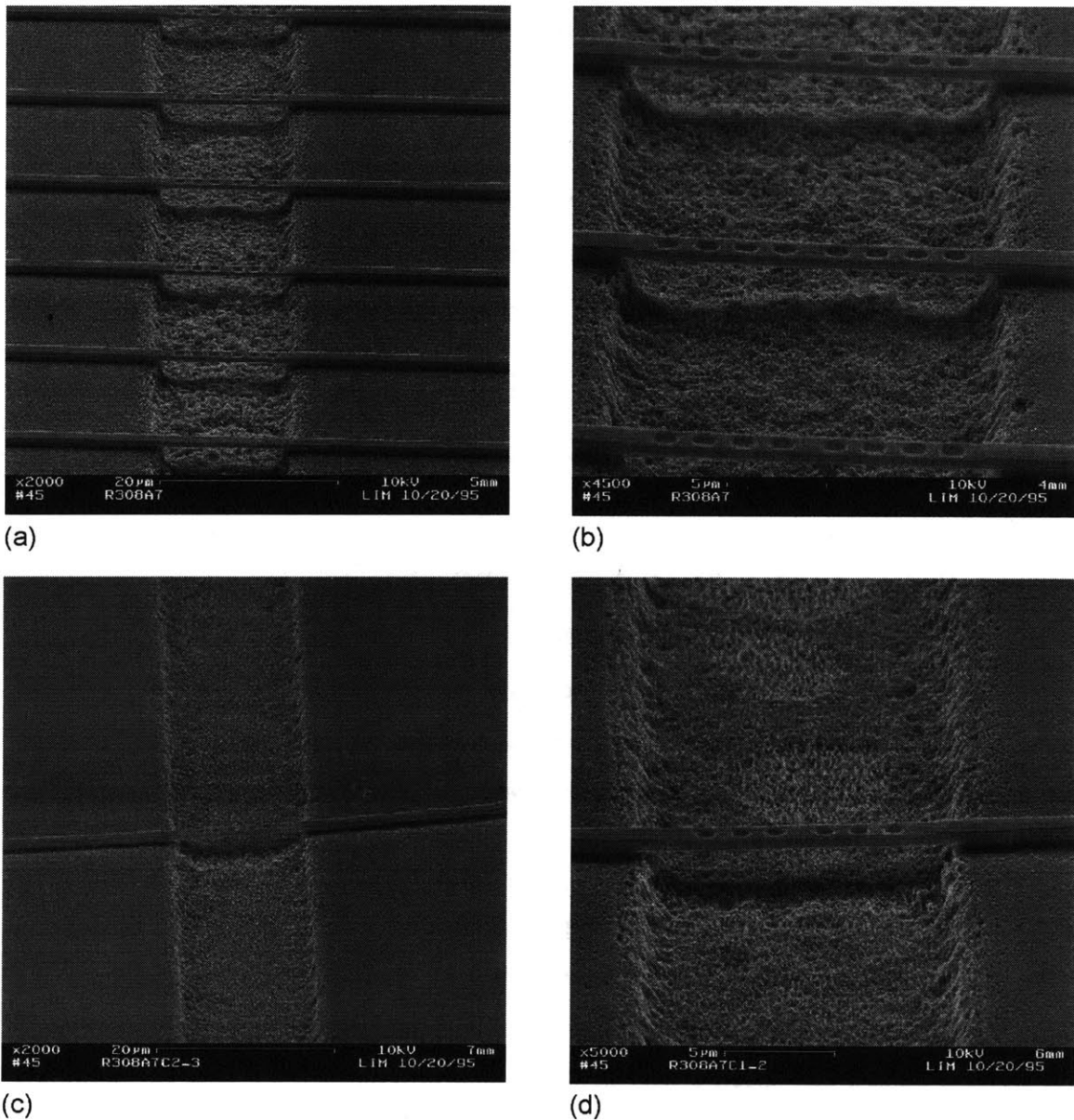
Figure 3-49: Scanning electron micrograph of 1-D PBG air-bridge microcavities designed to operate at λ=4.5μm, with the over- and underlayers omitted. (a) A series of air-bridge structures with a total of 6 holes in each structure. Note the presence of a single air-bridge structure with no holes at the bottom of the micrograph. This air-bridge waveguide structure is included to aid in alignment during optical characterization. (b) Air-bridge structures with a total of 8 holes in each structure. (c) Air-bridge structure with a total of 6 holes. (d) Higher magnification view of structure in (c).
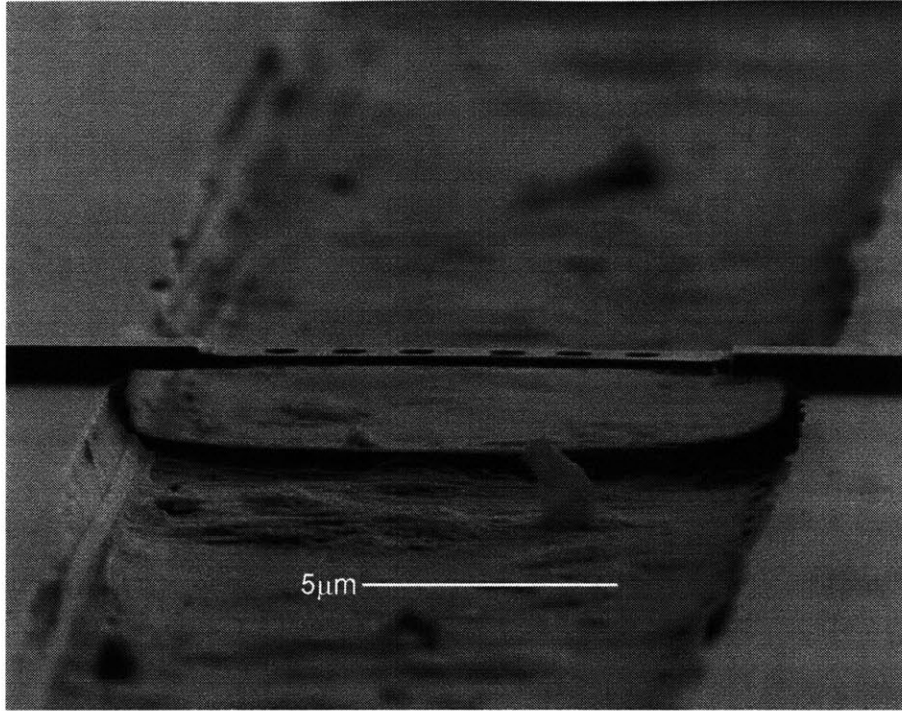
Figure 3-50: Scanning electron micrograph showing a 1-D PBG air-bridge microcavity designed to operate at λ=4.5μm. The over- and underlayers are present in this structure. The GaAs air-bridge structure is 0.4μm-thick and 1.8μm wide. The holes are 1μm in diameter and are separated by 0.8μm. The defect region in the center of the array of holes is 2.6μm wide.

3.8.B   1-D PBG Microcavities operating at $\lambda=1.55\mu m$

Figure 3-51 shows the top view Nomarski optical micrograph of an array of rectangular mesas, each $10\mu m$ by $30\mu m$ in dimensions. The rectangles form part of the wedge patterns that have been used to determine if the electron-beam lithographically generated patterns have been sufficiently exposed during the development of the e-beam resist (see Section 3.3). An area around the border of each rectangular mesa with a distinctive coloration is clearly visible and provides an indication of the lateral oxide extent.

Cross-sectional scanning electron micrographs of the input waveguides are shown in Figure 3-52 and Figure 3-53. Figure 3-52 shows a series of input waveguides flaring from approximately $2\mu m$ wide at the input waveguide facet to the width of the microcavity structure over a distance of about $100\mu m$. Figure 3-53 demonstrates the complete oxidation of the $Al_{0.9}Ga_{0.1}As$ material under the GaAs waveguide structure into the low refractive-index oxide material.
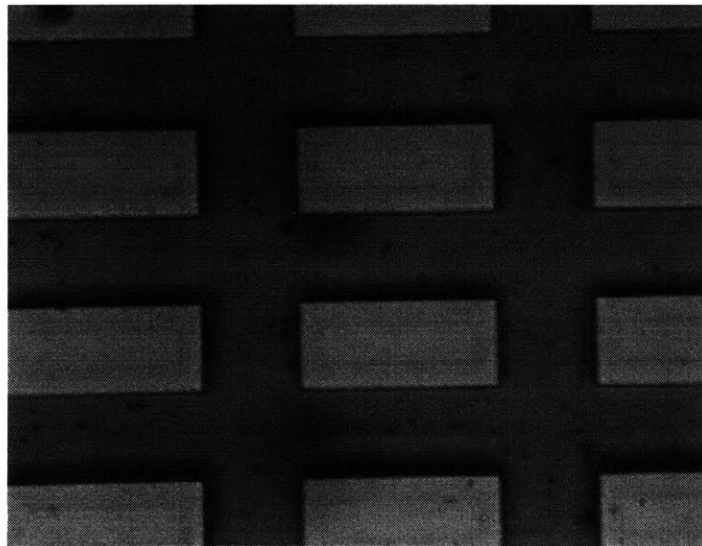
Figure 3-51: Top view Nomarski optical micrograph of an array of rectangular mesas that form part of the "wedge" patterns. The "wedge" patterns are used to determine if the electron-beam lithography patterns have been sufficiently exposed during the development of the e-beam resist (see Section 3.3).
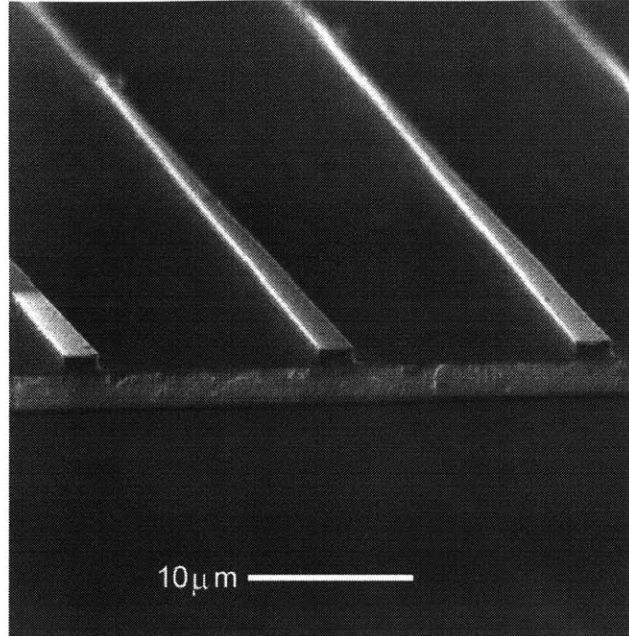
Figure 3-52: Scanning electron micrograph of a typical series of input waveguides. Note the flaring of the waveguide structure from approximately 2μm wide at the input facet to the width of the microcavity structure.

Finally, Figure 3-54 and Figure 3-55 show scanning electron micrographs of monorail and air-bridge microcavities designed to operate at the wavelength regime of 1.55μm. In Figure 3-54, the GaAs waveguide layer is clearly distinct from the oxide layer underneath. In Figure 3-55, the roughness in the trench region of the air-bridge structure is due to the roughening of the surface of the remaining, unetched sacrificial oxide by the diluted HF acid solution.
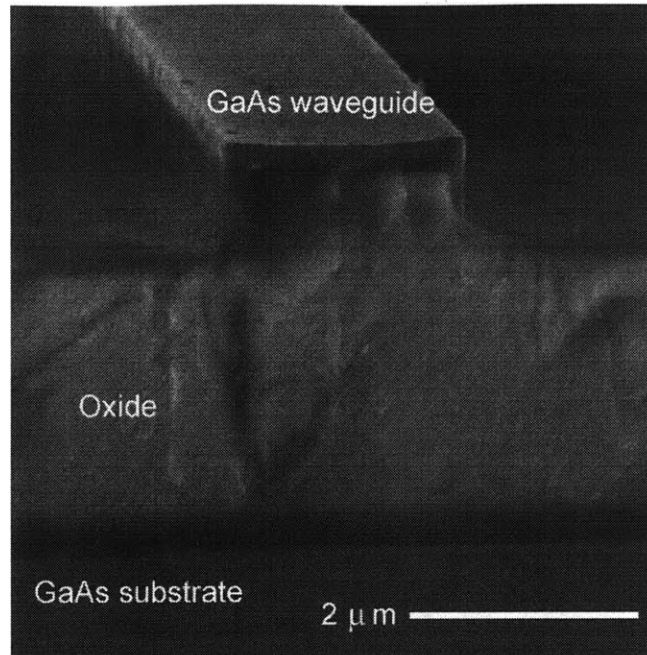
Figure 3-53: Cross-sectional scanning electron micrograph of an input waveguide facet. The $Al_{0.9}Ga_{0.1}As$ layer has been completely oxidized to form a 3µm-thick oxide layer under the GaAs waveguide
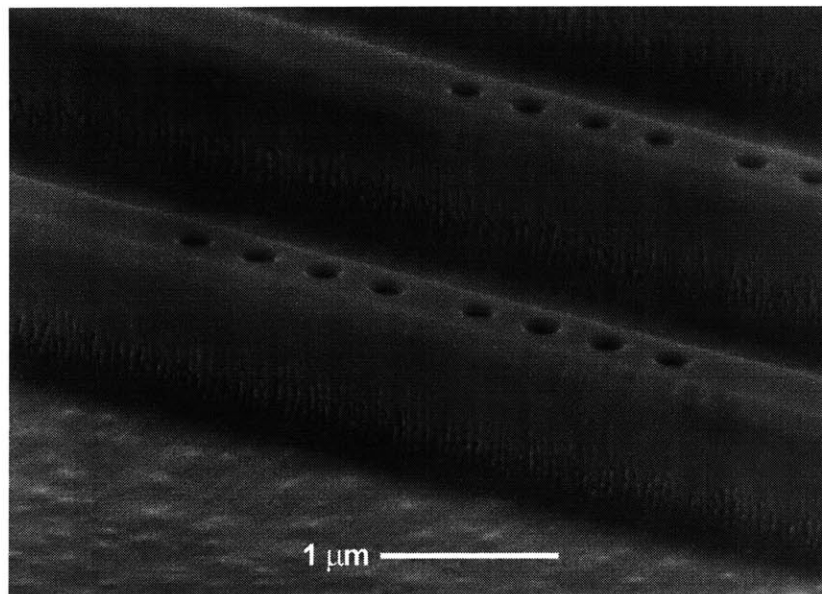
Figure 3-54: Scanning electron micrograph of monorail microcavities designed to operate at the wavelength of 1.55µm. The GaAs monorail structure is 553nm wide and 185nm thick. The holes are 194nm in diameter and are separated by 422nm. The defect region in the center of the array of holes is 590nm wide.
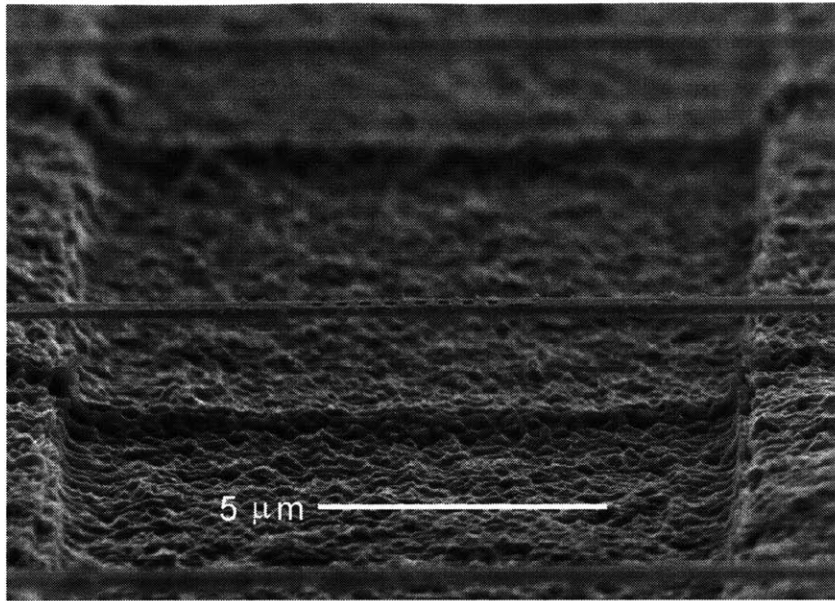
Figure 3-55: Scanning electron micrograph of an air-bridge microcavity designed to operate at the wavelength of 1.55μm. The GaAs air-bridge structure is 525nm-wide and 192nm thick. The holes are 201nm in diameter and separated by 439nm. The defect region in the center of the array of holes is 616nm wide.

3.9   Summary

In this chapter, the fabrication processes for the air-bridge microcavity designed to operate at 4.5μm wavelength regime, and for both the monorail and air-bridge microcavities designed to operate at 1.55μm wavelength regime, have been detailed. In addition, issues pertaining to the fabrication of these devices, particularly those involving electron-beam lithography, reactive ion etching, sacrificial etch and micromechanical considerations, have been covered. Finally, scanning electron micrographs of the microcavity structures provide the ultimate visual evidence of the success of the fabrication processes.

Chapter 4 One-dimensional photonic bandgap microcavity: optical measurements

Optical transmission measurements have been performed on microcavities that have been designed and fabricated to operate at wavelengths of both 4.5μm and 1.55μm. For the 1.55μm devices, in particular, both the monorail and air-bridge microcavities have been optically characterized whereas only the air-bridge configuration has been attempted in the 4.5μm wavelength regime. Attempts at attaining measurement output from the 4.5μm devices have been particularly futile. The subsequent shift to the effort at designing and fabricating the 1.55μm devices has effectively suspended the 4.5μm device effort. Details on the measurement setup proposed and constructed for the 4.5μm devices are documented in Ref. [47].

This chapter focuses on the optical transmission characterization process designed and performed by Daniel Ripin from Prof. Erich Ippen's research group at M.I.T. Optical transmission results of monorail and air-bridge microcavities at 1.55μm wavelength regime will be presented. The difficulties encountered in reproducing functional devices consistently will be addressed with results from ensuing investigations presented.

4.1 Optical measurement setup

A schematic of the optical measurement setup is shown in Figure 4-1. A continuous-wave NaCl:OH⁻ color-center laser with emission wavelengths tunable from approximately 1500nm to 1670nm acts as the source. The tunability in emission wavelength is achieved via the computer-controlled rotation of a birefringent plate within the laser cavity. The maximum output power at the peak of the laser's gain curve is about 250mW. The polarization of the laser output is adjusted by the combination of a polarizing beamsplitter, a quarter-wave and a half-wave plate. A chopper and a lock-in amplifier are used in tandem to enhance the signal-to-noise ratio of the measurement process. The laser beam is then coupled through an optical fiber and into an input waveguide of a device with a fiber lens assembly. Part of the input signal is directed to a photodetector via a fiber-coupler and serves as the input reference signal for relative transmission calculation.
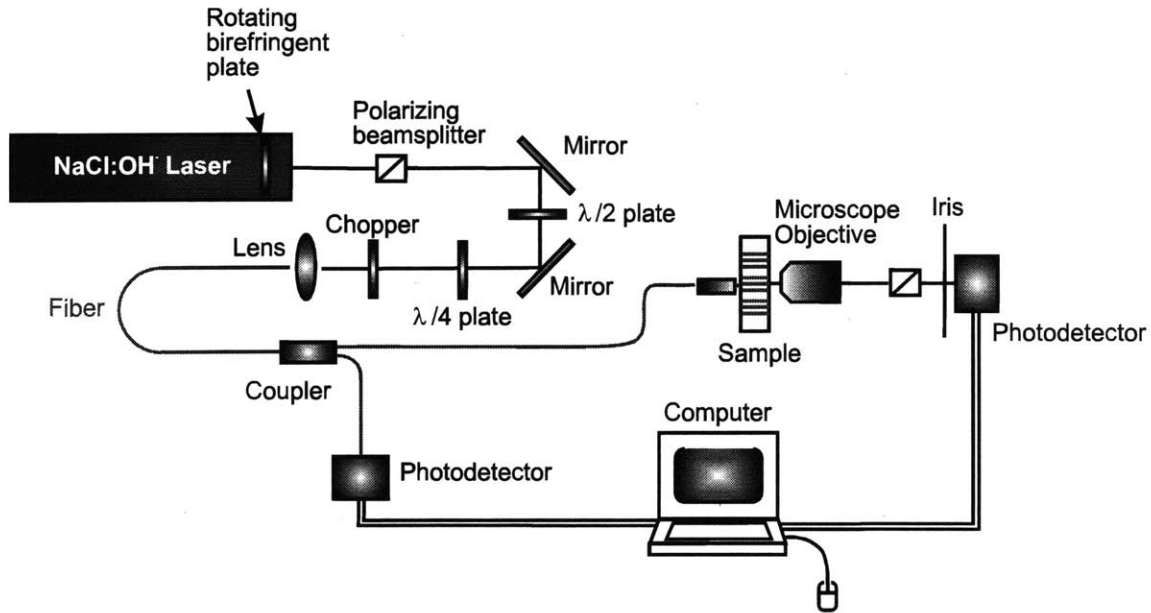
Figure 4-1: Schematic of the optical measurement setup used in the optical transmission characterization of the 1-D PBG microcavities at the wavelength regime of 1.55μm.

A 10× microscope objective collects the light from the output facet and images the output either onto a CCD camera or onto a photodetector through a pinhole. Figure 4-2 shows an image of the relative positions of the fiber-lens assembly, the sample and the microscope objective.

Alignment of the input signal into the input waveguide facets of the devices is first achieved by optimizing the signal transmitted through plain waveguide structures without the 1-D photonic crystals. The alignment process is aided by the imaging of the output facet on a CCD camera, where a bright spot can be seen when light is successfully guided through the device structures. Once a bright spot has been imaged, the photodetector replaces the CCD camera and fine adjustment is made to maximize the signal detected on the lock-in amplifier. A pinhole is used to further minimize the spurious background noise arising primarily from guided substrate light. Once the detected signal has been satisfactorily maximized, the laser emission wavelength is tuned by activating the data acquisition process on a computer. The detected signal is then compared to the input signal at the corresponding wavelengths to provide a plot of the relative transmission through the devices.
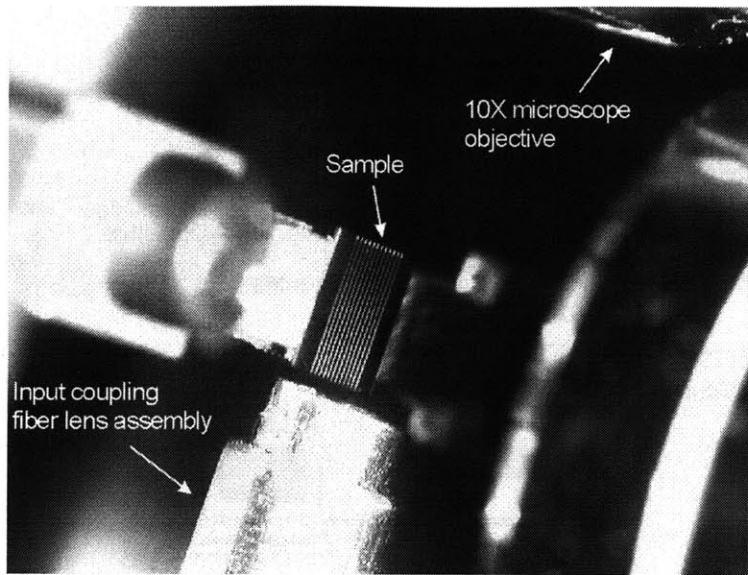
Figure 4-2: Visible-wavelength camera image showing a close-up view of the sample and the surrounding optical components. The bright lines apparent on the sample (tilted at an angle) represent clusters of 1-D PBG microcavity structures; each cluster is about 1.5mm in length and contains up to a total of 6 devices.

Optical characterization of various devices on the sample is then attained by translating the sample with respect to the input beam. As a device is separated from its nearest neighbor by about 20µm or more, the traversal from one device to the next is manifested by the vast change in detected signal on the lock-in amplifier between devices. This scheme allows the effective tracking of the particular device being measured in the process.

4.2 Results

Figure 4-3(a)-(d) shows infra-red camera images demonstrating the coupling of light into the waveguide structures and guiding of light through the waveguide structure. In Figure 4-3(a), the coupling of light into the flared input waveguide is apparent, where considerable scattering is observed at the input facet. As the image is taken from the top view of the sample, the brightness associated with the waveguide structure in the image also indicates considerable scattering within the waveguide structure. Figure 4-3(b) shows the transmission of light through the input waveguide structure up to the 1-D photonic crystal; propagation through the crystal is prohibited as the wavelength of the coupled light is within the photonic bandgap. Figure 4-3(c) shows the output waveguide

147

section of the sample imaged under the infra-red camera, when the wavelength of coupled light is on resonance. A white dashed line on the image indicates the edge of the sample. Figure 4-3(d) shows the cross-sectional view of the output waveguide facet and demonstrates the guiding of light through the entire device structure.

Figure 4-4 and Figure 4-5 show the relative transmission spectra of the monorail and air-bridge microcavities, respectively, within the range of measurement. Note that the wavelength range accessible with the measurement setup is narrower than the width of the 1-D photonic bandgap, and encompasses only the resonance peak and at most one of the band edges. The relative transmission is first obtained by calculating the ratio of the transmitted intensity to the input intensity as a function of wavelength. The peak relative transmission is then normalized as 1.0 when plotting the relative transmission spectrum for each device. The cavity quality factor, Q, of the resonance is defined as $\lambda_{res}/\Delta\lambda$, where λ_{res} is the resonant wavelength and $\Delta\lambda$ is the full-width at half-maximum of the resonance

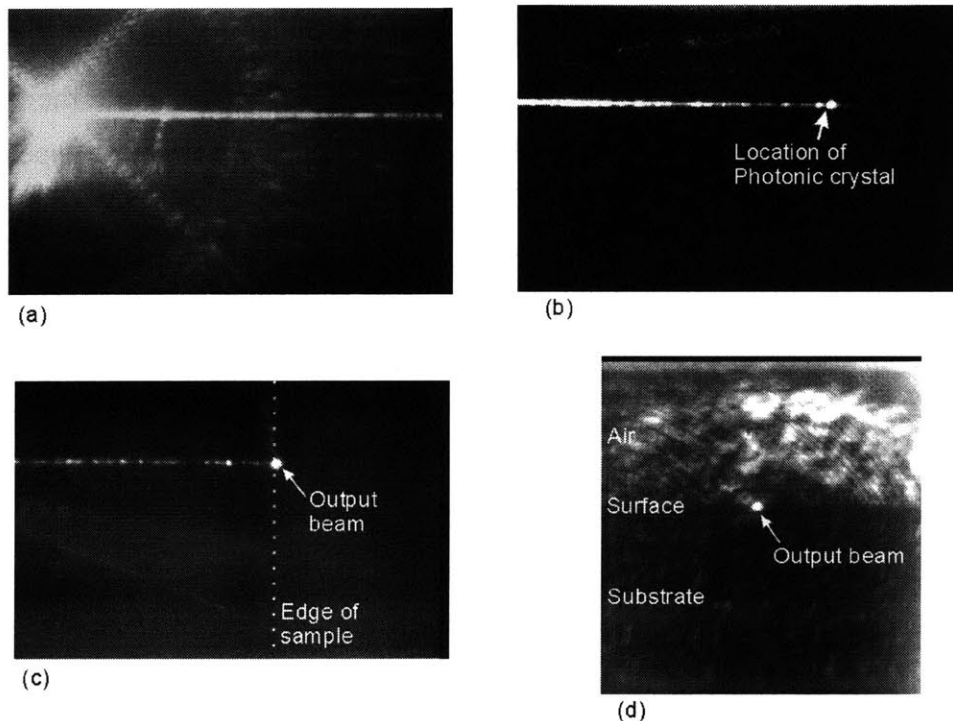Figure 4-3: Infrared camera images of (a) top view of sample at the input waveguide facet; (b) top view of the waveguide structure showing propagation inhibition at the 1-D photonic crystal; (c) top view of the sample at the output waveguide facet, with the dashed line indicating the edge of the sample; and (d) side view of the output facet showing the guided light through the waveguide structure.

peak.

For the monorail microcavities, the resonance peaks are located at 1522nm (Device 1 in Figure 4-4), 1536nm (Device 2) and 1566nm (Device 3), corresponding to 5% increments in defect sizes between devices from Device 1 to 3. An increase in the defect size clearly results in the shift of the resonance peak to a longer wavelength. The resonances have Q's of 136, 142 and 117 respectively. The air-bridge microcavity has a resonance at 1525nm with a higher Q of 230. The long wavelength edge of the photonic bandgap is also visible for this particular air-bridge microcavity. The resonant modal volumes associated with these microcavities are about $0.056\mu m^3$, implying one of the highest Q/V ratio that has ever been measured. This work also represents the first measurement at optical wavelengths of PBG microcavities realized with a direct bandgap semiconductor.

The relevant physical dimensions of the 1-D photonic crystals in the devices exhibiting resonances have been measured using the scanning electron microscope. Based on these physical dimensions and the GaAs film thickness measured using variable-angle spectroscopic ellipsometry, simulations are performed to compare the theoretical transmission spectra to the empirical data. Considerable discrepancies appear to exist between theory and experiment. For the air-bridge microcavity, for instance, the resonance is expected to reside at 1613nm, as compared to 1500nm as measured. The monorail microcavities also show empirical resonances at shorter wavelengths than theoretically predicted. Further, the Q's calculated from the empirically derived spectra are also lower than theoretically expected.

The incongruity between the theoretical and empirical resonance wavelengths may be attributed to the uncertainty in both the exact dimensions of the photonic crystal defect regions and the refractive index of thin-film GaAs. The determination of physical dimensions using the SEM lacks precision due to the lack of a calibrated standard. Furthermore, the SEM images at the high magnification necessary to observe the small feature sizes are lacking in focus, owing to the background mechanical vibrations and electron charging effects on the insulating sample. As such, it becomes difficult to

determine the exact location of the edges of the holes neighboring the defect region. The error in SEM measurement of dimensions is at least 20nm.

At the same time, the refractive index of GaAs used in the simulation has been obtained from the empirical data of bulk GaAs [134]. The exact refractive index of a thin-film GaAs layer grown by GSMBE on an AlGaAs layer is unknown. Further, it is shown in theoretical simulation that the resonance wavelength is highly sensitive to changes in the refractive index of GaAs. A mere 1.5% decrease in the assumed GaAs refractive index (from n_{GaAs}=3.3737 to 3.32), for instance, leads to a theoretical reduction in the resonance wavelength by about 3% (from 1613nm to 1571nm) [135].

The discrepancy between the theoretically determined and empirically calculated cavity Q's is likely due to the imperfections of the holes that form the photonic crystal. In particular, random aberrations inherent in the fabrication process leads to the lack of roundness of the holes and non-uniformity in hole sizes. As the hole sizes and uniformity affects the quality of the resonant mode confinement in the cavity region, a lower Q may result.

Finally, it is worthy to note that the tunability of the resonant wavelength by changing the defect dimensions also reflects the sensitivity of such high index-contrast systems to deviation in device dimensions. Consequently, stringent demand is placed on the nanoscale dimensional control of the fabrication process to achieve predictability in device performance.
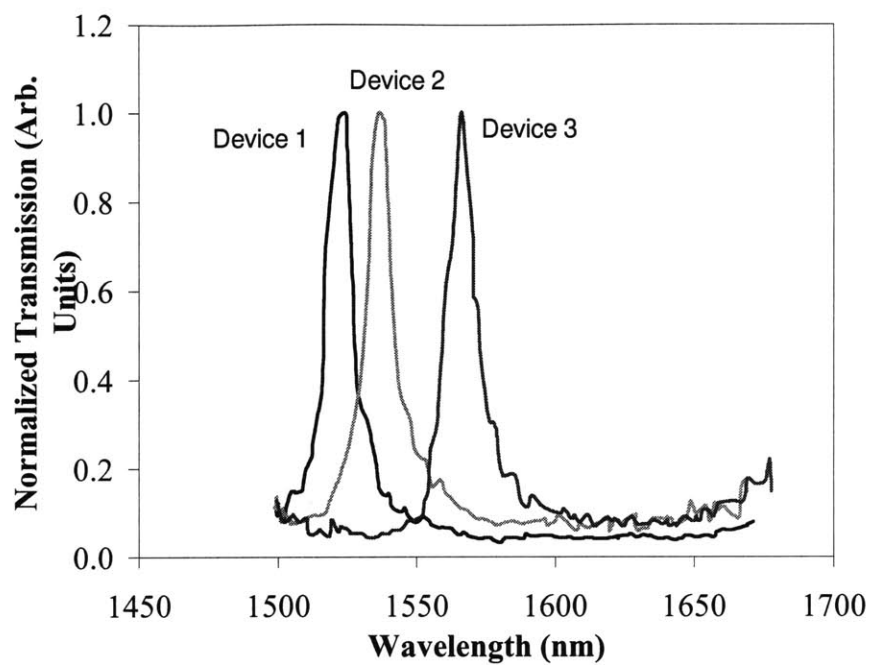
150

Figure 4-4: Relative transmission spectrum of three monorail microcavities. Increasing defect sizes from Device 1 to 3 can be seen to lead to increase in resonant wavelengths.
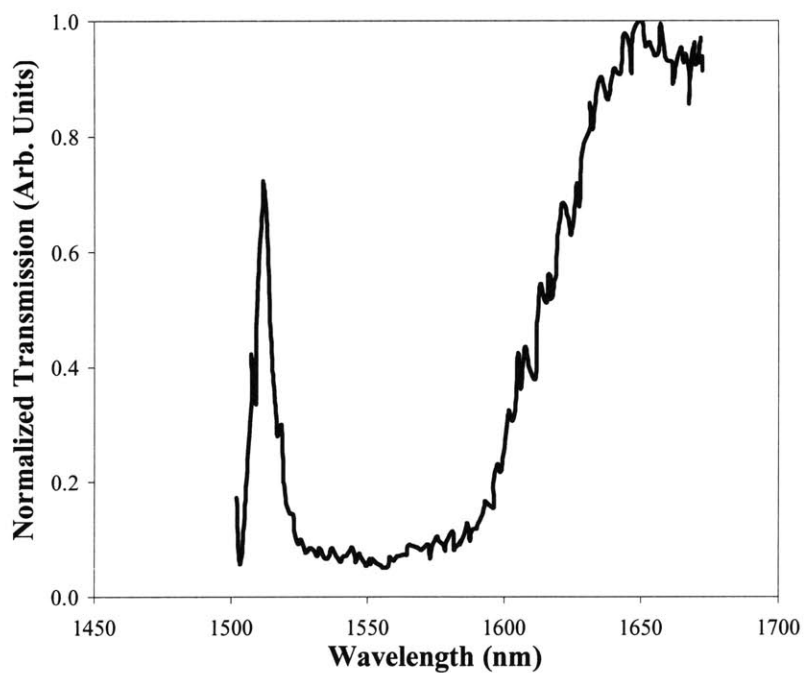

Figure 4-5: Relative transmission spectrum of an air-bridge microcavity. The long wavelength edge of the photonic bandgap is also visible for this particular device.

151

4.3 Difficulty in reproducibility

Following the demonstration of the first operating devices described above, attempts have been made to further characterize the devices through changes in device parameters. The devices fabricated for these attempts, however, exhibit poor transmission characteristics through the waveguide structures. In particular, a significant amount of light is observed to have radiated from the top surface of the waveguide structures during the optical characterization process (Figure 4-6).

Generally, losses in the optical measurement process in the 1-D PBG devices can arise from several sources, including scattering at the facets, roughness of waveguide surfaces and scattering at the waveguide/air-bridge interface. Scattering at the facet is a consequence of the modal mismatch and facet imperfections; the considerable facet coupling loss is apparent in Figure 4-3(a). The slight effective-index difference between the waveguide and the air-bridge structure also leads to scattering loss at the interface due to modal mismatch. The waveguide/air-bridge scattering loss, however, is lessened due to the strongly guided mode that already exists in the waveguide section. The roughness on the sidewalls of the waveguide structure will also contribute to scattering losses, particularly since the strongly guided modes are relatively sensitive to such roughness. The sidewall roughness depends on the quality of the mask used in the reactive ion etch process. In the fabrication process of the 1-D PBG devices, the SiO_2 mask roughness is a function of the granularity of the amorphous layer. The resultant waveguide sidewall roughness from the RIE process is estimated from SEM images to be on the order of 5nm or less, and is expected to cause relatively low scattering losses. Closer examination using the SEM finally reveals considerable roughness at the underside of the GaAs layers (Figure 4-7). The roughness is on the order of 100nm and is highly likely to lead to significant scattering losses.

Several experiments are then performed to investigate the cause of the roughness on the underside of the GaAs layer. First, the roughness is proposed to be: (i) pre-existing at the initial $GaAs-Al_xGa_{1-x}As$ interface; (ii) due to the oxidation process; or (iii) due to the wet sacrificial etch process. Further, the possible factors contributing to the interfacial roughness in any of the above situations are: (i) MBE growth temperature; (ii) Al-

composition of originating $Al_xGa_{1-x}As$ before oxidation; and (iii) initial thickness of originating $Al_xGa_{1-x}As$. To explore the various possibilities, samples drawn from six different MBE-grown wafers are used in the experiments; the salient features of the wafer from each growth are summarized in Table 4-1.

Growth number R620 and R621 correspond to GSMBE of heterostructures used in the fabrication of the air-bridge and monorail microcavity respectively. For the first set of experiments, square samples of $5mm^2$ area are cleaved from the center of wafers from growth number R599, R600, R601 and R603. These samples all contain $Al_xGa_{1-x}As$ layers grown at the low temperature of 480°C. Stripe patterns are then created in each sample by a combination of photolithography and reactive ion etching. The stripe patterns are 25μm in width and are separated by 5μm-wide trenches. The trenches are etched sufficiently deep to expose the $Al_xGa_{1-x}As$ layer in each sample. The samples are then thermally oxidized for the stipulated times in Table 4-1 and dipped in a diluted HF solution for 5s (see Section 3.3 for details of oxidation and wet etch process). The samples are then cleaved and the cross-sectional view of the stripe patterns observed under the scanning electron microscope.
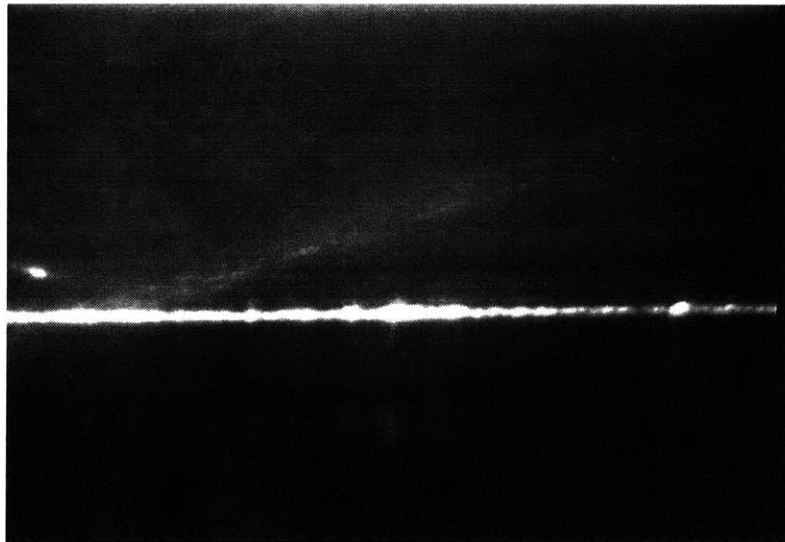
Figure 4-6: Infra-red camera image of the top view of an input waveguide structure during the optical characterization process. The brightness outlining the waveguide structure represents significant scattering loss of light through the top surface of the waveguide structure.

153
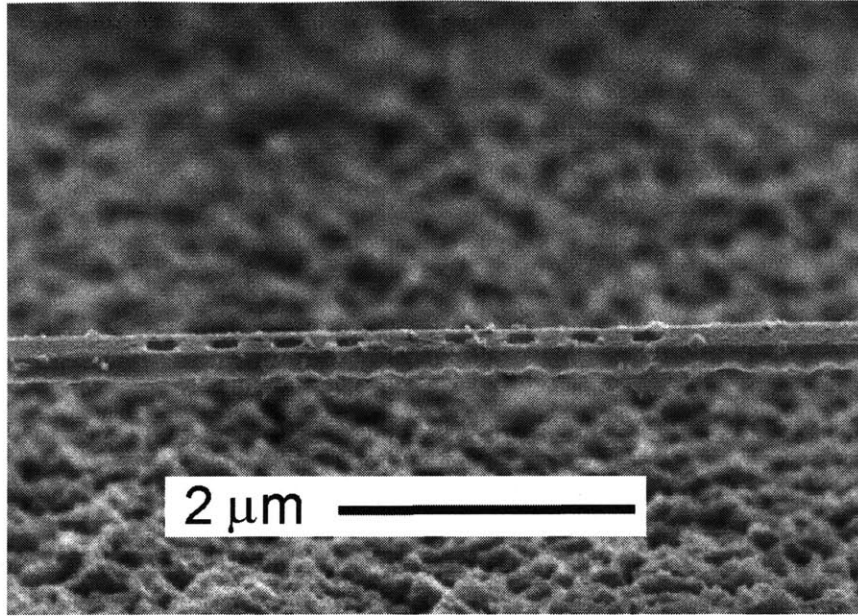
Figure 4-7: Scanning electron micrograph of an air-bridge microcavity structure, focussing on the 1-D photonic crystal. Note the roughness at the bottom surface of the structure.

Growth ID	R599	R600	R601	R603
Heterostructure description	GaAs(115nm) / AlGaAs(250nm)	GaAs(115nm) / AlGaAs(250nm)	GaAs(115nm) / AlGaAs(1000nm)	GaAs(115nm) / AlGaAs(250nm)
Al-composition (%)	97	100	94	97
Growth temp (°C)	480	480	480	480
Oxidation temp. (°C)	435	435	435	435
Oxidation time (min)	30	30	30	30

Table 4-1: Relevant parameters of samples used to investigate GaAs surface roughness. The heterostructure description is given starting from the top layer; for example, R599 has a 115nm-thick GaAs as the cap layer, followed by a layer of 250nm-thick AlGaAs layer on a GaAs substrate.

Growth ID	R620	R621
Heterostructure description	GaAs(192nm) / AlGaAs(3000nm)	GaAs(185nm) / AlGaAs(3000nm)
Al-composition (%)	93	93
Growth temp (°C)	715	715
Oxidation temp. (°C)	435	435
Oxidation time (min)	60	60

Table 4-1- continued.

154

Figure 4-8 show typical cross-sectional scanning electron micrographs of the samples from the above experiment. The GaAs/Al$_x$O$_y$ [Figure 4-8(b)] and GaAs/air [Figure 4-8(c)] interfaces for samples with the 250nm-thick Al$_x$Ga$_{1-x}$As layers are generally smooth. The sample with the 1000nm-thick Al$_x$Ga$_{1-x}$As layer, however, begins to exhibit discernible roughness at the GaAs/Al$_x$O$_y$ interface [Figure 4-8(d)]. These results indicate that the combination of low temperature and thin Al$_x$Ga$_{1-x}$As layers with high Al-composition may still result in smooth GaAs/Al$_x$O$_y$ interfaces. The interface quality deteriorates, however, when the Al$_x$Ga$_{1-x}$As layer thickness becomes increasingly thicker.

The next set of experiments is then performed with samples from growth number R620 and R621. These square samples, 5mm×5mm in area, are obtained either 10mm from the
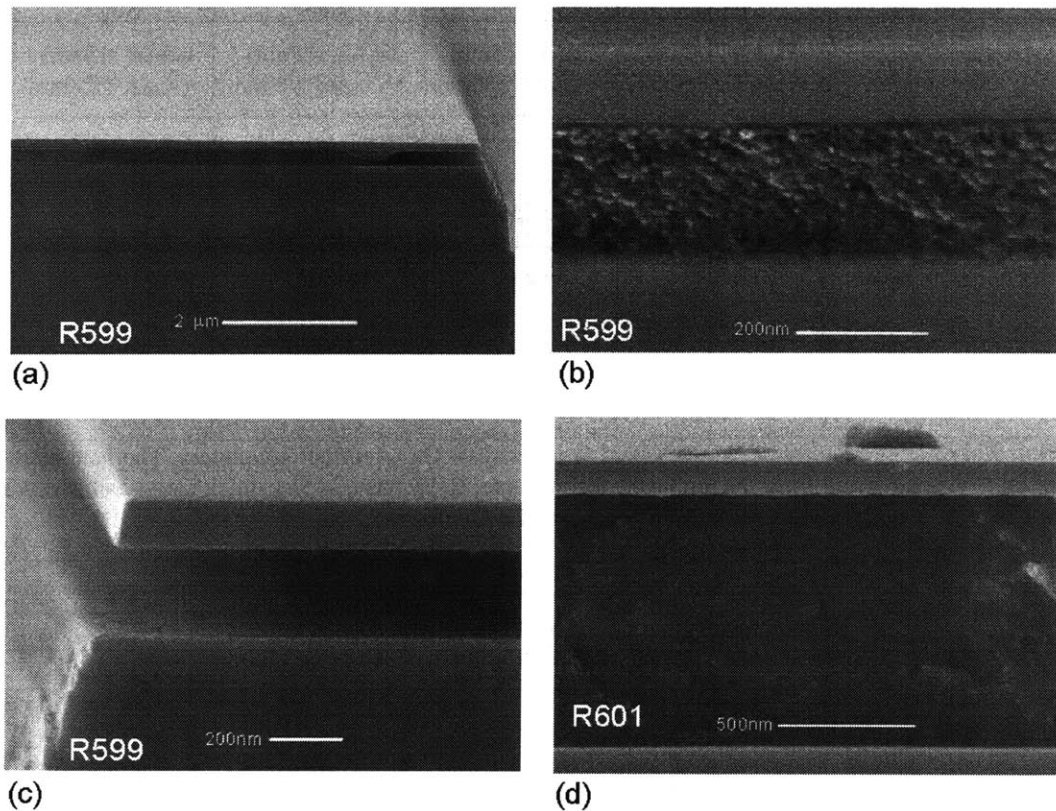
Figure 4-8: Typical cross-sectional scanning electron micrographs of samples with low-temperature grown AlGaAs that have been patterned, oxidized and etched in diluted HF solution, showing: (a) oxidation extent and sacrificial etch extent; (b) typical GaAs/Al$_x$O$_y$ interface from the oxidation of 250nm-thick AlGaAs; (c) typical GaAs surface quality after wet etch; and (d) typical GaAs/Al$_x$O$_y$ interface from the oxidation of 1000nm-thick AlGaAs

center or 5mm from the perimeter of the wafers. The samples are again lithographically patterned and etched as before. The samples taken 10mm from the center are first dipped in diluted HF solution for 2s, followed by thermal oxidation at 435°C for 60mins. The samples taken 5mm from the outer edge of the wafer are further cleaved into two halves: one half is oxidized at 435°C for 60mins only, while the other is dipped in diluted HF solution only. The samples are again cleaved and the cross-section is observed with an SEM.

The outcome from this experiment is particularly revealing. Figure 4-9 shows that both the GaAs/air and GaAs/Al_xO_y interfaces are smooth for the sample from the center of the wafer, despite the 3000nm-thick $Al_xGa_{1-x}As$ layer. Figure 4-10 and Figure 4-11, on the other hand, shows the drastic roughness of both the GaAs/Air and GaAs/Al_xO_y interfaces for the samples that are closer to the perimeter of the wafers.

The conclusions from the above experiments are as follows:

1. A thick $Al_xGa_{1-x}As$ layer grown at low temperature (~480°C) will result in a rough GaAs/$Al_xGa_{1-x}As$ interface.

2. A thick $Al_xGa_{1-x}As$ layer grown at high temperature can result in a smooth interface.

3. The roughness observed, as in Figure 4-7, is due to the pre-existing roughness at the GaAs/$Al_xGa_{1-x}As$ interface, and not due to the thermal oxidation process.

4. There exists a temperature gradient across the wafer during the GSMBE growth in the system described in Chapter 3. The temperature gradient results in a gradation of coloration observed on the post-GSMBE wafer, where an area of about 1-inch in diameter at the center of the 2-inch diameter wafer exhibits a uniform color to the eye. Outside of the 1-inch diameter circular area, the wafer assumes a different color. The 1-inch diameter circular area appears to correspond to the region on the wafer where the GaAs/$Al_xGa_{1-x}As$ interface is acceptably smooth. Outside of the 1-inch diameter circular area, the quality of the GaAs/$Al_xGa_{1-x}As$ interface becomes questionable.

The temperature differential between the center and the perimeter of the wafer is surmised to be as high as 40°C. The drastic differential is likely due to the presence of a molybdenum rim holding the 2-inch diameter wafer in place at its circumference during the GSMBE process. The metal acts as a conduction path for the heat, hence resulting in the lower temperature at the outer region of the wafer.

5. The roughness is a consequence of the combination of the large $Al_xGa_{1-x}As$ layer thickness, the high Al-composition and the intermediate growth temperature of the film. The Al atoms are comparatively less mobile than the Ga atoms during monolayer formation in an MBE growth. At a low temperature, the mobility of the Al atoms are low such that the distribution of the Al atoms at the substrate surface depends on the uniformity of the molecular beam. Roughness of the interfaces grown at the low temperature is not manifested in thinner films but begin to prevail in thicker films, as observed for samples from R599 and R601. At a much higher temperature, the Al atoms are sufficiently mobile that the interface is smooth despite the large thickness of the $Al_xGa_{1-x}As$ layer. At an intermediate temperature, however, the Al atoms are sufficiently mobile to form "islands" but are not mobile enough to become evenly distributed over the substrate. The combination of an intermediate temperature and a thick film lead to the propagation of these irregularities through the entire film, resulting in the roughness observed at the circumference of the wafer (as in Figure 4-10).

The above findings point to the importance of using a high growth temperature during the GSMBE growth of the 2.5μm-thick high Al-composition $Al_xGa_{1-x}As$ layer required for the fabrication process. In addition, only an area in the center of the wafer that is 1-inch in diameter should be deemed as adequate for device fabrication, given the current configuration of the GSMBE system at M.I.T.

157

Figure 4-9: Scanning electron micrograph showing the smooth interface between the GaAs and Al_xO_y material, where the latter is obtained from the thermal oxidation of $Al_{0.9}Ga_{0.1}As$. The initial $GaAs/Al_{0.9}Ga_{0.1}As$ structure has been grown in the monorail microcavity fabrication process. The sample is taken from a $5mm^2$ area about 10mm from the center of the 2-inch diameter wafer. The same phenomenon is observed in the heterostructure grown for the air-bridge microcavity fabrication process.
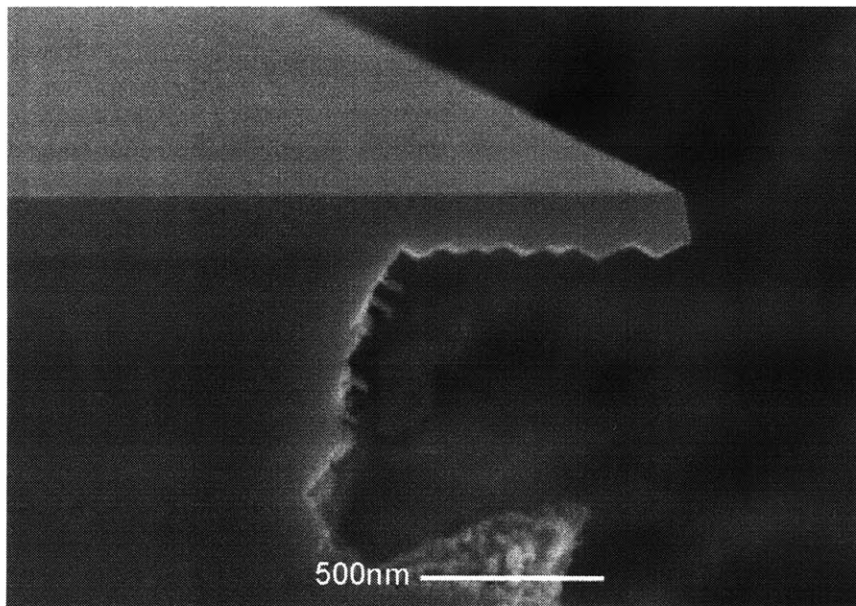
Figure 4-10: Scanning electron micrograph of the GaAs surface after wet sacrificial etch of $Al_{0.9}Ga_{0.1}As$ in the $GaAs/Al_{0.9}Ga_{0.1}As$ heterostructure grown in the air-bridge microcavity fabrication process. The sample has been taken from the outermost $5mm^2$ area along the radius of the 2-inch diameter substrate. The same phenomenon is seen in the heterostructure grown in the monorail microcavity fabrication process.
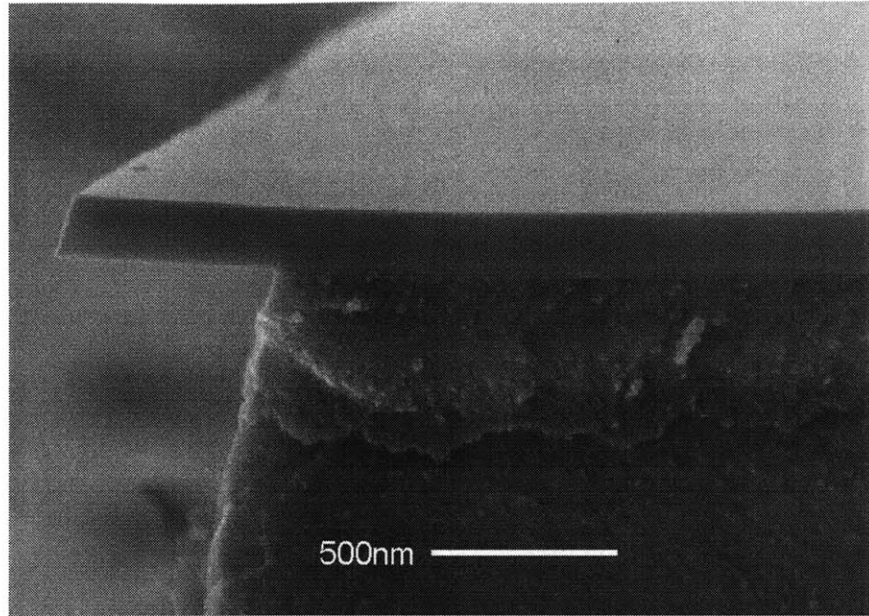
158
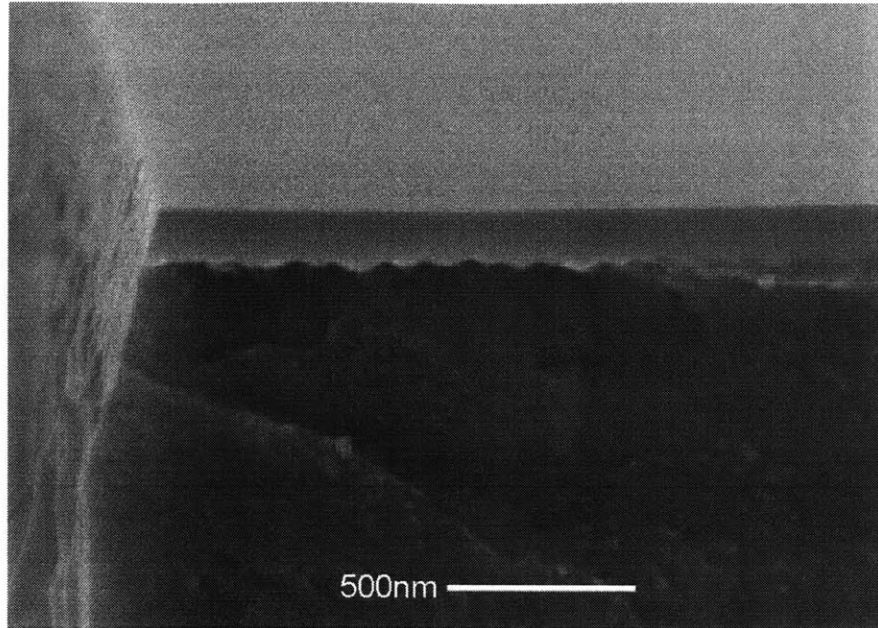
Figure 4-11: Scanning electron micrograph showing the interface between the GaAs and Al_xO_y, where the latter is obtained from the thermal oxidation of $Al_{0.9}Ga_{0.1}As$. The initial $GaAs/Al_{0.9}Ga_{0.1}As$ structure has been grown in the monorail microcavity fabrication process. The sample is taken from the outermost $5mm^2$ area along the radius of the 2-inch diameter wafer. The same phenomenon is observed in the case of the heterostructure grown in the air-bridge microcavity fabrication process.

4.4 Overcoming the problem of reproducibility

The evidence provided in the previous section suggests that the roughness on the underside of the GaAs waveguide layer is: (a) likely due to the GSMBE growth process; and (b) confined to the material outside a 1-inch diameter area in the center of the 2-inch diameter wafer. The pre-existing roughness at the $GaAs/Al_xGa_{1-x}As$ interface has thus led to the roughness observed under the GaAs air-bridge. The $GaAs/Al_xO_y$ interfaces at both the photonic crystal in the monorail microcavity and the coupling waveguides are also expected to exhibit the same roughness. Since the roughness is limited to material from a certain area of the wafer, careful choice of the starting material from the other "good" region of the wafer may thus provide the answer to the problem of reproducibility of operational devices.

To ascertain that the results of the first waveguide microcavities can be reliably reproduced, another sample with the $GaAs/Al_xGa_{1-x}As$ heterostructure for the fabrication

of the air-bridge microcavity is then grown by GSMBE. Using ex-situ variable-angle spectroscopic ellipsometry, it is determined that the $Al_xGa_{1-x}As$ layer has an Al-composition of 94±1% while the GaAs thickness is 185nm. Only material from within a 1-inch diameter area in the center of the wafer is then used in the fabrication of air-bridge microcavity structures designed to operate in the 1.55μm wavelength regime. During the optical characterization process, scattering of light through the top surface of the waveguide structure is observed to be vastly reduced. Further, the optical signal detected at the output facet is also considerably stronger (compared to devices fabricated from material with rough interfaces)[10].

Finally, resonance peaks for the air-bridge microcavities have been successfully detected, as shown in the normalized transmission spectra in Figure 4-12. In the plot, the three resonance peaks correspond to three air-bridge microcavities where the defect sizes in the 1-D photonic crystal are increased by 10% increments from Device 1 to Device 3 (i.e. from 632nm to 702nm to 773nm respectively). The other physical dimensions, common to all three devices, are designed to be as follows: width of 593nm, hole diameter of 230nm and hole separation of 500nm. The resonance peaks exhibit approximately 15dB decrease in transmission from on-resonance to off-resonance conditions, and is limited by the dynamic range of the signal processors in the measurement setup. As seen in Figure 4-12, the resonance peaks are centered at 1521.4nm, 1576.1nm and 1633.1nm for Device 1 to Device 3, respectively. The respective Q's for the devices are approximately 307, 334 and 310. The cause for the relatively higher intensity in the off-resonance wavelength range for Device 3 is still under investigation. In addition, the dimensions for these devices are initially designed to yield transmission spectra showing the shorter wavelength edge of the photonic bandgap within the wavelength range of the measurement process. The appearance of the resonance peaks, instead of the short-wavelength band-edge, is likely a consequence of the uncertainty in the refractive index

---

[10] Observation of the fabricated structures with the scanning electron microscope will not yield clear images without first coating the essentially semi-insulating sample with a thin layer of gold. This would, however, render the optical characterization of the sample impossible. Consequently, no SEM image is offered presently as evidence that roughness is not present at the GaAs/air or GaAs/oxide interfaces. The optical results, nonetheless, provide strong indication of the vast reduction, if not elimination, of the roughness in the devices.

of GaAs used in the design process. The present transmission spectra, together with subsequent determination of actual device feature sizes using the scanning electron microscope, will allow the empirical extraction of the refractive index of GaAs. The data in Figure 4-12 is particularly suitable for this purpose since the refractive index of air in this GaAs air-bridge structure is, by definition, 1. Knowing the refractive index of one of the two materials in the system therefore removes an uncertainty in the empirical data-fitting process.

Overall, the successful fabrication and optical characterization of the air-bridge microcavities above vindicate the initial postulation that the $GaAs/Al_xGa_{1-x}As$ interface roughness is the main reason for the previous inability to reproduce the initial optical results. The reproduction of the optical transmission spectra in the air-bridge microcavity structures in this Section asserts the integrity of the design and fabrication process.

Air-bridge Microcavities
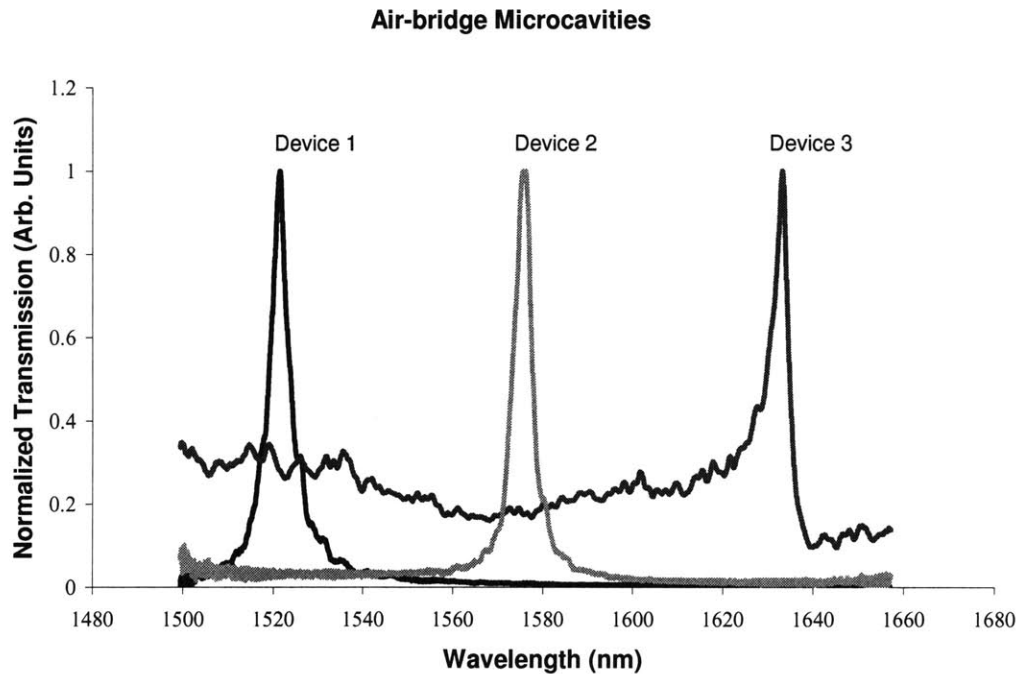
Figure 4-12: Transmission spectra of three air-bridge microcavities, where the defect sizes in the 1-D photonic crystals increase from Device 1 to Device 3 in 10% increments. Other physical dimensions are identical in all three devices.

4.5 Summary

The optical characterization setup and process have first been described in this chapter. Transmission characterization of both the monorail and air-bridge microcavities has been performed, verifying the performance of these devices. The discrepancies between the theoretical transmission spectra and the empirical data are speculated to be a consequence of: (a) the uncertainty in the exact feature sizes of the photonic crystal; (b) the uncertainty in the exact refractive index of thin-film GaAs; and (c) fabrication-related aberrations (such as hole sizes and roundness). The difficulty encountered in the consistent reproduction of the devices using the semiconductor material is attributed to the roughness present at the GaAs/Al$_x$Ga$_{1-x}$As interface on certain regions of the 2-inch diameter wafer. The roughness arises from the temperature gradient across the wafer during the GSMBE process, and results in an area in the center of the wafer of approximately 1-inch in diameter deemed acceptable for device fabrication.

Further fabrication of air-bridge microcavity structures using material from the 1-inch diameter area in the center of another wafer has then resulted in devices with excellent optical performance. The success of the fabrication and optical characterization of these devices confirms that the GaAs/Al$_x$Ga$_{1-x}$As interface roughness has been the primary problem in the inability to reproduce the initial optical data.

Chapter 5 **Two-dimensional photonic bandgap light emitting device**

5.1 Background

The light emitting diode (LED) is an important device that has found commercial applications in sensors, indicators, display devices and optical communications. In display applications, for instance, LED's are prime candidates in the implementation of high-resolution, high-brightness full-color flat panel displays with low power consumption. The success of the GaN-based LED's in achieving bright blue-green emission has further boosted the attractiveness of the LED as a display device. In optical communications, LED's have long served as optical sources for optical fibers.

While LED's are widely deployed today, the drive to improve the efficiency of LED's is relentless. The overall efficiency of an LED consists of two components: the device's internal quantum efficiency and extraction efficiency [136]. The internal quantum efficiency of an LED is defined as the rate of emission of photons divided by the rate of supply of charge carriers. It is strongly dependent on the quality of the material system of the LED, including the electrical contacts used for carrier injection. The ability to grow high quality material through techniques like molecular beam epitaxy, coupled with the use of double heterojunction device structure [137] and novel fabrication methods like epitaxial liftoff [138], has led to LED's with internal quantum efficiencies approaching 60-90%.

The extraction efficiency gives the ratio of the generated photons that actually emerge from the LED into the outside world. The extraction efficiency of an LED is primarily limited by reabsorption in the device's active region, free-carrier absorption in the bulk and total internal reflection at the device/air interface. Various schemes have been proposed and, in some cases, commercially implemented to increase the external extraction efficiency of an LED. Thin active layers, for example, have been used to reduce the reabsorption in the active region [137]. The wafer-bonding of a LED

heterostructure to a transparent substrate followed by the complete etch-removal of the original (absorbing) substrate material has served to reduce the loss due to absorption by the bulk [139]. To widen the escape angle of emitted light from the semiconductor material and hence to reduce loss through total internal reflection, hemispheric caps or domes made of relatively high index material are used [140]. Intentional roughening of the semiconductor surface also serves to increase the probability of the emitted photons radiating into free space [141].

The above schemes to enhance the extraction efficiency of an LED are based mainly either on geometrical considerations or on the reduction of photon absorption. The resonant microcavity LED (RCLED) represents a different approach where the spontaneous emission characteristics of the light-emitting device is modified [142, 143]. The presence of the microcavity increases the probability of photon emission in the directions normal to the semiconductor/air interface. The phenomenon of photon recycling, where photons that have undergone total internal reflection are reabsorbed and re-emitted, also contributes to the increased probability of light escaping from the LED [144]. The side effects of an RCLED, however, include increased directionality and narrower spectral linewidth of light emission. While these traits may be desirable in applications such as optical fiber communication, display devices, for example, require less directionality to allow the widest possible viewing angle.

Recently, Fan et. al. have proposed the use of a two-dimensional photonic crystal to enhance the extraction efficiency of an LED by altering the electromagnetic mode density available to the spontaneous emission in the device [43]. The 2-D photonic crystal suppresses any guided mode within the light emitting semiconductor material. Consequently, the emitted photons can only couple into the radiation modes into free space. Unlike the RCLED, where photon recycling implies an increase in the photon lifetime, the 2-D photonic bandgap (PBG) LED can result in higher response speed.
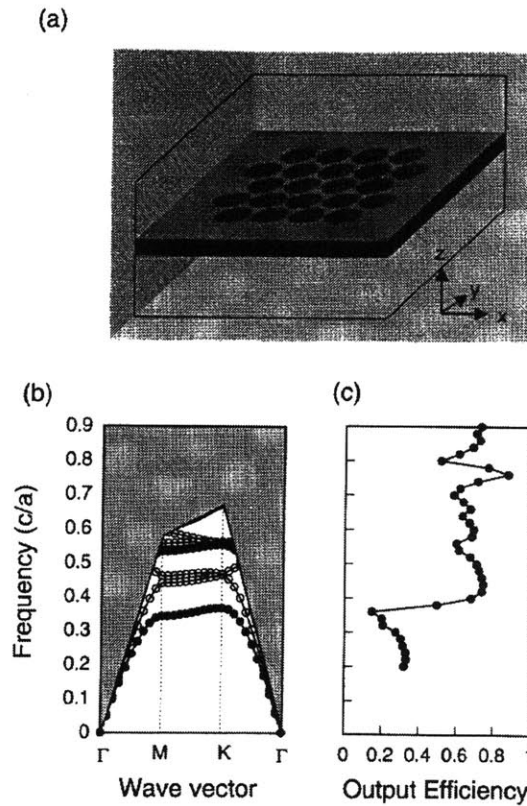
Figure 5-1: (a) Schematic of the computational model used in the simulation. The semiconductor slab has finite extent in the z-direction and a finite number of holes in the photonic lattice. (b) Dispersion relation of the structure in (a), but for an infinite number of holes. The gray area corresponds to the continuum of radiation modes. Filled circles in the plot represent the TE modes while the open circles represent the TM modes. (c) Extraction efficiency as a function of frequency for structure shown in (a). (From Ref. [43])

Figure 5-1 shows the results obtained from the simulation of the expected extraction efficiency associated with a representative LED structure. The simulated device consists of a slab of semiconductor material with an approximately 4×4 array of holes in the slab. An emitting dipole positioned in the middle of the slab couples either into the radiation modes (into free space) or into the guided modes within the semiconductor slab. Figure 5-1(b) shows the photonic band structure associated with such a device. The band structure exhibits a bandgap for the TE polarization with a gap size of about 36%. Figure 5-1(c) depicts the extraction efficiency of the LED as a function of frequency, where the extraction efficiency of the device is defined as the ratio of emitted flux through the top and bottom surface to the total emitted flux from the dipole. For frequencies in the bandgap, the extraction efficiency is about 70%. When the size of the photonic lattice is

165

increased by adding more holes, the extraction efficiency can be expected to approach 100%.

This chapter documents the design and fabrication of a light-emitting device with enhanced extraction efficiency using a 2-D photonic crystal. The light-emitter has been designed to emit at the wavelength of 980nm. Fabrication techniques such as gas source molecular beam epitaxy, direct-write electron beam lithography and reactive ion etching are employed to realize the 2-D PBG LED structure. Finally, a photoluminescent measurement setup has been modified to allow the optical characterization of these devices. The devices will be optically characterized by comparing the photoluminescence of devices with and without the 2-D photonic crystal.

5.2   Device Design

Schematics of the cross-sectional and top views of the 2-D photonic bandgap light-emitting device are shown in Figure 5-2 and Figure 5-3 respectively. The description for

2-D photonic crystal

158nm $In_{0.51}Ga_{0.49}P$
8nm $In_{0.2}Ga_{0.8}As$
32nm $In_{0.51}Ga_{0.49}P$
} Active Region

500nm Al_xO_y spacer layer

6 periods
68nm GaAs/140nm Al_xO_y
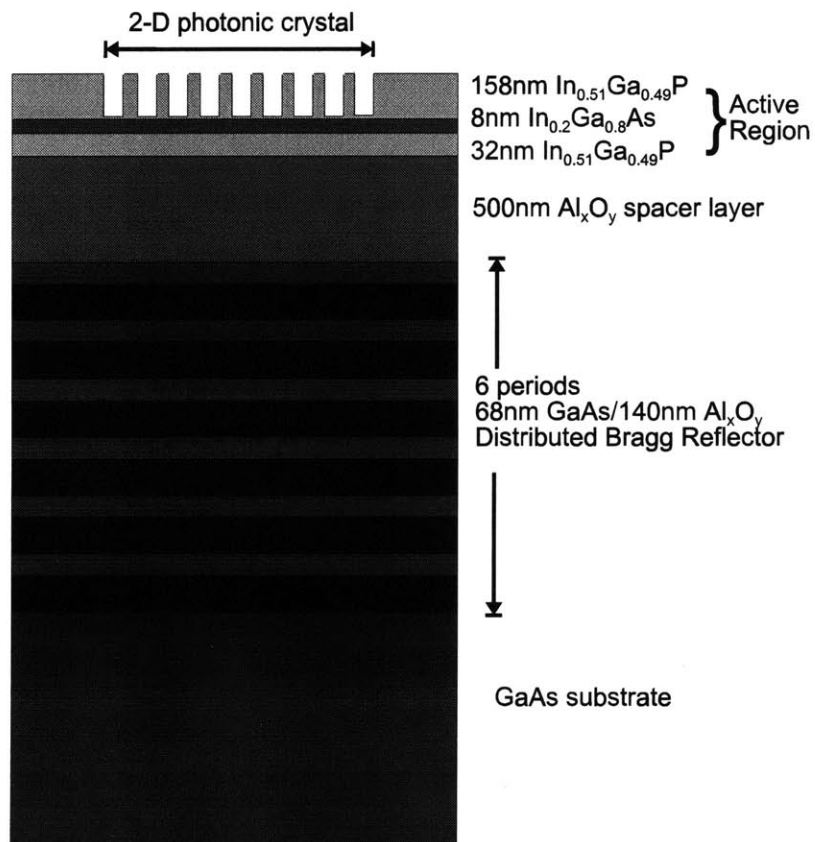Distributed Bragg Reflector

GaAs substrate

Figure 5-2: Schematic of cross-section of a 2-D photonic bandgap light emitting device.

166

the various layers in the structure is as follows:

- *Active region*: The active region consists of an $In_{0.51}Ga_{0.49}P/In_{0.2}Ga_{0.8}As/In_{0.51}Ga_{0.49}P$ quantum well heterostructure designed to emit at the wavelength of 980nm, where the $In_{0.2}Ga_{0.8}As$ quantum well has a thickness of 8nm. The difference in the thicknesses of the top and bottom $In_{0.51}Ga_{0.49}P$ cladding layers is dictated by the design of the photonic crystal (see below).

2-D Photonic Crystal: The 2-D photonic crystal is defined by a triangular lattice of air-holes etched into the top $In_{0.51}Ga_{0.49}P$ cladding layer of the heterostructure. The physical dimensions of the photonic crystal, specifically the hole diameter, the separation between holes and the depth of the holes, are constrained by two considerations. First, the holes can only be etched close to, but not into, the $In_{0.2}Ga_{0.8}As$ quantum well layer to avoid carrier recombination at any exposed surface and to preserve the active region material. Second, the minimum feature size in the photonic crystal is the distance between the edges of the holes. The direct-write electron-beam lithography scheme employed to generate the hole patterns (see Section 5.3) is deemed to be able to consistently resolve minimum hole separation of approximately 100nm.

Based on these constraints, the relevant physical dimensions necessary to create a sufficient photonic bandgap to suppress the guided modes in the LED device structure are: center-to-center distance between holes, a=316nm; hole diameter, D=222nm; and depth of holes, h~158nm. Note that the top cladding layer is consequently thicker than the bottom layer, so as to maximize the effects of the photonic crystal on the photons that will be generated from the quantum well. The bottom cladding layer, in fact, is made as thin as possible to reduce any loss of emitted photons via index-guiding in the layer.

In addition, the photonic crystal is made up of a 63×63 triangular lattice of holes in the semiconductor material, resulting in a total lattice area of approximately 20μm×20μm. The total area of the photonic crystal is chosen such that a focussed laser beam size of approximately 10μm can be easily positioned in the center of the crystal during photoluminescence studies of the devices. For a dipole located in the middle of a 2-D

photonic crystal, any increase in the size of the lattice beyond a 6×6 array of air-holes has shown (theoretically) little incremental suppression of the guided modes [145]. As such, the size of the lattice used in this particular device is expected to be sufficient to produce a discernible effect.

Finally, theoretical simulation [145] has shown that such a photonic crystal will result in a 2-D photonic bandgap in the plane of the device, for TE polarization, ranging from λ=950nm to 992nm. The TE polarization is especially relevant since light emitted from the quantum well structure is expected to be of this particular polarization.

- Al_xO_y *spacer layer*: The Al_xO_y spacer layer is formed by the thermal oxidation of a 500nm-thick $Al_{0.98}Ga_{0.02}As$ layer. The purpose of the low refractive-index oxide layer is to separate the light-emitting quantum-well structure from the higher index DBR structure underneath, since the DBR is not an omni-directional reflector. The oxide spacer layer hence serves to reduce the optical loss into the DBR and GaAs substrate.
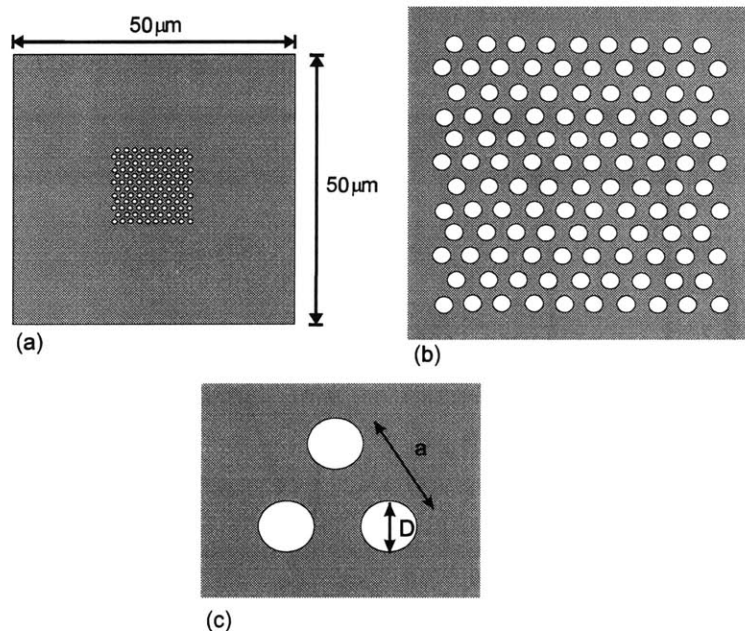

Figure 5-3: Schematics of top view of 2-D PBG LED device. (a) The overall mesa device structure, with the 2-D photonic crystal embedded. (b) Close-up view of the triangular lattice of air-holes forming the 2-D photonic crystal. (c) Physical parameters of the photonic lattice.

- *GaAs/Al$_x$O$_y$ distributed Bragg reflector*: The DBR mirror consists of six pairs of GaAs/Al$_x$O$_y$ layers, where the oxide material is obtained via the thermal oxidation of AlAs. Thicknesses of the different layers are designed to yield a stop-band in the DBR transmission spectrum centered at the emission wavelength of 980nm. The high-index contrast pairs used in the DBR structure leads to a wide stop-band of approximately 1μm. The DBR serves to reflect light propagating toward the substrate from the quantum well toward the top surface, hence increasing the extraction efficiency of the device. As the DBR is effectively a 1-D photonic bandgap structure, only light incident on the DBR within a certain angle cone will be reflected by the mirror.

Figure 5-4 shows the simulated reflectance spectrum of the DBR structure that has been grown by MBE for the 2-D PBG LED device. The layer thicknesses for the GaAs and AlAs layers used in the transfer matrix simulation is determined by X-ray diffraction measurement of the actual MBE-grown structure. Due to variation in layer thicknesses during the growth process, the expected DBR reflectance spectrum is not precisely centered at 980nm. The wide stop-band of the oxidized DBR structure, however, is anticipated to encompass the emission linewidth. Maximum reflectance of the simulated
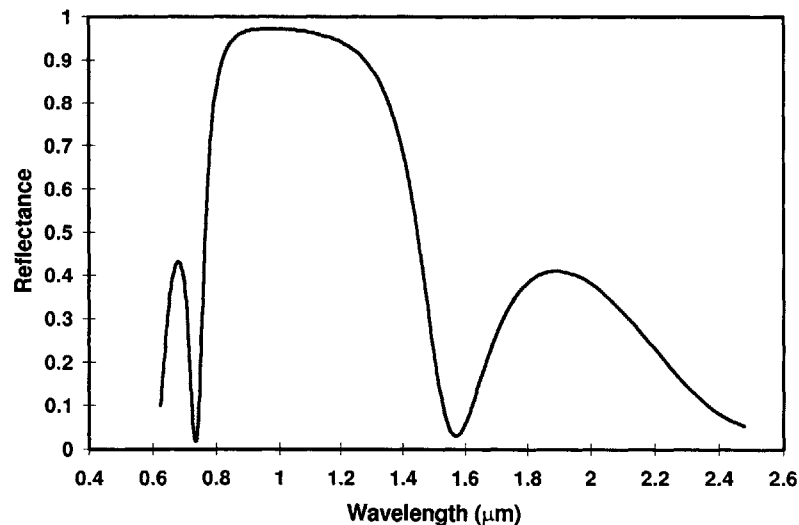

Figure 5-4: Simulated reflectance spectrum of the GaAs/Al$_x$O$_y$ distributed Bragg reflector (DBR) structure used in the 2-D PBG LED structure. The layer thickness of the GaAs and Al$_x$O$_y$ layers are based on values obtained from X-ray diffraction analysis of the actual MBE-grown GaAs/AlAs layers. No shrinkage in the AlAs layer thickness after oxidation is assumed.

spectrum is 97.2% at about 986nm.

The expected extraction efficiency of the entire device structure is also simulated, where an emitting dipole is placed under the photonic crystal and the electromagnetic flux emitted from the top surface of a 2-D PBG LED is computed. The expected flux outflow from the device top surface of the 2-D PBG LED is about 30% of the total electromagnetic flux emitted from the dipole. In comparison, flux outflow from the top surface of an LED without the 2-D photonic crystal is expected to be 5 times smaller [145]. A description of the simulation methodology can be found in Ref. [43].

5.3 Fabrication Process

The fabrication process is illustrated in Figure 5-5. The process begins with the gas-source molecular beam epitaxy of the starting material on a 2-inch diameter epi-ready GaAs wafer, where the various deposited layers deposited are shown in Figure 5-5a. During the GSMBE process, the growth rate for each layer is monitored *in-situ* using reflection high-energy electron diffraction (RHEED) patterns. Double-crystal high resolution X-ray diffraction analysis is conducted *ex-situ* to determine the actual thickness of the various layers. Figure 5-6 shows a plot of the single-axis X-ray diffraction measurement and the simulated theoretical fit to the experimental data. The layer thicknesses are subsequently used in the simulation of the expected reflectance spectrum of the DBR structure (see Section 5.2 above). Photoluminescent studies of the sample are also conducted at room temperature to determine the optical emission characteristics of the structure (Figure 5-7).

The next step in the fabrication process involves the plasma-enhanced chemical vapor deposition of a 50nm-thick layer of SiO_2 (Figure 5-5b). The SiO_2 will subsequently act as the mask during the etching step that transfers the photonic lattice patters into the top cladding layer. Thereafter, a 200nm-thick layer of the e-beam resist, 3% PMMA, is spun coated onto the sample, followed by an hour-long bake in a convection oven set at 180°C. The photonic lattice patterns are then generated in the PMMA layer using direct-write electron-beam lithography. The triangular array of holes, 20μm×20μm in dimensions, is created by using an e-beam with a base dose of 300μC/cm^2, a scan clock frequency of

450kHz and a scan field size of 100μm. Each hole in the array is made up of 10 pixels, where the scan field size is made up of 16384×16384 pixels that are individually addressable by the e-beam machine. The appropriate base dose and clock speed necessary to obtain the desired hole diameter have been pre-determined during a prior dose calibration experiment. Forty-nine sets of photonic lattices, in a 7×7 array, with varying hole sizes and hole separation are generated in the PMMA layer (see Figure 5-5i). The different hole sizes are attained by simply varying the e-beam dose.

After the patterns have been written into the PMMA layer, the e-beam resist is developed in a 2:1 solution of isopropanol and 1,1-methyl pyrrollidinone at 20°C for 90s, followed by a 1-min rinse in isopropanol. The end-result of the development process is the generation of relief structures in the PMMA film corresponding to the photonic lattice patterns (Figure 5-5c). The patterns are then transferred from the PMMA film into the SiO_2 mask layer by reactive ion etching (RIE) using CHF_3 plasma. The RIE parameters are CHF_3 flow rate of 15sccm, process pressure of 10mTorr and incident RF power of 150W. The total etch time of 3mins required to etch through the 50nm-thick SiO_2 is broken up into etch time of 15s in duration separated by 1min intervals. The intervals in the etch process is necessary to prevent the generation of excessive heat from the plasma that may cause the PMMA film to flow. Note also that as the etch selectivity of PMMA versus SiO_2 is about 3:1 in the CHF_3 plasma, the SiO_2 thickness is chosen as 50nm such that the SiO_2 layer may be fully etched without completely depleting the PMMA mask layer. The PMMA layer is subsequently removed with an RIE step using an O_2 plasma of 100sccm gas flow, process pressure of 50mTorr and incident RF power of 50W for 5mins.

The next process step involves the transfer of the photonic lattice patterns from the SiO_2 layer into the top $In_{0.51}Ga_{0.49}As$ cladding layer with RIE (Figure 5-5e). The RIE process parameters are CH_4 gas flow rate of 10sccm, H_2 gas flow rate of 40sccm, process pressure of 20mTorr and incident RF power of 225W. The total etch duration is 4.5mins with an expected etch rate of 21nm/min. The timed etch is intended to stop short of the $In_{0.2}Ga_{0.8}As$ active layer, as explained in the previous section. An O_2 RIE is conducted after the first 3min and at the end of the CH_4/H_2 RIE to eliminate the buildup of polymer

that is inherent in the CH_4/H_2 RIE process. The O_2 RIE process parameters are O_2 flow rate of 100sccm, process pressure of 300mTorr and incident RF power of 230W for 2mins. As the polymer buildup on the sidewalls of the SiO_2 mask layer effectively narrows the diameter of the holes, the RIE removal of the polymer is critical in maintaining fidelity in the pattern transfer process.

After the device patterns have been transferred into the top $In_{0.51}Ga_{0.49}P$ cladding layer, the SiO_2 mask is removed using a CF_4/O_2 RIE process (CF_4 flow rate of 32sccm, O_2 flow rate of 2sccm, process pressure of 45mTorr, incident RF power of 225W for 5mins). A photolithography step is next performed to define a 9×9 array of 50μm×50μm size mesa patterns, as shown in Figure 5-5i. The mesa patterns are aligned on the sample such that the photonic lattice patterns are positioned approximately in the center of the mesas. The 7×7 array of photonic lattices is bordered by mesas that represent devices with no lattices, for the purpose of comparative PL study during the optical characterization stage. Each mesa is separated by a distance of 50μm from its nearest neighboring mesa pattern.

The photolithography process (Figure 5-5f) first entails the spin coating of about 2.5μm-thick Shipley 1827 photoresist on the sample at 4000rpm for 30s. After a soft bake of the sample at 90°C for 30mins, the sample is exposed to UV-radiation from a Karl-Suss aligner with the existing photonic lattice patterns aligned to the mesa patterns on a quartz mask. The sample is then subsequently developed in Shipley MF319 photoresist developer for 60s and rinsed in deionized water for 60s. An inspection of the sample under a Nomarksi microscope followed by a hard bake of 30mins at 130°C concludes the photolithography process.

After the mesa patterns have been lithographically defined, the patterns are transferred through all the epitaxially grown layers by a series of RIE process steps (Figure 5-5g). A 12min-long CH_4/H_2 RIE process, with parameters identical to those described above, first etches through the $In_{0.51}Ga_{0.49}P/In_{0.2}Ga_{0.8}As/In_{0.51}Ga_{0.49}P$ quantum well layers. Unlike the previously CH_4/H_2 RIE process described, however, the O_2 RIE step for polymer removal is bypassed since the photoresist mask will otherwise be etched away by the O_2 plasma.

172

Further, the effect on device dimensions of the polymer accumulation is likely to be marginal for the large mesa features.

Following the CH_4/H_2 RIE, an RIE process using $BCl_3/SiCl_4$ gas mixture is next employed to etch through the $Al_{0.98}Ga_{0.02}As$ and the GaAs/AlAs DBR layers. The RIE process parameters are BCl_3 flow rate of 30sccm, $SiCl_4$ flow rate of 20sccm, process pressure of 30mTorr and incident RF power of 250W. As mentioned in Chapter 3, the RIE process is performed with the sample placed on an alumina plate covering the electrode of the RIE system. The RIE process lasts for 20mins and the Shipley 1827 photoresist mask is sufficiently thick to withstand the etch. At the end of the RIE process, the photoresist is removed by rinsing the sample first in acetone for 1min followed by isopropanol for 1min. A 10-min O_2 RIE then serves to remove any residual resist that remains on the sample (O_2 flow rate of 99sccm, process pressure of 100mTorr, incident RF power of 100W).

The final step in the fabrication process involves the thermal oxidation of the high Al-composition AlGaAs layers in the device (Figure 5-5h). Details of the oxidation process have been provided in Chapter 3. The sample is oxidized at the temperature of 435°C for 45mins with N_2 flow rate of about $2l/min$ and water temperature maintained around 90°C. The oxidation process completely oxidizes the AlGaAs layers in the 50μm×50μm size mesas, and concludes the entire fabrication process for the 2-D PBG LED devices. Figure 5-5j shows a schematic of an angled view of the mesa structures, both with and without the presence of the 2-D photonic lattice.

The results of the fabrication process are shown in Figure 5-8 to Figure 5-12. A top-view Nomarski optical micrograph of a single 2-D PBG LED device is shown in Figure 5-8, where the 2-D photonic lattice is visible as a patch of dense patterns located approximately in the center of the 50μm×50μm mesa structure. An angled view of the 9×9 array of mesas under the SEM is shown in Figure 5-9. Note that the mesas forming the border of the array are structures without the 2-D photonic lattice incorporated. These "plain" devices allow the comparison of the photoluminescent characteristics of devices with and without the effects of the 2-D photonic lattice. Figure 5-10(a) shows a scanning

electron micrograph of a mesa structure when viewed at an angle. The lower panel [Figure 5-10(b)] gives a magnified view of the area within the rectangular inset in Figure 5-10(a), demonstrating the triangular lattice of holes forming the 2-D photonic lattice. Figure 5-11 shows a closer view of Figure 5-10(b) and demonstrates the anisotropic etch through the top $In_{0.51}Ga_{0.49}P$ layer that defines the vertical extent of the photonic crystal. Finally, Figure 5-12 presents the top-view scanning electron micrograph of one of the devices with physical dimensions close to the intended design value. Note that both the hole diameter and the separation between holes have been varied across the array of mesas, as mentioned previously.

a. Gas source molecular beam epitaxy of starting material

$In_{0.51}Ga_{0.49}P$
$In_{0.2}Ga_{0.8}As$
$In_{0.51}Ga_{0.49}P$

$Al_{0.98}Ga_{0.02}As$

6 pairs GaAs/AlAs DBR

GaAs Substrate

d. Reactive ion etch (RIE) of SiO_2 layer, followed by PMMA removal

b. Plasma-enhanced chemical vapor deposition of SiO_2

SiO_2

e. RIE of top $In_{0.51}Ga_{0.49}P$ cladding layer

c. Generation of photonic lattice patterns in PMMA with direct-write electron-beam lithography

PMMA

f. RIE etch of SiO2; Photolithography to define mesa pattern
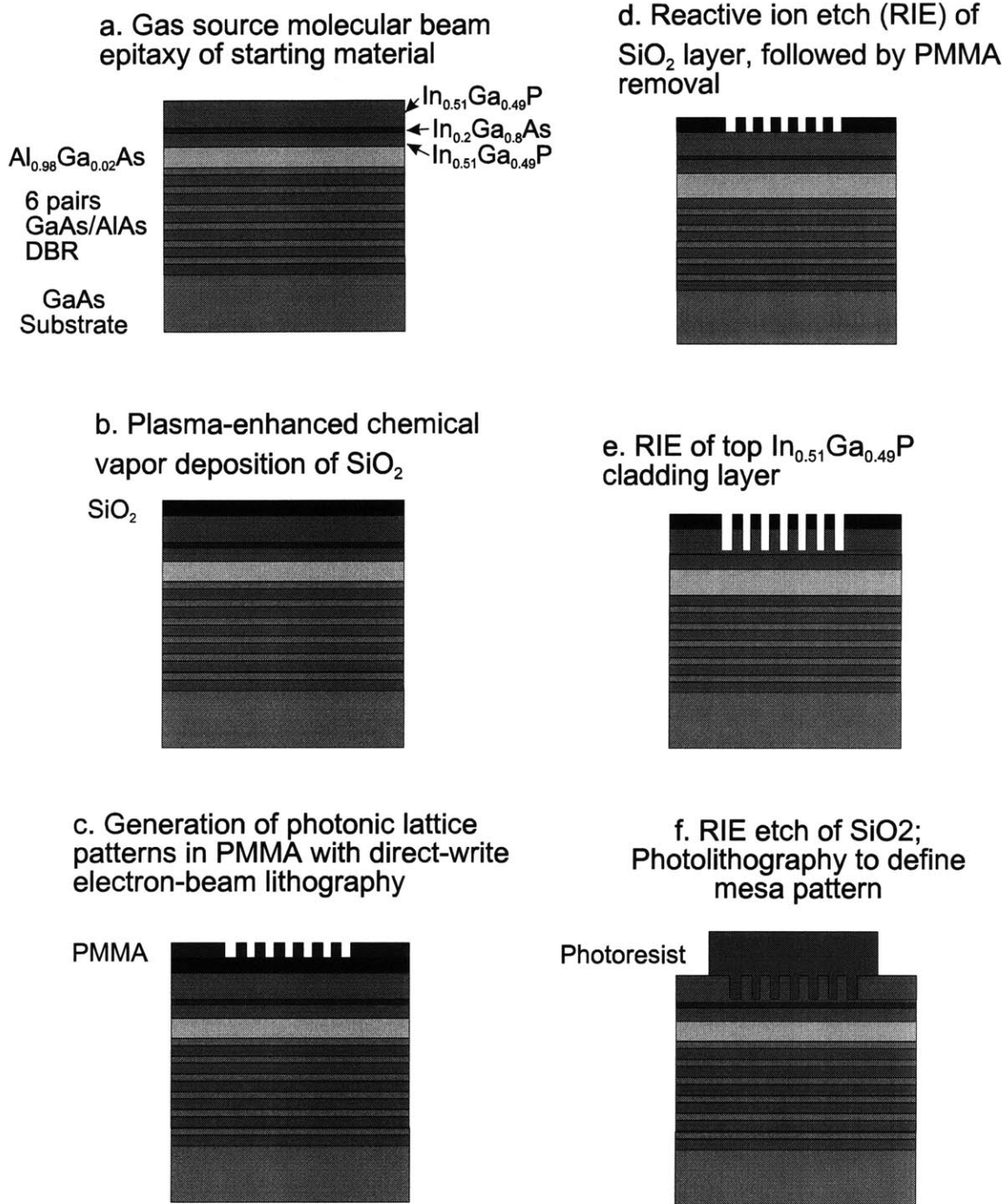
Photoresist

Figure 5-5: Schematics of fabrication process for the 2-D PBG LED devices depicting cross-sectional views of the structure. (Continued next page)

175

g. RIE of active region, spacer layer and DBR layers to create mesa structure

i. Overall layout of mesa structures

Increase in hole size

Increase in hole separation

With photonic lattice

Without photonic lattice

h. Removal of photoresist; thermal oxidation of $Al_xGa_{1-x}As$ layers

Al_xO_y

6x GaAs/Al_xO_y DBR

j. Schematic of final devices
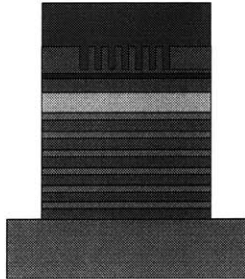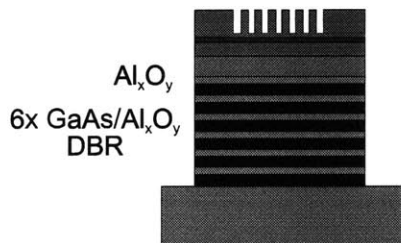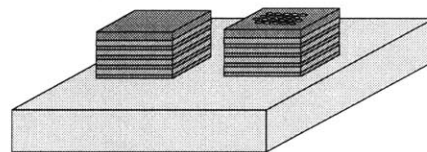
Figure 5-5: Schematics of fabrication process for the 2-D PBG LED devices depicting cross-sectional views of the structure.

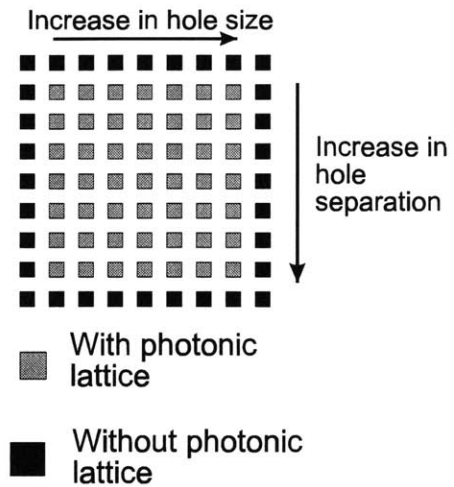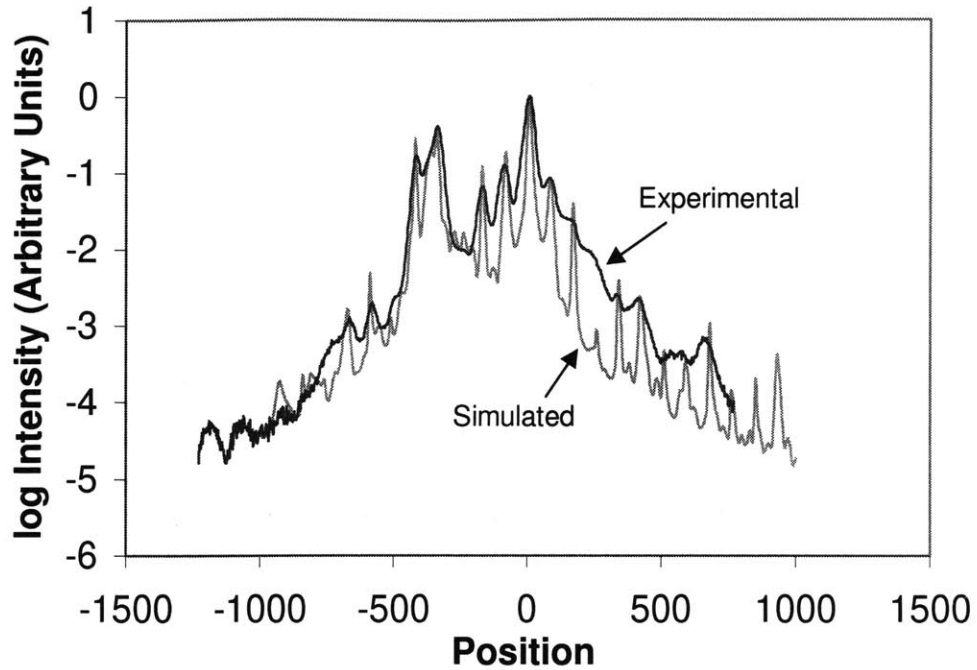Figure 5-6: Double-crystal high-resolution X-ray diffraction measurement of GSMBE-grown sample for the 2-D PBG LED structure. A theoretical plot is fitted to the experimental data where the thicknesses of the constituent layers in the heterostructure are hence determined. The theoretical fit is performed with a simulation program from Bede Scientific Corporation. The empirical data and theoretical fit are obtained by Dr. G.S. Petrich at M.I.T. (Courtesy of Dr. G.S Petrich).
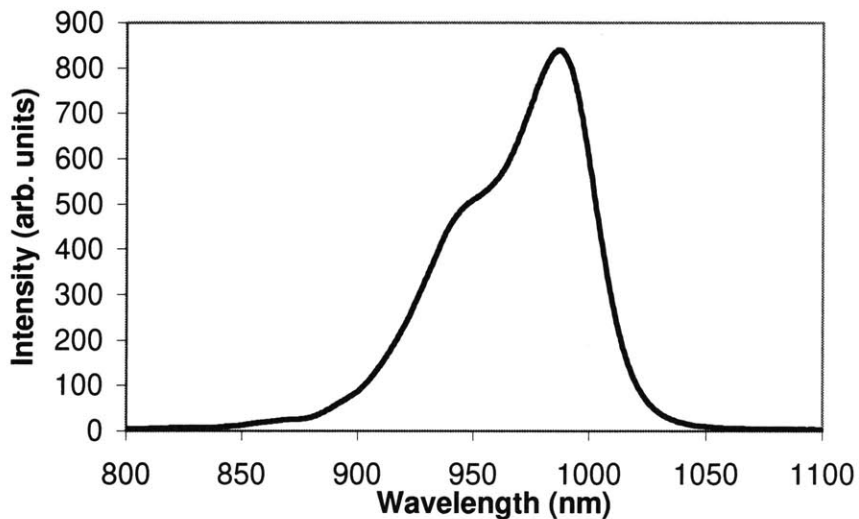
Figure 5-7: Photoluminescence (PL) spectrum of sample grown for the fabrication of the 2-D PBG LED. The PL is conducted at room temperature and demonstrates the emission at approximately 980nm of the quantum well structure.

177
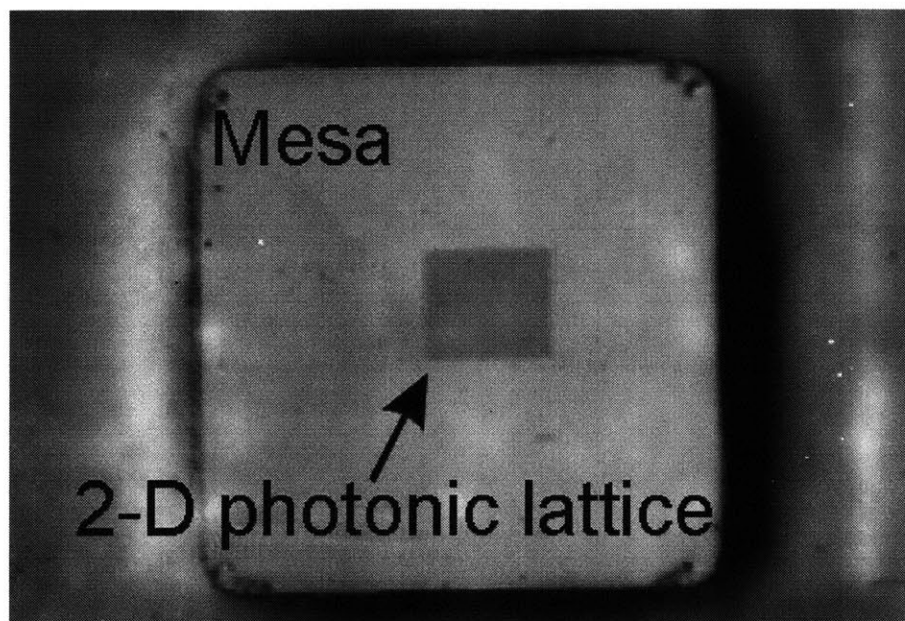
Figure 5-8: Top view Nomarksi micrograph of a single 2-D PBG LED device. The mesa is 50μm×50μm in dimensions, with the 2-D photonic lattice located approximately in the center of the mesa. Under the low magnification available on the optical microscope, the 2-D photonic lattice appears as a patch of dense patterns.
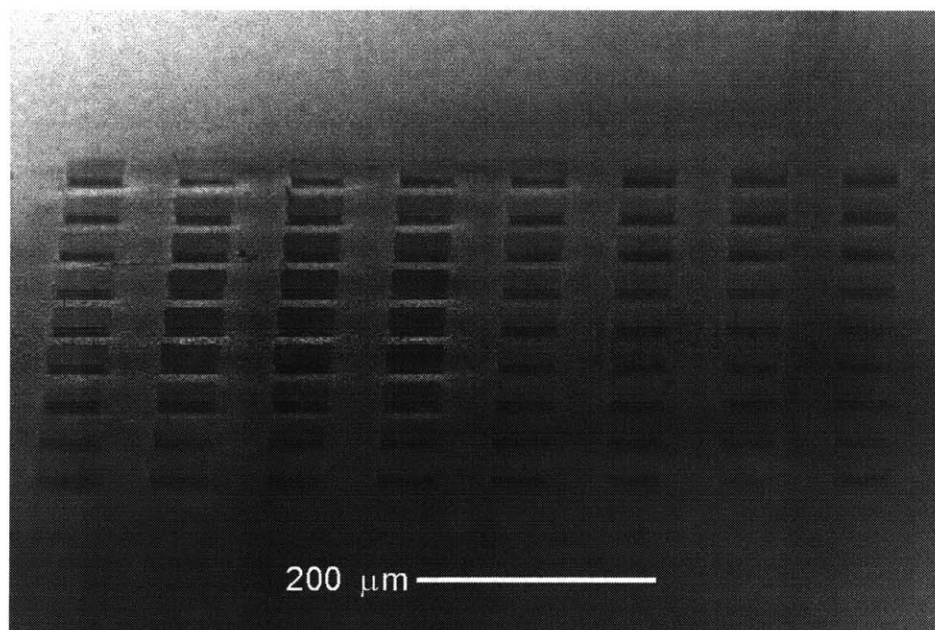
Figure 5-9: Scanning electron micrograph of an angled view of the 9×9 array of 2-D PBG LED mesa structures (one column is hidden from view). The outermost mesas bordering the array are mesa structures without the presence of the 2-D photonic lattice, and are used for comparative photoluminescence studies.
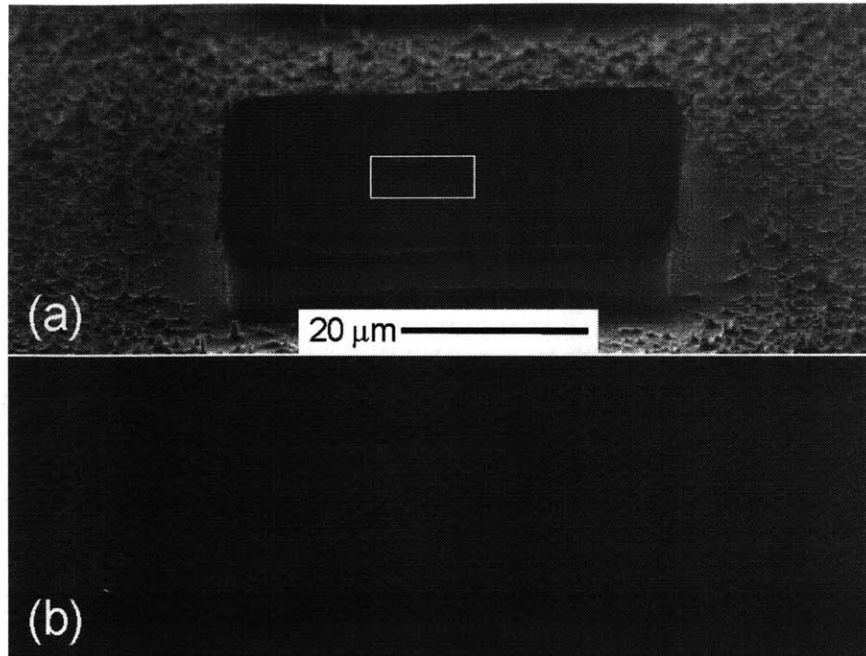
Figure 5-10: Scanning electron micrograph of (a) an angled view of 2-D PBG LED device; and (b) higher magnification view of area defined by inset rectangle in the upper panel.
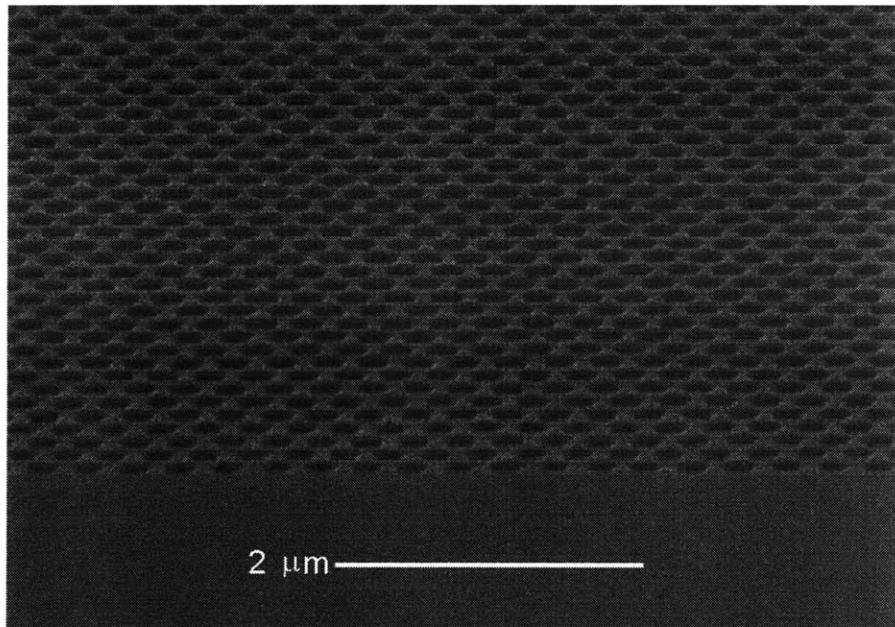
Figure 5-11: Scanning electron micrograph of an angled view of the 2-D photonic lattice, showing the boundary of the lattice.
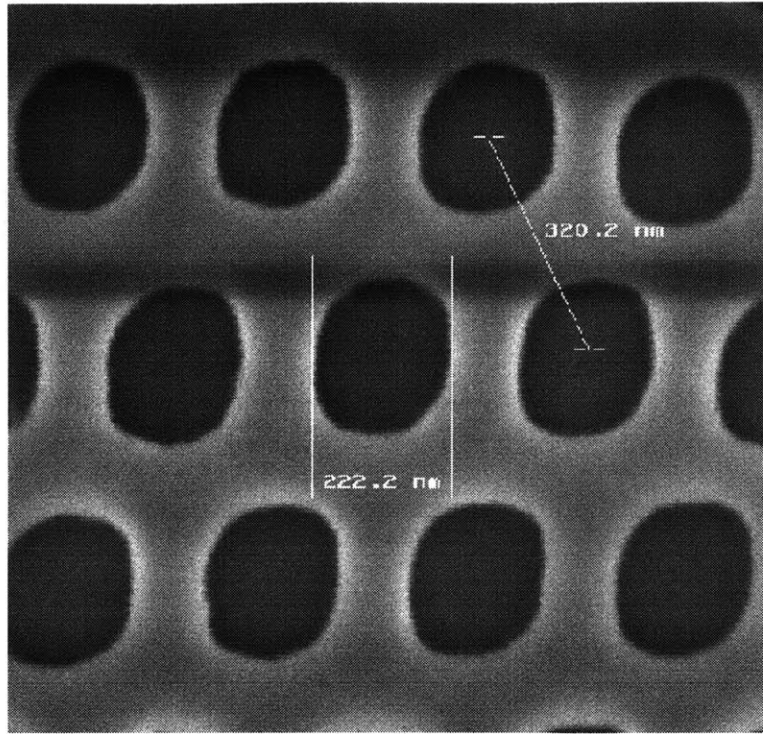
Figure 5-12: Top-view scanning electron micrograph showing the holes in the 2-D photonic lattice and the relevant physical dimensions as measured on the scanning electron microscope.

5.4   Optical Characterization

The goal of the research effort is to demonstrate the effect of a 2-D photonic lattice on the extraction efficiency of an LED structure. To this end, devices have been fabricated to allow the comparison of photoluminescence intensity between a 2-D PBG LED and one without the presence of the 2-D photonic lattice. An existing photoluminescence measurement setup has thus been modified to implement the spatially resolved photoluminescence characterization of the LED's that have been fabricated (as described in the previous section).

Figure 5-13 shows a schematic of the photoluminescent setup constructed for the optical characterization of the LED's. An argon ion laser emitting at the wavelength of 514.5nm provides the photoexcitation source. The laser beam is routed through a chopper that
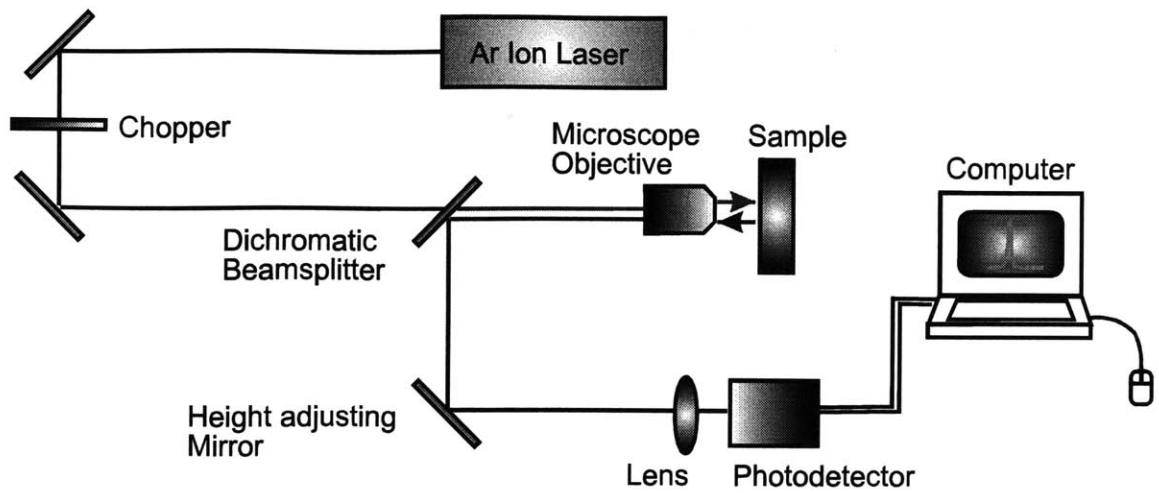
Figure 5-13: Schematic of the photoluminescence measurement setup to be used in the optical characterization of the 2-D PBG LED devices.

serves to improve the signal-to-noise ratio of the measurement, and via a dichromatic beamsplitter. The beamsplitter transmits light with wavelengths shorter than approximately 750nm while reflecting light with longer wavelengths. The beamsplitter hence allows the transmission of the laser beam through the beamsplitter to the sample, while reflecting the 980nm-wavelength light emitted from the LED's toward the detector. A microscope objective is then used to focus the beam down to the desired beam size. The sample is mounted on an X-Y-Z stage that allows the movement of the sample such that different devices in the array can be characterized. The relatively large dimensions of the mesa structures allow the coarse alignment of the devices with respect to the laser beam. The 50μm-wide gaps between mesas serve as indicators of movement between devices during the measurement process.

The light emitted by the devices is then routed via the dichromatic beamsplitter and a height-adjusting mirror set into a spectrometer and onto a silicon photodetector. The detected signal is subsequently amplified and analyzed on a computer.

5.5 Summary

Light emitting devices with enhanced extraction efficiency by the use of a 2-D photonic crystal have been designed and fabricated. The devices are designed to emit at the wavelength of 980nm and include other practical design refinements to optimize the light emitted through the top surface of the LED. These design refinements take into account the consequences of surface recombination at the exposed active layer surfaces, as well as improved light extraction with a distributed Bragg reflector structure. The devices have been successfully fabricated using techniques of gas source molecular beam epitaxy, direct-write electron-beam lithography, reactive ion etching and thermal oxidation of high Al-composition AlGaAs semiconductors. Optical characterization is underway on a modified photoluminescence measurement setup.

5.6 Author's note

Special mention is reserved for Alexei Erchak, a fellow graduate student and a coworker, for his instrumental role in the work described in this chapter. Much of the planning, design and execution of the effort in this project has been conducted in tandem with Mr Erchak. Mr Erchak, in particular, has been responsible for the success of the fabrication process. The author expresses immense gratitude for his effort.

Chapter 6 **Conclusion & future directions**

6.1   Conclusion

The concept of the photonic crystal has drawn widespread interest since its introduction. The successful implementation of a three-dimensional photonic crystal at the optical wavelength regime will not only be a technological feat, but will also have far-reaching implications in its potential applications. At a time when the photon is assuming an increasingly prominent role in the technological advancement of humankind, photonic bandgap (PBG) device research will serve to perpetuate the drive toward a world where photonics is as commonplace as electronics. In fact, it is almost imperative that photonic bandgap devices be successfully implemented in the optical wavelength regimes, for the concept of the photonic crystal to have reached its much touted potential.

The realization of a 3-D photonic crystal in optical wavelength regimes, however, is a non-trivial endeavor. The conditions for the creation of a complete bandgap in a high index-contrast system dictate that the photonic crystal be of *nanometer lengthscale* and of considerable *geometrical complexity*. None of the commercial microelectronic fabrication facilities available today will be able to produce such a photonic crystal in any volume. The nanofabrication of a 3-D photonic crystal therefore remains an effort confined to the research laboratories today. Fortunately, the relentless drive toward ever smaller and denser ultra-large scale integrated (ULSI) circuits will help to create the infrastructure and technology required for the commercial viability of the photonic crystal in the future. It is conceivable that the photonic crystal may ride on the coat tails of the ULSI efforts to its own prominence.

In the near term, the one-dimensional and two-dimensional manifestations of the photonic crystal are not only attainable, but will also serve to support the theoretical underpinning of photonic bandgap device research. The spawning of interesting and potentially beneficial optical devices using 1-D and 2-D photonic crystals will also

demonstrate the prowess of the concept of the photonic crystal. Equally important is the interest that successes with these devices will generate, hence vindicating the efforts that have already been invested, and justifying that to be further devoted.

In this thesis, both 1-D and 2-D PBG devices have been successfully designed and fabricated. The 1-D PBG devices, in particular, have been optically characterized and demonstrated to operate in the 1.55µm optical communication wavelength regime. The behavior of the 1-D PBG devices is shown to generally correspond to that predicted in theory. The 2-D PBG devices are still being optically characterized at the time of the writing of this document, and results are soon to be expected.

The fabrication of both the 1-D and 2-D PBG devices has formed the focal point of this thesis. The fabrication of the 1-D PBG microcavities have entailed the use of advanced techniques such as gas-source molecular beam epitaxy, direct-write electron beam lithography and reactive ion etching. Furthermore, the 1-D PBG air-bridge microcavity fabrication process has involved micromechanical issues that are rarely present in other photonic devices. The confluence of optical and micromechanical, and eventually electronic, concepts on a single device presents an exciting opportunity for the research community. Specifically, researchers may increasingly bring to bear various capabilities available to the fabrication engineer on the design of innovative devices.

The design of both the 1-D and 2-D devices in the optical wavelength regimes has resulted in device dimensions of nanometer length-scale. The realization of such feature sizes has required the use of high-resolution lithographic techniques, such as the direct-write electron beam lithographic (EBL) technique employed in this thesis. For device fabrication at a larger scale, however, a pattern generation process with higher throughput will clearly be necessary. In the case of the waveguide microcavities, a combination of optical lithography to generate the waveguide patterns and direct-write EBL to create the hole patterns within the waveguides is certainly a viable approach. The price of such an approach is increased process complexity, with higher throughput and lower lithography-related costs the potential payoffs.

Besides the ability to generate nanometer feature sizes, the uniformity of feature shapes and sizes across devices is also especially salient. For high refractive index-contrast systems inherent to photonic bandgap devices, in particular, device performance is highly sensitive to feature uniformity. As this thesis has demonstrated, the resonant wavelengths of the waveguide microcavities shift with varying defect sizes in the photonic crystals. Consequently, consistent reproduction of features from device to device will be a requirement for a commercially viable fabrication process for the photonic bandgap devices.

Equally significant is the use of the thermal oxidation of III-V semiconductors to achieve high refractive index-contrast systems in the thesis. The thermal oxidation process has been successfully implemented and employed in both the 1-D and 2-D PBG devices. In the 1-D PBG devices, the thermal oxide forms a critical component of the high index-contrast waveguide system where the propagating electromagnetic mode is strongly guided within the waveguide. For the monorail microcavity, the high index-contrast between the photonic crystal and the supporting oxide is instrumental for the strong mode confinement at the defect region. In the case of the air-bridge microcavity, the thermal oxide also acts as a sacrificial material in the suspension of the micromechanical structure. Finally, the thermal oxide is used both in an index-confining layer and in a wide bandwidth distributed Bragg reflector mirror for the 2-D PBG LED. In sum, the thesis has demonstrated the incorporation of a new fabrication technique (i.e. the III-V thermal oxidation process) and a new material (i.e. the III-V thermal oxide) into a set of innovative device structures.

Overall, the devices described in this work have been designed and fabricated using III-V semiconductors. While the transmission characteristics of the 1-D PBG devices, in particular, have been demonstrated with indirect bandgap materials such as silicon[49], such devices will largely be limited to passive applications in the near term. The use of the direct bandgap III-V semiconductors introduces the immediate possibility of active device applications. The ability of the microcavity to vastly reduce the lasing threshold of an active device, for instance, will certainly be of immense interest and commercial promise. Device fabrication with III-V semiconductors, however, is clearly more

challenging than that with Si material. It is the hope of the author that this work has uncovered certain fabrication-related issues and laid the groundwork for extensions to the current effort.

Finally, the results reported in this thesis are truly the culmination of the collaboration between three primary research groups (see Chapter 1). The collaborative process has always been cordial, but not without inefficiencies and occasional misunderstanding. Yet, this thesis reflects the irreversible need for theorists and experimentalists of various backgrounds to cooperate on innovative research endeavors. In the realization of a novel photonic device such as the 1-D PBG air-bridge microcavity, for instance, the collective expertise of the physicists, the materials and fabrication engineers, and the optical characterization experts is ultimately the essential ingredient. Future research breakthroughs will undoubtedly depend on the complementary strengths of the various parties. This author believes that the experience gained in this cooperative effort presages fruitful collaboration within the photonic bandgap device research group at M.I.T. in the future.

6.2   Future Directions

The research described in this thesis has the luxury of being one of the earlier experimental efforts at realizing photonic bandgap devices in the optical wavelength regimes. As such, the future possible directions afforded by such a position are wide-ranging. Future extensions of the current work can be broadly demarcated into three levels, namely *materials, devices and systems*:

- **Materials**: The III-V thermal oxidation process is an invaluable capability for optical device design and fabrication. The electrical and optical confinement properties of the III-V thermal oxide are well documented, but further understanding of the nature of the oxide is required for consistent and reliable performance in device application. Information on the quality of the semiconductor/oxide interface and its effects on electrical and optical device properties, stress in the device structure induced by the oxidation process and heat recycling effects remain inadequate and anecdotal. While the literature provides considerable amount of data on the nature of the thermal oxide,

186

it is often prudent to verify the information with materials and processes unique to a particular device with a specific oxidation setup. In addition, the thermal oxidation processes of other III-V semiconductors, for instance InP-based compound semiconductor, should also be established and studied to widen the portfolio available for device and fabrication process design.

Another area pertaining to materials worthy of investigation is the suppression of non-radiative recombination at the exposed surfaces of the active regions. Most high index-contrast photonic bandgap devices require the formation of holes in semiconductors or dielectric columns. The ability to eliminate or reduce surface carrier recombination may be important for the success of active PBG devices.

- **Devices**: The currently passive 1-D PBG microcavity devices are excellent candidates for the realization of active PBG devices, such as ultralow threshold nanolasers. Optical excitation may be necessary for initial manifestations of the devices to reduce process complexity. An immediate issue with an active 1-D PBG microcavity device is the reabsorption in the non-active part of the device, as the microcavity region is small compared to the overall device. Once optically excited active devices have been demonstrated, added complexity arising from electrical injection of carriers will have to be resolved. In this regard, the thermal oxide may play a pivotal role in the formation of oxide-confined current aperture (see Figure 6-1). Also, a transparent air-bridge contact made of indium-tin oxide may be necessary for carrier injection into the top surface of the microcavity region.

Another area worthy of investigation is the active tuning of the currently passive devices. The ability to shift the resonance wavelength of the waveguide microcavities, for instance, may be attractive for wavelength division multiplexing applications in telecommunications. Further, active device tuning may be a solution to the correction of aberrations in device performance arising from the fabrication process.
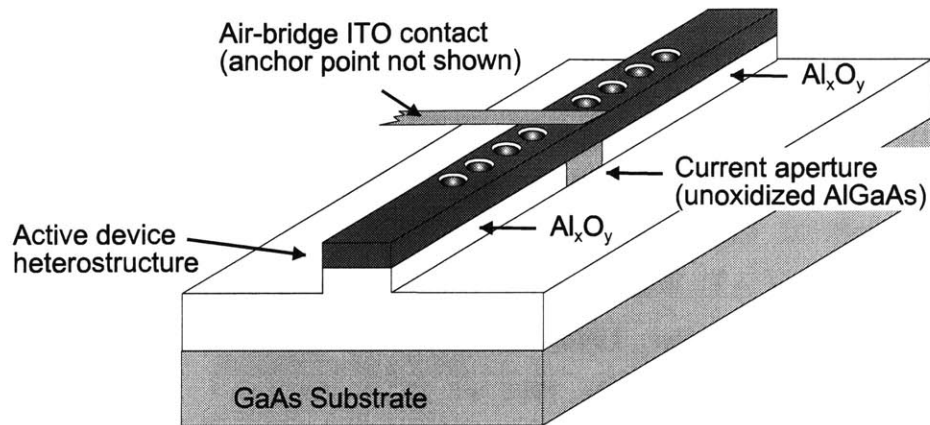
Figure 6-1:Schematic of proposed active 1-D PBG monorail microcavity device using an oxide-confined current aperture and an air-bridge transparent indium-tin-oxide (ITO) for carrier injection from the bottom and top surfaces of the microcavity region respectively.

Looking beyond the devices presented in this thesis, other PBG-based photonic devices can also be fabricated using III-V semiconductors based on the fabrication techniques explored in this work.

- **Systems**: The integration of PBG-based photonic devices and other photonic devices (PBG-based or otherwise) will clearly be a natural and invaluable progression of the research effort. Optical communication systems serve as the most likely entry point for PBG-based devices as mainstream components. Ultimately, the PBG devices may be critical in the implementation of an optical computing system.

Bibliography

1. I. Hayashi, in *Spontaneous emission and laser oscillation in microcavities*, H. Yokoyama and K. Ujihara, Editors. **1995**, CRC Press, New York. p. 337.

2. H.J. Caulfield, *Computer*, **1998**, *31*, 22.

3. M.W. Derstine, A.C. Walker, and T. Yatagai, *Appl. Optics*, **1998**, *37*, 2809.

4. E.M. Purcell, *Phys. Rev.*, **1946**, *69*, 681.

5. D. Kleppner, *Phys. Rev. Lett.*, **1981**, *47*, 233.

6. A.G. Vaidyanathan, W.P. Spencer, and D. Kleppner, *Phys. Rev. Lett.*, **1981**, *47*, 1592.

7. P. Goy, J.M. Raimond, M. Gross, and S. Haroche, *Phys. Rev. Lett.*, **1983**, *50*, 1903.

8. D. Meschede, H. Walther, and G. Mueller, *Phys. Rev. Lett.*, **1985**, *54*, 551.

9. W. Jhe, A. Anderson, E.A. Hinds, D. Meschede, L. Moi, and S. Haroche, *Phys. Rev. Lett.*, **1987**, *58*, 666.

10. D.J. Heinzen, J.J. Childs, J.E. Thomas, and M.S. Feld, *Phys. Rev. Lett.*, **1987**, *58*, 1320.

11. D.J. Heinzen and M.S. Feld, *Phys. Rev. Lett.*, **1987**, *59*, 2623.

12. T. Numai, T. Kawakami, T. Yoshikawa, M. Sugimoto, Y. Sugimoto, H. Yokoyama, K. Kasahara, and K. Asakawa, *IEEE J. Quantum Electron.*, **1993**, *27*, 1347.

13. T. Baba, T. Hamano, F. Koyama, and K. Iga, *IEEE J. Quantum Electron.*, **1991**, *27*, 1347.

14. S.L. McCall, A.F.J. Levi, R.E. Slusher, S.J. Pearton, and R.A. Logan, *Appl. Phys. Lett.*, **1992**, *60*, 289.

15. A.F.J. Levi, R.E. Slusher, S.L. McCall, S.J. Pearton, and W.S. Hobson, *Appl. Phys. Lett.*, **1993**, *62*, 2021.

16. M.S. Unlu and S. Strite, *J. of Appl. Physics*, **1995**, *78*, 607-39.

17. H. Yokoyama and S.D. Brorson, *J. Appl. Phys.*, **1989**, *66*, 4801.

18. J.D. Joannopoulos, R.D. Meade, J.N. Winn, and P.S.J. Russell, *Nature*, **1996**, *381*, p. 290.

19. P.R. Villeneuve and J.D. Joannopoulos, *Working at the speed of light: The fine art of making photonic crystals*, in *Science Spectra*. 1997. p. 18-24.

20. J.D. Joannopoulos, P.R. Villeneuve, and S. Fan, *Nature*, **1997**, *386*, 143.

21. E. Yablonovitch, *Phys. Rev. Lett.*, **1987**, *58*, 2059-62.

22. S. John, *Phys. Rev. Lett.*, **1987**, *58*, 2486.

23. A. Mekis, J.C. Chen, I. Kurland, S. Fan, P.R. Villeneuve, and J.D. Joannopoulos, *Phys. Rev. Lett.*, **1996**, *77*, 3787.

24. A. Yariv, in *Quantum Electronics*, John Wiley & Sons, New York 1975, .

25. E. Yablonovitch and T.J. Gmitter, *Phys. Rev. Lett.*, **1989**, *63*, 1950.

26. S. Satpathy, Z. Zhang, and M.R. Salehpour, *Phys. Rev. Lett.*, **1990**, *64*, 1239.

27. K.M. Leung and Y.L. Liu, *Phys. Rev. B*, **1990**, *41*, 10188.

28. K.M. Ho, C.T. Chan, and C.M. Soukoulis, *Phys. Rev. Lett.*, **1990**, *66*, 393.

29. H.S. Sozuer and J.W. Haus, *J. of the Optical Society of America. B, Optical*, **1993**, *10*, 296.

30. E. Yablonovitch, T.J. Gmitter, and K.M. Leung, *Phys. Rev. Lett.*, **1991**, *67*, 2295-8.

31. E. Yablonovitch, T.J. Gmitter, R.D. Meade, A.M. Rappe, K.D. Brommer, and J.D. Joannopoulos, *Phys. Rev. Lett.*, **1991**, *67*, 3380-3.

32. J.D. Joannopoulos, R.D. Meade, and J.N. Winn, in *Photonic crystals: Molding the flow of light*, Princeton University Press, Princeton, New Jersey 1995, .

33. C.C. Cheng and A. Scherer, *J. Vac. Sci. Technol.*, **1995**, *13*, p. 2696.

34. C.C. Cheng, A. Scherer, V. Arbet-Engels, and E. Yablonovitch, *J. Vac. Sci. Technol.*, **1996**, *14*, 4110.

35. H.S. Sozuer and J.P. Dowling, *J. of Modern Optics*, **1994**, *41*, 231.

36. R. Biswas, E. Ozbay, and K.M. Ho, *J. of Appl. Physics*, **1996**, *80*, 6749-53.

37. S. Noda, N. Yamamoto, and A. Sasaki, *Jpn. J. Appl. Phys. Part 2*, **1996**, *35*, L909.

38. S. Fan, P.R. Villeneuve, R.D. Meade, and Joannopoulos, *Appl. Phys. Lett.*, **1994**, *65*, 1466.

39. R.D. Meade, A.M. Rappe, and K.D. Brommer, *J. of the Optical Society of America. B, Optical*, **1993**, *10*, 328.

40. R.D. Meade, A. Devenyi, and J.D. Joannopoulos, *J. of Appl. Physics*, **1994**, *75*, 4753.

41. J.R. Wendt, G.A. Vawter, P.L. Gourley, T.M. Brennan, and B.E. Hammons, *J. Vac. Sci. Technol. B*, **1993**, *11*, 2637.

42. P.L. Gourley, J.R. Wendt, G.A. Vawter, T.M. Brennan, and B.E. Hammons, *Appl. Phys. Lett.*, **1994**, *64*, 687.

43. S. Fan, P.R. Villeneuve, J.D. Joannopoulos, and E.F. Schubert, *Phys. Rev. Lett.*, **1997**, *78*, 3294.

44. P.R. Villeneuve, S. Fan, J.D. Joannopoulos, K.-Y. Lim, J.C. Chen, G.S. Petrich, L.A. Kolodziejski, and R. Reif, in *Proceedings of NATO Advanced Studies*

Institute on Photonic Band Gap Materials, (Elounda, Crete, Greece), **1995**, Kluwer Academic Publishers, pp. 411.

45.   K.-Y. Lim, M.Eng. Thesis, Department of Electrical Engineering and Computer Science, Massachusetts Institute of Technology, (Cambridge MA), **1994.**

46.   P.R. Villeneuve, S. Fan, J.D. Joannopoulos, K.-Y. Lim, G.S. Petrich, L.A. Kolodziejski, and R. Reif, *Appl. Phys. Lett.*, **1995**, *67*, 167.

47.   C.N. Tziligakis, S.M. Thesis, Department of Electrical Engineering and Computer Science, Massachusetts Institute of Technology, (Cambridge, MA), **1996.**

48.   J.C.-y. Chen, Ph.D. Thesis, Electrical Engineering and Computer Science, Massachusetts Institute of Technology, (Cambridge, MA), **1996.**

49.   J.S. Foresi, P.R. Villeneuve, J. Ferrera, E.R. Thoen, G. Steinmeyer, S. Fan, J.D. Joannopoulos, L.C. Kimerling, H.I. Smith, and E.P. Ippen, *Nature*, **1997**, *390*, 143.

50.   M.H. MacDougal, H. Zhao, P.D. Dapkus, M. Ziari, and W.H. Steier, *Electron. Lett.*, **1994**, *30*, 1147.

51.   T.F. Krauss, B. Voegele, C.R. Stanley, and R.M. De La Rue, *IEEE Photon. Technol. Lett.*, **1997**, *9*, 176.

52.   P.R. Villeneuve, S. Fan, S.G. Johnson, and J.D. Joannopoulos, *Submitted to IEE Proceedings - Optoelectronics Special Issue on Photonic Crystals and Photonic Microstructures*, **1998,**

53.   J.P. Zhang, D.Y. Chu, S.L. Wu, W.G. Bi, R.C. Tiberio, R.M. Joseph, A. Taflove, C.W. Tu, and S.T. Ho, *IEEE Photon. Technol. Lett.*, **1996**, *8*, 491.

54.   J.C. Chen, H.A. Haus, S. Fan, P.R. Villeneuve, and J.D. Joannopoulos, *J. of Lightwave Technology*, **1996**, *14*, 2575.

55.   P.R. Villeneuve, D.S. Abrams, S. Fan, and J.D. Joannopoulos, *Optics Letters*, **1996**, *21*, 2017.

56.   Z.L. Zhang, G.A. Porkolab, and N.C. MacDonald, in *Micro Electro Mechanical Systems '92*, (Travemuende, Germany), **1992**, pp. 72.

57.   K. Fricke, H.L. Hartnagel, S. Ritter, and J. Wuerfl, *Microelectronic Engineering*, **1992**, *19*, 195.

58.   C. Ovren, M. Adolfsson, and B. Hok, *Opt. Lasers Eng.*, **1984**, *5*, 155.

59.   J. Soderkvist and K. Hjort, *J. Micromech. Microeng.*, **1994**, *4*, 28.

60.   E. Yablonovitch, D.M. Hwang, T.J. Gmitter, L.T. Florez, and J.P. Harbison, *Appl. Phys. Lett.*, **1990**, *56*, 2419.

61.   X.S. Wu, L.A. Coldren, and J.L. Merz, *Electron. Lett.*, **1985**, *21*, 558.

62.   A.W. Adamson and A.P. Gast, in *Physical Chemistry of Surfaces*, Wiley Interscience, New York, NY., **1997.**

63. M. Schubert, V. Gottschalch, C.M. Herzinger, H. Yao, P.G. Snyder, and J.A. Wollam, *J. Appl. Phys.*, **1995**, *77*, 3416.

64. K.-Y. Lim, S.B. Thesis, Electrical Engineering and Computer Science, Massachusetts Institute of Technology, (Cambridge, MA), **1994.**

65. E.A. Marley, S.M. Thesis, Electrical Engineering and Computer Science, Massachusetts Institute of Technology, (Cambridge, MA), **1996.**

66. J.L. House, Sc.D. Thesis, Electrical engineering and computer science, MIT, (Cambridge, MA), **1997.**

67. J. Ferrera, S.M. Thesis, Electrical Engineering and Computer Science, M.I.T., (Cambridge, MA), **1994.**

68. H.I. Smith, S.D. Hector, M.L. Schattenburg, and E.H. Anderson, *J. Vac. Sci. Technol.*, **1991**, *9*, 2992.

69. Shipley Corporation, *Microposit SAL 601 E-Beam Resist Technical Specifications*, **1991**.

70. H.-Y. Liu, J. Seeger, E. Poon, R.J. Olsen, K.A. Graziano, and S.E. Anderson, *J. Vac. Sci. Technol. B*, **1989**, *7*, 1740.

71. C.Y. Chang and S.M. Sze, in *ULSI Technology*, John Wiley & Sons, New York **1996**.

72. K. Hjort, *J. Micromech. Microeng.*, **1996**, *6*, 370.

73. A. Spisser, R. Ledantec, C. Seassal, J.L. Leclercq, T. Benyattou, D. Rondi, R. Blondeau, G. Guillot, and P. Viktorovitch, *IEEE Photon. Technol. Lett.*, **1998**, *10*, 1259.

74. N. Tas, T. Sonnenberg, H. Jansen, R. Legtenberg, and M. Elwenspoek, *J. Micromech. Microeng.*, **1996**, *6*, 385.

75. C.H. Mastrangelo and C.H. Hsu, *IEEE J. of Microelectromechanical systems*, **1993**, *2*, 44.

76. Y. Backlund, K. Hermansson, and L. Smith, *J. Electrochem. Soc.*, **1992**, *139*, 2299.

77. G.A. Spierings and J. Haisma, in *1st Int. Symp. on Semiconductor Wafer Bonding, Science, Technology and Applications*, (Phoenix, AZ.), **1991**, pp. 18.

78. C.H. Mastrangelo and C.H. Hsu, *IEEE J. of Microelectromechanical systems*, **1993**, *2*, 33.

79. L.S. Fan, Y. Tai, and R.S. Muller, *Sensors Actuators*, **1989**, *20*, 41.

80. Y. Yee, K. Chun, and J.D. Lee, in *8th Int. Conf. on Solid-State Sensors and Actuators (Transducers '95)*, (Stockholm), **1995**, 206.

81. H.V. Jansen, J.G.E. Gardeniers, J. Elders, H.A.C. Tilmans, and M.C. Elwenspoek, *Sensors Actuators A*, **1994**, *41*, 136.

82. C.J. Kim, J.Y. Kim, and B. Sridharan, *Sensors and actuators A*, **1998**, *64*, 17.

83.   N. Takeshima, K.J. Gabriel, M. Ozaki, J. Takahashi, H. Horiguchi, and H. Fujita, , **1991,**, 63.

84.   M.J. Madou, in*Fundamentals of microfabrication*, CRC Press, Boca Raton, Fl. **1997**.

85.   R.J. Schutz, in *VLSI Technology*, S.M. Sze, Editor. **1988**, McGraw-Hill,New York. p. 676.

86.   PlasmaTherm Incorporated, *PlasmaTherm Inc. Series 700 RIE/PECVD System: RIE Documentation*, **1987.**

87.   A.J. Carter, B. Thomas, D.V. Morgan, and J.K. Bhardwj, *Mat. Res. Soc. Symp. Proc.*, **1989,** *144*, 683.

88.   W.T. Tsang, *Appl. Phys. Lett.*, **1978,** *33*, 426.

89.   W.T. Tsang, M. Olmstead, and R.P.H. Chang, *Appl. Phys. Lett.*, **1979,** *34*, 408.

90.   J.M. Dallesasse, N. Holonyak, Jr., A.R. Sugg, T.A. Richard, and N. El-Zein, *Appl. Phys. Lett.*, **1990,** *57*, 2844.

91.   J.M. Dallesasse, N.J. Holonyak, A.R. Sugg, T.A. Richard, and N. El-Zein, *J. Appl. Phys.*, **1990,** *68*, 2235.

92.   J.M. Dallesasse and N.J. Holonyak, *Appl. Phys. Lett.*, **1991,** *58*, 394.

93.   S.A. Maranowski, A.R. Sugg, E.I. Chen, and N. Holonyak, Jr., *Appl. Phys. Lett.*, **1993,** *63*, 1660.

94.   F.A. Kish, S.J. Caracci, N.J. Holonyak, J.M. Dallesasse, K.C. Hsieh, M.J. Ries, S.C. Smith, and R.D. Burnham, *Appl. Phys. Lett.*, **1991,** *59*, 1755.

95.   G.M. Yang, M.H. MacDougal, and P.D. Dapkus, *Electron. Lett.*, **1995,** *31*, 886.

96.   K.D. Choquette, R.P. Schneider, K.L. Lear, and K.M. Geib, *Electron. Lett.*, **1994,** *30*, 2043.

97.   K.L. Lear, K.D. Choquette, R.P. Schneider, S.P. Kilcoyne, and K.M. Geib, *Electron. Lett.*, **1995,** *31*, 208.

98.   M.H. MacDougal, P.D. Dapkus, V. Pudikov, and H.G.M. Yang, *IEEE Photon. Technol. Lett.*, **1995,** *7*, 229.

99.   A. Fiore, V. Berger, E. Rosencher, N. Laurent, S. Theilmann, N. Vodjdani, and J. Nagle, *Appl. Phys. Lett.*, **1996,** *68*, 1320.

100.   S.J. Caracci, M.R. Krames, N. Holonyak, Jr., C.M. Herzinger, A.C. Crook, T.A. DeTemple, and P.A. Besse, *Appl. Phys. Lett.*, **1993,** *63*, 2265.

101.   O. Blum, K.L. Lear, H.Q. Hou, and M.E. Warren, *Electron. Lett.*, **1996,** *32*, 1406.

102.   L. Kou, D.C. Hall, and H. Wu, *Appl. Phys. Lett.*, **1998,** *72*, 3411.

103.   E.I. Chen, N. Holonyak Jr, and S.A. Maranowski, *Appl. Phys. Lett.*, **1995,** *66*, p. 2688.

104. P.A. Grudowski, R.V. Chelakara, and R.D. Dupuis, *Appl. Phys. Lett.*, **1996**, *69*, 388.

105. O. Blum, K.M. Geib, M.J. Hafich, J.F. Klem, and C.I.H. Ashby, *Appl. Phys. Lett.*, **1996**, *68*, 3129.

106. H. Gebretsadik, K. Kamath, W.-D. Zhou, P. Bhattacharya, C. Caneau, and R. Bhat, *Appl. Phys. Lett.*, **1998**, *72*, 135.

107. C.I.H. Ashby, J.P. Sullivan, P.P. Newcomer, N.A. Missert, H.Q. Hou, B.E. Hammons, M.J. Hafich, and A.G. Baca, *Appl. Phys. Lett.*, **1997**, *70*, 2443.

108. K.D. Choquette, K.M. Geib, C.I.H. Ashby, B.O. Twesten, H.Q. Hou, D.M. Follstaedt, B.E. Hammons, D. Mathes, and R. Hull, *IEEE J. of Selected Topics in Quantum Electronics*, **1997**, *3*, 916.

109. W.J. Mitchell, C.H. Chung, S.I. Yi, E.L. Hu, and W. Weinberg, *Surface science*, **1997**, *384*, 81.

110. C.I.H. Ashby, J.P. Sullivan, K.D. Choquette, K.M. Geib, and H.Q. Hou, *J. Appl. Phys.*, **1997**, *82*, 3134.

111. C.I.H. Ashby, R.D. Twesten, K.D. Choquette, D.M. Follstaedt, K.M. Geib, O. Blum, and H.Q. Hou, in *40th Electronic Materials Conference*, (University of Virginia, Charlottesville, VI), **1998**.

112. R.D. Twesten, D.M. Follstaedt, and K.D. Choquette, in *Proceedings of SPIE:Vertical-Cavity Surface-Emitting Lasers*, (San Jose, CA), **1997**, pp. 55.

113. R.S. Burton and T.E. Schlesinger, *J. Appl. Phys.*, **1994**, *76*, 5503.

114. J.H. Kim, D.H. Lim, K.S. Kim, G.M. Yang, and L.H. Lim, *Appl. Phys. Lett.*, **1996**, *69*, 3357.

115. K.M. Geib, K.D. Choquette, H.Q. Hou, and B.E. Hammons, *Proc. SPIE Int. Soc. Opt. Eng.*, **1997**, *3003*, 69.

116. B.E. Deal and A.S. Grove, *J. Appl. Phys.*, **1965**, *76*, 5503.

117. M. Ochiai, G.E. Giudice, H. Temkin, J.W. Scott, and T.M. Cockerill, *Appl. Phys. Lett.*, **1996**, *68*, 1898.

118. F.A. Kish, S.A. Maranowski, G.E. Hofler, N.J. Holonyak, S.J. Caracci, J.M. Dallesasse, and K.C. Hsieh, *Appl. Phys. Lett.*, **1992**, *60*, 3165.

119. T. Yoshikawa, H. Saito, H. Kosaka, Y. Sugimoto, and K. Kasahara, *Appl. Phys. Lett.*, **1998**, *72*, 2310.

120. R.L. Naone and L.A. Coldren, *J. of Appl. physics*, **1997**, *82*, 2277.

121. O. Blum, C.I.H. Ashby, and H.Q. Hou, *Appl. Phys. Lett.*, **1997**, *70*, 2870.

122. R.L. Naone, E.R. Hegbloom, B.J. Thibeault, and L.A. Coldren, *Electron. Lett.*, **1997**, *33*, 300.

123. K.D. Choquette, K.M. Geib, H.C. Chui, B.E. Hammons, H.Q. Hou, T.J. Drummond, and R. Hull, *Appl. Phys. Lett.*, **1996**, *69*, 1385.

124. M.H. MacDougal and P.D. Dapkus, *IEEE Photon. Technol. Lett.*, **1997**, *9*, 884.

125. K.D. Choquette, K.M. Geib, H.C. Chui, B.E. Hammons, H.Q. Hou, T.J. Drummond, and R. Hull, *Appl. Phys. Lett.*, **1996**, *69*, 1385.

126. J.P. Landesman, A. Fiore, and J. Nagle, *Appl. Phys. Lett.*, **1997**, *71*, 2520.

127. J.A. Kash, B. Pezeshki, F. Agahi, and N.A. Bojarczuk, *Appl. Phys. Lett.*, **1995**, *67*, 2022.

128. S.S. Shi, E.L. Hu, J.-P. Zhang, Y.-l. Chang, P. Parikh, and U. Mishra, *Appl. Phys. Lett.*, **1997**, *70*, 1293.

129. A.R. Pratt, T. Takamori, and T. Kamijoh, *Appl. Phys. Lett.*, **1997**, *71*, 1394.

130. H. Gebretsadik, K. Zhang, and K. Kamath, *Appl. Phys. Lett.*, **1997**, *71*, 3865.

131. M.H. MacDougal, J. Geske, C.-K. Lin, A.E. Bond, and P.D. Dapkus, *IEEE Photon. Technol. Lett.*, **1998**, *10*, 15.

132. A.R. Sugg, E.I. Chen, T.A. Richard, N. Holonyak, K.C. Hsieh, J.E. Baker, and N. Finnegan, *J. Appl. Phys.*, **1993**, *74*, 3880.

133. S.G. Hummel, M.H. MacDougal, and P.D. Dapkus, *Electron. Lett.*, **1995**, *31*, 972.

134. E.D. Palik, in *Handbook of optical constants of solids*. **1991**, Academic Press, Boston. p. 429.

135. P.R. Villeneuve, *Personal communication with Dr. Pierre R. Villeneuve on 1-D PBG microcavity simulations*, **1998**.

136. H. De Neve, J. Blondelle, R. Baets, P. Demeester, P. Van Daele, and G. Borghs, *IEEE Photonics Technol. Lett.*, **1995**, *7*, 287.

137. P. Bhattacharya, in *Semiconductor optoelectronic devices*, Prentice-Hall Inc., Englewood Cliffs, NJ. **1994**, pp. 535.

138. E. Yablonovitch, T.J. Gmitter, J.P. Harbison, and R. Bhat, *Appl. Phys. Lett.*, **1987**, *51*, 2222.

139. F.A. Kish, D.A. Vanderwater, D.C. Defevere, D.A. Steigerwalad, G.E. Hofler, K.G. Park, and F.M. Steranka, *Electron. Lett.*, **1996**, *32*, 132.

140. W.N. Carr and G.E. Pittman, *Appl. Phys. Lett.*, **1963**, *3*, 173.

141. I. Schnitzer and E. Yablonovitch, *Appl. Phys. Lett.*, **1993**, *63*, 2174.

142. E.F. Schubert, N.E.J. Hunt, M. Micovic, R.J. Malik, D.L. Sivco, A.Y. Cho, and G.J. Zydzik, *Science*, **1994**, *265*, 943.

143. H. Benisty, H. De Neve, and C. Weisbuch, *IEEE J. Quantum Electron.*, **1998**, *34*, 1612.

144. H. De Neve, J. Blondelle, P. Van Daele, P. Demeester, R. Baets, and G. Borghs, in *Light emitting diodes: researc h, manufacturing, and applications.*, (San Jose, CA.), **1997**, pp. 74.

145. S. Fan, *Personal communication with Dr. S. Fan on the design of the 2-D PBG LED structure*, **1998**.